INFORMATION TO USERS

This manuscript has been reproduced from the microfilm master. UMI films the text directly from the original or copy submitted. Thus, some thesis and dissertation copies are in typewriter face, while others may be from any type of computer printer.

The quality of this reproduction is dependent upon the quality of the copy submitted. Broken or indistinct print, colored or poor quality illustrations and photographs, print bleedthrough, substandard margins, and improper alignment can adversely affect reproduction.

In the unlikely event that the author did not send UMI a complete manuscript and there are missing pages, these will be noted. Also, if unauthorized copyright material had to be removed, a note will indicate the deletion.

Oversize materials (e.g., maps, drawings, charts) are reproduced by sectioning the original, beginning at the upper left-hand corner and continuing from left to right in equal sections with small overlaps.

Photographs included in the original manuscript have been reproduced xerographically in this copy. Higher quality 6" x 9" black and white photographic prints are available for any photographs or illustrations appearing in this copy for an additional charge. Contact UMI directly to order.

Bell & Howell Information and Learning
300 North Zeeb Road, Ann Arbor, MI 48106-1346 USA

UMI®
800-521-0600

ANALYTICAL MODELING OF REINFORCED CONCRETE BEAM COLUMN CONNECTIONS FOR SEISMIC LOADING

By

MOSTAFA SAAD ELDINE ELMORSI, B Sc., M.Eng.

A Thesis

Submitted to the School of Graduate Studies

in Partial Fulfilment of the Requirements

for the Degree

Doctor of Philosophy

McMaster University

© Copyright by Mostafa Elmorsi, June 1998.

ANALYTICAL MODELING OF REINFORCED CONCRETE BEAM COLUMN CONNECTIONS FOR SEISMIC LOADING

To my dear wife, Riham,

for her love and continuous support

DOCTOR OF PHILOSOPHY (1998) McMaster University

(Civil Engineering) Hamilton, Ontario, Canada

TITLE: ANALYTICAL MODELING OF REINFORCED CONCRETE BEAM COLUMN CONNECTIONS FOR SEISMIC LOADING

AUTHOR: Mostafa Saad Eldine Elmorsi, B.Sc. (Ain Shams University)
M.Eng. (McMaster University)

SUPERVISORS: Dr. W. K. Tso and Dr. M. R. Kianoush

NUMBER OF PAGES: xix, 236

ABSTRACT

Reinforced concrete beam column joints are critical members in frame structures since they can be subjected to high shear forces under earthquake loading. As a consequence, they can experience high shear and bond slip deformations that contribute significantly to the story drift. Moreover, the joint capacity may be exceeded leading to a joint shear failure that can have a major impact on the overall stability of the entire structure. This condition is particularly pronounced in lightly reinforced concrete structures where the beam column joints are typically the weakest link in the lateral load resistant frame. There is a persistent need to develop an analytical model that accounts for their shear and bond slip deformations in order to predict realistically their response and assess their safety.

A finite element based analytical model is developed in this thesis for the beam column connection region. The model overcomes the need of using refined meshes of simple elements by using high power elements in the critical regions of the joint panel and the plastic hinge zones in the beams and the columns. The proposed model takes into account the shear and bond slip deformations in the joint panel as well as flexural and shear deformations in the plastic hinge zones in the beams and the columns. Material non-linearities associated with the concrete and steel behavior are

taken into account. Bond slip relationship between the beam reinforcement and concrete in the joint panel is considered. The material models developed in this thesis are verified at the element level before the verification is made to the entire beam column connection model. The predictions of the model are compared with experimental data for beam column subassemblies experiencing high shear and/or bond slip deformations. The success of the proposed model is demonstrated by the good correlation achieved with the experimental data. The model is then used in the analysis of a three story reinforced concrete frame structure designed without consideration of earthquake loads. The structure is analyzed using different joint detailing schemes using pushover and time history analyses to investigate the effect of the joint detailing on the response of the structure.

It is concluded that the proposed beam column connection model can be used successfully for the dynamic analysis of a complete multistory structure.

ACKNOWLEDGMENT

The author wishes to express his sincere appreciation to Dr. W. K. Tso and Dr. M. R. Kianoush for their guidance, advice, and friendly supervision during the course of this study. Special thanks are due to Dr. A. Ghobarah and Dr. D. S. Weaver, members of my supervisory committee, for their valuable comments and suggestions. The advise and encouragements of Dr. F. Mirza and Dr. R. Sowerby are also deeply appreciated.

The financial support of McMaster University and Ryerson Polytechnic University are gratefully acknowledged.

Thanks are due to the author's family, wife, and friends at McMaster University, for their encouragement and moral support which made this work a reality.

TABLE OF CONTENTS

Page

ABSTRACT iii

ACKNOWLEDGMENT v

TABLE OF CONTENTS vi

LIST OF TABLES x

LIST OF FIGURES xii

CHAPTER 1 INTRODUCTION

1.1 BACKGROUND AND MOTIVATION 1

1.2 LITERATURE REVIEW 3
1.2.1 Equilibrium Criteria for Connections 3
1.2.2 Experimental Studies 3
1.2.3 Analytical Models 7

1.3 OBJECTIVES AND SCOPE 10

1.4 ORGANIZATION OF THE THESIS 11

CHAPTER 2 KINEMATIC MODEL FOR THE BEAM COLUMN CONNECTION

2.1 GENERAL 17

2.2 JOINT PANEL MODEL 17

2.3 BEAM COLUMN CONNECTION MODEL 19

2.4 ELEMENTS SHAPE FUNCTIONS AND STIFFNESS MATRIX 20

2.5 COMPATIBILITY OF TRANSITION AND LINE ELEMENTS 25

2.6 PC-ANSR COMPUTER PROGRAM 30

2.7 DISPLACEMENT CONTROL PROGRAM 31

2.8 LINEAR ELASTIC ANALYSIS 32

2.9 CONCLUSIONS 34

CHAPTER 3 MATERIAL MODEL FOR REINFORCED CONCRETE

3.1 GENERAL 41

3.2 MATERIAL MODEL FOR CONCRETE 43

3.3 THE NORMAL STRESS FUNCTION 45
3.3.1 Concrete Tension Envelop 46
3.3.2 Concrete Compression Envelop 47
3.3.3 Strength and Stiffness Degradation Effects Parallel to the Crack Direction 51
3.3.4 Cyclic Tensile Stress Strain Relations 52
3.3.5 Cyclic Compressive Stress Strain Relations 55
3.3.6 Interaction between Tension and Compression Models . 56

3.4 THE SHEAR STRESS FUNCTION 57
3.4.1 Shear Stiffness of Cracked Concrete 58
3.4.2 Cyclic Shear Transfer Model 60

3.5 MATERIAL MODEL FOR STEEL REINFORCEMENT 61
3.5.1 Cyclic Stress Strain Relationship for Reinforcing Steel . 62

3.6 GLOBAL AXES TRANSFORMATION 65

3.7 EXPERIMENTAL VERIFICATION 66

3.8 CONCLUSIONS 68

3.9 LIST OF SYMBOLS 70

CHAPTER 4 BOND SLIP MODEL

4.1 GENERAL 93

4.2 FINITE ELEMENT MODEL FOR BOND SLIP 96

4.3 BOND RESISTANCE MECHANISM 100
4.3.1 Bond Resistance Mechanism for Monotonic Loading . 100
4.3.2 Bond Resistance Mechanism for Cyclic Loading 102

4.4 ANALYTICAL BOND SLIP MATERIAL MODEL 104
4.4.1 Monotonic Envelope 105
4.4.2 Reduced Envelopes 106
4.4.3 Unloading and Friction Branch 108
4.4.4 Effects of Variations of Properties 109

4.5 VERIFICATION OF THE BOND SLIP MODEL 109
4.5.1 Specimens Tested under Increasing Monotonic Loading 110
4.5.2 Specimens Tested under Reversed Cyclic Loading ... 113

4.6 PROPOSED BEAM COLUMN JOINT MODEL 114

4.7 CONCLUSIONS 115

4.8 LIST OF SYMBOLS 116

CHAPTER 5 VERIFICATION OF THE BEAM COLUMN CONNECTION MODEL

5.1 GENERAL 132

5.2 TESTS UNDER INCREASING MONOTONIC LOADING . 132

5.3 TESTS UNDER REVERSED CYCLIC LOADING 134

5.3.1 Specimens Tested by Kaku and Asakusa (1991) 134
5.3.2 Specimen Tested by Fujii and Morita (1991) 137
5.3.3 Specimens Tested by Viwathanatepa et al. (1979) 138

5.4 CONCLUSIONS 142

CHAPTER 6 DYNAMIC ANALYSIS OF A THREE STORY FRAME BUILDING

6.1 GENERAL 164

6.2 DESCRIPTION OF THE STRUCTURE 164

6.3 PUSHOVER ANALYSIS 166
6.3.1 Overall Displacements and Drifts 167
6.3.2 Failure Mechanisms 168
6.3.3 Joints Deformations 169
6.3.4 Beams and Columns Deformations 171

6.4 DYNAMIC ANALYSIS 172
6.4.1 Selection of Earthquake Records 174
6.4.2 Roof Displacement Time Histories 174
6.4.3 Envelopes of Story Shear and Failure Mechanisms 175
6.4.4 Envelopes of Lateral Displacements and Interstory Drifts 176
6.4.5 Envelopes of Joint Deformations 177
6.4.6 Envelopes of Beam and Column Deformations 178

6.5 CONCLUSIONS 180

CHAPTER 7 CONCLUSIONS AND RECOMMENDATIONS

7.1 SUMMARY AND CONCLUSIONS 209

7.2 RECOMMENDATIONS FOR FUTURE RESEARCH 212

REFERENCES 214

APPENDIX A MANUAL FOR NEW ELEMENTS IN PC-ANSR . . . 222

APPENDIX B ATTACHED DISK

APPENDIX C INPUT DATA FOR TESTED SPECIMENS 230

LIST OF TABLES

Table	Title	Page
3.1	Material properties of PCA wall specimens	74
4.1	Parameters for bond stress slip envelope curve for 25 mm bar	117
5.1	Properties of test specimens (Kaku and Asakusa, 1991)	143
5.2	Properties of test specimen (Fujii and Morita, 1991)	144
6.1	Properties of selected earthquakes	181

LIST OF FIGURES

Figure	Title	Page
1.1	Example of beam column joint failures in the 1985 Mexico earthquake (Cheung et al., 1993)	13
1.2	Equilibrium of interior beam column subassemblage (Paulay, 1989)	4
1.3	Diagonal shear cracking of the joint core	15
1.4	Concentrated bond rotations at the beam column interface	15
1.5	Idealization of the beam column joint by Pessiki et al. (1990)	16
2.1	Reinforced concrete elements	35
2.2	Proposed beam column connection element	36
2.3	Twelve node plane stress element	37
2.4	Ten node plane stress element	37
2.5	Compatibility of a horizontal line element with; (a) two transition elements; (b) a transition element and a line element	38
2.6	Compatibility of a vertical line element with; (a) two transition elements; (b) a transition element and a line element	38
2.7	Displacement control program	39
2.8	Three models for an exterior beam column connection; (a) a finite element mesh of twenty two 12 node quadrilateral elements; (b) the proposed model; (c) rigid connection	39
2.9	Load deflection curves for an exterior beam column connection	40
2.10	Shear stress distribution in the joint panel region	40

3.1 The coordinates of cracked concrete 75

3.2 Stress strain curve for concrete in tension 76

3.3 Stress strain curve for concrete in compression 76

3.4 Stress strain curves for confined and unconfined concrete in compression 76

3.5 Deteriorated compression response of cracked concrete 77

3.6 Softening coefficient for cracked concrete 77

3.7 Typical cyclic stress crack width relationship (Yankelevsky and Reinhardt (1989)) 78

3.8 Proposed cyclic stress strain curve for crack opening and closing 78

3.9 Proposed cyclic stress strain curve for concrete in compression 79

3.10 Estimation of the unloading stiffness 79

3.11 Unconfined cyclic compression test by Karsan and Jirsa (1969); (a) complete test; (b) first two cycles; (c) last three cycles 80

3.12 Unconfined cyclic compression test by Karsan and Jirsa (1969); (a) complete test; (b) first three cycles; (c) last two cycles 81

3.13 Unconfined cyclic compression test by Okamoto et al. (1976); (a) complete test; (b) first two cycles; (c) last two cycles 82

3.14 Typical analytical normal stress strain relationship for concrete 83

3.15 Relationship between cracked shear stiffness and normal strain across the cracks 83

3.16 Proposed cyclic shear transfer model 84

3.17 Typical stress strain relationship for steel reinforcement under cyclic loading 85

3.18 Stress strain curve for bar number BR01 from Seckin (1981); (a) Experimental results; (b) Analytical results 86

3.19 Stress strain curve for bar number BR07 from Seckin (1981); (a) Experimental results; (b) Analytical results 87

3.20 Stress strain curve for bar number BR13 from Seckin (1981); (a) Experimental results; (b) Analytical results 88

3.21 Nominal dimensions of the PCA wall specimen and the finite element descretization 89

3.22 Load deflection curve for wall B2; 1 kip = 4.448 kN, 1 in = 25.4 mm .. 90

3.23 Load deflection curve for wall B5; 1 kip = 4.448 kN, 1 in = 25.4 mm .. 91

3.24 Load deflections curve for wall R2; 1 kip = 4.448 kN, 1 in = 25.4 mm . 92

4.1 Boundary conditions of bonded bar 118

4.2 Proposed bond slip element 118

4.3 Bond resistance mechanism for monotonic loading (Eligehausen et al., 1983) 119

4.4 Bond resistance mechanism for cyclic loading (Eligehausen et al., 1983) 120

4.5 Proposed analytical material model for bond stress - slip relationship . 121

4.6 Monotonic envelop curve for bond stress - slip relationship 122

4.7 Different regions and corresponding bond stress slip envelop curves in an interior joint (Eligehausen et al., 1983) 122

4.8 Ratio between τ_3 of reduced envelop and monotonic envelop as a function of the damage factor d (Eligehausen et al., 1983) 123

4.9 Relationship between the damage factor d, and the dimensionless energy dissipation E/Eo (Eligehausen et al., 1983) 123

4.10 Relationship between τ_f of initial cycle and τ_3 (Eligehausen et al., 1983) 124

4.11 Relationship between the damage factor, d_f, and the dimensionless energy dissipation E_f / E_o (Eligehausen et al., 1983) 124

4.12 Comparison of the proposed bond slip model and Eligehausen's model 125

4.13 Monotonic pull out test for anchored specimen tested by Viwathanatepa et al. (1979) 126

4.14 Monotonic push pull test for anchored specimen tested by Viwathanatepa et al. (1979) 127

4.15 Slip distribution across anchored length for pull out test specimen ... 128

4.16 Slip distribution across anchored length for push pull test specimen .. 128

4.17 Stress slip response of anchored bar; load cycles before yielding of reinforcing steel; (a) Experimental (Viwathanatepa et al., 1979), (b) Analytical (Monti et al., 1997), (c) Analytical (Proposed model) 129

4.18 Stress slip response of anchored bar; load cycles after yielding of reinforcing steel; (a) Experimental (Viwathanatepa et al., 1979), (b) Analytical (Monti et al., 1997), (c) Analytical (Proposed model) 130

4.19 Proposed beam column connection element 131

5.1 Dimensions and reinforcement details of specimen tested by Otani et al. (1985) 145

5.2 Finite element idealization for specimen C1; (a) Pantazopoulou and Bonacci's model, (b) proposed model 146

5.3 Story shear force story drift relationships for specimen tested by Otani et al. (1985) 146

5.4 Dimensions and reinforcement details of specimen tested by Kaku and Asakusa (1991) 147

5.5 Beam shear force story drift relationships for specimen tested by Kaku and Asakusa (1991) 148

5.6 Envelopes of cyclic beam shear force story drift curves 149

5.7 Envelopes of cyclic shear stress shear strain in the joint 149

5.8 Beam shear force story drift relationships for specimen tested by Kaku and Asakusa (1991) 150

5.9 Envelopes of cyclic beam shear force story drift curves 151

5.10 Envelopes of cyclic shear stress shear strain in the joint 151

5.11 Dimensions and reinforcement details of specimen tested by Fujii and Morita (1991) 153

5.12 Beam shear force story drift relationships for specimen tested by Fujii and Morita (1991) 153

5.13 Envelopes of cyclic beam shear force story drift curves 154

5.14 Envelopes of cyclic shear stress shear strain in the joint 154

5.15 Dimensions and reinforcement details of specimens tested by Viwathanatepa et al. (1979) 155

5.16 Load application to Filippou's model (Filippou et al., 1983a, b) 156

5.17 Load application to the proposed beam column connection model . . . 156

5.18 Moment rotation relationship for specimen BC4 (West beam) 157

5.19 Moment rotation relationship for specimen BC4 (East beam) 157

5.20 Moment slip relationship for specimen BC4 158

5.21 Moment slip relationship for specimen BC4 159

5.22 Moment slip relationship for specimen BC4 160

5.23 Moment slip relationship for specimen BC4 161

5.24 Moment rotation relationship for specimen BC3 (West beam) 162

5.25 Moment rotation relationship for specimen BC3 (East beam) 163

6.1 Typical floor plan 182

6.2 Details of analyzed frame 183

6.3 Analyzed beam column joints configurations 184

6.4 Lateral load distribution for push over analysis 185

6.5 Base shear roof displacement relationship due to pushover loading 185

6.6 Maximum story displacements and interstory drifts due to pushover loading 186

6.7 Plastic hinges formation due to push over loading 187

6.8 Envelopes of joint deformations for connections on column C1 due to push over loading 188

6.9 Envelopes of joint deformations for connections on column C2 due to pushover loading 189

6.10 Envelopes of joint deformations for connections on column C3 due to pushover loading 190

6.11 Envelopes of joint deformations for connections on column C4 due to pushover loading 191

6.12 Base shear joint deformation relationships for joint J11 due to pushover loading 192

6.13 Base shear joint deformation relationships for joint J12 due to pushover loading 193

6.14 Base shear joint deformation relationships for joint J13 due to pushover loading 194

6.15 Base shear joint deformation relationships for joint J14 due to pushover loading 195

6.16 Envelopes of beam bar strain ratios due to pushover loading 196

6.17 Envelopes of column bar strain ratios due to pushover loading 196

6.18 Response spectra for selected earthquakes 197

6.19 Scaled acceleration time histories for selected earthquakes 198

6.20 Roof displacement time histories due to El Centro earthquake 199

6.21 Roof displacement time histories due to San Fernando earthquake . . . 200

6.22 Maximum story shear force due to El Centro earthquake 201

6.23 Maximum story shear force due to San Fernando earthquake 201

6.24 Plastic hinges formation due to El Centro earthquake 202

6.25 Plastic hinges formation due to San Fernando earthquake 202

6.26 Maximum story displacements due to El Centro earthquake 203

6.27 Maximum story displacements due to San Fernando earthquake 203

6.28 Maximum interstory drifts due to El Centro earthquake 204

6.29 Maximum interstory drifts due to San Fernando earthquake 204

6.30 Maximum joints shear deformations due to El Centro earthquake 205

6.31 Maximum joints shear deformations due to San Fernando earthquake . 205

6.32 Maximum joints bond slip deformations due to El Centro earthquake 206

6.33 Maximum joints bond slip deformations due to San Fernando earthquake 206

6.34 Maximum beam bar strain ratios due to El Centro earthquake 207

6.35 Maximum beam bar strain ratios due to San Fernando earthquake . . . 207

6.36 Maximum column bar strain ratios due to El Centro earthquake 208

6.37 Maximum column bar strain ratios due to San Fernando earthquake . . 208

CHAPTER 1

INTRODUCTION

1.1 BACKGROUND AND MOTIVATION

There are many thousands of multistory reinforced concrete frame buildings that have been designed before the 1970's when the knowledge and awareness of seismic performance of such structures was inadequate. Since then, the detailing requirements have been updated by building codes to reflect the gain in understanding of the behavior of such buildings during earthquakes. Consequently, a lot of existing structures fall short of complying with current standards even though they may have been properly designed according to earlier codes. Reinforced concrete structures designed prior to the 1970's in the areas of low to moderate seismicity are historically designed for gravity loads without regard to any significant lateral forces. This class of structures is referred to as gravity load designed (GLD) structures or lightly reinforced concrete (LRC) structures. Many of the construction details used in these buildings do not meet the current code requirements and may even be considered contrary to proper seismic detailing practice. Thus the lateral load resistance of these structures is questionable, particularly when subjected to moderate to severe seismic loading.

Since the early 1990's, LRC structures have received attention from the researchers and a number of experimental investigations have been conducted on scaled models of the beam column connections of LRC structures. These investigations have attempted to gain a better understanding of the general behavior of these connections when subjected to lateral loads. However on the analytical side, there have only been limited attempts to model this type of connections due to the complexity in their behavior.

The beam column connections are typically the weakest link in lateral load resistance mechanism of LRC frame buildings. Repeated joint failures in recent earthquakes justify the concern for the structural adequacy of these elements. An example of joint failure of a structure which suffered severe damage after the 1985 Mexico earthquake is shown in Figure 1.1. It is noticed from the Figure that the damage is mainly concentrated in the joint while the framing beams and columns have remained intact.

Under severe earthquakes, reinforced concrete beam column joints can be subjected to high shear forces when the adjacent beams and columns develop their maximum strengths. As a consequence, beam column joints can experience high shear deformations that contribute significantly to the story drift. Moreover, the joint shear capacity may be exceeded leading to a joint shear failure which can have a major impact on the overall stability of the entire structure.

Bond slip deformations in the beam column joint panel can also have a

significant effect on the story drift. Once yielding of beam reinforcement takes place, the bond resistance deteriorates along the bar portion that has yielded resulting in a relative slip between the reinforcing bar and the surrounding concrete. This gives rise to concentrated rotations between columns and beams thus increasing the story drift. In a more severe situation, the beam reinforcement is being pulled out and this can seriously affect the stability of the structure.

Most of the structural analysis computer programs consider the beam column joints to be rigid connections regardless of the joints detailing. This oversimplification is clearly unrealistic. Therefore there is a persistent need to develop an analytical model that accounts for the shear and bond slip deformations of these joints. The ultimate purpose of such a model is to be incorporated in frame analyses in order to predict more realistically the overall response and assess the seismic safety of reinforced concrete frame structures with different joint details.

1.2 LITERATURE REVIEW

In this section, the general equilibrium criteria for reinforced concrete beam column connections are discussed and a brief review on the experimental and the analytical studies on these elements is introduced.

1.2.1 Equilibrium Criteria for Connections

An interior beam column connection extending between points of

contraflexure, at approximately half story heights and half beam lengths, may be isolated as a free body as shown in Figure: 1.2 (reproduced from Paulay, 1989). Forces introduced by reinforced beams to the column are shown to be internal horizontal tension T_b, compression C_b, and vertical shear V_b forces, as shown in Figure 1.2b. The shear force diagram for the column is shown in Figures 1.2c. From the equilibrium conditions, the horizontal joint shear force across the mid depth of the joint core is equal to

$$V_{jh} = C_b + T_b - V_c \tag{1.1}$$

Similar forces introduced by reinforced columns to the beam are shown to be internal vertical tension T_c, compression C_c, and horizontal shear V_c forces, as shown in Figure 1.2d. The shear force diagram for the beam is shown in Figures 1.2e. From the equilibrium of the vertical forces, the vertical joint shear force is equal to

$$V_{jv} = C_c + T_c - V_b \tag{1.2}$$

From the above considerations, it is recognized that the horizontal and the vertical shear forces introduced to the beam column joints are of much greater magnitude than those experienced by the surrounding columns and beams respectively. The shear forces result in internal diagonal tensile and compressive

stresses which can lead to diagonal cracking of the joint core as shown in Figure 1.3. Unless adequate shear resistance is provided, joint shear failure can occur either as a tension or a compression failure.

The interaction of beam bars with concrete in the joint panel plays an important role in the equilibrium of the beam column connection. As the end moments exceed the cracking moment in the beam, at the beam column interfaces, cracks form at these locations. Under unfavourable bond conditions in the joint panel, reinforcing steel gradually slips through the joint and thus allowing these cracks to grow larger giving rise to concentrated bond rotations, as shown in Figure 1.4. Bond resistance inside the joint core limits the amount of shear forces (T_b and C_b) transmitted into the core by the beam reinforcement. Degradation of bond resistance inside the joint panel can ultimately lead to a "pull out" of the beam reinforcement and failure of the connection is in this case a bond failure. This condition is usually experienced in GLD connections with discontinuous bottom beam reinforcement where the steel is terminated within the beam column joint.

1.2.2 Experimental Studies

A number of experimental studies on LRC beam column joints are available in the literature. These experimental studies aimed at studying the joint shear and bond slip deformations, the joint shear capacity, and the degradation of the joint strength and stiffness due to cyclic load application. Experimental studies by Pessiki et al.

(1990) were conducted on reinforced concrete joints with continuous positive bottom beam reinforcement in the joint region and with no joint shear reinforcement. These experiments showed extensive shear cracking in the joints at failure and the damage was confined to the joint panel region. These joints showed a joint shear strength of about $1.08\sqrt{f'_c}$ (f'_c is the compressive strength of concrete in joint panel zone in MPa). However these specimens showed a rapid deterioration in stiffness and strength of the connection, resulting in an increase of drift. The inclusion of joint shear reinforcement helped distribute the cracks within the joint panel and increased the ability of the joint to maintain peak resistance with cycling at larger drifts. However the peak resistance was not significantly changed. This was in agreement with the findings of Ghobarah et al. (1996).

Beres et al. (1992) noticed that shear capacity provided by concrete in reinforced concrete joints was much higher than that predicted by the equations of the ACI-ASCE 352R (1976) which are the only formulae available in the literature for calculating the concrete contribution to joint shear strength. This indicates the lack of analytical tools for calculating the basic information about the joint capacity. Fujii and Morita (1991) carried out an experimental investigation targeting the factors affecting the basic shear strength of beam column joints. Their experimental studies on connections with joint shear reinforcement ratios ranging from 0.4 to 1.1 %, indicated that at a joint shear strain of about 0.5 % the degradation of shear rigidity was accelerated under subsequent load reversals. Ultimate shear strength was

obtained at shear strain of 2.8 % for internal and 1.5 % for exterior connections. Kaku and Asakusa (1991) conducted an experimental program on specimens with a ratio of shear stress at yielding of beams to joint shear strength of less than 0.50. They noticed that a large number of these specimens failed due to joint shear under the repetition of reversed loading following the yielding of the beams. For these specimens the joint shear deformations increased rapidly after a joint shear strain of about 0.80%.

Experimental investigations targeting the study of bond slip deformations in the joint panel region were carried out by Viwathanatepa et al. (1979). In these studies, the effect of cyclic loading on the pull out of beam longitudinal bars anchored in beam column connections was investigated. Experimental studies by Pessiki et al. (1990) on specimens with discontinuous bottom beam reinforcement showed that failure was initiated by pullout of discontinuous beam reinforcement from the beam column joint under cyclic loading.

1.2.3 Analytical Models

There are only a limited number of analytical models that are available in the literature that consider the shear and the bond slip deformations in reinforced concrete beam column joints. Pessiki et al. (1990) indicated that most of the frame analysis programs consider the joint to be perfectly rigid and introduced an alternative approach for the joint modeling. Figure 1.5 shows their approach where the beams

and the columns frame into rigid members which are pin connected to form a box at the joint location. The stability of the box is maintained by the diagonal spring. However this empirical attempt for joint modeling has yet to be translated into a working analytical joint model.

Another attempt to model these elements was carried out by Hoffmann et al. (1992). Their approach relied on bypassing the problem of the joint modeling by adjusting the properties of the members framing into the joint. This was done by reducing the capacity of the flexural members to reflect the joint shear capacity. In that analysis, the joint capacity was estimated using the ACI-ASCE 352R (1976) equations for calculating the shear strength of the joint. The same approach was used in dealing with the problem of the bond slip of beam reinforcement in the joint core. In their approach, discontinuous positive beam reinforcement was considered by using an equivalent moment capacity of the beams prone to bar slip, "pull out moment". For calculating the pull out moment, the effective area of reinforcement was calculated as the ratio between the embedment length and the development length as estimated by the ACI-318 equations. Finally, the hysteretic parameters needed for the analysis were calibrated with the experimental results. However this approach has several draw backs. First, the validity of calculating the joint shear capacity using the equations of the ACI-ASCE 352R (1976) is questionable especially with the weak correlation of their results with the experimental data of Pessiki et al. (1990), as discussed in the previous section. Second, this model ignores representing the shear and bond slip

deformations of the joint and gives a false impression of lower strengths in the adjacent members. Finally, using experimental calibrations to adjust the properties of other members instead of considering the real deformations occurring in the beam column joint is a semi-empirical approach. It is doubtful that such an approach can be applied to specimens with different detailing.

Another attempt to model reinforced concrete beam column connections was conducted by Bracci et al. (1992). This attempt relied on reducing the stiffness of the beams and columns of the structure by multiplying their moments of inertia by certain coefficients. These coefficients were identified either from engineering approximations or results of experimental component tests. Again this attempt bypasses the problem of joint modeling, and thus has the same deficiencies of the model of Hoffman et al.

Some sophisticated finite element models that consider the shear and the bond slip deformations in these connections are available in the literature. Some of these models were used in analyzing specimens tested under increasing monotonic loading (Pantazopoulou and Bonacci, 1994). Others were used in the analysis of specimens tested under reversed cyclic loading (Noguchi (1985) and Berra et al. (1994)). However, these models relied on using quite a large number of elements to model the shear and the bond slip deformations in these connections which make them impractical to be implemented in computer frame programs for general frame analysis use.

1.3 OBJECTIVES AND SCOPE

The main objective of this study is to develop an analytical model to predict the response of reinforced concrete beam column connections subjected to increasing monotonic and/or reversed cyclic loading. The model should be able to describe the shear, flexural and bond slip deformations in the critical regions. Another objective of this research is to incorporate this connection model into a structural analysis computer program that can be used in analyzing full LRC structures under earthquake loading.

To achieve the above objectives the following scope of work is followed:

1. Develop a *kinematic* model to represent:
   (a) Shear and bond slip deformations in the beam column joint panel.
   (b) Shear and flexural deformations in the plastic hinge regions in the beams and the columns.

2. Develop a *material* model to represent the inelastic behavior of reinforced concrete in the joint panel and in the critical plastic hinge regions under increasing monotonic and reversed cyclic loading.

3. Develop a *bond slip* element to represent the concrete reinforcement bond slip relationship in the joint panel under increasing monotonic and reversed cyclic

loading.

4. Incorporate the combined kinematic and material models into a structural analysis computer program and examine the validity of the combined model by comparing its predictions with available experimental data.

5. Study the behavior of a full reinforced concrete frame structure with deformable joints by conducting pushover and time history analyses.

1.4 ORGANIZATION OF THE THESIS

This thesis includes seven Chapters and three Appendices. Chapter 1 describes the general equilibrium criteria for the beam column joint and introduces a brief literature survey on the experimental and the analytical research on these connections.

Chapter 2 presents the kinematic model for the beam column connection. This includes describing the different elements used to model the beam column joint panel, the plastic hinge regions and the elastic regions of the beams and the columns. In this Chapter, elastic analysis for an exterior beam column connection is conducted to examine the validity of the kinematic model.

The reinforced concrete model is described in Chapter 3. In this Chapter, verification examples are given to examine the validity of the reinforced concrete model in describing the behavior of simple structures experiencing high levels of shear

deformations under reversed cyclic loading.

In Chapter 4, a bond slip model for anchored reinforcing bars is introduced. Verification examples are given to compare the predictions of the model with experimental data for anchored bars tested under increasing monotonic and reversed cyclic loading. This Chapter also includes a description of the incorporation of the bond slip model into the global beam column connection model.

Chapter 5 describes the verification process for the combined kinematic and the material models. This includes comparisons between the predictions of the beam column connection model and the available experimental data for different connections. The specimens tested are chosen to include connections that experience high shear and/or bond slip deformations.

In Chapter 6, a three story structure is analyzed using the proposed model to represent the beam column connections. The responses of three structures are studied; the first structure has poorly detailed connections representing typical LRC connections; the second structure has well detailed connections representing code designed connections; and the third structure is assumed to have rigid connections. Pushover analysis as well as time history analysis are conducted on the structures. Comparisons are made to the response of the three structures to examine the effect of joint detailing on the global behavior.

In Chapter 7, conclusions of the study and recommendations for future research are presented.

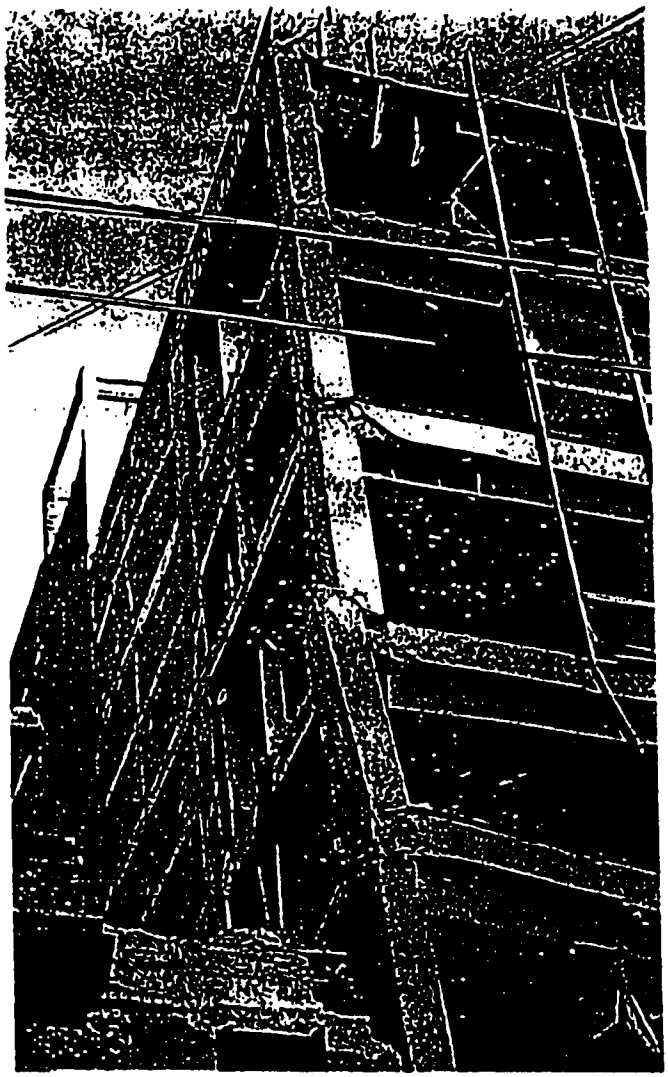

Figure 1.1 Example of beam column joint failures in the 1985 Mexico earthquake (Cheung et al., 1993)

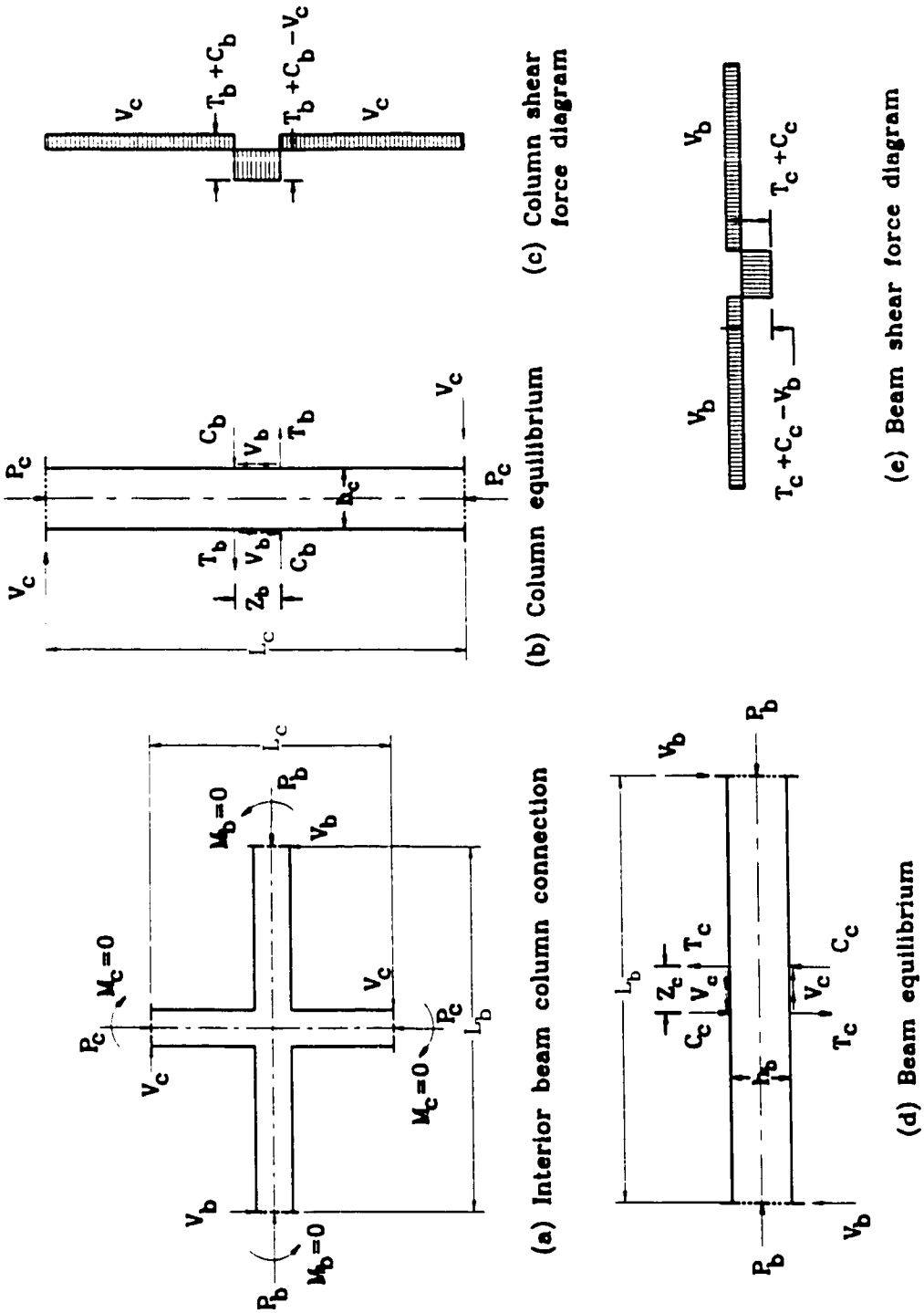

Figure 1.2 Equilibrium of interior beam column subassemblage (Paulay, 1989)

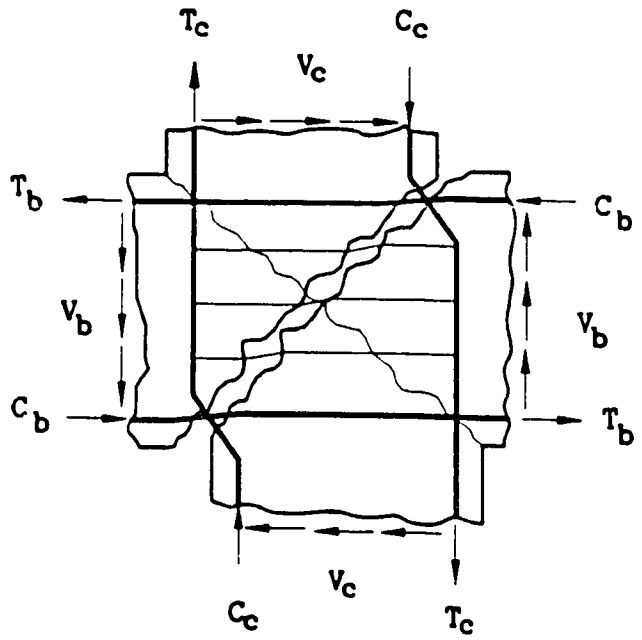

Figure 1.3 Diagonal shear cracking of the joint core

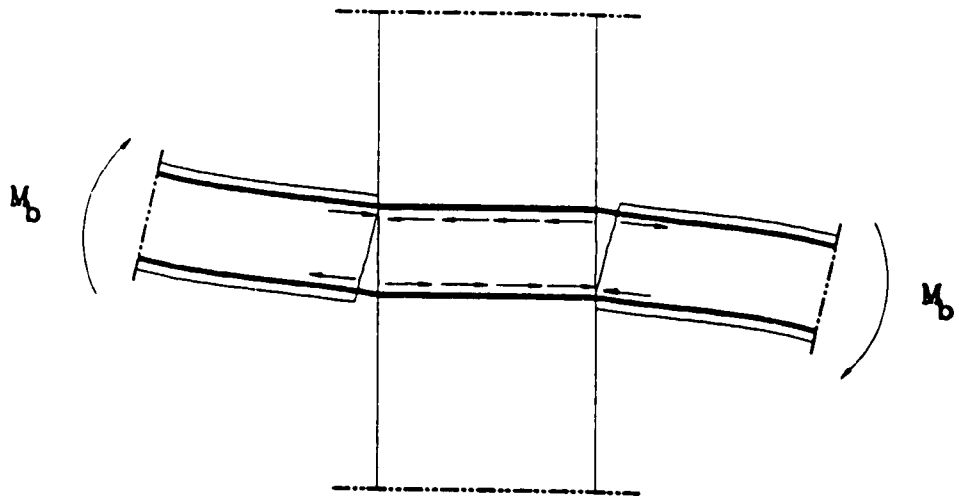

Figure 1.4 Concentrated bond rotations at the beam column interface

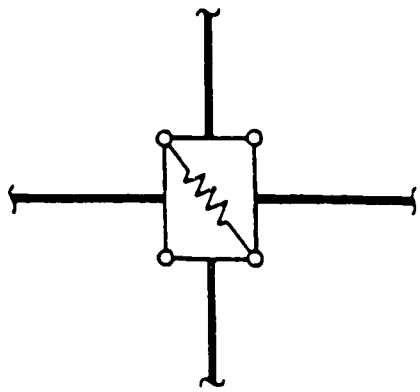

Figure 1.5 Idealization of the beam column joint by Pessiki et al. (1990)

CHAPTER 2

KINEMATIC MODEL FOR THE BEAM COLUMN CONNECTION

2.1 GENERAL

In this Chapter, the modeling aspects of the beam column connection are described. The model considers the shear deformations in the joint panel as well as flexural and shear deformations in the plastic hinge zones in the beams and the columns. The proposed model is among the first finite element models to account for the shear deformations in reinforced concrete joints without using a refined mesh. Details on the kinematic model for the beam column connection are given in the following sections.

2.2 JOINT PANEL MODEL

Under the effect of earthquake loading horizontal and vertical shear forces are induced in the joint panel region. In order to model the resulting shear deformations by a single element special attention should be given to the choice of the order of the displacement field of the element. The difference between the finite element analysis results and the exact solution is caused by the fact that the displacement field of the finite element only models parts of the solution with the same or a lower order (power).

Elements with quadratic displacement fields, such as eight node elements, have linear strain distribution. These elements are thus a good choice for modeling flexural deformations. However the constraint of the linear strain distribution makes these elements incapable of describing the shear deformations in a region on an individual basis. Since the shear strain distribution is quadratic, an element with a cubic displacement field is needed for its representation. For this reason it was decided to use an element with a cubic displacement field to represent the joint region. There are two ways to provide sufficient degrees of freedom in a quadrilateral element having a cubic displacement field. One approach is to use a four node element (Figure 2.1a) with six degrees of freedom per node; two displacements (u, v), and four displacement derivatives; $\partial u/\partial x$, $\partial u/\partial y$, $\partial v/\partial x$, $\partial v/\partial y$. Another approach is to use a twelve node element (Figure 2.1b) with two displacement degrees of freedom per node (u, v). The first approach was successfully used by Stevens et al. (1987) in analyzing reinforced concrete shear walls and beams. However their attempts to use this element in modeling reinforced concrete beam column joints have met with little success. One possible reason for this is that the nodal degrees of freedom for that element are strains. This element thus enforces continuity of strains across inter element boundaries at the nodes and hence limits its range of applicability.

In the current study, the twelve node quadrilateral element is used to model the joint panel. This element has the advantage of having a cubic displacement field while not enforcing strain continuity at the nodes. The use of a single cubic

displacement field element to represent the joint panel also takes advantage of the smeared nature of the constitutive relationships used for reinforced concrete as will be explained.

2.3 BEAM COLUMN CONNECTION MODEL

Figure 2.2 describes the proposed beam column connection model. The beam column joint panel is represented by a twelve node inelastic plane stress element. The joint panel is surrounded by transition elements which are connected to the neighboring beams and columns. The transition elements are ten node inelastic plane stress elements. These element are used to provide a gradual transition from the cubic displacement field at the beam column interface to a linear displacement field at their connection with the neighboring beams and columns. Each transition element extends to a distance of one full depth of the member that is connected to it. It is within this distance that most of the non linearities associated with the material behavior are expected to occur. This representation is more realistic than the commonly used oversimplified concentrated plastic hinges found in most structural analysis computer programs. The remaining length of the beam and the column is modelled using an elastic beam line element. Incompatibility can arise due to the existence of the rotational degrees of freedom of the line elements where they are connected to the corresponding transition elements which have only translation degrees of freedom. Details regarding the solution of the incompatibility problem are addressed later in

this Chapter.

Flexural reinforcement in the beams, the columns, and the joint panel are represented using inelastic truss elements that are compatible with the adjacent plane stress elements. Bond slip relationship between beam reinforcing steel and concrete in the joint panel is considered using bond slip element as will be discussed in Chapter 4. Shear reinforcement is represented using smeared reinforcement in the joint and in the transition elements where it is assumed to be uniformly distributed over the plane stress elements.

2.4 ELEMENTS SHAPE FUNCTIONS AND STIFFNESS MATRIX

The global displacements u and v, which are the displacements in x and y directions respectively, for the twelve node element are given as follows;

$$u = \sum_{i=1}^{12} \phi_i \, u_i \tag{2.1}$$

$$v = \sum_{i=1}^{12} \phi_i \, v_i \tag{2.2}$$

where u_i and v_i are the degrees of freedom of node i in the global coordinate system x and y. ϕ_i are the cubic shape functions and are given as follows (Kardestuncer (1987) and Surana (1983));

$$\phi(1) = \frac{1}{32}(1-S)(1-T)(-10+9(S^2+T^2)) \tag{2.3}$$

$$\phi(2) = \frac{9}{32}(1-T)(1-S^2)(1-3S) \tag{2.4}$$

$$\phi(3) = \frac{9}{32}(1-T)(1-S^2)(1+3S) \tag{2.5}$$

$$\phi(4) = \frac{1}{32}(1+S)(1-T)(-10+9(S^2+T^2)) \tag{2.6}$$

$$\phi(5) = \frac{9}{32}(1+S)(1-T^2)(1-3T) \tag{2.7}$$

$$\phi(6) = \frac{9}{32}(1+S)(1-T^2)(1+3T) \tag{2.8}$$

$$\phi(7) = \frac{1}{32}(1+S)(1+T)(-10+9(S^2+T^2)) \tag{2.9}$$

$$\phi(8) = \frac{9}{32}(1+T)(1-S^2)(1+3S) \tag{2.10}$$

$$\phi(9) = \frac{9}{32}\,(1+T)\,(1-S^2)\,(1-3S) \tag{2.11}$$

$$\phi(10) = \frac{1}{32}\,(1-S)\,(1+T)\,(-10+9\,(S^2+T^2)) \tag{2.12}$$

$$\phi(11) = \frac{9}{32}\,(1-S)\,(1-T^2)\,(1+3T) \tag{2.13}$$

$$\phi(12) = \frac{9}{32}\,(1-S)\,(1-T^2)\,(1-3T) \tag{2.14}$$

where S and T are the local coordinates as shown in Figure 2.3.

The stiffness matrix [k] for the twelve node element can be obtained from the expression

$$[k] = \int\int\int [B]^T\,[D]\,[B]\,dV \tag{2.15}$$

or

$$[k] = t\int_{-1}^{+1}\int_{-1}^{+1} [B]^T\,[D]\,[B]\,\det[J]\,ds\,dt \tag{2.16}$$

where

$[B]$, $[B]^T$ = Strain displacement matrix and its transpose

$[D]$ = Constitutive matrix which will be described in Chapter 3

t = Thickness of the element

[J] = Jacobian matrix

The integration of the above expression is carried out numerically by Gauss Quadrature procedure using four by four Gauss integration points for each element.

The strain displacement matrix is given as;

$$[B] = \begin{bmatrix} \frac{\partial \phi_i}{\partial x} & 0 \\ 0 & \frac{\partial \phi_i}{\partial y} \\ \frac{\partial \phi_i}{\partial y} & \frac{\partial \phi_i}{\partial x} \end{bmatrix} \tag{2.17}$$

The same approach in evaluating the stiffness matrix is followed for the ten node element. The shape functions of the ten node element are (Kardestuncer (1987) and Surana (1983));

$$\phi(1) = \frac{1}{32} (1-S) (1-T) (-10 + 9 (S^2 + T^2)) \tag{2.18}$$

$$\phi(2) = \frac{9}{32} (1-T) (1-S^2) (1-3S) \tag{2.19}$$

$$\phi(3) = \frac{9}{32} (1-T) (1-S^2) (1+3S) \tag{2.20}$$

$$\phi(4) = \frac{1}{32}(1+S)(1-T)(-1+9(S^2+T^2)) \quad (3.21)$$

$$\phi(5) = \frac{1}{32}(1+S)(1+T)(-1+9S^2) \quad (2.22)$$

$$\phi(6) = \frac{9}{32}(1+T)(1-S^2)(1+3S) \quad (2.23)$$

$$\phi(7) = \frac{9}{32}(1+T)(1-S^2)(1-3S) \quad (2.24)$$

$$\phi(8) = \frac{1}{32}(1-S)(1+T)(-10+9(S^2+T^2)) \quad (2.25)$$

$$\phi(9) = \frac{9}{32}(1+3T)(1-T^2)(1-S) \quad (2.26)$$

$$\phi(10) = \frac{9}{32}(1-T^2)(1-3T)(1-S) \quad (2.27)$$

where S and T are the local coordinates as shown in Figure 2.4.

2.5 COMPATIBILITY OF TRANSITION AND LINE ELEMENTS

Figure 2.5a shows the incompatibility that arises at the connection of the transition elements with the horizontal line elements (beams). This condition exists at the connection of the horizontal beams with the joint. The rotational degrees of freedom of the line element are replaced by translation degrees of freedom of the corresponding transition element using the following relationships.

$$\theta_{B1} = \frac{u_1 - u_2}{L} \tag{2.28}$$

$$\theta_{B2} = \frac{u_4 - u_3}{L} \tag{2.29}$$

$$u_{B1} = \frac{u_1 + u_2}{2} \tag{2.30}$$

$$u_{B2} = \frac{u_3 + u_4}{2} \tag{2.31}$$

$$v_{B1} = v_1 = v_2 \tag{2.32}$$

$$v_{B2} = v_3 = v_4 \tag{2.33}$$

where

θ_{B1}, θ_{B2} = rotations at ends 1 and 2 respectively

u_1, u_2, u_3, u_4 = horizontal translation degrees of freedom

v_1, v_2, v_3, v_4 = vertical translation degrees of freedom

L = length of the vertical side of the transition element

From these relations it is noticed that the two vertical degrees of freedom of each transition element are constrained to be equal at the connection with the line element (v_1=v_2). This condition has to be given in the data file of any problem solved using this model. Constraining any degrees of freedom to be equal to another degrees of freedom is a feature that is available in most of the structural analysis computer programs (PC-ANSR, SAP, DRAIN 2D, ... etc.). The above relations are written in matrix form as follows

$$\begin{bmatrix} u_{B1} \\ v_{B1} \\ \theta_{B1} \\ u_{B2} \\ v_{B2} \\ \theta_{B2} \end{bmatrix} = \begin{bmatrix} 0.5 & 0 & 0.5 & 0 & 0 & 0 & 0 & 0 \\ 0 & 0.5 & 0 & 0.5 & 0 & 0 & 0 & 0 \\ 1/L & 0 & -1/L & 0 & 0 & 0 & 0 & 0 \\ 0 & 0 & 0 & 0 & 0.5 & 0 & 0.5 & 0 \\ 0 & 0 & 0 & 0 & 0 & 0.5 & 0 & 0.5 \\ 0 & 0 & 0 & 0 & -1/L & 0 & 1/L & 0 \end{bmatrix} \begin{bmatrix} u_1 \\ v_1 \\ u_2 \\ v_2 \\ u_3 \\ v_3 \\ u_4 \\ v_4 \end{bmatrix} \tag{2.34}$$

(i.e. $\{U_B\} = [T]\{U\}$)

The stiffness matrix for the compatible line element can be obtained from the expression:

$$[K]_T = [T]^T [K] [T] \tag{2.35}$$

where

$[K]_T$ (8,8) = element stiffness matrix corresponding to translation degrees of freedom

$[T]^T$ (8,6) = transpose of [T]

[K] (6,6) = element stiffness matrix corresponding to translation and rotational degrees of freedom

Figure 2.5b shows the incompatibility that arises when a beam element is connected to a transition element from one side and an element with a rotational degree of freedom from the other side. This condition arises in the study of external

or internal connections where the beam is connected to a transition element from one node and the other node is hinged. The same procedure previously described is applied in that case also. However the dimension and the components of [T] are altered. The new matrix [T] is given as follows

$$\begin{bmatrix} 0.5 & 0 & 0.5 & 0 & 0 & 0 & 0 \\ 0 & 0.5 & 0 & 0.5 & 0 & 0 & 0 \\ 1/L & 0 & -1/L & 0 & 0 & 0 & 0 \\ 0 & 0 & 0 & 0 & 1.0 & 0 & 0 \\ 0 & 0 & 0 & 0 & 0 & 1.0 & 0 \\ 0 & 0 & 0 & 0 & 0 & 0 & 1.0 \end{bmatrix} \tag{2.36}$$

Figure 2.6a shows the incompatibility that arises at the connection of the transition elements with the vertical line elements (columns). This condition exists at the connection of the columns with the joint. In this case [T] takes the following form

$$\begin{bmatrix} 0.5 & 0 & 0.5 & 0 & 0 & 0 & 0 & 0 \\ 0 & 0.5 & 0 & 0.5 & 0 & 0 & 0 & 0 \\ 0 & 1/L & 0 & -1/L & 0 & 0 & 0 & 0 \\ 0 & 0 & 0 & 0 & 0.5 & 0 & 0.5 & 0 \\ 0 & 0 & 0 & 0 & 0 & 0.5 & 0 & 0.5 \\ 0 & 0 & 0 & 0 & 0 & -1/L & 0 & 1/L \end{bmatrix} \tag{2.37}$$

It should be noted that in this case the two horizontal components of the transition element are constrained to be equal at the connection with the line element.

Note also that L in this case is the length of the horizontal side of the transition element.

Figure 2.6b shows the incompatibility that arises when a column element is connected to a transition element from one side and an element with a rotational degrees of freedom from the other side. Again this condition arises when studying external or internal connections where the column is connected to a transition element from one node and the other node is hinged. In this case [T] takes the following form

$$\begin{bmatrix} 0.5 & 0 & 0.50 & 0 & 0 & 0 & 0 \\ 0 & 0.5 & 0 & 0.5 & 0 & 0 & 0 \\ 0 & 1/L & 0 & -1/L & 0 & 0 & 0 \\ 0 & 0 & 0 & 0 & 1.0 & 0 & 0 \\ 0 & 0 & 0 & 0 & 0 & 1.0 & 0 \\ 0 & 0 & 0 & 0 & 0 & 0 & 1.0 \end{bmatrix} \tag{2.38}$$

The elements described in this Chapter are incorporated into the computer program PC-ANSR. The input data required for the elements are given in Appendix A. The source code for the added parts are given in Appendix B. Details regarding PC ANSR are given in the following section.

2.6 PC-ANSR COMPUTER PROGRAM

PC-ANSR is based on ANSR-1 program originally developed for main frame computer. PC-ANSR is a general purpose program for static and dynamic analysis of inelastic structures. The program was developed by Bruce F. Maison (1992) at University of California, at Berkeley. The program consists of a base program to which a number of auxiliary programs can be added to include new elements. The theory and solution procedure used are based on the finite element formulation of the displacement method, with the nodal displacements as the field variables. The structure mass is assumed to be lumped at the nodes, so that the mass matrix is diagonal. Viscous damping effects may be included.

Loads must be applied at nodes only. For static analysis, a number of static force patterns can be applied. Static loads are then applied in a series of load increments, each increment being specified as a combination of static force patterns. This feature allows nonproportional loads to be applied. The dynamic loading may consist of earthquake ground accelerations, time dependant nodal loads, and prescribed values of nodal velocities and accelerations. These dynamic loadings can be specified to act singly or in combination. Values of initial velocity and acceleration may be specified at each node. For the case of static analysis followed by dynamic analysis, the displacements at the start of the dynamic analysis are assumed to be those at the end of the static analysis.

The program incorporates a solution strategy defined in terms of a number of control parameters. By assigning appropriate values to these parameters, a wide variety of solution schemes, including step by step, iterative and mixed schemes, may be constructed. For static analysis, a different solution scheme may be employed for each load increment. This feature reduces the solution time for structures in which the response must be precisely calculated for certain loading ranges only. In such cases a sophisticated soiution scheme with equilibrium iterations can be used for the critical ranges of loading, whereas a simpler step by step scheme without iteration can suffice for other loading ranges. The dynamic response is computed by step wise time integration of the incremental equation of motion using Newmark's β-γ-δ operator. A variety of integration operators may be obtained by assigning appropriate values to the parameters β and γ.

2.7 DISPLACEMENT CONTROL PROGRAM

Most of the experimental programs are carried out using displacement control type of loading especially when they are conducted to study the cyclic response of a specimen. In this procedure, load is applied to a certain point in the structure until the desired displacement is achieved at that point. In order to compare the analytical results with the experimental data of a specimen the same loading procedure has to be applied to the analytical model. This is especially significant when the specimen examined is in the post yield branch of the response and a very small change in the

applied force can lead to significant change in the displacements.

As mentioned in the above section, the program PC-ANSR allows only the application of the loads at the nodes. In order to carry out a displacement control program, displacements rather than the loads should be specified at the nodes. A simple technique is adopted in this thesis to conduct displacement control programs without making internal modifications to the aforementioned computer program that performs only load control programs. In this procedure a stiff spring is placed at the node where a displacement needs to be specified as shown in Figure 2.7. The stiffness of the spring is chosen to be much higher than the stiffness of the structure in the direction of the specified displacement. A reasonable ratio between the stiffness of the structure (k1) to the stiffness of this spring (k2) is 1 to 1000. In this case the displacement of the considered point is governed only by the stiffness of the spring and the applied load. To specify a certain displacement, Δ, at the considered point, a load P is applied at that point. The value of P is equal to ($k2 \times \Delta$).

2.8 LINEAR ELASTIC ANALYSIS

The following example is given to show the ability of the proposed kinematic model to describe the elastic behaviour of a beam column connection under increasing monotonic loading. In this example comparison is made between three different modelling schemes for an exterior connection as shown in Figure 2.8. The first model is a finite element model consisting of twenty two 12 node elements. The

second model is the proposed connection model. The third model consists of 3 beam line elements and a rigid connection. The finite element model should represent the most accurate solution for this problem. The elastic modulus for the concrete used is 25000 MPa and the thicknesses of the joint, the beam, and the columns are 250 mm.

Figure 2.9 shows the load deflection curves at the beam end for the three models. The deflections predicted using the proposed model are only 5% less than those using the finite element model. The rigid connection deflections are 20% less than those of the finite element model. This indicates that ignoring the connections shear deformation, by using the line elements with the rigid joint, can underestimate the total deflection by 20% even at the load stage where the response is still in the linear elastic range. In the inelastic range this difference can get more significant if adequate shear reinforcement is not provided as the inelastic shear deformation increases rapidly.

Figure 2.10 shows the shear stress distribution in the joint region as predicted by the proposed model. From the shear stress distribution contours, it is noticed that the maximum shear stresses occur near the centre of the joint and decrease gradually towards its border. The centre of the maximum shear stresses is shifted towards the right side of the joint due to the fact that the load is transmitted to the joint from the beam on the right hand side of the joint.

2.9 CONCLUSIONS

In this Chapter, a finite element model for reinforced concrete beam column connections is presented. The proposed model represents the shear deformations in the joint panel as well as the flexural and shear deformations in the plastic hinge zones in the beams and the columns. The model avoids the need to use refined meshes of simple elements by using a single high power element in the critical regions of the joint panel and also at the plastic hinge zones in the beams and the columns. This is achieved by taking advantage of the smeared nature of the constitutive reinforced concrete model. In the model, a joint, a transition and a line element is used. Compatibility between the transition and the line element is discussed. Finally, a linear elastic analysis for an exterior beam column connection is carried out to show that shear deformations in the connection can have pronounced effects on the total deflection even when the response is still in the elastic stage.

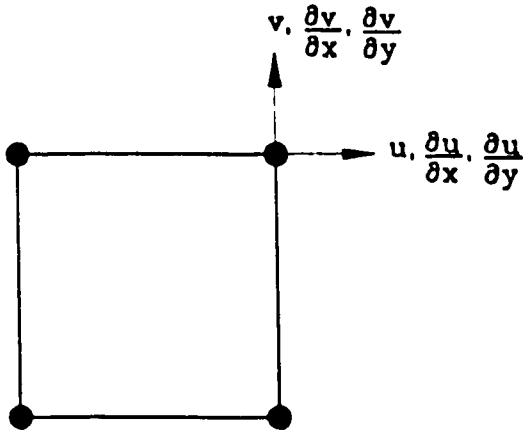

(a) Four node element

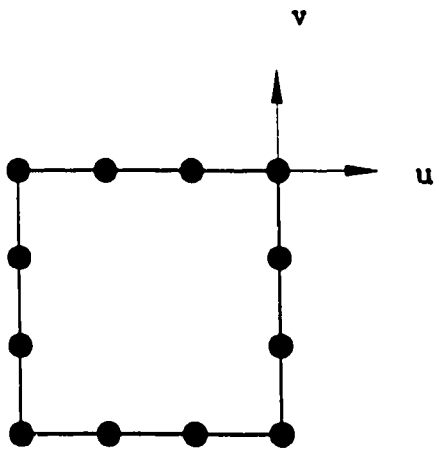

(b) Twelve node element.

Figure 2.1 Reinforced concrete elements

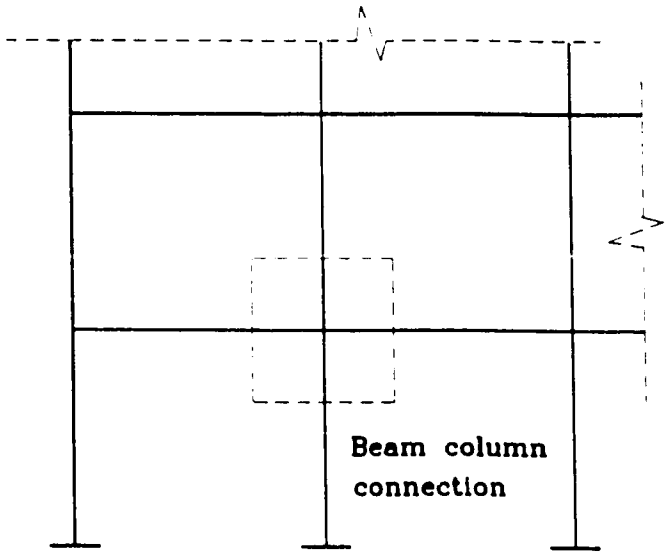

(a) Part of a typical R.C. frame

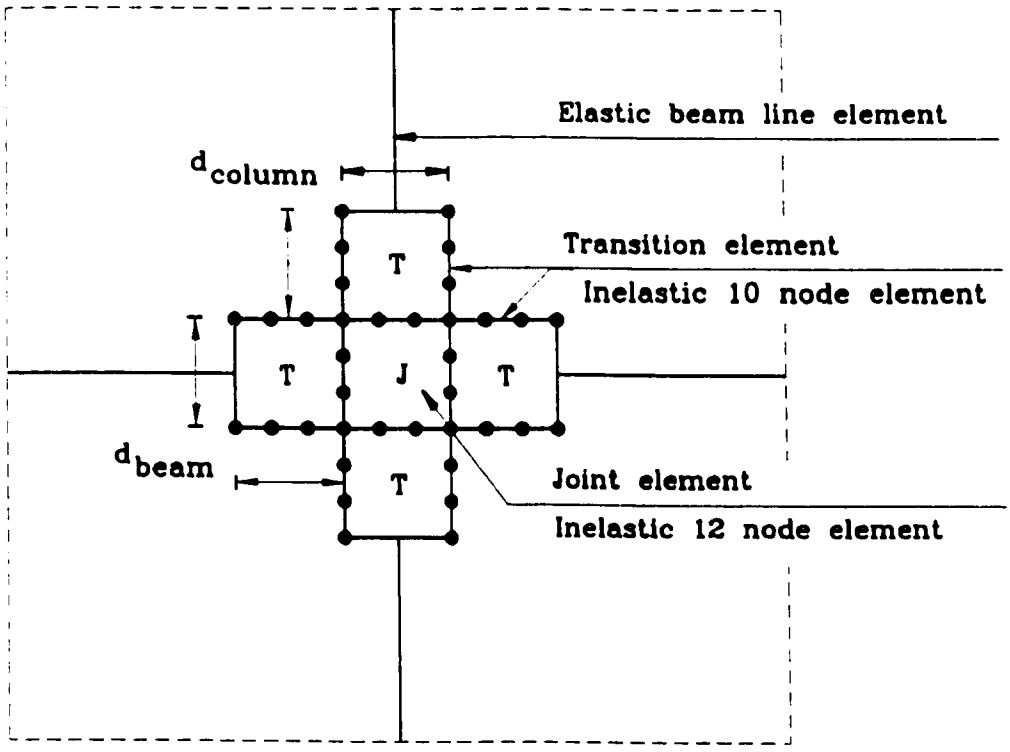

(b) Proposed element

Figure 2.2 Proposed beam column connection element

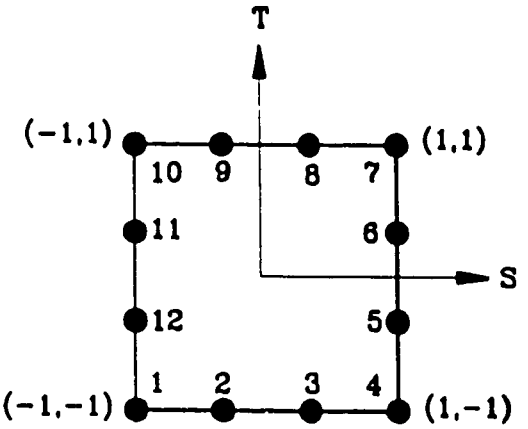

Figure 2.3 Twelve node plane stress element

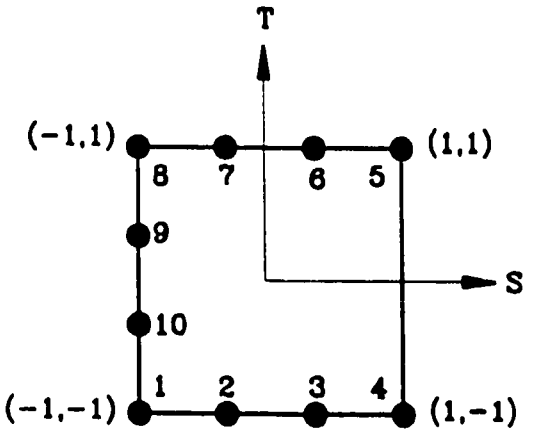

Figure 2.4 Ten node plane stress element

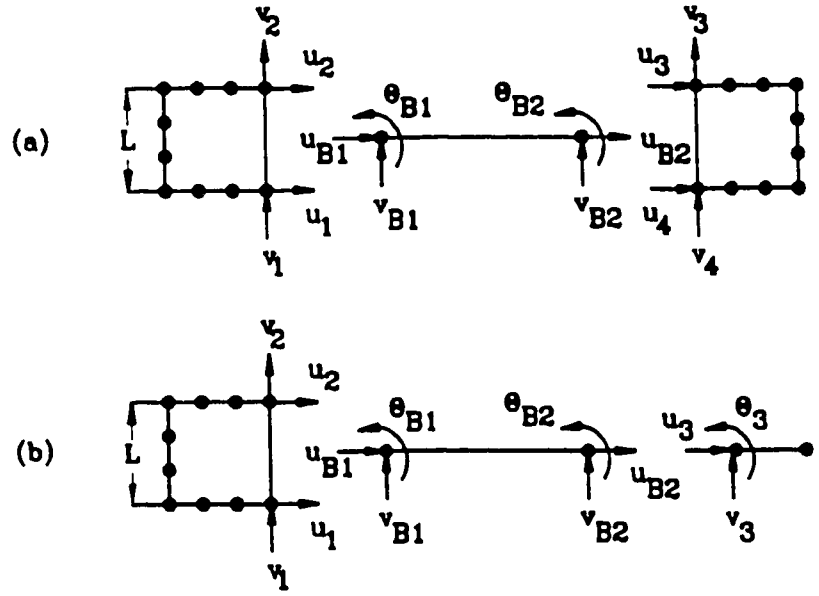

Figure 2.5 Compatibility of a horizontal line element with; (a) two transition elements; (b) a transition element and a line element

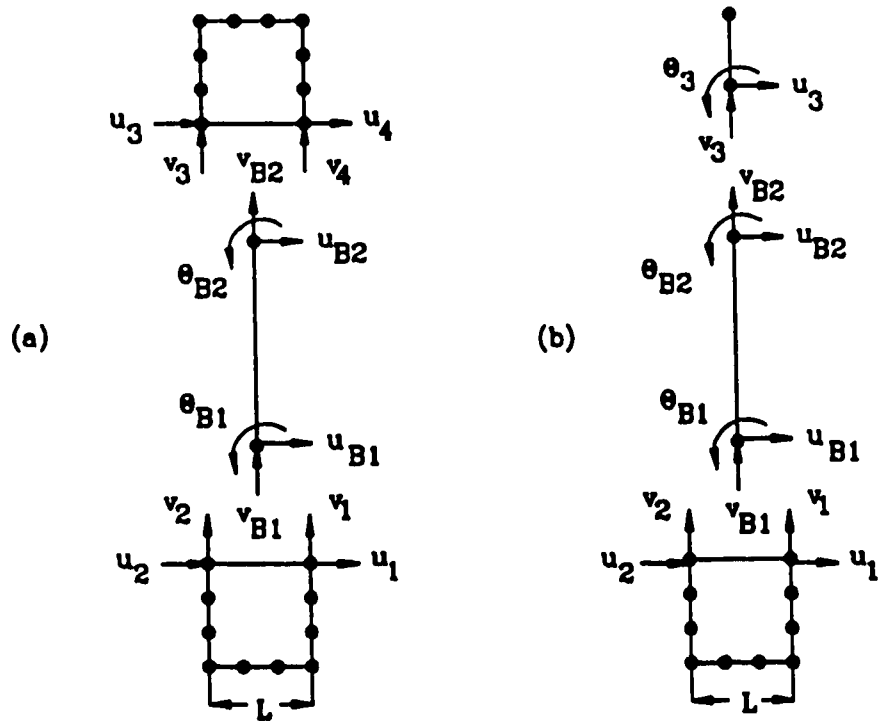

Figure 2.6 Compatibility of a vertical line element with; (a) two transition elements; (b) a transition element and a line element

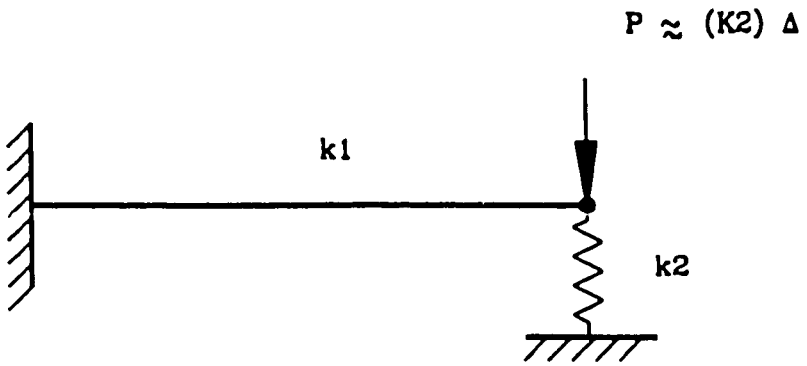

Figure 2.7 Displacement control program

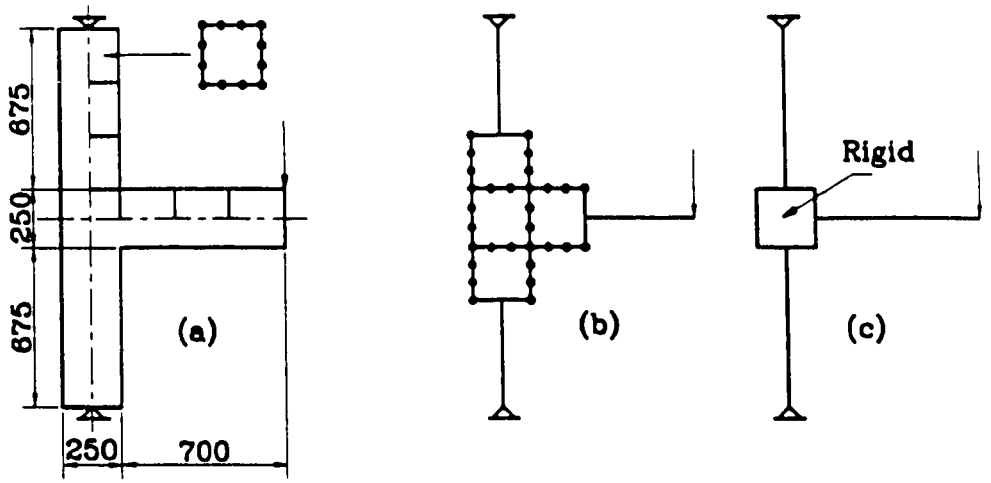

All dimensions are in mm

Figure 2.8 Three models for an exterior beam column connection; (a) a finite element mesh of twenty two 12 node quadrilateral elements; (b) the proposed model; (c) rigid connection

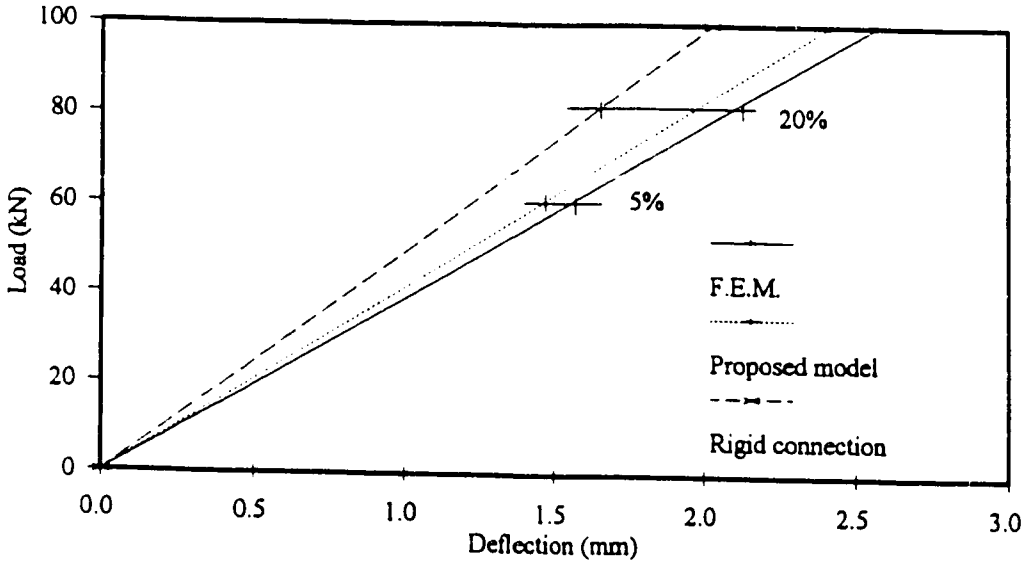

Figure 2.9 Load deflection curves for an exterior beam column connection

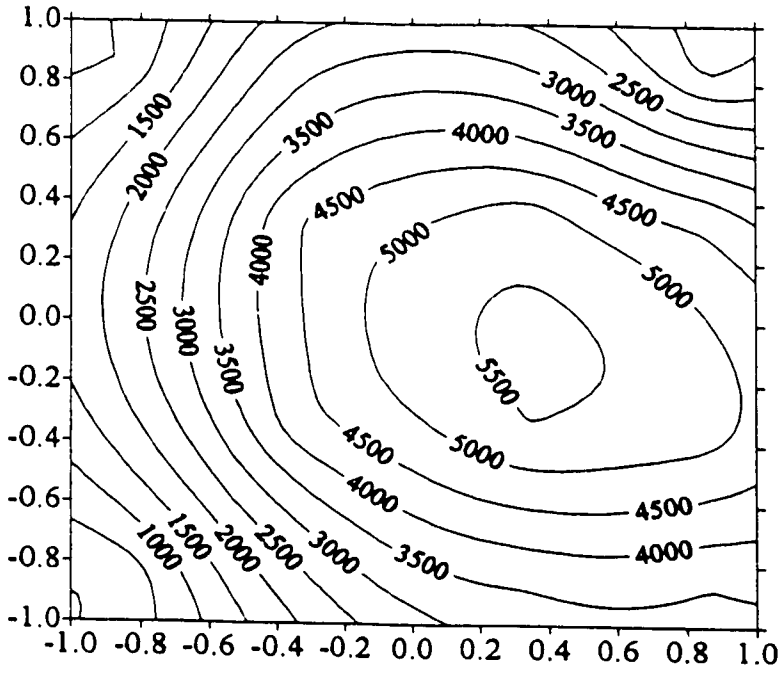

Figure 2.10 Shear stress distribution in the joint panel region

CHAPTER 3

MATERIAL MODEL FOR REINFORCED CONCRETE

3.1 GENERAL

Over the last three decades a considerable amount of work has gone into the development of constitutive models for reinforced concrete. As more information on the behavior of reinforced concrete (RC) becomes available, more refined RC constitutive models are developed. Most of the work in the non linear finite element analysis on RC has been concentrated on its behavior under monotonic loading. Due to the complexities in the behavior and modeling of RC structures under cyclic loading, only a limited number of finite element analyses have been performed on RC structures subjected to reversed cyclic loading. Numerical problems associated with the complex rules describing their stress strain relationship under cyclic loading limited their applications. However during the past decade some refined models describing the behavior of RC under cyclic loading have been developed (Stevens et al. (1987), Xu (1991), Sittipunt and Wood (1993)).

Stevens et al. (1987) proposed a concrete model based on the compression field theory and used the rotating crack model approach under both increasing monotonic and reversed cyclic loading conditions. In their approach, the axes of

orthotropy at which the material properties are calculated do not remain fixed but are always aligned with the principal strain direction. The rotating crack model is usually used when significant crack rotations occur. This takes place when the old cracks becomes less dominant and new cracks are being formed (Gupta and Akbar, 1984). The crack rotation causes discontinuities in the stresses and strains in the crack direction. This means that stresses and strains at the end of one load step are different from stresses and strains in the new crack direction at the beginning of next load step. This complicates the rules defining the stress strain relationships under cyclic loading. This is due to the fact that not only one curve is needed to define a certain region of the response, which is the case for the fixed crack model, but a whole family of curves are needed. Xu (1991) proposed a cyclic non orthogonal multicrack model for concrete as a solution to correct the deficiencies of the fixed crack and the rotating crack models. This approach involved decomposing the total strain increment into a concrete strain increment and a crack strain increment. Such crack decomposition allows intact concrete and cracks to be modeled separately. However this approach involves a great deal of computational effort for calculating the constitutive relations. It includes a number of matrix inversion, addition, subtraction and multiplication at each integration point. Although these models (Stevens et al. (1987), and Xu (1991)) showed great success at the element level, they have not been applied to the analysis of complete RC structures. Sittipunt and Wood (1993) proposed a cyclic concrete model based on the fixed crack approach that ignores the compression degradation

of concrete properties. This model was successfully used in the analysis of complete RC structures under large number of cyclic load reversals. Further details on nonlinear finite element analysis of RC structures subjected to cyclic loading can be found elsewhere (Bicanic and Mang, 1990).

In this chapter, a constitutive model for predicting the response of RC under cyclic loading is introduced. The proposed model is simple enough to be incorporated into any nonlinear finite element analysis program to be used in analyzing full structures. The proposed model is based on the findings of previous experimental and analytical studies. The fixed crack approach is adopted in the proposed model. Simplified hysteretic rules defining the cyclic stress strain curves of concrete and steel are used. The stiffness and strength degradation of cracked concrete are included in the formulation.

3.2 MATERIAL MODEL FOR CONCRETE

Concrete is assumed to be an orthotropic material in the principal strain directions and is treated as an incremental linear elastic material. At the end of each load increment, the material stiffnesses are corrected to reflect the latest changes in the material properties. The incremental constitutive relationship referred to the principal axes is described as follows:

$$\{d\sigma\} = [D]_{12} \{d\epsilon\} \tag{3.1a}$$

$$\begin{bmatrix} d\sigma_1 \\ d\sigma_2 \\ d\tau_{12} \end{bmatrix} = \frac{1}{1-\nu^2} \begin{bmatrix} E_{11} & \nu\sqrt{E_{11}E_{22}} & 0 \\ \nu\sqrt{E_{11}E_{22}} & E_{22} & 0 \\ 0 & 0 & G_{12} \end{bmatrix} \begin{bmatrix} d\epsilon_1 \\ d\epsilon_2 \\ d\epsilon_{12} \end{bmatrix} \qquad (3.1b)$$

where

E_{11} , E_{22} = Tangent moduli of elasticity in the two principal directions

ν = Poisson's ratio

G_{12} = Shear modulus in the principal directions and is equal to 0.25 (E_{11} + E_{22} - $2\nu\sqrt{E_{11}E_{22}}$)

$d\sigma_1$, $d\sigma_2$ = Incremental normal stresses in the principal directions

$d\tau_{12}$ = Incremental shear stress in the principal directions

$d\epsilon_1$, $d\epsilon_2$ = Incremental normal strains in the principal directions

$d\epsilon_{12}$ = Incremental shear strain in the principal directions

For each load increment, the values of the material properties E_{11} and E_{22} are determined as a function of the state of stress and strain throughout the analysis procedure. In this model, only two cracks can form at a point. The two cracks are assumed to be orthogonal and the crack orientation is determined by the orientation of the first crack. The second crack is assumed to be perpendicular to the first one. The orientation of the cracks is fixed during the entire computational process, (fixed crack model). Figure 3.1 shows the principal coordinates for a cracked concrete

element. The effect of Poisson's ratio is neglected after cracking. Therefore the material stiffness matrix after cracking can be expressed as follows:

$$\begin{bmatrix} d\sigma_1 \\ d\sigma_2 \\ d\tau_{12} \end{bmatrix} = \begin{bmatrix} E_{11} & 0 & 0 \\ 0 & E_{22} & 0 \\ 0 & 0 & G_{12} \end{bmatrix} \begin{bmatrix} d\epsilon_1 \\ d\epsilon_2 \\ d\epsilon_{12} \end{bmatrix} \qquad (3.2)$$

The normal stress function is used to calculate the concrete stresses σ_1, and σ_2 as well as the tangent moduli E_{11} and E_{22}. τ_{12} and G_{12} are calculated using the shear stress function.

3.3 THE NORMAL STRESS FUNCTION

The normal stress function defines the stress strain relationship for concrete in the direction of the cracks. Uniaxial stress strain relationships are used to describe the concrete behavior in each direction. Therefore to calculate σ_1 and σ_2 from ϵ_1 and ϵ_2, the uniaxial stress strain relations will be used in which the stress and the strain are referred to as f_c and ϵ_c. The effect of biaxial stress is included in the analysis by considering the degradation of the concrete properties in the direction parallel to the crack as will be discussed.

It has been commonly accepted that the envelope curve for the cyclic tensile and compressive stress strain curves for concrete is the monotonic curve. Therefore to develop a suitable hysteretic model it is necessary to have a monotonic stress strain

curve to define the envelope curve. In the following sections the monotonic tension and compression curves for concrete are first introduced and then the cyclic part of the model is discussed.

3.3.1 Concrete Tension Envelope

The concrete tensile response before cracking is assumed to be linearly elastic and is represented using the following relation.

$$f_c = E_1 \varepsilon_c \tag{3.3}$$

where E_1 is the initial tangent modulus, f_c is the concrete stress, and ϵ_c is the concrete strain.

After cracking, the concrete between the cracks still carries some tensile stress which is transferred through bond between the steel reinforcement and the surrounding concrete commonly referred to as tension stiffening. Such behavior makes the average stiffness of a reinforcing bar embedded in concrete greater than that of a plain bar. Since the tension stiffness behavior is caused by interaction between concrete and steel, its characteristic depends on the properties of both materials, such as crack spacing, reinforcement ratio, and interface bond transfer (Balakrishnan and Murray, 1988). Experimental studies on the tension stiffening behavior of concrete exhibit a large amount of scatter, and the stress strain relationship for tension is not well defined. In this study, the tension stiffening relation

developed by Stevens et al. (1987) is adopted. This relation is shown in Figure 3.2 and is expressed as follows:

$$\frac{f_c}{f_{cr}} = (1 - \alpha)\, e^{-\lambda_t (\epsilon_c - \epsilon_{cr})} + \alpha \qquad (3.4)$$

where f_{cr} and ϵ_{cr} are the cracking stress and strain respectively, ϵ_c is the concrete strain, $\alpha = 75\,(\rho_s / d_b)$ (mm), ρ_s is the steel ratio, d_b is the bar diameter (mm). The parameter λ_t controls the rate at which the response decays and is equal to:

$$\lambda_t = \frac{270}{\sqrt{\alpha}} \qquad \lambda_t \leq 1000 \qquad (3.5)$$

3.3.2 Concrete Compression Envelope

The properties of the ascending branch of the uniaxial compression stress strain curve of concrete shown in Figure 3.3 has been extensively discussed by many researchers ((Chang and Mander, 1994), (Collins and Mitchell, 1991), (Saenz,1964), (Sulayfani and Lamirault,1987), and (Tsai, 1988)). The widely used stress strain curve proposed by Saenz (1964), is used in this study as follows:

$$f_c = \frac{E_1 \varepsilon_c}{1 + (\frac{E_1}{E_s} - 2)\,(\frac{\varepsilon_c}{\varepsilon_c'}) + (\frac{\epsilon_c}{\epsilon_c'})^2} \qquad (3.6)$$

where ϵ_c' is the strain at peak stress f_c' . E_1 is the initial tangent stiffness and is equal

to $2f_c'/\epsilon_c'$. E_s is the secant modulus at the peak stress and is equal to f_c'/ϵ_c'. In most cases ϵ_c' is not known while f_c' is known. In the absence of sufficient data, ϵ_c' can be evaluated using the following relations (Sulayfani and Lamirault, 1987):

$$\varepsilon_c' = \frac{f_c'^{1/4}}{4000} \ (psi) \qquad or \qquad \varepsilon_c' = \frac{f_c'^{1/4}}{1153} \ (MPa) \tag{3.7}$$

The curve given by Saenz is simplified using a trilinear curve as shown in Figure 3.3. Breaking the curve into three linear segments reduces the computational effort by eliminating the need to differentiate equation (3.6) at each strain increment to estimate the tangent stiffness. Another advantage of this simplification is that it ensures the tangent stiffness to be exactly equal to E_1 at low strain levels. This condition is helpful in dealing with the problem of crack closing as will be discussed. The trilinear curve is defined using the following relations:

$$f_c = E_1 \varepsilon_c \quad < 0.75f_c' \qquad 0 < \varepsilon_c < 0.375\varepsilon_c' \tag{3.8}$$

$$f_c = 0.75f_c' + E_2 (\varepsilon_c - 0.375\varepsilon_c') \ \le f_c' \qquad 0.375\varepsilon_c' < \varepsilon_c < 0.80\varepsilon_c' \tag{3.9}$$

$$f_c = f_c' \qquad 0.80\varepsilon_c' < \varepsilon_c < \varepsilon_c' \tag{3.10}$$

where $E_2=0.3E_1$, and $E_3=0$.

The strain softening branch of the compression stress strain curve is described here for unconfined and confined concrete as indicated in Figure 3.4. The relation used for unconfined concrete has been developed by Collins and Mitchell (1991) and is expressed as follows:

$$f_c = \left(\frac{rx}{r - 1 + x^{kr}}\right) f_c' \qquad (3.11)$$

where $x = \epsilon_c/\epsilon_c'$ and

$$r = 0.8 + \frac{f_c'}{17} \qquad MPa \qquad (3.12)$$

and

$$k = 0.67 + \frac{f_c'}{62} \qquad MPa \qquad (3.13)$$

To avoid numerical problems, the tangent stiffness modulus of the descending branch is assumed to be zero. In this case the unbalanced stress (f_{unb}), is redistributed in the next load increment as shown in Figure 3.3.

The strain softening branch for confined concrete is represented using the

model of Kent and Park (1971) that was later extended by Scott et al. (1982). Even though other accurate models have been proposed since, they are not as simple. The so called modified Kent and Park model offers a good balance between simplicity and accuracy. According to the modified Kent and Park model, the strain softening branch is expressed as follows:

$$f_c = K f_c' [1 - Z(\varepsilon_c - \varepsilon_{co})] \geq 0.2 K f_c' \tag{3.14}$$

where

$$\varepsilon_{co} = \varepsilon_c' K \tag{3.15}$$

$$K = 1 + \frac{\rho_s f_{yh}}{f_c'} \tag{3.16}$$

$$Z = \frac{0.5}{\frac{3 + 0.29 f_c'}{145 f_c - 1000} + 0.75\rho_s\sqrt{\frac{h'}{S_h}} - \varepsilon_c' k} \tag{3.17}$$

ϵ_{co} is the concrete strain at maximum stress for confined concrete, K is a factor that accounts for the strength increase due to confinement, Z is the strain softening slope, f_{yh} is the yield strength of stirrups in MPa, ρ_s is the ratio of the volume of hoop reinforcement to the volume of concrete core measured to outside of stirrups, h' is

the width of concrete core measured to outside of stirrups, and S_h is the center to center spacing of stirrups or hoop sets.

3.3.3 Strength and Stiffness Degradation Effects Parallel to the Crack Direction

The primary characteristic of the constitutive laws of concrete in compression is the softening of the peak stress in compression with respect to f_c'. The commonly used approach to calculate the peak stress of the uniaxial curve has been the failure surfaces of biaxially stressed plain concrete. In the early 1980's, the softening coefficients were first developed by Vecchio and Collins (1986). Their softening coefficient takes a form that depends primarily on the principal tensile strain, ϵ_1. In their approach, the reductions in the compression strength and stiffness of cracked concrete are calculated as a function of the transverse tensile strain. They applied the softening coefficients to the peak stress and the strain at the peak stress in one model, and to the peak stress alone in another.

Another form of a strength softening coefficient was developed by a Miyahara et al. (1988) which is also primarily dependant on ϵ_1. Miakme et al. (1991) adopted a strength softening coefficient that depends on ϵ_1, the angle between the reinforcement and the crack direction, the crack spacing, and the stress in the rebar. Belarbi and Hsu (1991) developed a softening coefficient for the peak stress and another for the strain at the peak stress. Their softening coefficients depends on ϵ_1, the orientation of the cracks to the reinforcement and the type of loading.

The gross differences between different softening coefficients available in the literature indicates the lack of understanding on the softening response and in determining the compressive stress strain relationship for cracked concrete (Belarbi and Hsu, 1995). In a comparative study by Vecchio and Collins (1993), they concluded that applying their softening coefficient to the peak stress and the strain at the peak stress provided the best correlation to the experimental results. For this reason their softening coefficient is used in the present study. Figure 3.5 shows the effect of the softening coefficient on the trilinear curve representing the uniaxial stress strain relationship for concrete. The relation used for calculating the softening coefficient is shown in Figure 3.6 and takes the following form:

$$\beta = \frac{1}{0.80 + 0.34\epsilon_1/\epsilon_c'} \leq 1.0 \qquad (3.18)$$

3.3.4 Cyclic Tensile Stress Strain Relations

Reinforced concrete members subjected to cyclic loading experience crack opening and closing throughout their loading history. As the crack status changes from open to close, the concrete stiffness changes in a gradual manner from zero stiffness to almost the maximum initial stiffness when the crack is fully closed. Figure 3.7 shows a typical relationship between concrete stress and crack width (Yankelevsky and Reinhardt (1989)).

In the smeared crack model, the strain normal to the crack is used for defining

the crack opening and closing. Early researchers (Cervenka (1985)) faced numerical problems associated with crack opening and closing. They had to use very small load increments to prevent excessive compressive strain caused by assuming zero stiffness in the load step prior to crack closing. Other researchers (Darwin and Pecknold (1974 and 1976) included a gradual increase in the concrete stiffness as the crack closes to overcome this numerical problem. Recently some relationships varying in their degree of difficulty have been proposed (Sittipunt and Wood (1993), Xu (1991), Stevens et al. (1987), and Okamura (1987)).

In the current model, a simpler relation is used to define the process of crack opening and closing. Rules used for crack opening and closing are shown in Figure 3.8. Cracks are considered fully closed when the compressive strain exceeds the strain of the focal point (f_{fp}, ϵ_{fp}). A smooth transition curve connecting the unloading point (f_{un}, ϵ_{un}) and the focal point is used to define the crack opening and closing. The stress at the focal point is assumed to be $0.1f_c'$ and the stiffness at this point is equal to the initial tangent stiffness E_1. The slope of this curve changes gradually as it connects the unloading point and the focal point. This slope is equal to the slope of the tangent line from the origin to (f_{un}, ϵ_{un}) at the unloading point. The slope at the focal point is equal to the slope of the tangent line from the origin to (f_{fp}, ϵ_{fp}) which is the initial tangent stiffness E_1.

The curve used to describe the crack opening and closing was originally developed by Monegotto and Pinto (1973) to define the stress strain curve of

reinforcing steel. For this current application, the equation of this curve is expressed as follows:

$$f_c^* = b\varepsilon^* + \frac{(1 - b)\,\varepsilon^*}{(1 + \epsilon^{*\,R})^{1/R}} \tag{3.19}$$

where b is set equal to:

$$b = \frac{f_{un} / \varepsilon_{un}}{f_{fp} / \varepsilon_{fp}} \tag{3.20}$$

and

$$R = R_o - \frac{a_1\,\epsilon_{un}}{a_2 + \epsilon_{un}} \tag{3.21}$$

f * and ϵ* are set equal to:

$$f^* = \frac{(f_{fp} - f_c)}{f_{fp}} \tag{3.22}$$

$$\epsilon^* = \frac{(\epsilon_{fp} - \epsilon_c)}{\epsilon_{fp}} \tag{3.23}$$

R_o, a_1, and a_2 are constants which are assumed to be 20, 18.5, and 0.0015 respectively.

3.3.5 Cyclic Compressive Stress Strain Relations

The cyclic response of concrete under uniaxial compression has been investigated by a number of researchers (Chang and Mander (1994), Sittipunt and Wood (1993), Xu (1991), Stevens et al. (1987), Okamura (1987) and Darwin and Pecknold (1976)). Models with varying degrees of complexity has been proposed to define the cyclic response of concrete under uniaxial compression. In the present study, a simplified model is used to define the cyclic compression response, the details of which are discussed presently.

The key points for the proposed model are shown in Figure 3.9. The point where unloading begins is termed (f_{un}, ϵ_{un}) and the point where reloading starts is called (f_{rl}, ϵ_{rl}). The unloading curve consists of two regions; the initial unloading region and the zero stiffness region. The initial unloading region is a straight line starting from (f_{un}, ϵ_{un}) and having a slope E_{un}. The unloading stiffness E_{un} is a function of the unloading strain and the strain at peak stress. The following equation is proposed for predicting E_{un}:

$$\frac{E_{un}}{E_1} = 1 - 0.3 \left(\frac{\epsilon_{un}}{\epsilon_c} - 1\right) \qquad (3.24)$$

where

$$E_i \geq E_{un} \leq 0.25E_i \qquad (3.25)$$

The above relation is shown in Figure 3.10. If reloading takes place in the initial unloading region, it follows back on the same unloading curve until it reaches the envelope curve.

The initial unloading region ends when the stress drops to zero and then continues on the zero stress region with a zero slope till the origin is reached. Once the curve reaches the origin, it follows the rules set for the tension cyclic model. Reloading from the zero stress region starts at the point (f_{rt}, ϵ_{rt}). It then follows a straight line connecting the reloading point and the common point (f_{cp}, ϵ_{cp}). The common point represents the focal point of the reloading curve in compression. In this model, the focal point is assumed to be the intersection of the initial unloading curve and the reloading curve and f_{cp} is assumed to be 0.7 f_{un}.

Figures 3.11 to 3.13 provide a comparison of the model with the experimental results of three load histories run by Karsan and Jirsa (1969) and Okamoto (1976). The Figures indicate that the proposed model although simple is comparing fairly well with the experimental results.

3.3.6 Interaction between Tension and Compression Models

Under reversed cyclic loadings, concrete experiences repetitive cycles of crack opening and closing, and compression and tension loading and unloading in each of

its principal directions. This means that there must be an interaction between the cyclic tension and compression models. This interaction will allow a continuous loop for any loading history.

Figure 3.14 shows a sketch of two typical connected loops . In the first loop, loading begins in tension until concrete cracks and follows the tension stiffening curve. At point (a), the load direction is reversed and the crack closing curve is followed until the compression monotonic curve is reached. Loading continues on the compression envelope and at point (b), the strain softening branch begins. The load direction is again reversed at point (c), and the unloading compression curve is followed to point (d) where the zero stress region begins. Loading then resumes till the origin and a straight line is followed back to point (a) where the tension envelope is reached. Loading continues on the tension envelope curve and at point (e) the load direction is reversed. The crack closing curve is followed and at point (f) (the focal point), the compression reloading curve is followed up to point (g) on the compression softening branch. The load direction is reversed at point (h) and the compression unloading curve is again followed to the origin and then to point (e) back on the tension envelop.

3.4 THE SHEAR STRESS FUNCTION

In order to correctly model the cyclic shear response of RC, the shear stress function must include the most important characteristics of the cyclic shear behavior

of RC members. After cracking has taken place, cracked reinforced concrete can still transfer shear forces at a reduced rate through aggregate interlock, shear friction, and dowel action of steel reinforcement. The shear transfer mechanism in reinforced concrete has been investigated by a number of researchers over the past three decades. In the smeared crack model, two approaches have been used to represent the shear stiffness of cracked concrete; the reduced shear stiffness approach and the varied shear stiffness approach. In the reduced shear stiffness approach, a reduced shear stiffness μG is retained with retention factors (μ) varying from 0 to 1.0. Among the researchers using this approach are; Chung and Ahmad (1995), Bolander and Wight (1991), Hu and Schnobrich (1990), Massicotte and MacGregor (1990), Barzegar (1989), and Crisfield and Wills (1989). In the varying shear stiffness approach, the shear stiffness of cracked concrete is assumed to be a function of the strain normal to the crack. Several functions have been proposed (Balakrishnan and Murray (1988), Cervenka (1985), Fardis and Buyukozturk (1980), and Al-Mahaidi (1978)) to represent the shear stiffness of cracked concrete. Both the reduced and the varied shear stiffness approach give satisfactory results under monotonic loading. However under cyclic loading the concrete response is more complicated than that assumed in either of these two approaches.

3.4.1 Shear Stiffness of Cracked Concrete

In the proposed concrete model, the cracked shear stiffness of RC is assumed

to be due to interface shear stiffness only. Shear stiffness due to dowel action is ignored in the current model. Analytical studies by Sittipunt and Wood (1993) shows that the contribution of the interface shear stiffness is usually more pronounced than that of the dowel action stiffness. In the proposed model, the total shear stiffness of cracked concrete, G_{cr}, is evaluated using the following relation (Sittipunt and Wood (1993) :

$$G_{cr} = 2 \left(\frac{1}{G_{cr}^{1}} + \frac{1}{G_{cr}^{2}}\right)^{-1} \tag{3.26}$$

where G^1_{cr}, and G^2_{cr} are the shear stiffnesses in crack directions 1 and 2 respectively. The cracked shear stiffness is represented using the following relations (Fardis and Buyukozturk (1980)) as shown in Figure 3.15:

$$G_{cr}' = \mu\, G_{conc} \qquad \varepsilon_{nn} < \varepsilon_{cr} \tag{3.27}$$

$$G_{cr}' = \mu \frac{\varepsilon_{min} - \varepsilon_{nn}'}{\varepsilon_{min} - \varepsilon_{cr}} G_{conc} \qquad \varepsilon_{cr} \le \varepsilon_{nn}' < \varepsilon_{min} \tag{3.28}$$

$$G_{cr}' = G_{min} \qquad \varepsilon_{min} \le \varepsilon_{nn}' \tag{3.29}$$

where

μ = Parameter used to relate interface shear transfer stiffness to shear stiffness of uncracked concrete

ϵ^{i}_{nn} = The normal crack strain in i direction

ϵ_{cr} = The tensile strain when concrete cracks

ϵ_{min} = The normal crack strain where $G^{i}_{cr} = G_{min}$

G_{min} = The minimum value of G_{cr}

G_{conc} = The shear stiffness of uncracked concrete ($E_1 / 2(1+ v)$)

Based on the analytical studies by Sittipunt and Wood (1993), the values selected for the parameters in this model are $\mu = 0.20$ and $\epsilon_{min} = 15\ \epsilon_{cr}$. G_{min} is set a value other than zero to avoid numerical problems. G_{min} is set to be equal to 0.01 G_{conc} in the proposed model.

3.4.2 Cyclic Shear Transfer Model

Although several researchers have studied the shear transfer mechanism for both reinforced and unreinforced concrete subjected to cyclic loading (Mattock (1981), Laible et al. (1977), Jimenez et al. (1976), and Paulay et al. (1974)), few analytical models are available for such behavior (Sittipunt and Wood (1993), Xu (1991), Okamura et al. (1987), and Jimenez et al. (1978)). The proposed model for cyclic shear transfer is a simplified version of the model used by Xu (1991) and

Sittipunt and Wood (1993). As shown in Figure 3.16, the relationship between the shear stress, τ_{12}, and the shear strain, ϵ_{12} , consists of three regions, loading, unloading, and slip. In the loading region (b-c and a-e) the relationship between τ_{12} and ϵ_{12} depends on G_{cr}. The unloading region (c-d and e-f) is defined by a line originating at the point where ϵ_{12} starts reversing its direction with a constant stiffness G_{un} , which is given a value of $0.2G_{conc}$. The unloading region ends where the unloading line intersects the strain axes at the point $(0, \epsilon_{12}^{max})$ or $(0, \epsilon_{12}^{min})$ depending on the loading direction. The slip region (a-b and d-f) connects the points $(0, \epsilon_{12}^{max})$ and $(0, \epsilon_{12}^{min})$.

3.5 MATERIAL MODEL FOR STEEL REINFORCEMENT

For each steel reinforcement component, a constitutive matrix $[D]_i$ is set in the reinforcement direction as follows:

$$D_i = \begin{bmatrix} \rho_i E_i & 0 & 0 \\ 0 & 0 & 0 \\ 0 & 0 & 0 \end{bmatrix} \tag{3.30}$$

where ρ_i is the reinforcement ratio and E_i is the tangent modulus.

The evaluation of the stress and tangent modulus for steel components in each direction is carried out by the use of the nonlinear cyclic model for reinforcing steel, the details of which are described.

3.5.1 Cyclic Stress Strain Relationship for Reinforcing Steel

The monotonic stress strain curve for reinforcing steel consists of three regions; the linear region, the yield plateau, and the strain hardening region. A bilinear curve is usually an acceptable approximation for the monotonic curve. However, under reversed cyclic loading, the behavior is different as shown in Figure 3.17. At load reversals, the unloading stiffness is the same as the initial stiffness E_i. When loading continues in the opposite direction, the stress strain curve exhibits the Bauschinger effect, which causes a non linear stress- strain relationship and softening of the stress strain curve before the stress reaches the yield stress in the opposite direction (Aktan et al. (1973), and Menegotto and Pinto (1973)). Using the bilinear approximation, which is appealing because of its simplicity, is considered a crude approximation of the actual behavior.

A number of models have been developed to describe the cyclic stress strain curve of reinforcing steel (Stevens et al. (1987), Aktan et al. (1973), and Menegotto and Pinto (1973)). The most widely used of which is that of Menegotto and Pinto (1973) which is also used in the current study. The mathematical expression is similar to equation (3.19) where:

$$\epsilon^* = \frac{(\epsilon - \epsilon_r)}{(\epsilon_o - \epsilon_r)} \tag{3.31}$$

$$\sigma^* = \frac{(\sigma - \sigma_r)}{(\sigma_o - \sigma_r)} \qquad (3.32)$$

This expression represents a curved transition from a straight line with slope E_o to another asymptote with slope E_1 as represented by lines (a) and (b) respectively as shown in Figure 3.17. The parameter b is the strain hardening ratio between E_1 and E_o. σ_o and ϵ_o are the coordinates of the point where the asymptotes of the branch under consideration meet and σ_r and ϵ_r are the stress and strain of the point where the last strain reversal having stress of the same sign of σ_o took place. σ_o, ϵ_o, σ_r, and ϵ_r are updated at each strain reversal. R is the parameter that controls the shape of the transition curve and allows the representation of the Bauschinger effect. The expression for R is as follows:

$$R = R_o - \frac{a_1 \xi}{a_2 + \xi} \qquad (3.33)$$

R is a decreasing function of ξ which is the strain difference between the current asymptote intersection point (σ_o, ϵ_o) and the previous load reversal point with maximum or minimum strain depending on whether the corresponding steel stress at reversal is positive or negative (σ_r, ϵ_r), as shown in Figure 3.17. ξ is updated following a strain reversal. R_o, a_1, a_2, are experimentally determined parameters. In this model it is assumed that $R_o = 20$, $a_1 = 18.5$, and $a_2 = 0.0015$.

This formulation allows a good representation of complete stress strain cycles, but for partial loading or unloading, it is necessary to introduce some rules to extend the validity of the model. Filippou et al. (1983) proposed a set of rules limiting the memory of the model to four fundamental curves:

(I) The initial monotonic envelope;

(ii) The ascending upper branch curve, originating at the reversal point with the smallest ϵ value;

(iii) The descending lower branch curve, originating at the reversal point with the largest ϵ value and;

(iv) The current curve originating at the most recent reversal point.

Figures 3.18 to 3.20 provide a comparison between the non linear steel model, the bilinear model, and the experimental results of three load histories carried out by Seckin (1981). The Figures indicate that the proposed model agrees well with the experimental results.

The deficiencies of the bilinear model are also illustrated in the same Figures. Because in the bilinear model, unloading continues with the same initial stiffness, yielding is achieved in the reversed cycle earlier than in reality. Also when unloading occurs, the bilinear model predicts much higher stresses as compared to the true response at the same strains. This occurs at the time when crack closure takes place. It is recommended that the bilinear model should not be used when crack closing is

of significant importance to the structural response.

The energy dissipation of the bilinear model appears to be significantly different from the actual response. Figure 3.18 shows the case where significant plastic deformation takes place in tension and compression. In this case the bilinear model is shown to dissipate much larger energy than the actual response. Figure 3.19 and 3.20 show the case where partial load reversals take place. In this case, the bilinear model dissipates less energy compared with the actual response. This is a direct result of the fact that unloading in bilinear model continues with the initial stiffness up till yielding.

3.6 GLOBAL AXES TRANSFORMATION

In the previous discussion, the concrete properties have been evaluated in the crack planes. In order to transfer these properties into the global X-Y axes, the transformation matrix [T] is used as follows:

$$D_{conc} = [T]^T [D]_{12} [T] \qquad (3.34)$$

where

D_{conc} = Constitutive matrix defined in the frame of reference of the element local axes.

D_{12} = Constitutive matrix defined in the frame of reference of the principal axes of orthotropy.

[T] = Transformation matrix

$[T]^T$ = Transpose of T

[T] is given as follows:

$$T = \begin{bmatrix} c^2 & s^2 & sc \\ s^2 & c^2 & -sc \\ -2sc & 2sc & c^2-s^2 \end{bmatrix} \tag{3.35}$$

where c=cosθ, s=sinθ, and $\theta = \theta_{conc} + \theta_{element}$. θ_{conc} is the angle between the principal planes and the local axes of the element. $\theta_{element}$ is the angle between the local axes of the element and the global X-Y axes .

Transformation must also be applied to convert the component steel reinforcement stiffnesses to the global system as follows:

$$D_{steel} = \sum_{I=1}^{n} [T]^T [D]_I [T] \tag{3.36}$$

where [T] and $[T]^T$ are as described previously. In this case, $\theta = \theta_{steel} + \theta_{element}$. θ_{steel} is the angle between the direction of steel reinforcement of group *I* and the local axes of the element. Finally, the total [D] of the element is the sum of $[D]_{conc}$ and $[D]_{steel}$.

3.7 EXPERIMENTAL VERIFICATION

The nonlinear material models for concrete and steel reinforcement described above have been incorporated into PC-ANSR (Maison (1992)), a general purpose structural analysis computer program. Experimental data from three walls tested at

the Portland Cement Association (Oesterle et al. (1978)) are used to verify the proposed model. The wall dimensions are shown in Figure 3.21. Barbell (B2 and B5) and Rectangular (R2) cross sections are used in the investigation. The material properties and the reinforcement ratios are listed in Table 1. These wall specimens are chosen for comparison because shear deformations governed their response.

The finite element descretization of the walls used in the current analysis is also shown in Figure 3.21. The concrete wall is modeled using twelve node quadrilateral plane stress elements. A total of thirty two (32) elements are used to represent the full wall. The use of the twelve node element with its cubic displacement field have allowed the selection of such a coarse mesh. The maximum aspect ratio for all the elements is kept less than three to avoid numerical errors. Nodes at the base of the wall are restrained against horizontal and vertical translations. The top slab is considered to be rigid to distribute the load to the entire cross-section. Steel reinforcement is modeled using smeared representation over the element. The experimental cyclic displacement history of each specimen is imposed at the upper left corner of the wall (displacement control method). The displacement history is characterized by pushing the specimen in one direction several times during each load cycle, and then increasing the displacement level during subsequent cycles.

Figures 3.22 to 3.24 show the experimental and the analytical load deflection relationships for tested walls. These walls have also been analytically studied previously by Sittipunt and Wood (1993). Their load deflection curves are also shown

in the same Figures. It is however worth mentioning that Sittipunt and Wood used a refined mesh of one hundred and eighty (180) four node quadrilateral elements to model the concrete, with three hundred and seventy eight (378) truss elements to model the steel reinforcement.

The experimental load deflection curves shows pinched hysteretic loops indicating shear dominant behavior. This is mainly because the shear behavior of a RC structure is mainly governed by the concrete response. This type of behavior represents a severe test of the cyclic constitutive model used in the present study. The flexural response of RC can be usually predicted using any crude concrete model since the response is heavily dependant on the steel reinforcement. The success of the proposed analytical RC model as well as Sittipunt and Wood's model can be noticed by the close correlation between the predicted and the actual response. The analytically predicted hysteretic loops follow the same trend observed experimentally. The stiffness deterioration of the walls caused by the application of the reversed cyclic loading is well represented analytically. The analytical peak values of the lateral loads are almost of the same magnitude as those experimentally recorded.

3.8 CONCLUSIONS

A non linear finite element RC model is presented in this Chapter. The model promises to be a reliable analytical tool and is capable of reproducing most of the characteristic features of RC behavior under reversed cyclic loading. The model

adopts the concept of smeared crack approach with orthogonal cracks and assumes plane stress condition. It comprises two independent functions; the normal stress function and the shear stress function. The normal stress function defines the stress strain behavior of concrete under cyclic tension and compression. The important aspects of concrete behavior included in the normal stress function are tension stiffening, crack opening and closing, compression hardening and softening, degradation of concrete strength and stiffness in the direction parallel to the crack, and compression unloading and reloading. The shear stress function defines the cyclic relationship between the shear stress and the shear strain of concrete. A smeared reinforcing steel model is included to describe the cyclic stress strain behavior of the steel reinforcement. The aspects included in the steel model are yielding, strain hardening, Bauschinger effect as well as the cyclic unloading and reloading rules.

The predictions of the proposed model shows good correlation with the available analytical and experimental results. The model is able to successfully predict the stiffness degradation and the peak load deflection values of RC walls with high shear deformation under the effect of reversed cyclic loading. The use of high power elements, such as the twelve node quadrilateral element, with smeared reinforcement have allowed the use a smaller number of elements to represent the behavior of RC members.

3.9 LIST OF SYMBOLS

d_b Bar diameter (mm).

D_{12} Constitutive matrix of concrete defined in the frame of reference of the principal axes of orthotropy.

D_{conc} Constitutive matrix of concrete defined in the frame of reference of the element local axes.

$[D]_i$ Steel constitutive matrix in the *i* direction.

D_{steel} Constitutive matrix of steel defined in the frame of reference of the element local axes.

E_{11} , E_{22} Tangent moduli of elasticity in the two principal directions.

E_1 Initial tangent stiffness for concrete and is equal to $2f_c'/\epsilon_c'$.

E_2 , E_3 Tangent stiffnesses for concrete in compression and are equal to $0.3E_1$ and 0 respectively.

E_s Secant modulus for concrete at the peak compressive stress and is equal to f_c'/ϵ_c'.

E_{un} Unloading concrete stiffness in compression (equation 3.24).

f_c Concrete stress.

f_c' Concrete compressive strength.

f_{cr} Concrete tensile strength.

f_{cp}, ϵ_{cp} Stress and strain of the common point which represents the focal point

of the reloading curve in compression (Figure 3.9).

f_{fp}, ϵ_{fp} Stress and strain of the focal point when the cracks are considered fully closed (Figure 3.8).

f_{rl}, ϵ_{rl} Stress and strain of the reloading point (Figure 3.9).

f_{yh} Yield strength of stirrups in MPa.

f_{un}, ϵ_{un} Stress and strain of the unloading point (Figures 3.8 and 3.9).

f_{unb} Unbalanced concrete stress (Figure 3.3).

G_{12} Shear modulus in the principal directions and is equal to 0.25 (E_{11} + E_{22} - $2\nu\sqrt{E_{11}E_{22}}$).

G_{conc} Shear stiffness of uncracked concrete (E_1 / 2(1+ v)).

G_{cr} Shear stiffness of cracked concrete (equation 3.26).

G^1_{cr}, G^2_{cr} Shear stiffnesses in crack directions 1 and 2 respectively.

G_{min} The minimum value of G_{cr}.

G_{un} Unloading shear stiffness.

h' Width of concrete core measured to outside of stirrups.

k, r Coefficients defining the strain softening branch of the compression stress strain curve for concrete (equations 3.12 and 3.13).

K Coefficient that accounts for the strength increase due to confinement (equation 3.16).

R Parameter that controls the shape of the transition curve for steel reinforcement and allows the representation of the Bauschinger effect

(equation 3.33).

R_o, a_1, a_2 Constants defining the crack closing and opening curve (Figure 3.8).

S_h Center to center spacing of stirrups or hoop sets.

$[T]$, $[T]^T$ Transformation matrix and its transpose.

ν Poisson's ratio.

Z Strain softening slope for confined concrete (equation 3.17).

ϵ_1, ϵ_2 Normal strains in the principal directions.

$d\epsilon_1$, $d\epsilon_2$ Incremental normal strains in the principal directions.

ϵ_{12} Shear strain in the principal directions.

$d\epsilon_{12}$ Incremental shear strain in the principal directions.

ϵ_c Concrete strain.

ϵ_{cr} Concrete strain at cracking.

ϵ_c' Concrete strain at maximum stress.

ϵ^i_{nn} Normal crack strain in *i* direction.

ϵ_{min} Normal crack strain where $G^i_{cr} = G_{min}$ (equation 3.15).

ϵ_{co} Concrete strain at maximum stress for confined concrete.

ξ Strain difference between ϵ_o and ϵ_r (Figure 3.17).

σ_1, σ_2 Normal stresses in the principal directions.

$d\sigma_1$, $d\sigma_2$ Incremental normal stresses in the principal directions.

σ_o, ϵ_o Stress and strain of the point where line (a) meets the asymptote of line (b) (Figure 3.17).

σ_r, ϵ_r Stress and strain of the point where the last strain reversal having stress of the same sign of σ_o took place (Figure 3.17).

τ_{12} Shear stress in the principal directions.

$d\tau_{12}$ Incremental shear stress in the principal directions.

β Softening coefficient to the peak stress and the strain at the peak stress (equation 3.18).

ρ_i Steel reinforcement ratio in the *i* direction.

ρ_s Ratio of the volume of hoop reinforcement to the volume of concrete core measured to outside of stirrups.

α 75 (ρ_s / d_b) (mm).

λ_t Parameter that controls the concrete tension stiffening (equation 3.5).

μ Parameter that relates interface shear transfer stiffness to shear stiffness of uncracked concrete.

θ_{conc} Angle between the principal planes and the local axes of the element.

$\theta_{element}$ Angle between the local axes of the element and the global X-Y axes.

θ_{steel} Angle between the direction of steel reinforcement of group *i* and the local axes of the element.

Table 3.1 Material properties of PCA wall specimens

	Wall B2	Wall B5	Wall R2
Cross section shape	Barbell	Barbell	Rectangular
Concrete compressive strength f_c' MPa (psi)	53.6 (7780)	45.3 (6570)	46.5 (6740)
Yield stress of boundary elements reinforcement, MPa (ksi)	410.3 (59.5)	444 (64.4)	450.2 (65.3)
Yield stress of vertical web reinforcement MPa (ksi)	532.3 (77.2)	444 (64.4)	535.1 (77.6)
Yield stress of horizontal web reinforcement, MPa (ksi)	532.3 (77.2)	444 (64.4)	535.1 (77.6)
Boundary element reinforcement ratio	3.67	3.67	4.00
Vertical web reinforcement ratio	0.29	0.29	0.25
Horizontal web reinforcement ratio	0.63	0.63	0.31
Confinement reinforcement ratio *	---	1.35	1.45

* Area of confinement reinforcement in boundary element divided by amount required in ACI 318-89.

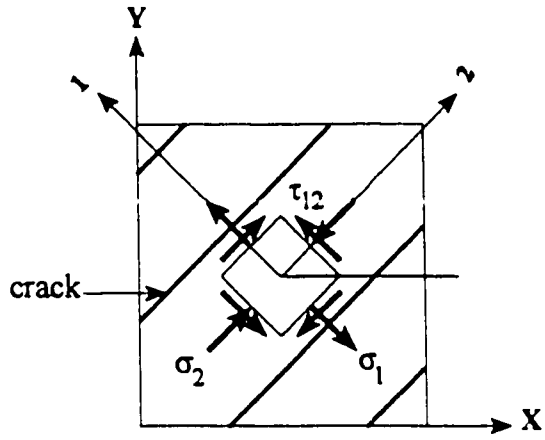

Figure 3.1 The coordinates of cracked concrete

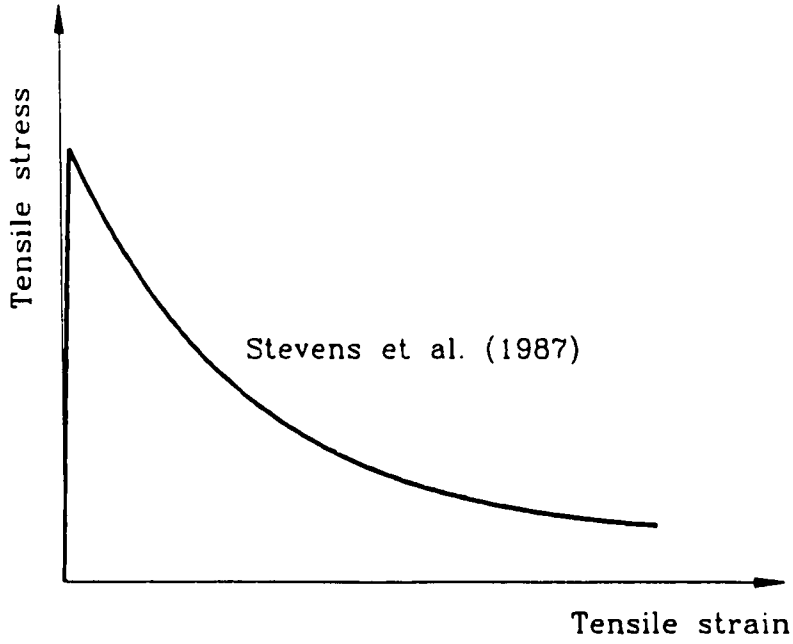

Figure 3.2 Stress strain curve for concrete in tension

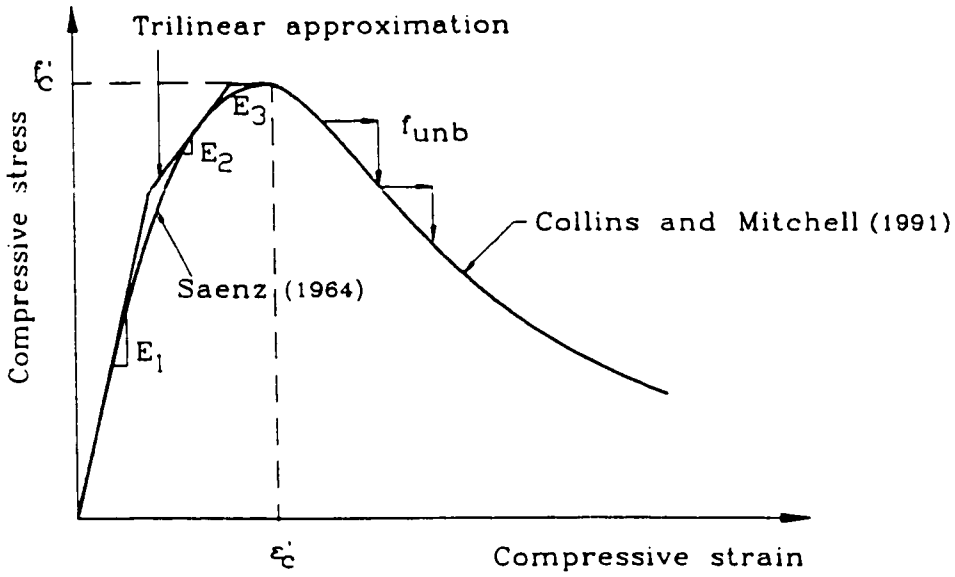

Figure 3.3 Stress strain curve for concrete in compression

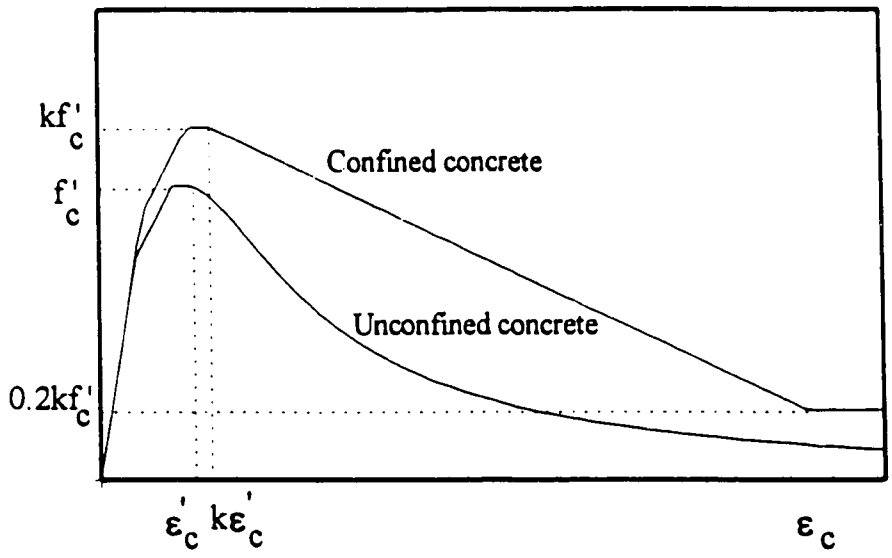

Figure 3.4 Stress strain curves for confined and unconfined concrete in compression

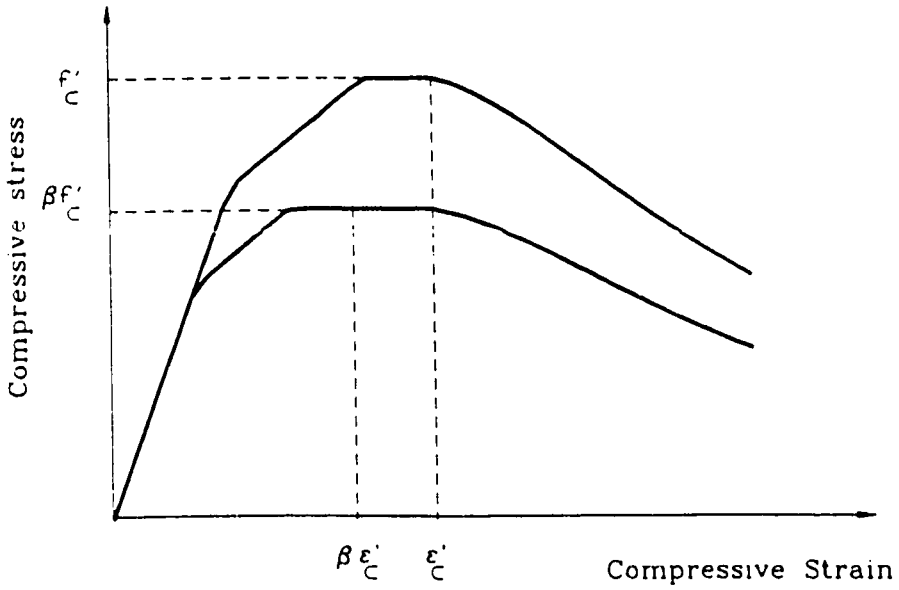

Figure 3.5 Deteriorated compression response of cracked concrete

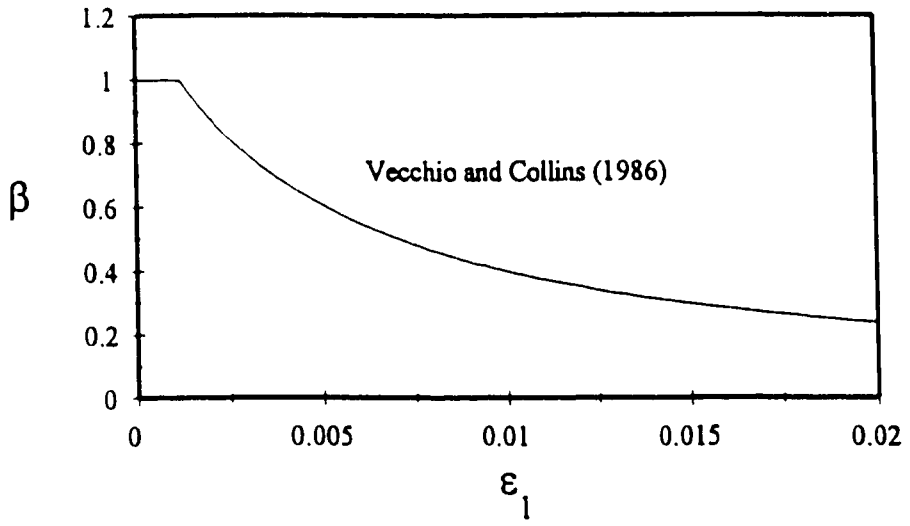

Figure 3.6 Softening coefficient for cracked concrete

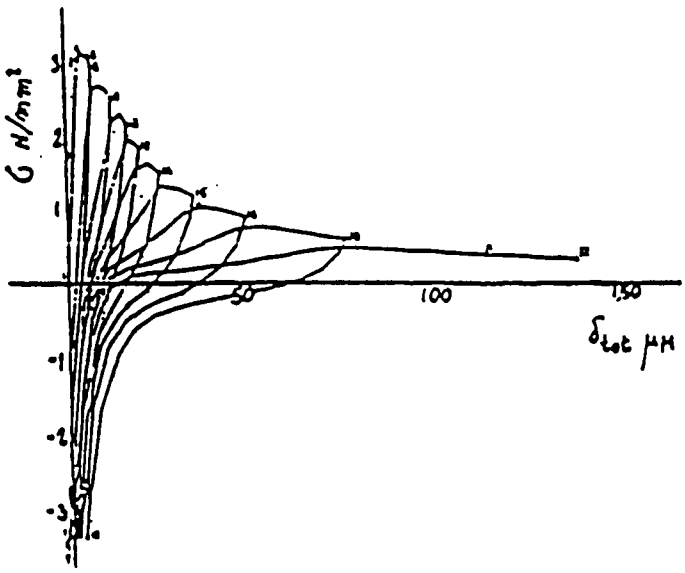

Figure 3.7 Typical cyclic stress crack width relationship (Yankelevsky and Reinhardt, 1989)

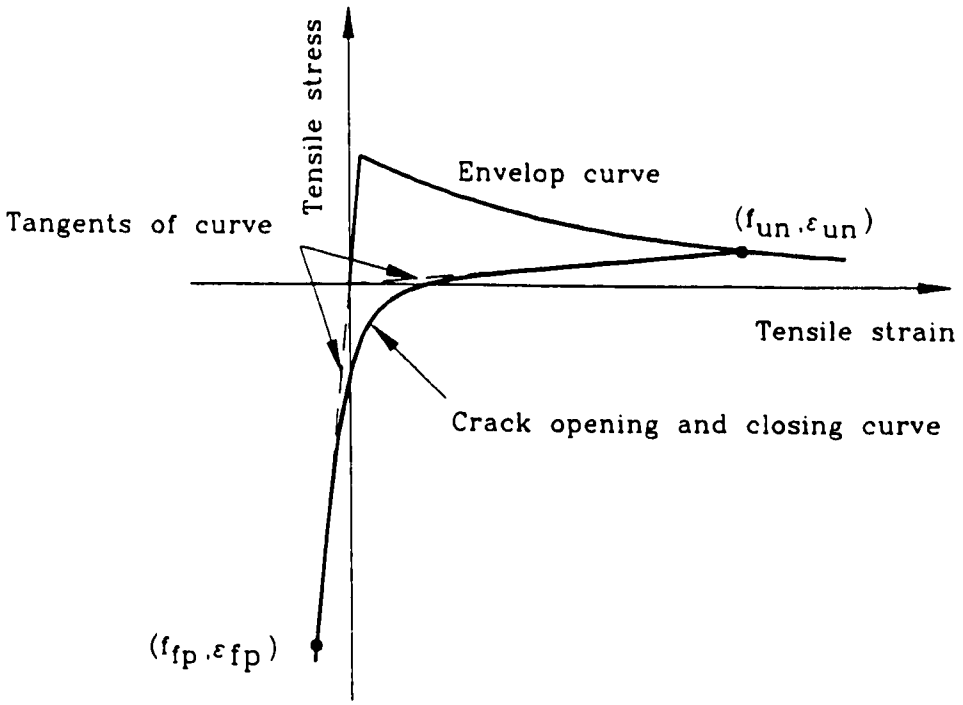

Figure 3.8 Proposed cyclic stress strain curve for crack opening and closing

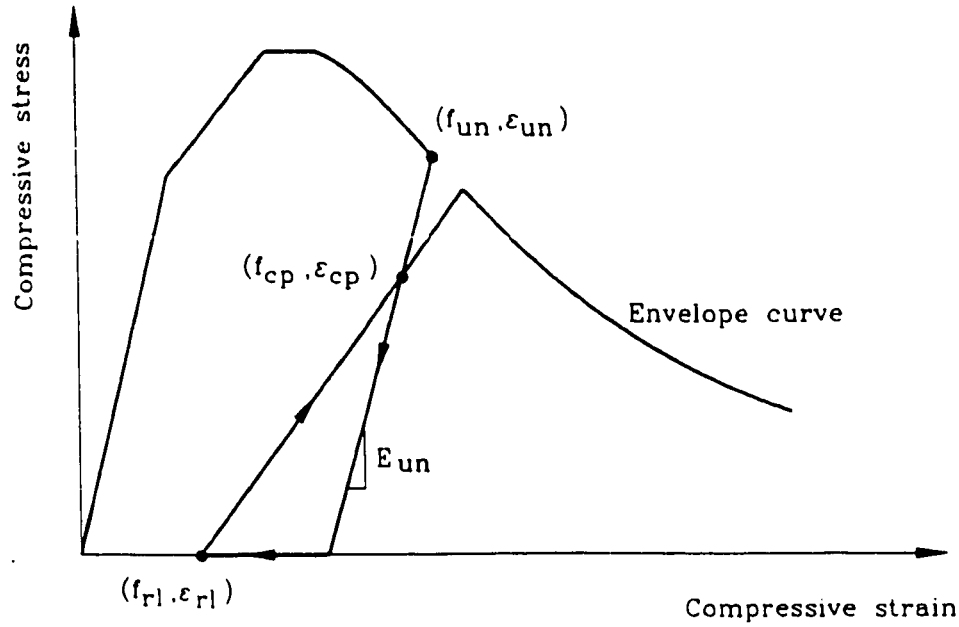

Figure 3.9 Proposed cyclic stress strain curve for concrete in compression

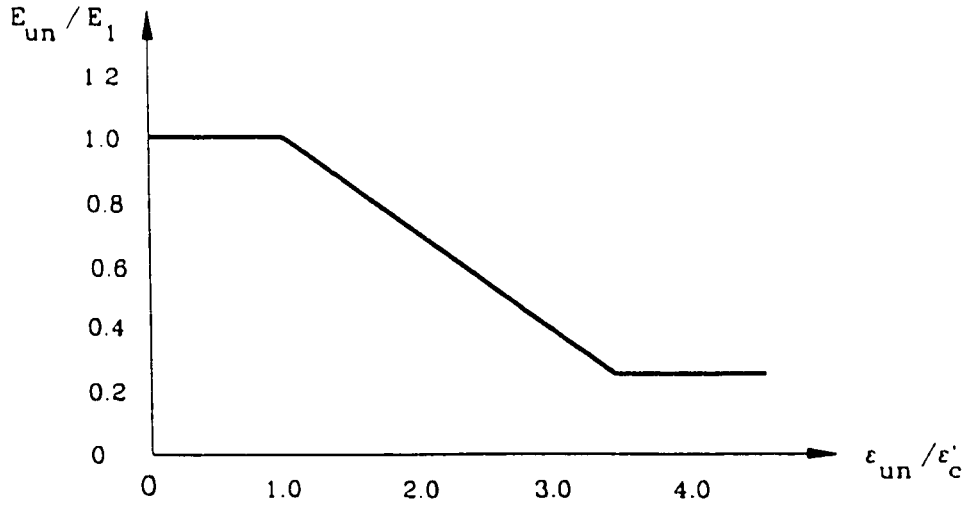

Figure 3.10 Estimation of the unloading stiffness

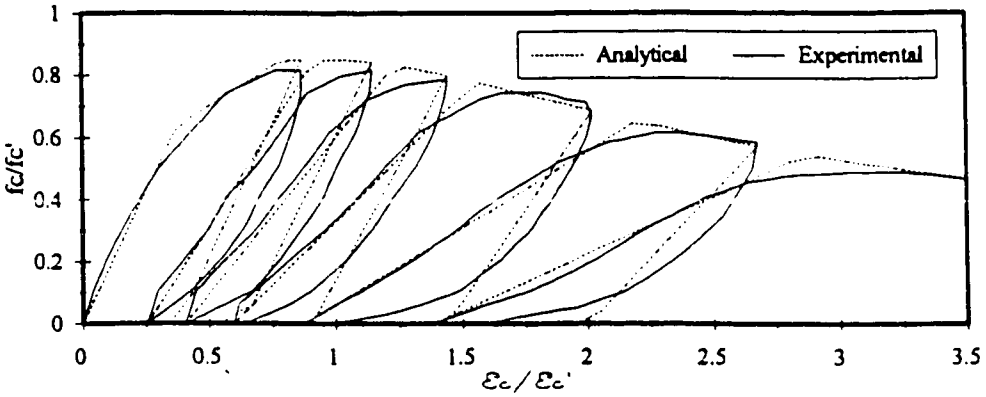

(a)

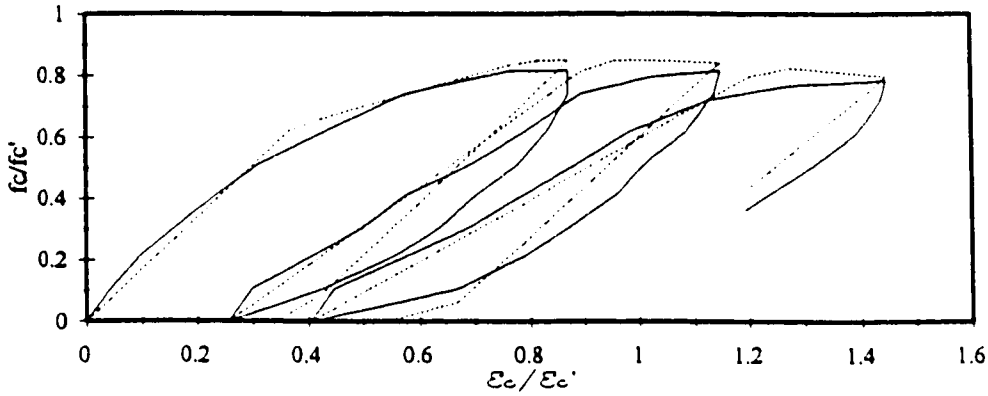

(b)

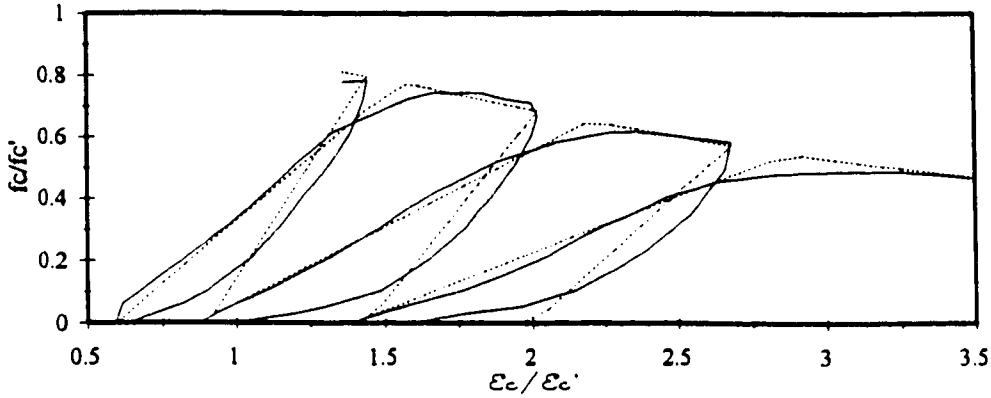

(c)

Figure 3.11 Unconfined cyclic compression test by Karsan and Jirsa (1969); (a) complete test; (b) first two cycles; (c) last three cycles

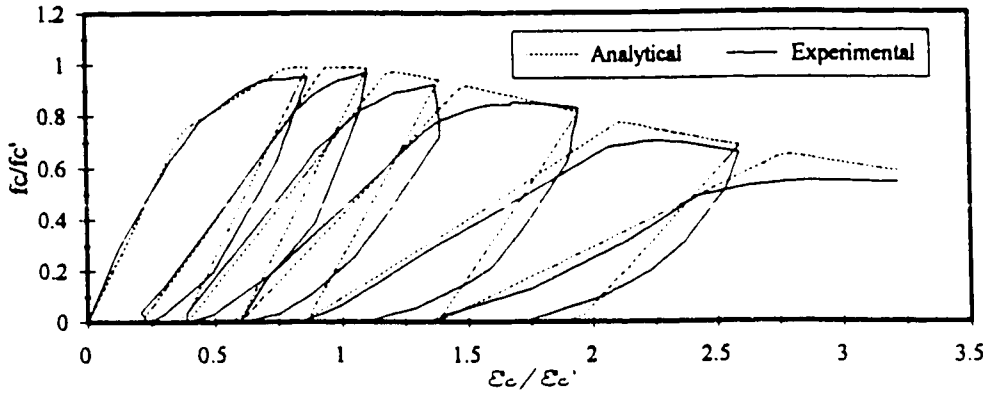

(a)

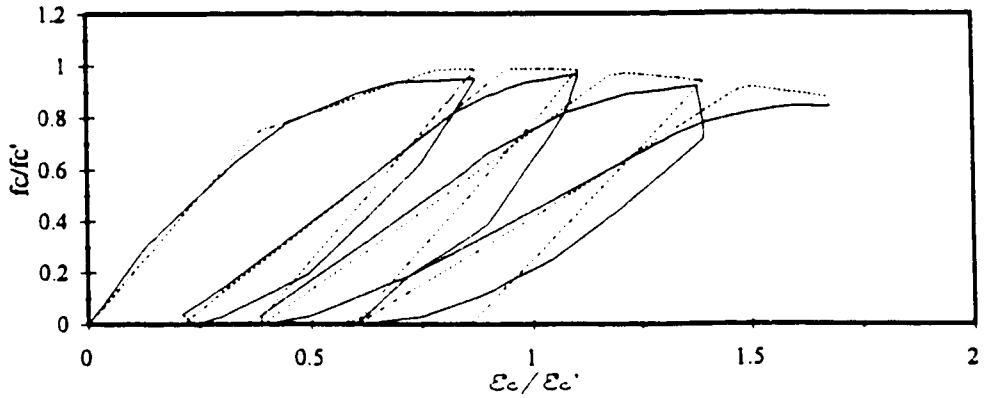

(b)

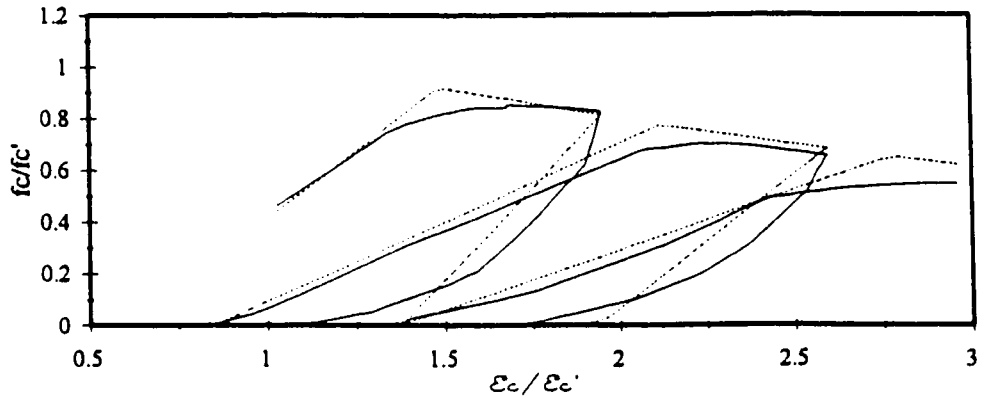

(c)

Figure 3.12 Unconfined cyclic compression test by Karsan and Jirsa (1969); (a) complete test; (b) first three cycles; (c) last two cycles

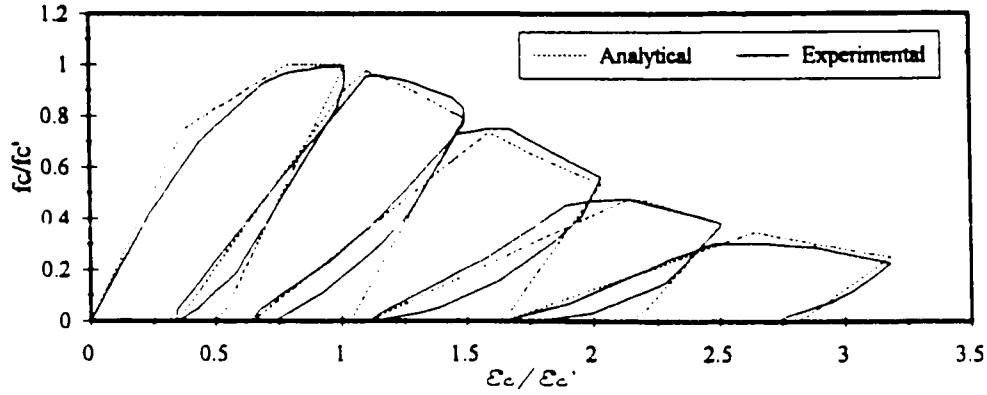

(a)

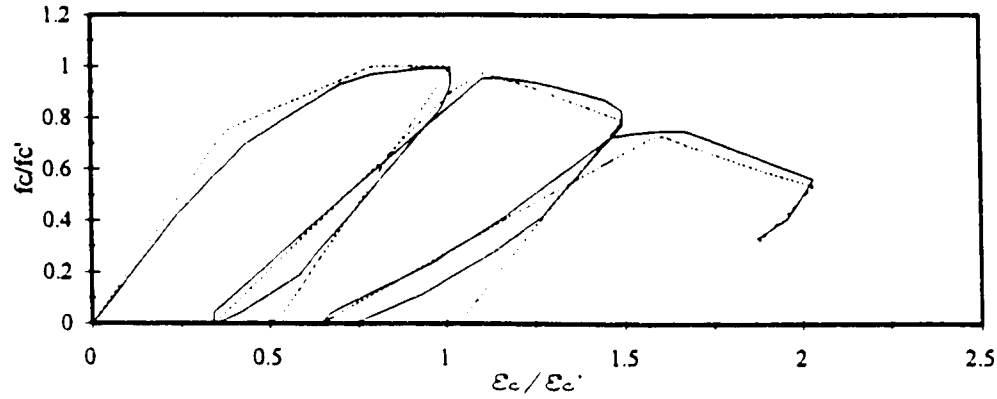

(b)

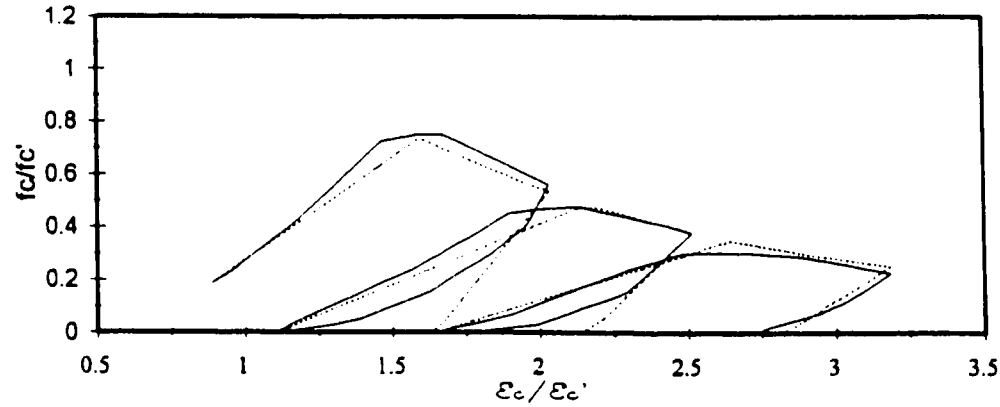

(c)

Figure 3.13 Unconfined cyclic compression test by Okamoto et al. (1976); (a) complete test; (b) first two cycles; (c) last two cycles

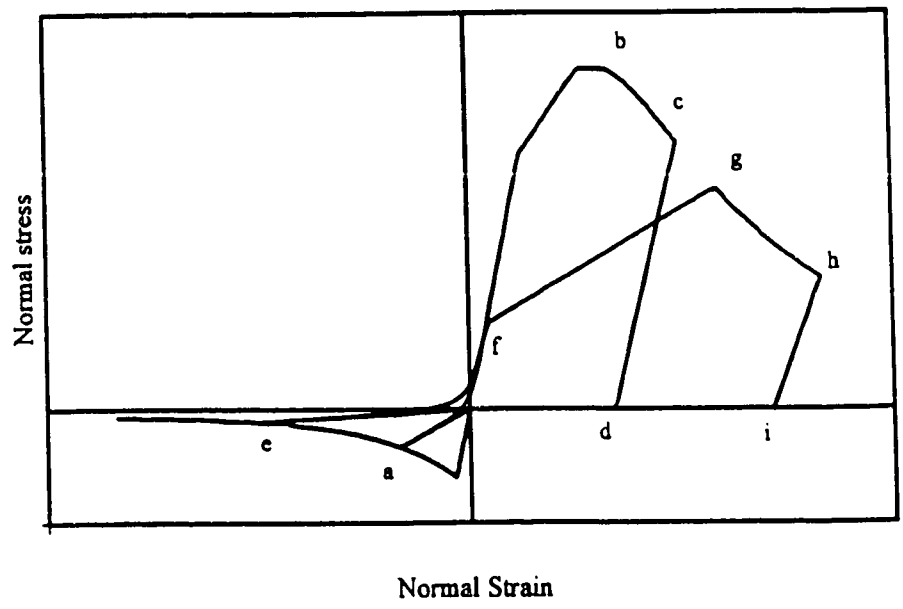

Figure 3.14 Typical analytical normal stress strain relationship for concrete

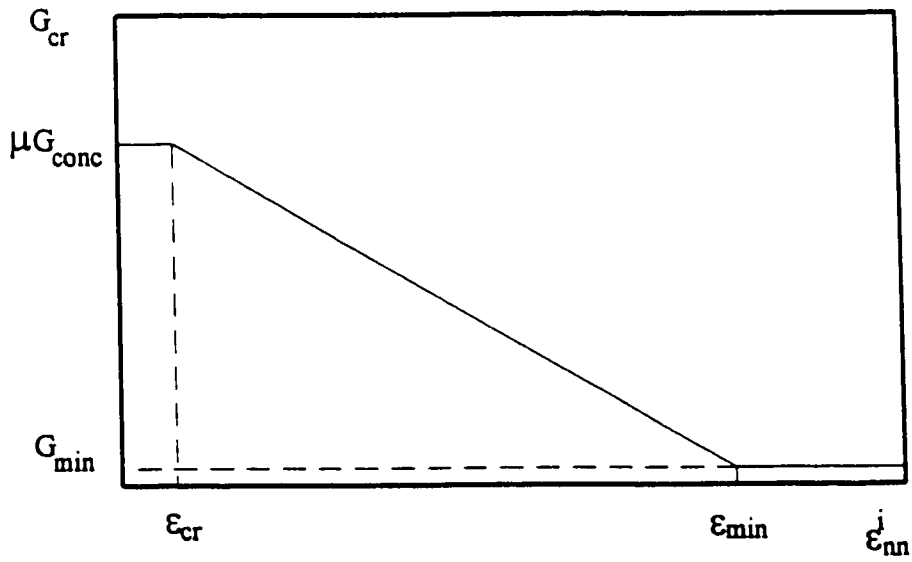

Figure 3.15 Relationship between cracked shear stiffness and normal strain across the cracks

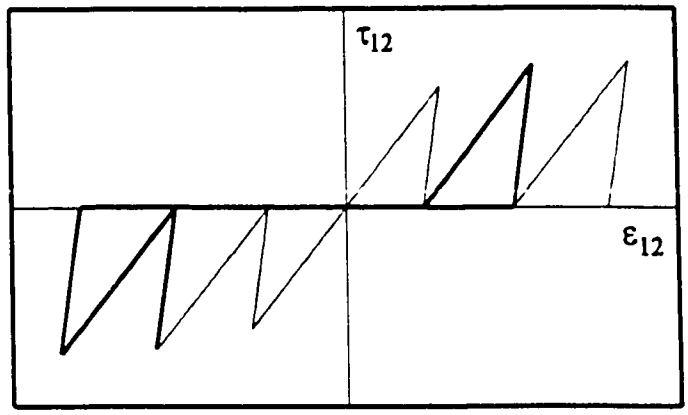

(a) Typical analytical shear stress strain relationship for concrete

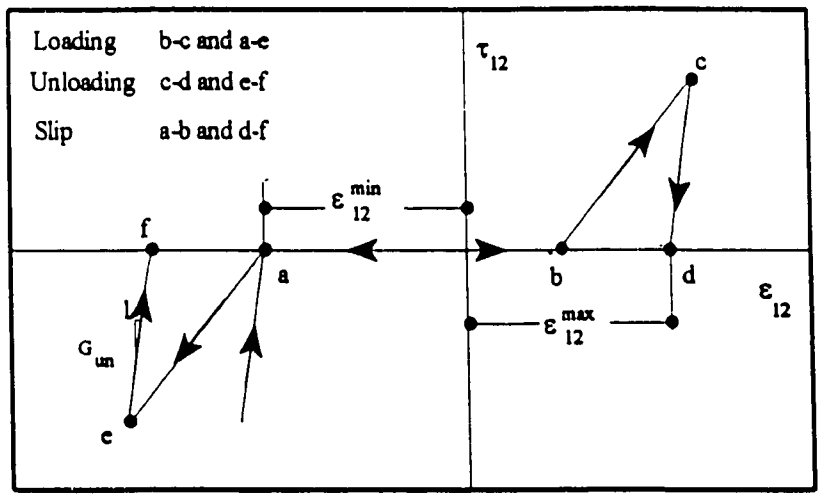

(b) Cyclic loading rules for the shear model

Figure 3.16 Proposed cyclic shear transfer model

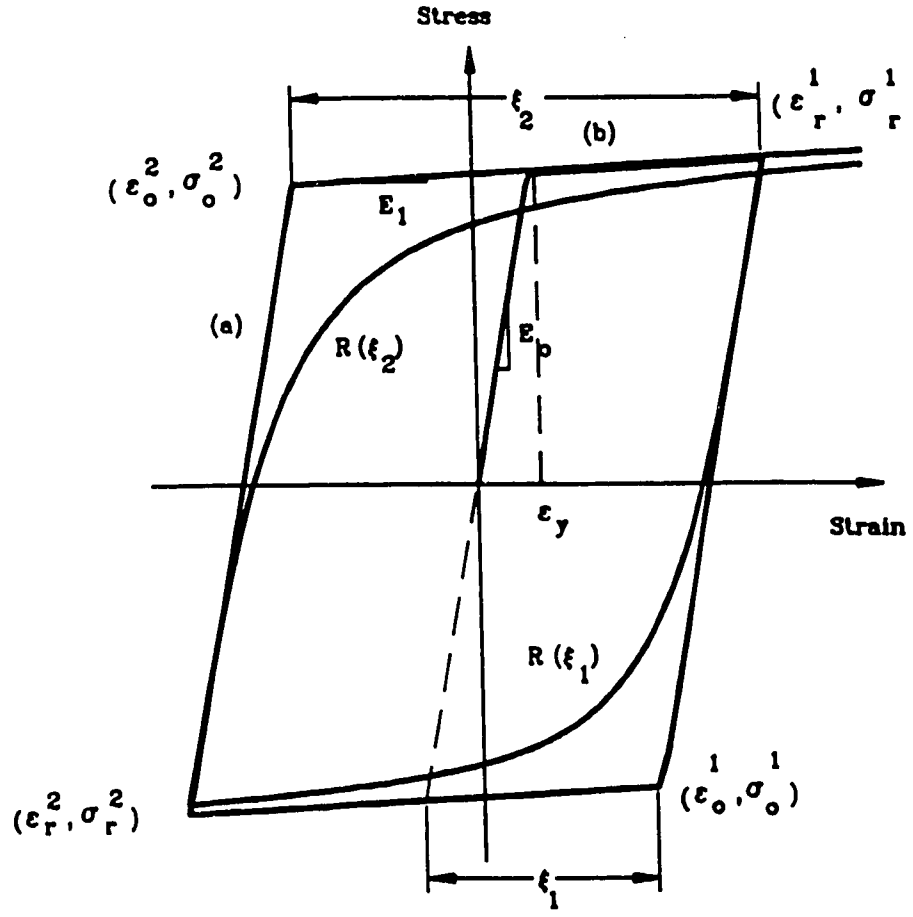

Figure 3.17 Typical stress strain relationship for steel reinforcement under cyclic loading

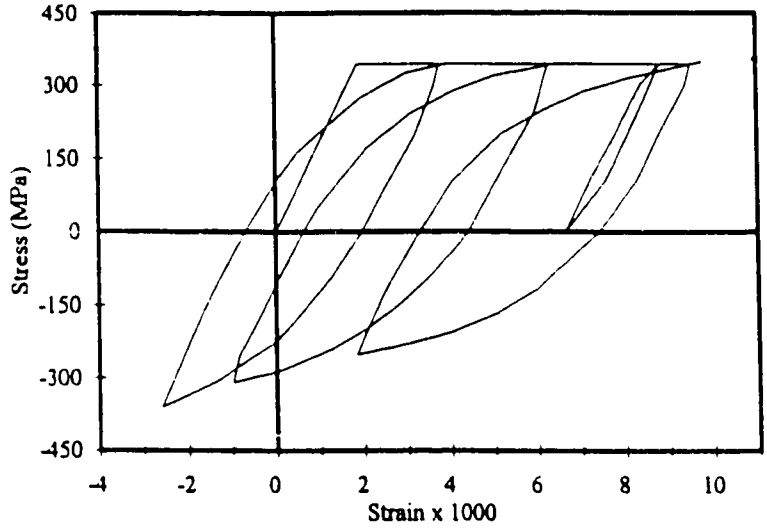

(a) Experimental Results

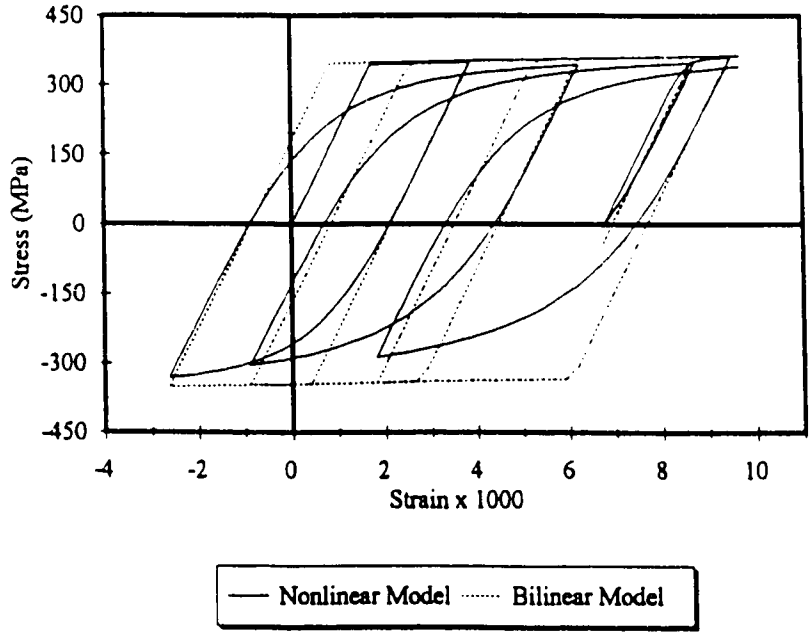

(b) Analytical Results

Figure 3.18 Stress strain curve for bar number BR01 from Seckin (1981); (a) Experimental results; (b) Analytical results

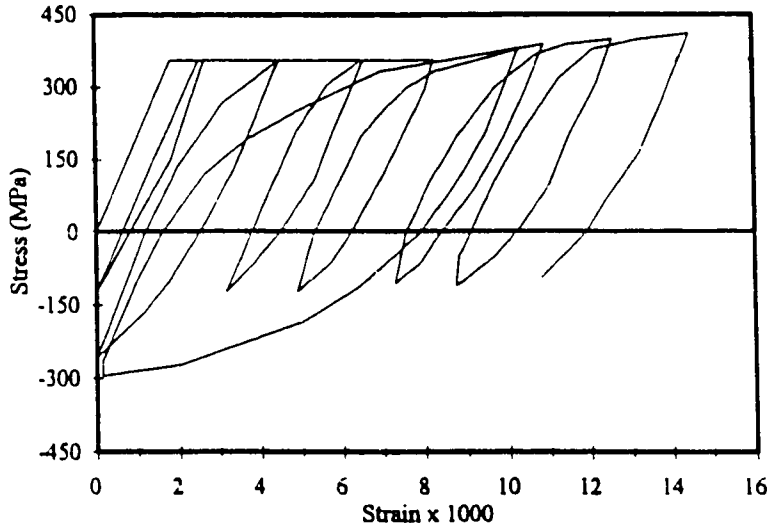

(a) Experimental Results

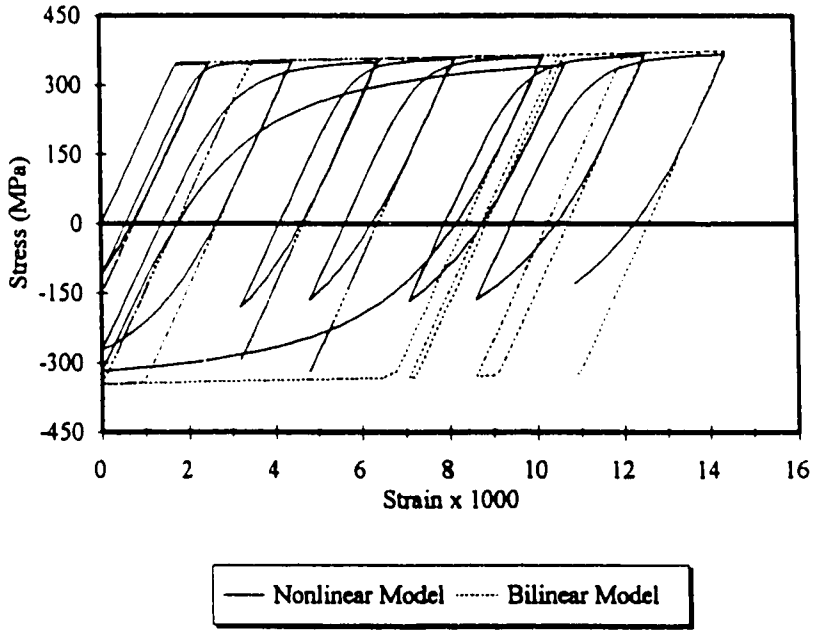

(b) Analytical Results

Figure 3.19 Stress strain curve for bar number BR07 from Seckin (1981); (a) Experimental results; (b) Analytical results

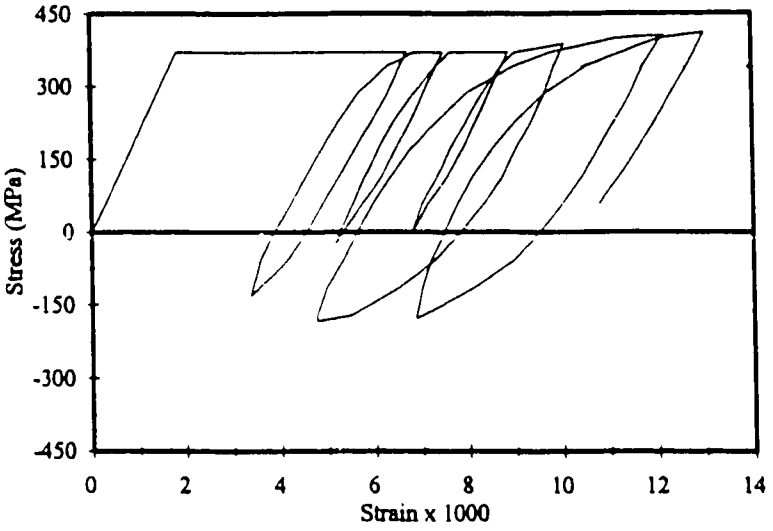

(a) Experimental Results

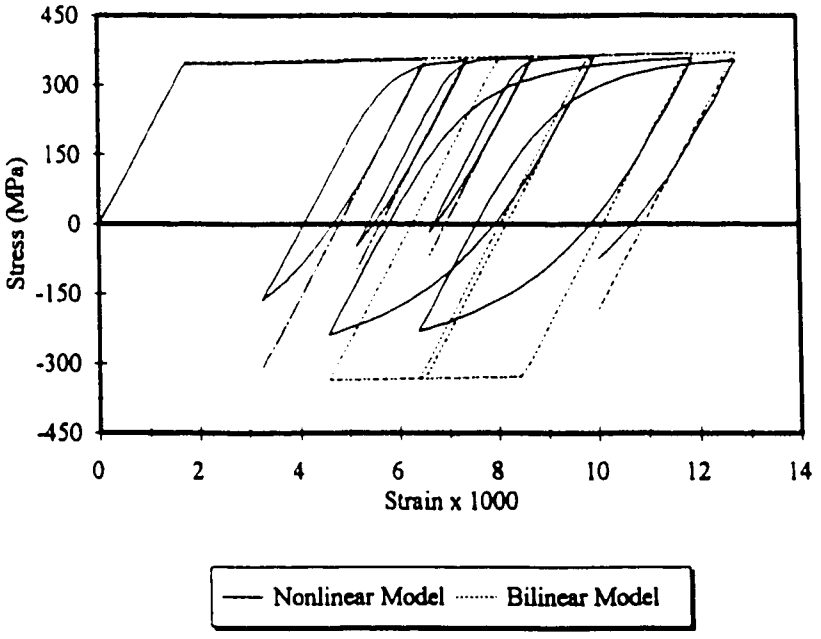

(b) Analytical Results

Figure 3.20 Stress strain curve for bar number BR13 from Seckin (1981); (a) Experimental results; (b) Analytical results

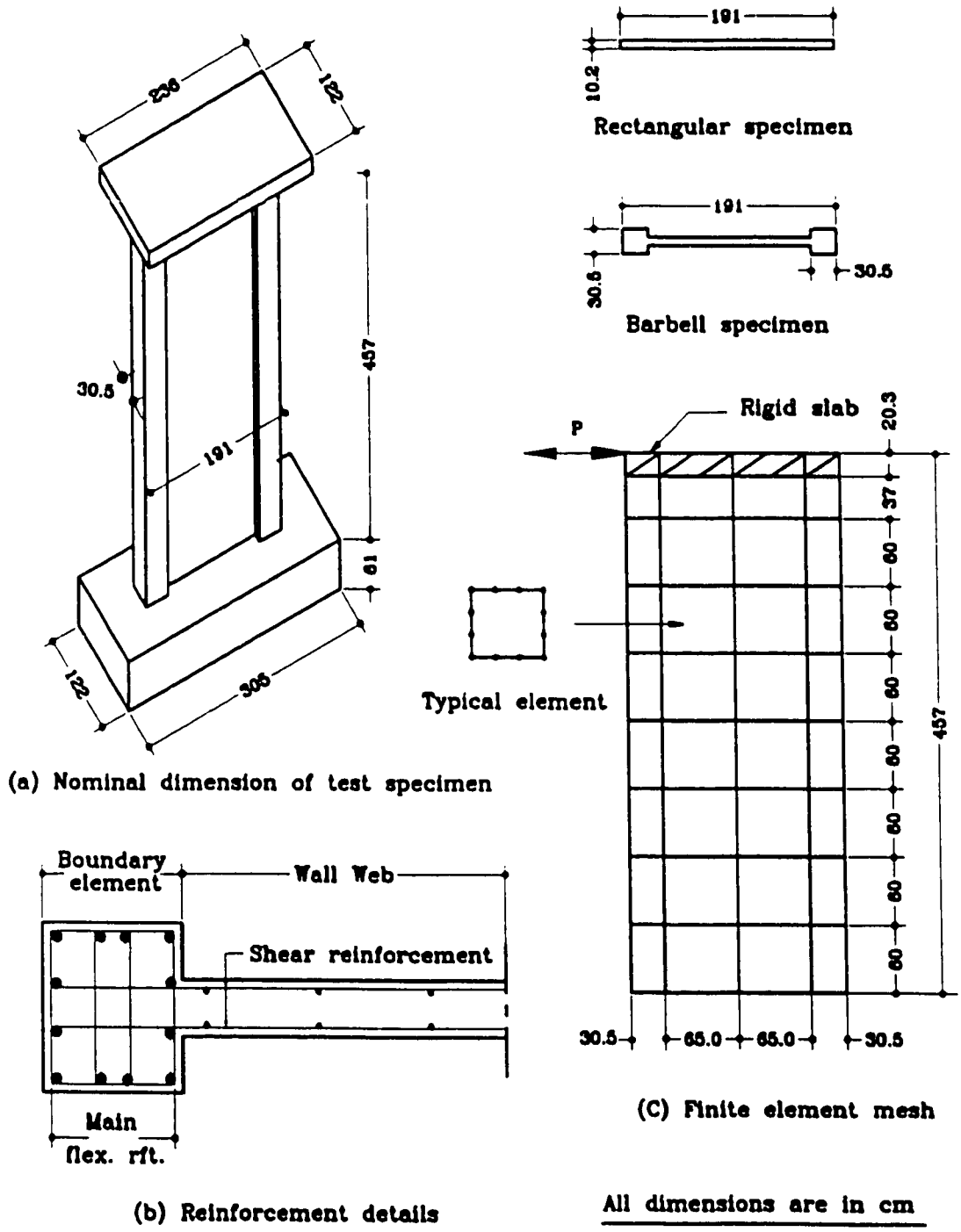

Figure 3.21 Nominal dimensions of the PCA wall specimen and the finite element descretization

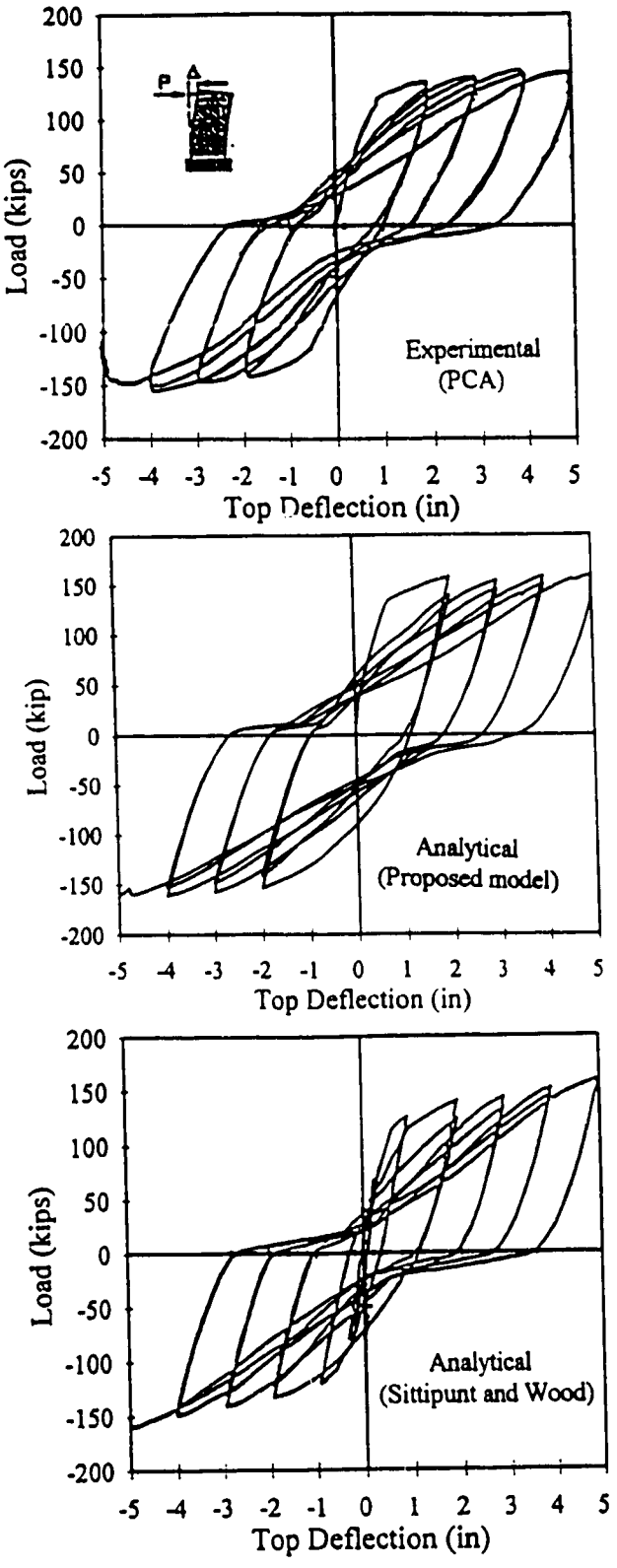

Figure 3.22 Load deflection curves for wall B2; 1 kip = 3.448 kN, 1 in = 25.4 mm

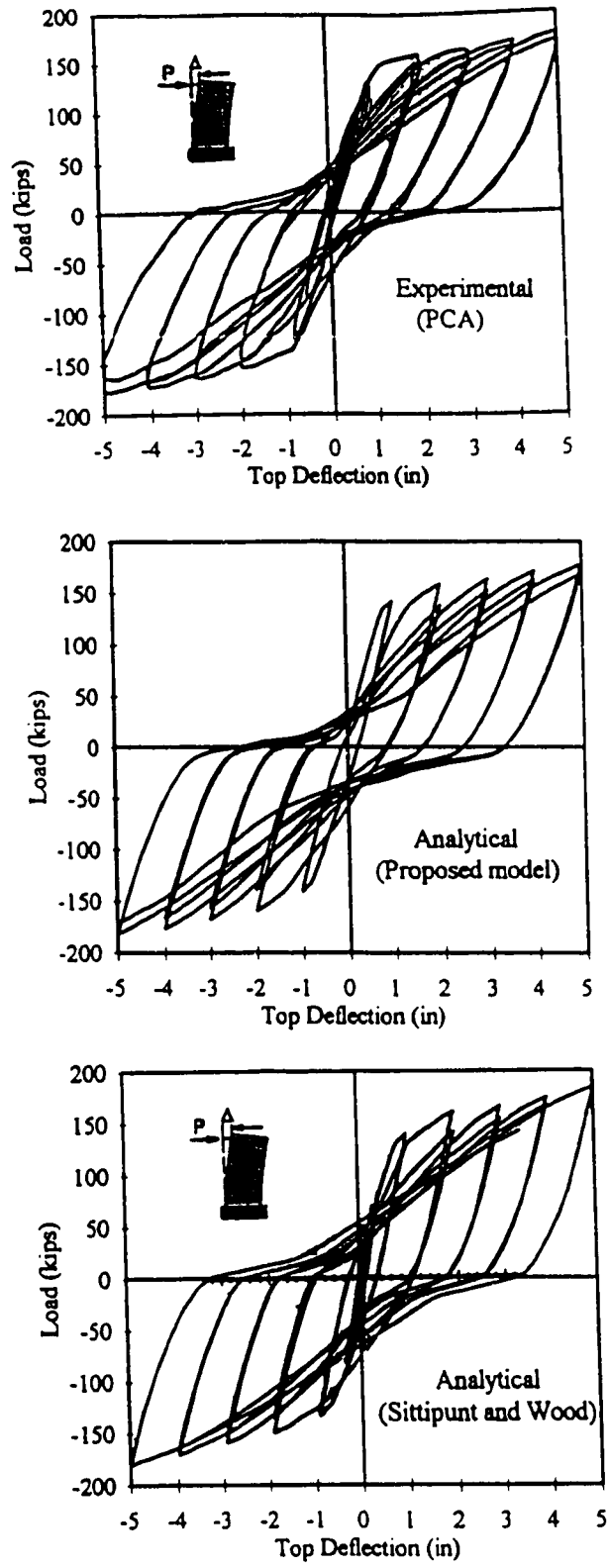

Figure 3.23 Load deflection curves for wall B5; 1 kip = 3.448 kN, 1 in = 25.4 mm

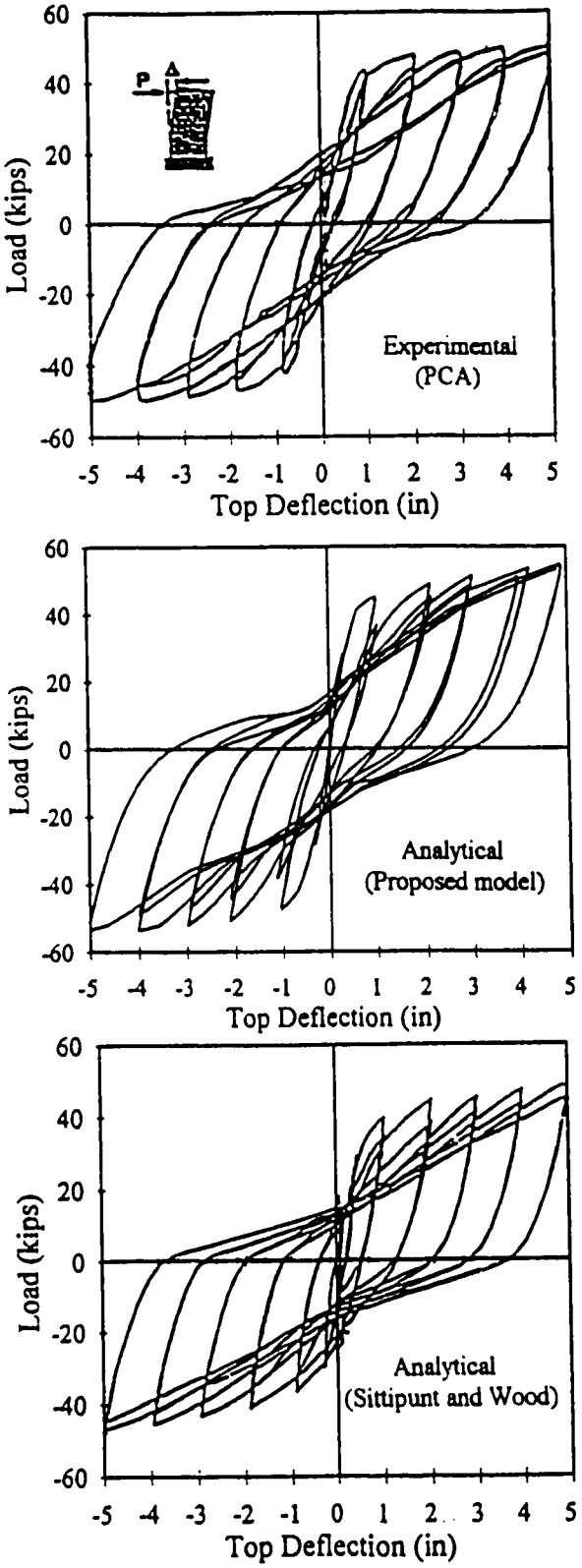

Figure 3.24 Load deflection curves for wall R2; 1 kip = 4.448 kN, 1 in = 25.4 mm

CHAPTER 4

BOND SLIP MODEL

4.1 GENERAL

The contribution of the beam column connection to story displacements is made by shear and bond slip in the joint panel region. In this Chapter, deformations resulting from bond slip are studied and an analytical model for their representation is introduced.

Most of the analytical studies on the hysteretic behavior of reinforced concrete connections to date are based on the assumption of perfect bond between steel and concrete. Experimental studies on reinforced concrete beam column subassemblies (Bertero and Popov (1977)) have shown that perfect bond approximates the actual behavior between steel and concrete only before yielding of steel reinforcement. Once yielding takes place, the bond resistance deteriorates along the bar portion that has yielded resulting in a relative slip between the reinforcing bar and the surrounding concrete. This gives rise to concentrated rotations between columns and beams called "fixed end rotations" (Filippou (1983a, b)).

Experimental studies have shown that under lateral loading, the most unfavorable bond conditions exist in the interior beam column connections leading to significant fixed end rotations at the beam column interfaces. These fixed end

rotations under cyclic lateral loads can contribute up to 50% of the overall deflections of the beam column subassemblies after yielding of the steel reinforcement. It is therefore crucial to consider the inelastic deformations due to bond slip in the analysis of reinforced concrete connections. This is especially important for LRC connections due to the deficiencies in their detailing.

Despite the fact that accurate constitutive relations for bond have been established based on experimental test results under cyclic loading (Eligehausen et al., 1983), there is no robust analytical model available for incorporation into a general purpose finite element program to describe the complex hysteretic behavior of the bond slip relation under cyclic excitations (Monti et al., 1997). The first model for bond slip of reinforcing bars was proposed by Ngo and Scordelis (1967). They developed a linear elastic finite element model of a simply supported beam. Concentrated bond link elements were introduced at the nodes connecting the concrete and steel elements. The bond link element had no physical dimension. It was represented by two orthogonal springs. Nilson (1972) used the same approach and introduced non linear constitutive relations for steel, concrete and bond slip. Keuser and Mehlhorn (1987) introduced a continuous interaction between steel and concrete instead of the concentrated link elements. However none of these studies directly addressed the analysis of an anchored reinforcing bar under cyclic excitations.

Filippou et al. (1983a,b) used the weighted residual method to solve the differential equations of equilibrium and compatibility of an anchored reinforcing bar.

Their development did not reach the stage to permit the model to be incorporated into a general purpose finite element analysis program. Monti et al. (1997) also developed a model for reinforcing bars anchored in concrete. Their model used force instead of displacement interpolation functions. This formulation was based on the approximation of reinforcing steel and bond stress fields along anchored reinforcing bar resulting in a flexibility based element formulation. In this method, the concrete deformations were neglected since in the post yield range of reinforcing steel they have little effect on the hysteretic behavior of anchored reinforcing bars. This element was implemented in a general purpose finite element program based on the displacement (stiffness) method to describe the behavior of anchored reinforcing bars at the element level. Noguchi (1985) and Berra et al. (1994) have successfully developed a beam column joint model capable of representing bond slip of beam reinforcing bars. Concentrated bond links were used to represent the bond slip effect. However this required the use of refined meshes with a large number of elements which in turn limits the application of these models for frame analysis use, where a large number of beam column joints are involved.

In the proposed model, a bond slip (displacement) interpolation function is used to provide a continuous interaction between reinforcing steel and concrete, resulting in a simple displacement element formulation. The contact element connects and transmits forces between concrete and steel. The accuracy of the proposed model is first examined at the element level by comparing its predictions with available

experimental and analytical data for anchored reinforcing bars, under increasing monotonic and reversed cyclic loading. This model is then incorporated into the global reinforced concrete beam column joint element. Details on the bond slip element are discussed in the following sections.

4.2 FINITE ELEMENT MODEL FOR BOND SLIP

The boundary value problem of a reinforcing bar embedded in concrete involves four unknown fields; the steel stress, f_s, the bond stress, τ, at the surface between the bar and the concrete, the strain in the reinforcing bar, ϵ_s, and the relative slip, s, which is the difference between the steel and concrete displacements. All unknown fields are defined in the one dimensional domain of the embedded length, L, of the bar by the following equilibrium, compatibility and constitutive relations:

$$A \frac{df}{dx} = \tau \sum o \quad (\textit{Equilibrium}) \tag{4.1}$$

$$\tau = Q\ (s) \quad (\textit{Bond slip constitutive relation}) \tag{4.2}$$

$$f_s = F\ (\epsilon_s) \quad (\textit{Steel constitutive relation}) \tag{4.3}$$

$$\frac{ds}{dx} = \epsilon_s - \epsilon_x \quad (Compatibility) \tag{4.4}$$

where f_s is the steel stress as a function of the steel strain, F (ϵ_s), and τ is the bond stress as a function of the bond slip, Q (s), A is the reinforcing bar area ($\pi d_b^2/4$) and Σo is the reinforcing bar circumference (πd_b).

The above equations can be solved provided that sufficient boundary conditions are given. The boundary conditions of this problem are the loads and the displacements at the two ends of the bonded bar as shown in Figure 4.1. A number of techniques can be used to solve this two point boundary value problem using the finite element method. These techniques basically fall under two categories: (i) the stiffness method which involves the approximation of the bond slip field and; (ii) the flexibility method which approximates the stress field as exemplified by the work of Monti et al. (1997).

The first approach is adopted in the current study where the bond slip is approximated using a cubic displacement field. Four nodes are placed along the anchored length of the reinforcing bar as shown in Figure 4.2. These nodes provide the required four degrees of freedom for the use of a cubic displacement field. The degrees of freedom are the translations at points a, b, c, d along the length of the reinforcing bar. The bond slip distribution along the anchored bar is expressed in the local coordinates as follows:

$$(s) = (\Phi_1\ \Phi_2\ \Phi_3\ \Phi_4\ -\Phi_1\ -\Phi_2\ -\Phi_3\ -\Phi_4)\begin{bmatrix} u_1 \\ u_2 \\ u_3 \\ u_4 \\ u_5 \\ u_6 \\ u_7 \\ u_8 \end{bmatrix} \tag{4.5}$$

where

$$\phi_1 = \frac{1}{16}(1 - S)(-10 + 9(S^2 + 1)) \tag{4.6}$$

$$\phi_2 = \frac{9}{16}(1 - S^2)(1 - 3S) \tag{4.7}$$

$$\phi_3 = \frac{9}{16}(1 - S^2)(1 + 3S) \tag{4.8}$$

$$\phi_4 = \frac{1}{16}(1 - S)(-10 + 9(S^2 + 1)) \tag{4.9}$$

where S varies from 1 to -1 as shown in Figure 4.2.

The above equations can be expressed in a general form as: {s} = [B] {u}, where s and u are the relative displacement and the translation degrees of freedom

in the X axis direction respectively. [B] is defined in the above equations. The stiffness matrix of the bond slip element is calculated using the following expression

$$[K] = \frac{\pi L d_b}{2} \int [B]^t (k) [B] \, ds \qquad (4.10)$$

where $[K]_{(8,8)}$ is the stiffness matrix of the bond slip element, and $(k)_{(1,1)}$ is the tangent modulus of the bond stress-slip curve. The above integration is performed numerically by using six integration (Gaussian) points along the bar length to represent the change in k due the change in bond conditions from confined to unconfined as will be discussed. In this approach, one bond slip element with four nodes, is placed along the entire anchorage length. The adequacy of using such a single element will be justified later.

The success of the proposed bond slip model in describing the behavior of anchored reinforcing bars under reversed cyclic loading depends upon the adequacy of both the kinematic model, described above, and the material models used representing concrete, reinforcing steel and bond slip. The material models for concrete, and reinforcing steel have been discussed in Chapter 3. The bond slip model is introduced in the next sections but the bond resistance mechanism is first discussed as it is the basis for the bond slip model development.

4.3 BOND RESISTANCE MECHANISM

In this section the theory of bond resistance mechanism for monotonic and cyclic loading is presented. The theory for the bond resistance mechanism is valid for confined concrete, where the width of splitting cracks are kept small so as the ultimate failure is caused by bar pull-out rather than a breakout of a concrete cone which occurs for unconfined concrete. This interpretation for bond resistance mechanism is made by Eligehausen et al. (1983) as a result of an extensive experimental program aimed at evaluating the bond slip relationships of deformed bars under generalized excitations.

4.3.1 Bond Resistance Mechanism for Monotonic Loading

When a small value for slip is induced, cracks are initiated at relatively low bond stresses at the point of contact between steel and concrete as shown in Figure 4.3a. With increasing induced slip, the concrete in front of the lugs will be crushed. The bond forces which transfer the steel forces into the concrete are inclined with respect to the longitudinal bar axis. At this relatively low loading stage the angle is relatively small (about 30 degrees).

Increasing the stress further, more slip occurs because more local crushing takes place and later shear cracks in the concrete keys between the lugs are initiated. This happens when the slope of the bond stress slip curve decreases rapidly

(approximately at Point B in Figure 4.3b). At maximum bond resistance (Point C) part of concrete key between the lugs has been sheared off, depending on the ratio of clear lug distance to average lug height. At this loading stage, the bond forces will spread into the concrete under an increasing angle of 45 degrees because of the wedging action of sheared off concrete. For bars with a ratio of clear lug spacing to lug height of 9, maximum bond resistance, τ_{max}, is reached at a slip, S_{max}, equal to about 1.2 times the lug height.

When more slip is induced, an increasingly longer part of concrete is sheared off without much drop in bond resistance. The resistance at a slip equal to approximately 3 times S_{max} is about 85% of maximum bond resistance (Point D in Figure 4.3c). Increasingly less force is needed to shear off the remaining bits of concrete keys. When the slip is equal to the clearing distance, that means that lugs have traveled into the position of the neighboring rib (point E), only frictional resistance is left. This resistance will be practically independent of the deformation pattern or the related rib area.

It should be noted that gradual shearing off the concrete is only possible in confined concrete. If the confinement offered by transverse reinforcement can not prevent excessive growth of splitting cracks, the bars will be pulled-out before the concrete keys will be totally or partially sheared off.

4.3.2 Bond Resistance Mechanism for Cyclic Loading

For the loading cycle OA, shown in Figure 4.3a, the response is as described in the previous section. In Figure 4.4a it is assumed that the slip is reversed before shear cracks develop in the concrete keys. Upon unloading (path AF) a gap remains open with a width equal to the slip at point F between the left side of the lug and the surrounding concrete. Only the small fraction of slip that is caused by elastic deformations is recovered during unloading. Imposing additional slip in the reversed direction builds up frictional resistance. This resistance is rather small because the concrete surface surrounding the bar is relatively smooth. At H the lug is again in contact with concrete but a gap has opened at the lugs right side. Due to the concrete blocking any further movement of the bar lug, a sharp rise in stiffness of the hysteretic curve (path HI) occurs. The increase in resistance may start a little before H due to the load transfer by some pieces of broken concrete that is produced during loading from O to A. With increasing load, the old cracks close, allowing the transfer of compressive stresses across the cracks without noticeable reduction in stiffness. Inclined cracks perpendicular to the old cracks will then open if negative bond stress continues to rise and the bond stress slip relationship for loading in the opposite direction follows very closely the monotonic envelope.

At I, a gap with a width equal to S_{FI}, that is the difference between slip of points F and I, has opened. When slip is again reversed at I, the bond mechanism of

path IKL is similar to that of the path AFH described earlier. However the bond resistance starts only to increase again at L, when the lug starts to press broken pieces of concrete against the previous bearing face. With further movement stresses are built up to close the crack previously opened and open those previously closed. At M, the lug and concrete are fully in contact again. If more slip is imposed, the monotonic envelope is again reached.

A different behavior is followed if slip is reversed after the initiation of shear cracks in the concrete keys (path OABC in Figure 4.4b). The shear cracks causes reduction in the bond resistance compared to the monotonic envelope. When loading in the reverse direction (path CFGHI), the lug presses against a key whose resistance is lowered by shear cracks over a part of its length induced by the first half cycle. Furthermore, the old relatively wide inclined cracks will probably close at higher loads than in the cycle considered in Figure 4.4a thus complicating the transfer of the inclined bond forces into the surrounding concrete. Therefore shear cracks in the undamaged side of concrete will be initiated at lower loads and the bond resistance is reduced compared to the monotonic envelope. When reversing the slip again (path IKLMN) only the remaining parts of concrete between the lugs will be sheared off resulting in even lower maximum resistance than that at point I.

In the next example, it is assumed that large slip is imposed during the first half cycle (path OABCD) in Figure 4.4c, resulting in shearing off almost the total concrete key. When moving back a higher frictional resistance must be overcome

than in the cases described previously because the concrete surface is rough along the entire width of the lugs. At H the lugs are again in contact with the remaining intact part of the keys which do not offer much resistance. Therefore the maximum resistance during the second half cycle is almost the same as the frictional resistance of the monotonic envelope. During reloading (path JKEMNO), an even lower resistance is offered because the concrete at the cylindrical surface whose shear failure occurred has been smoothed already during the previous cycle.

4.4 ANALYTICAL BOND SLIP MATERIAL MODEL

The assumed bond model is presented in Figure 4.5a. The model is similar to the one developed by Eligehausen et al. (1983) with some modifications as will be discussed.

When loading a specimen the first time, a bond stress-slip relationship is followed which is referred to herein as the "monotonic envelope" (path OABCD or $OA_1B_1C_1D_1$ in Figure 4.5b). Imposing a slip reversal follows a stiff "unloading branch" up to the point where frictional resistance, τ_f^-, is reached (path of EFG). Further slippage in the negative direction takes place without an increase in τ up to the intersection of the "friction branch" with the curve OA'_1 (path GH). A bond stress slip relationship similar to the monotonic curve is then followed, but with reduced values of τ (path $HA_1'I$). This curve ($OA'_1B'_1C'_1D'_1$) is called the "reduced envelope". Reversing the slip again at I follows the unloading branch and then the

frictional branch with $\tau=\tau_f'$ up to point M. A gradual increase in bond resistance then starts at point M until point E', which lies on the unloading branch EFG (path KME'). At E' the reduced envelope is reached and a relationship similar to the monotonic curve is then followed but with reduced values of τ (path E'C'D'). To complete the model description, details for the different branches referred to in the above discussion are given in the following section.

4.4.1 Monotonic Envelope

The simplified monotonic envelope simulates the experimentally obtained curve under monotonicaly increasing slip as shown in Figure 4.6. It consists of three parts as follows:

$$\tau = \tau_1 \left(\frac{s}{s_1}\right)^{\alpha} \qquad s \le s_1 \tag{4.11}$$

$$\tau = \tau_1 \qquad s_1 \le s \le s_2 \tag{4.12}$$

$$\tau = \tau_1 - \frac{(\tau_1 - \tau_3)}{(s_3 - s_2)} (s - s_2) \le \tau_3 \qquad s > s_2 \tag{4.13}$$

In this curve the ultimate frictional bond resistance, τ_3, is reached at s_3 which is equal to the clear distance between the lugs. Considering the scatter in

experimental data, average values for s_1, s_2, s_3, τ_1, τ_3, α are given in Table 4.1 for confined and unconfined concrete as well as for hooks in confined concrete. The values listed are valid for # 8 (25 mm) reinforcing bars with concrete strength of 30 MPa .

The bond conditions in a joint vary along the embedment length as shown in Figure 4.7. The envelope curve for the inner portion of the joint is that of confined concrete while the outer portion is that for unconfined concrete. The dividing line between the two zones is not sharply defined. The length to which the unconfined portion extends into the column is equal to 3-4 d_b, where d_b is the bar diameter, according to Viwathanatepa et al. (1979) and is equal to 5 d_b according to Cowell et al. (1982).

4.4.2 Reduced Envelopes

Reduced envelopes are obtained from monotonic envelopes by reducing bond stresses τ_1 and τ_3 through reduction factors which are functions of one parameter called the "damage factor". For no damage, d=0, the reduced curve is the same as the monotonic curve whereas d=1.0 indicates full damage ($\tau = 0$). The relations proposed by Eligehausen et al. (1983) take the following from:

$$\tau_1 (N) = \tau_1 (1 - d) \qquad (4.14)$$

$$\tau_3 (N) = \tau_3 \left(1 - \frac{d}{2 - d} \right) \tag{4.15}$$

where τ_1 and τ_3 are the characteristic values on the monotonic curve. τ_1 (N) and τ_3 (N) are the corresponding values after N cycles. Figure 4.8 shows the reduction of τ_3 as a function of the damage factor d which is assumed to be a function of the total energy dissipated and takes the following form:

$$d = 1 - e^{-1.2 \left(\frac{E}{E_o}\right)^{1.1}} \tag{4.16}$$

where E is the total energy dissipated and E_o corresponds to the energy absorbed under monotonicaly increasing slip up to the value s_3 as shown in Figure 4.9.

An additional relation is used in establishing the frictional resistance, τ_f, which depends upon the peak value of slip, S_{max}, reached in either direction. For first slip reversal, τ_f is calculated using the following relation:

$$\tau_f = 2 \left(\frac{S_{max}}{s_3}\right) \tau_3 \qquad \leq \tau_3 \tag{4.17}$$

Figure 4.10 illustrates the reduction of τ_f for the first slip reversals as a function of S_{max}/s_3. For subsequent cycles frictional resistance, τ_f, is reduced according to a reduction factor d_f as follows:

$$\tau_f (N) = \tau_{fo} (1 - d_f) \qquad (4.18)$$

where τ_{fo} is the value of τ_f in the first cycle and $\tau_1 (N)$ is the corresponding value after N cycles. The damage parameter d_f is assumed to be a function of the total energy dissipated and takes the following form :

$$d_f = 1 - e^{-1.2 (\frac{E_f}{E_{of}})^{0.67}} \qquad (4.19)$$

where E_f is the energy dissipated by friction alone, as shown in Figure 4.11 and E_{of} is equal to the product $\tau_3 s_3$ and is thus related to the monotonic envelope.

For unconfined concrete the envelope curve for the case when the bar is pushed is different from the case when the bar is pulled as previously mentioned. The cyclic parameters (E_o, E_{of}) are related to the monotonic envelope for push in loading.

4.4.3 Unloading and Friction Branch

The slope of any unloading branch (paths EFG or IJK in Figure 4.5) is taken as k=200 N/mm^3. This value is fixed throughout the analysis and is not changed by the number of cycles. The friction curve proposed in this study differs from that proposed by Eligehausen et al. (1983) as shown in Figure 4.12. The curve used in this study shows a gradual increase in the force carried by the bar whereas the model of

Eligehausen et al. (1983) does not show any increase in the force until reaching the maximum slip value imposed during previous cycles. Experimental results also show this gradual increase in the force. Other analytical studies by Filippou et al. (1983a, b), Russo et al. (1990), and Soroushian et al. (1991) proposed different changes to the friction curve of Eligehausen et al. (1983) to include this gradual increase.

4.4.4 Effects of Variations of Properties

The analytical model described above is based on the experimental test results for bar diameter: d_b = 25 mm (#8 bars) and concrete strength of 30 MPa. In the case of the variation of these parameters modifications to the model should be made as proposed by Eligehausen et al. (1983).

For #6 bars (d_b = 19 mm) instead of #8 bars (d_b = 24.5 mm) τ_1 is to be increased by 10%. When using #10 bars (d_b = 32 mm) τ_1 is to be decreased by 10%.

To account for the change in the concrete strength, τ_1, τ_3, and K are to be multiplied by $(f_c'/30)^{\beta}$, where $\beta \approx$ ½ to 2/3 and f_c' is in MPa. Also s_1 should be changed in proportion to $\sqrt{f_c'}$

4.5 VERIFICATION OF THE BOND SLIP MODEL

In this section, the accuracy and the numerical stability of the proposed bond slip model is examined. The validity of using a single bond slip element along the anchored length is also discussed. This is done by comparing the predictions of the

proposed model with other analytical and experimental results for anchored reinforcing bars. In these examples, the response under increasing monotonic and reversed cyclic loading is studied. This includes predictions of the proposed model under the postpeak softening range of the response. The behavior of the anchored reinforcement is studied until the failure is caused by its pull out.

4.5.1 Specimens Tested under Increasing Monotonic Loading

Viwathanatepa et al. (1979) tested a number of specimens under conditions simulating the seismic excitations of anchored reinforcing bars in interior beam column joints. Of these specimens two reinforcing bars are selected for the current study. Both tests were conducted on straight #8 (25 mm) reinforcing bars that were embedded in a confined concrete block with an anchorage length of 25 bar diameters. The material parameters of the monotonic envelope for reinforcing steel stress strain are: Young's modulus = 205,000 MPa; Yield strength = 468.5 MPa; and strain hardening ratio = 1 %. Material parameters for monotonic bond stress - slip curve are: τ_1 = 13.5 MPa; τ_3 = 6.0 MPa; s_1 = 1.0 mm; s_2 = 3.0 mm; and s_3 = 10.5 mm.

In the first test specimen, the reinforcing bar is subjected to a pull out force from one end only. Two analyses using the proposed slip element are carried out to represent the test. In the first analysis, only one bond slip element including four nodes is used over the anchored length and is referred to as Model (a). This simulates the

condition of the bond slip element which will be used in the global beam column joint model. In the second analysis, two bond slip elements including seven nodes are used over the anchored length and is referred to as Model (b). In both cases bond slip increments are imposed at one end of the reinforcing bar and the other end is left free. Figure 4.13 compares the analytical predictions using the two proposed models, Model (a) and Model (b), with the experimental results. The Figure also includes the analytical predictions of Monti et al. (1997) which are based on using five elements with six nodes over the anchored length.

Figure 4.13 shows good correlation between the proposed analytical models and the experimental results. The main difference between the predictions of Model (a) and the experimental results is in the higher steel stresses predicted at the same bond slip level. This difference reaches its maximum at the initiation of yielding where a difference of about 15 % in the steel stress can be noticed. This difference then gets smaller as the bond slip level gets higher and the analytical results tend to be more correlated to the experimental values. This discrepancy should be of minor significance to the overall bond slip deformation since it takes place at the initial stage where the bond slip effect is limited. When two elements are used, Model (b), the analytical predictions converged towards the experimental values. Since the use of two bond slip elements implies the use of a more refined mesh for the joint panel it is considered that Model (a) is a sufficiently accurate model of bond slip within a beam column joint. The Figure also shows that the analytical model of Monti et al. (1997),

with the five elements, is equally as good as Model (b) in describing the behavior of the anchored bar.

In the next example the same reinforcing bar is subjected to pull out from one end and push from the other. Figure 4.14 compares the analytical results of Model (a) and Model (b) with the experimental results. The same observation is also made here where Model (b) shows a better correlation to the experimental results. The discrepancy in the results is again in the higher steel stresses predicted by Model (a) with a maximum difference of about 15% at the initiation of yielding. The results of Model (a) are still considered acceptable and the slight variation in the response as compared to the experimental does not justify the use of a more refined mesh such as Model (b). Both models (a) and (b) show a stable post peak response and a good ability to simulate the failure of the specimen. The model of Monti et al. (1997) also shows good correlation with the experimental results. However all these models predict strength drops that deviate from the experiment. The proposed models (a) and (b) shows a strength drop at a higher slip value than that experimentally predicted. The model of Monti et al. (1997) shows the strength drop to occur at a slip value less than that experimentally predicted. The discrepancy in calculating the slip at peak load can be attributed to the scatter in the bond strength values recorded experimentally and used as data for the monotonic bond stress slip curve.

The global results of the two examples presented above verifies the validity of using a single bond slip element along the entire anchorage length, namely Model

(a). The local response of the bar subjected to pull only at one end is then studied using Model (a) as shown in Figure 4.15. The Figure compares the analytical and the experimental bond slip distribution across the anchored length at an intermediate step. The results show good correlation. The local response of the bar subjected to push pull condition is shown in Figure 4.16. The same good correlation is observed.

4.5.2 Specimens Tested under Reversed Cyclic Loading

The same reinforcing bar described in the previous examples is then subjected to push pull loading history with cycles of gradually increasing end displacement. Figure 4.17 shows the cycles before yielding of reinforcing bar while cycles after yielding are shown in Figure 4.18. The Figures compare the analytical predictions of Model (a), the experimental data of Viwathanatepa et al. (1979), and the analytical results of the model of Monti (1997). The Figures show the ability of the proposed model to simulate the gradual damage and loss of strength and stiffness of the anchored bar under cyclic excitations.

The discrepancies between the predictions of the analytical models and the experimental results are more pronounced in the cycles before yielding of reinforcing steel. This is mainly due to the assumed friction strength of the bond stress slip relation. The experimental curves show complete loss of frictional resistance during reloading phase. Also the experimental results shown in Figures 4.17 and 4.18 indicate that the stresses in the reinforcing bar reach higher values than those

analytically predicted. The discrepancy reaches about 35% for the steel stresses associated with negative slip values as shown in Figure 4.17. This discrepancy reaches about 50% at a slip value of -0.02 inch as shown in Figure 4.18. The agreement between the two analytical models, the proposed model and Monti's model, indicates that the overestimation of the bond slip effect that have resulted in lower stress levels is a result of the discrepancies in the values used for the bond stress slip curve rather than a deficiency of the proposed model. The values used for the monotonic stress slip curve are based on average experimental data. Experimental observations by Eligehausen et al. (1983) indicate that the bond strength scatters as much as 15% from the average value.

4.6 PROPOSED BEAM COLUMN JOINT MODEL

The proposed bond slip model is incorporated into the global beam column connection model as shown in Figure 4.19. As previously described in Chapter 2 the beam column joint panel is represented by a twelve node inelastic plane stress element. Beam flexural reinforcement is represented in the joint panel by inelastic truss elements placed at the lower and upper fibers of the joint panel. Bond slip relationship between reinforcing steel and concrete in the joint panel is considered in this model using the bond slip contact element shown in Figure 4.19c. The proposed bond slip model connects and transmits forces between the concrete and steel and allows a continuous interaction between them in the joint panel.

4.7 CONCLUSIONS

In this Chapter, the problems associated with modeling bond slip of anchored reinforcing bars are discussed. The formulation of a finite element for anchored reinforcing bars and a series of analytical studies for the validation of the proposed element are described. This includes validation examples under increasing monotonic and reversed cyclic loading. This study shows that bond slip along the entire bar anchorage length can be represented with sufficient accuracy with only one bond slip element. The proposed bond slip element which uses displacement interpolation functions have shown a stable behavior in the postpeak range of the response. The model considers the gradual damage of bond and the resulting loss of strength and stiffness of anchored bar under reversed cyclic loading. The proposed bond slip model is examined at the element level by comparing its predictions with other analytical and experimental results. The success of the proposed model is demonstrated by the good correlation achieved between the predictions and the experimental data. The verification examples show the ability of the model to simulate the bond deterioration and eventual pull out of anchored reinforcing bars under severe cyclic excitation.

The proposed bond slip model is then incorporated into the global beam column connection model. The bond slip contact element connects and transmits forces between the beam reinforcing steel and concrete in the joint panel and allows a continuous interaction between them in the joint panel region.

4.8 LIST OF SYMBOLS

d, d_f	Damage factors (equations 4.16 and 4.19 respectively).
d_b	Diameter of reinforcing bar.
E	Total energy dissipated (Figure 4.9).
E_f	Energy dissipated by friction alone (Figure 4.11).
E_o	Energy absorbed under monotonicaly increasing slip up to the value s_3 (Figure 4.9).
E_{of}	Energy absorbed by friction and is equal to the product $\tau_3 s_3$ (Figure 4.11).
f_s	Steel stress in reinforcing bar.
$[K]_{(8,8)}$	Stiffness matrix of the bond slip element.
$(k)_{(1,1)}$	Tangent modulus of the bond stress-slip curve.
L	Embedded length of reinforcing bar.
s	Relative slip between steel and concrete displacements.
S_{max}	Peak value of slip, S_{max} , reached in either positive or negative direction.
u	Translation degree of freedom in X direction.
τ	Bond stress at the surface between the bar and the concrete.
τ_f	Frictional bond resistance.

ϵ_c Strain in concrete.

ϵ_s Strain in reinforcing bar.

Σo Circumference of reinforcing bar (πd_b).

Table 4.1 Parameters for bond stress slip envelope curve for 25 mm bar

Parameter	Confined Concrete	Hooks in Confined Concrete	Unconfined Concrete	
	Bar is pushed or pulled	Bar is pushed or pulled	Bar is pulled	Bar is pushed
s_1 (mm)	1.0	1.0	0.3	1.0
s_2 (mm)	3.0	3.0	0.3	3.0
s_3 (mm)	10.5	100.0	1.0	10.5
τ_1 (MPa)	13.5	22.0	5.0	20.0
τ_3 (MPa)	5.0	4.0	0	7.5
α	0.40	0.20	0.4	0.4

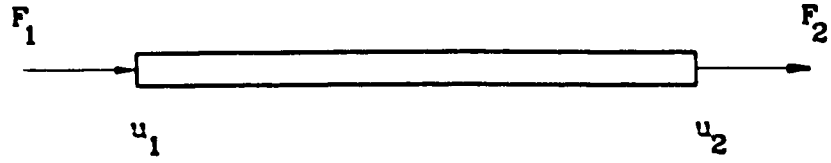

F_1, F_2 = Axial loads at ends of bonded bar
u_1, u_2 = Displacements at ends of bonded bar

Figure 4.1 Boundary conditions of bonded bar

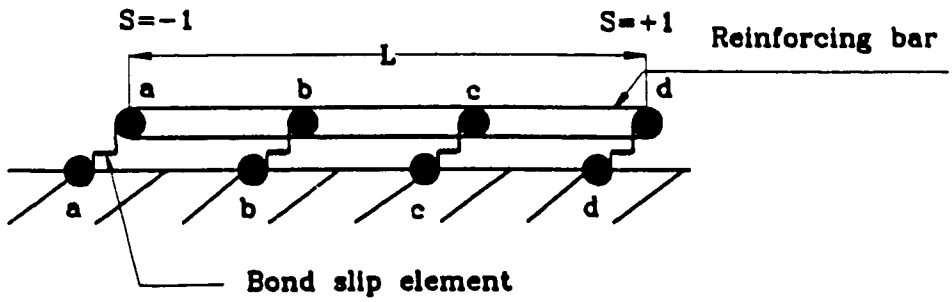

Figure 4.2 Proposed bond slip element

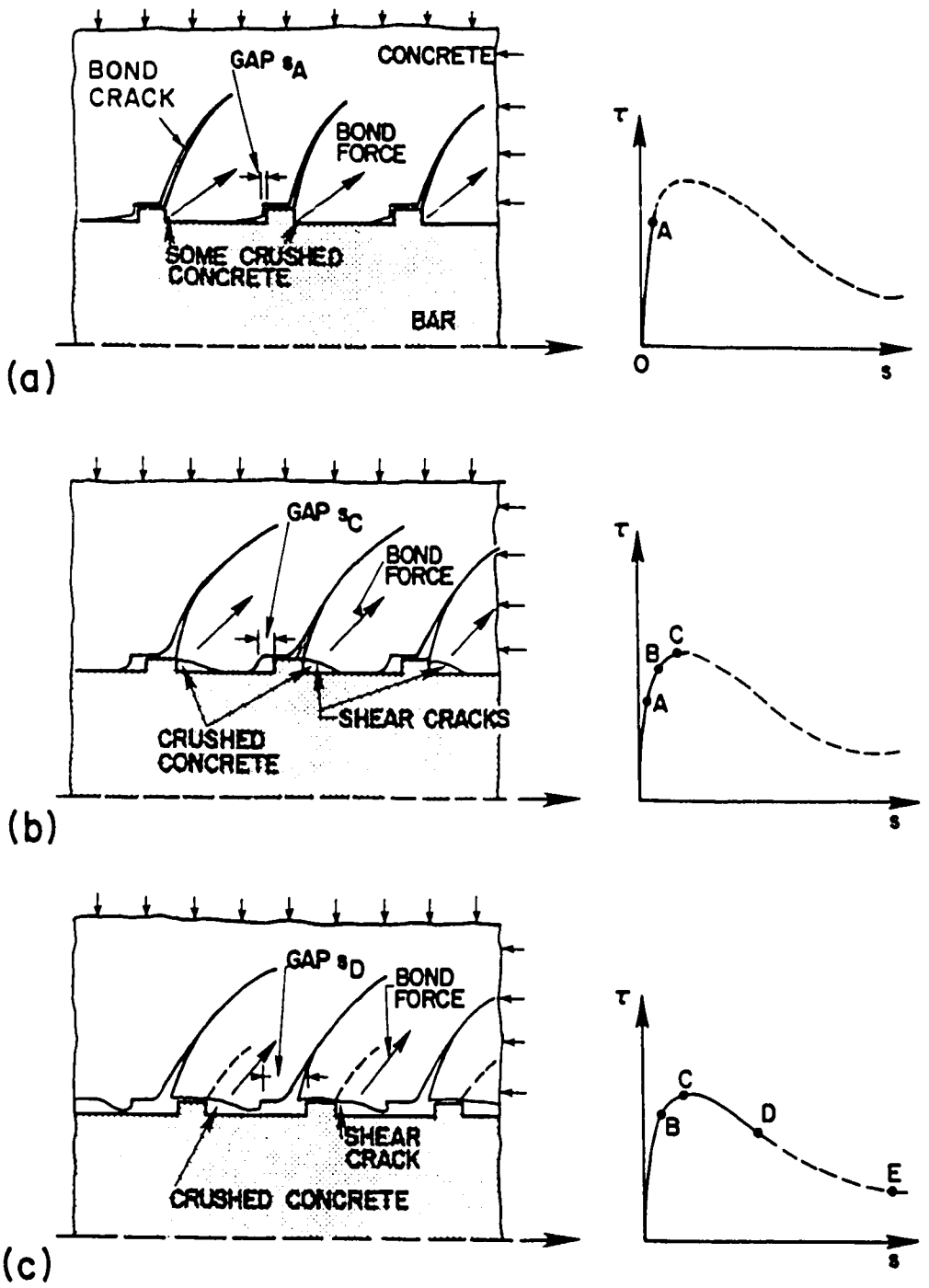

Figure 4.3 Bond resistance mechanism for monotonic loading (Eligehausen et al., 1983)

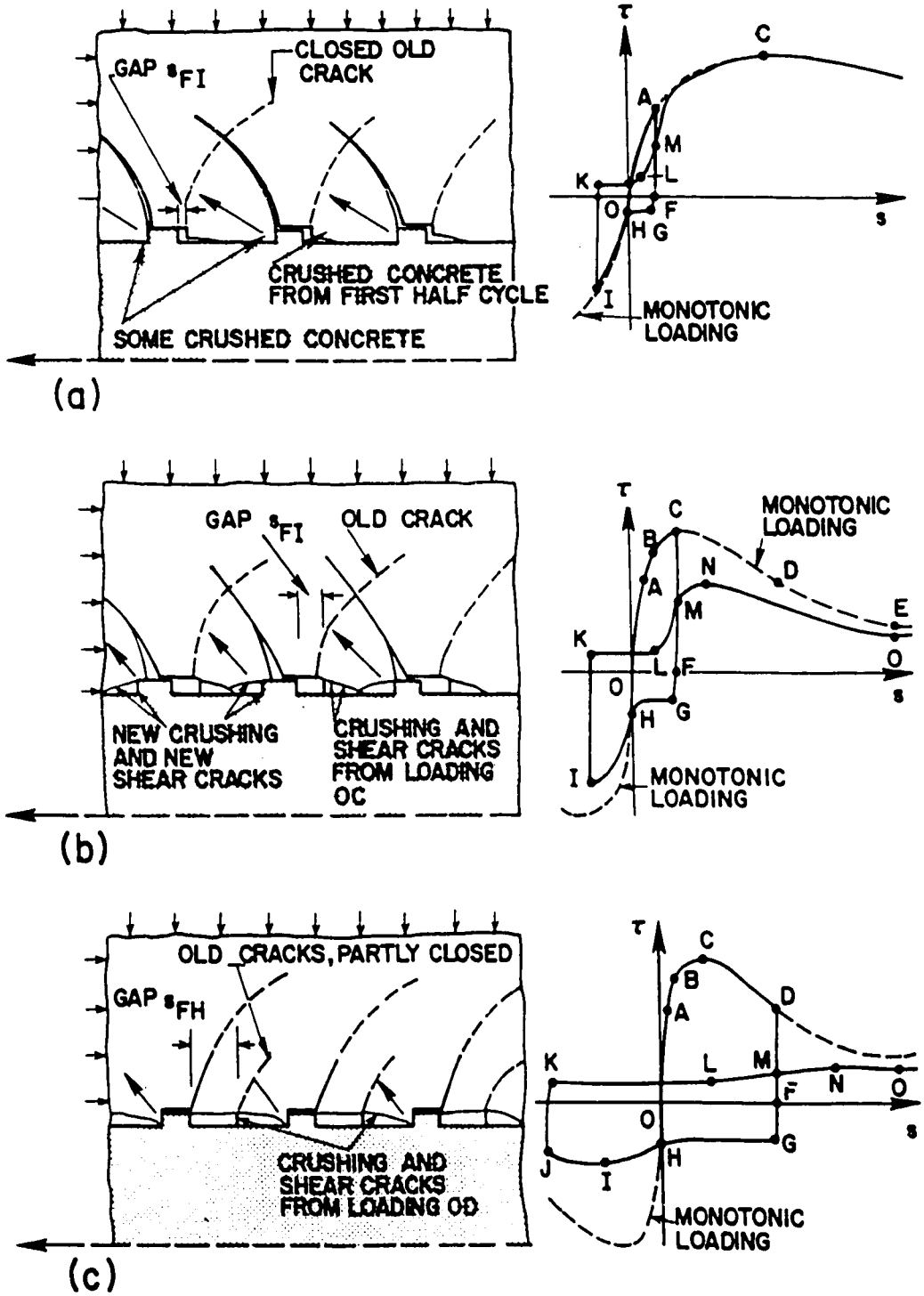

Figure 4.4 Bond resistance mechanism for cyclic loading (Eligehausen et al., 1983)

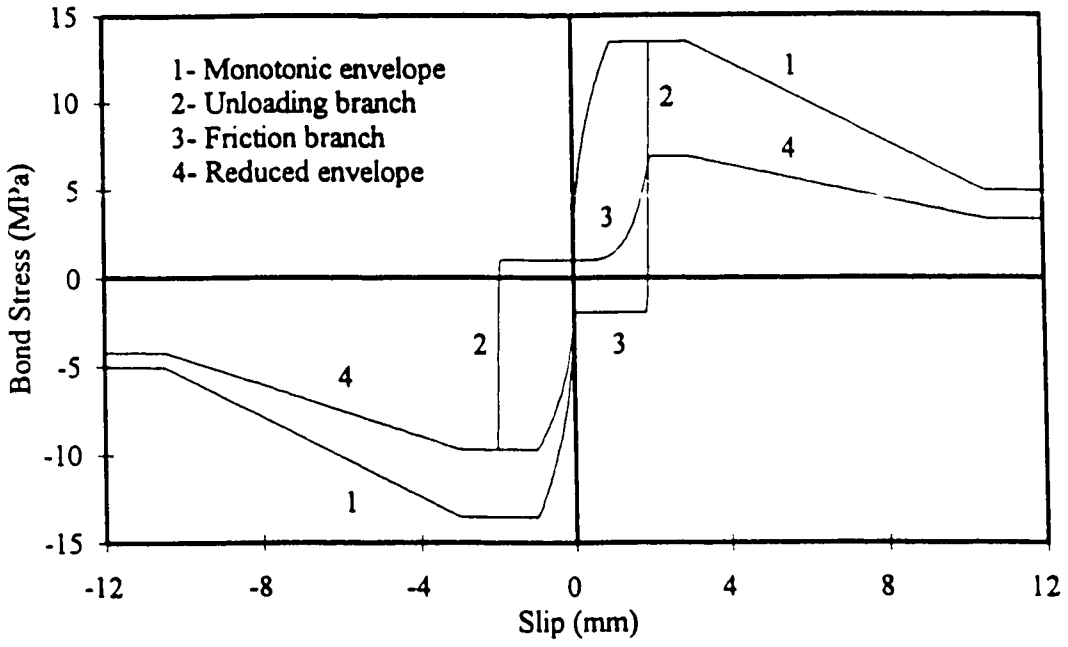

(a)

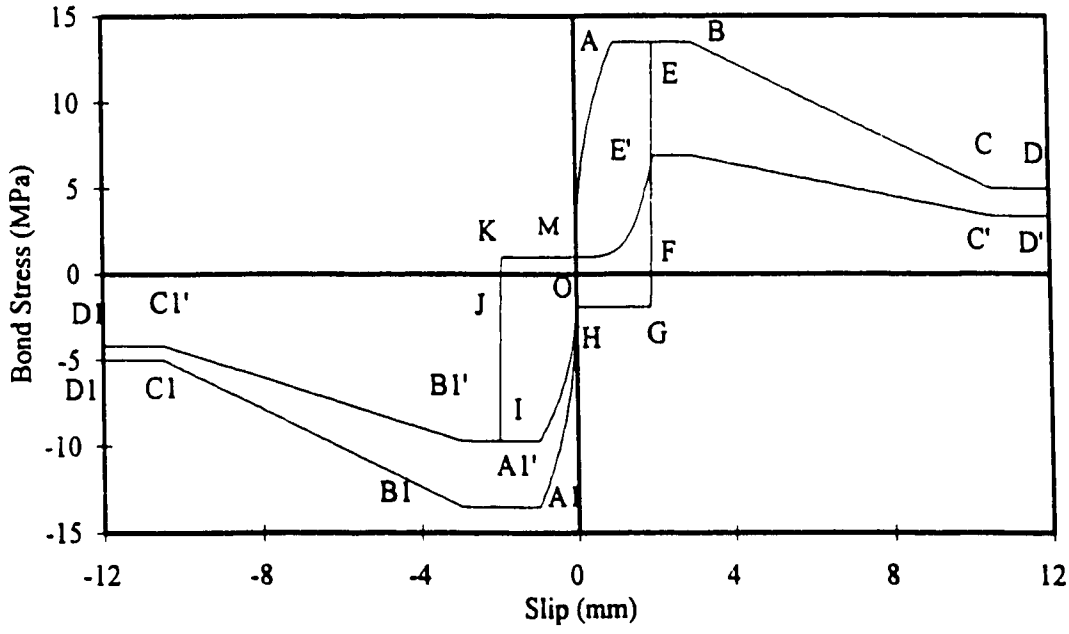

(b)

Figure 4.5 Proposed analytical material model for bond stress - slip relationship

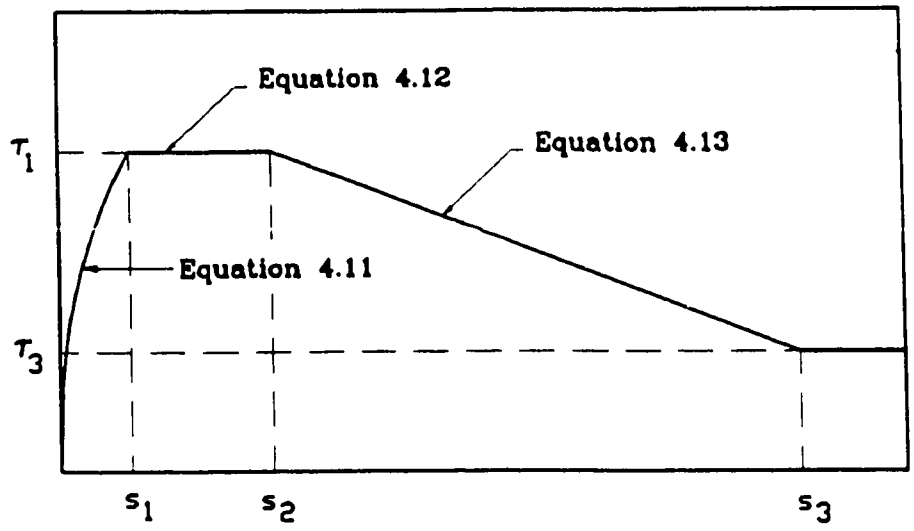

Figure 4.6 Monotonic envelope curve for bond stress - slip relationship.

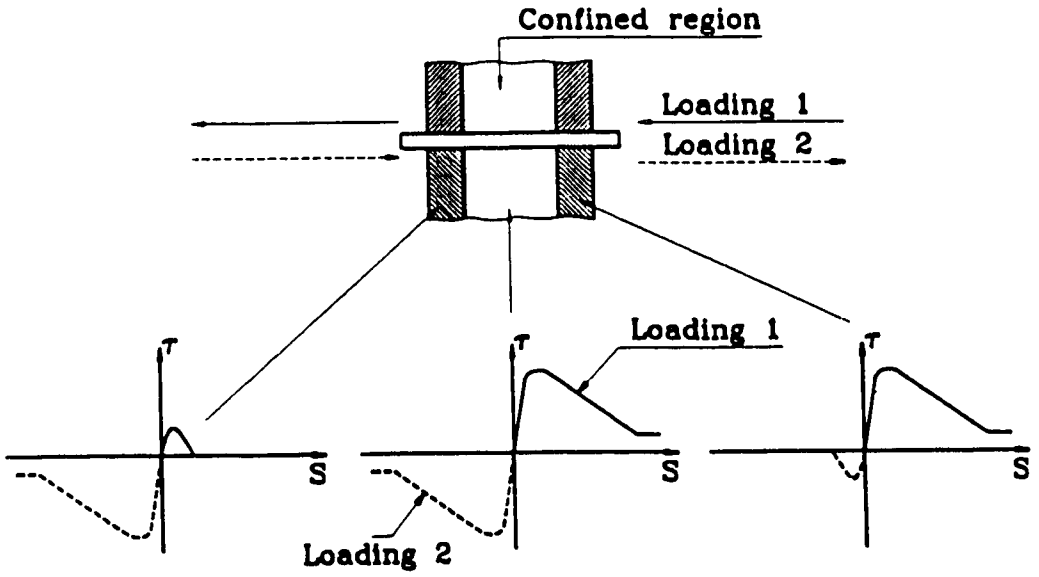

Figure 4.7 Different regions and corresponding bond stress slip envelope curves in an interior joint (Eligehausen et al., 1983)

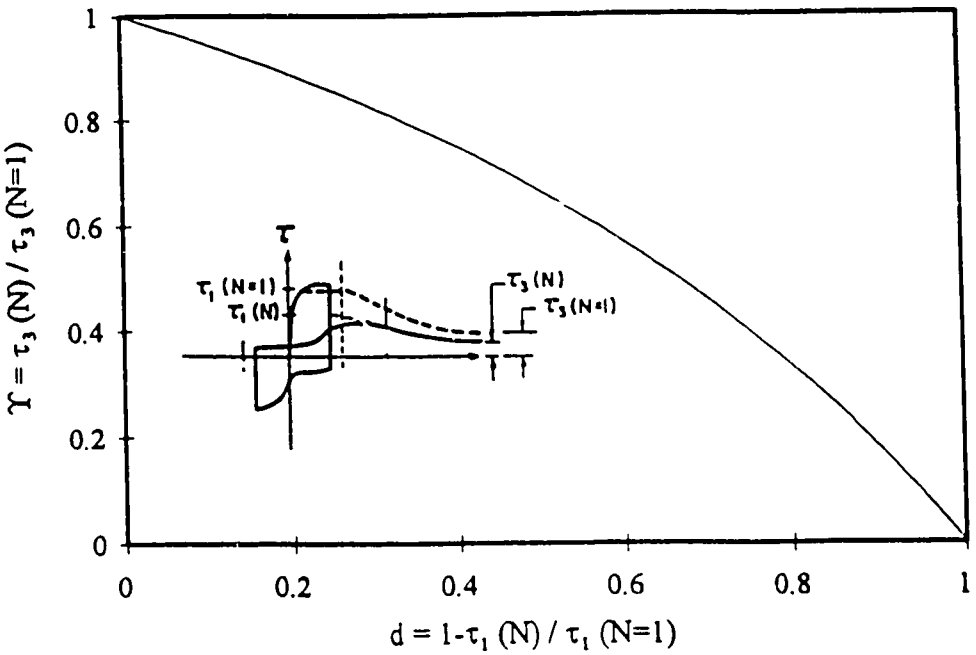

Figure 4.8 Ratio between τ_3 of reduced envelop and monotonic envelop as a function of the damage factor d (Eligehausen et al., 1983)

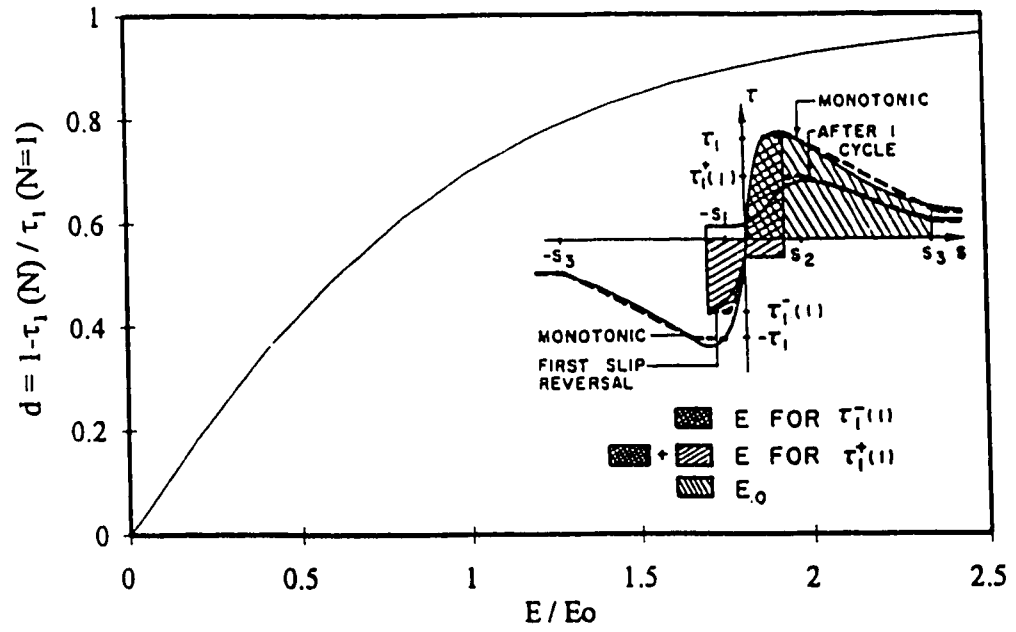

Figure 4.9 Relationship between the damage factor d, and the dimensionless energy dissipation E/Eo (Eligehausen et al., 1983)

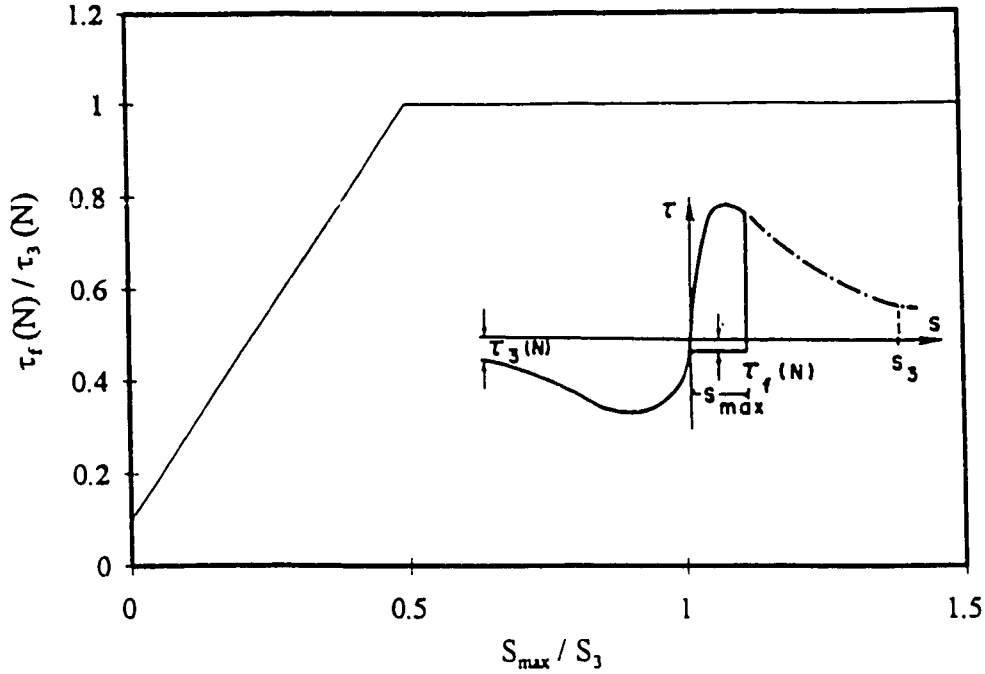

Figure 4.10 Relationship between τ_f of initial cycle and τ_3 (Eligehausen et al., 1983)

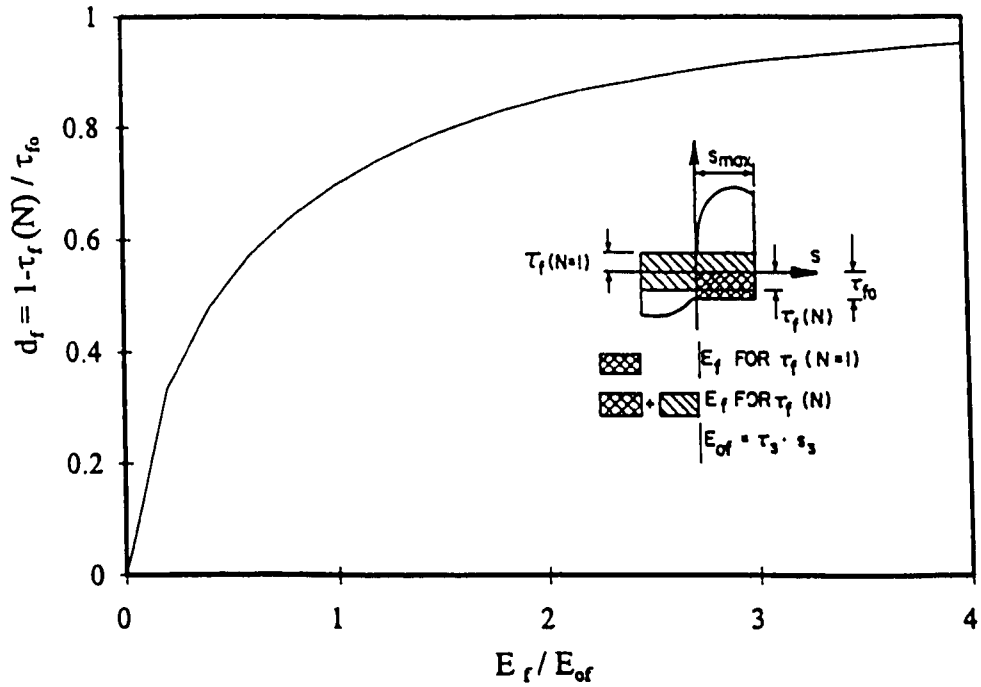

Figure 4.11 Relationship between the damage factor, d_f, and the dimensionless energy dissipation E_f / E_o (Eligehausen et al., 1983)

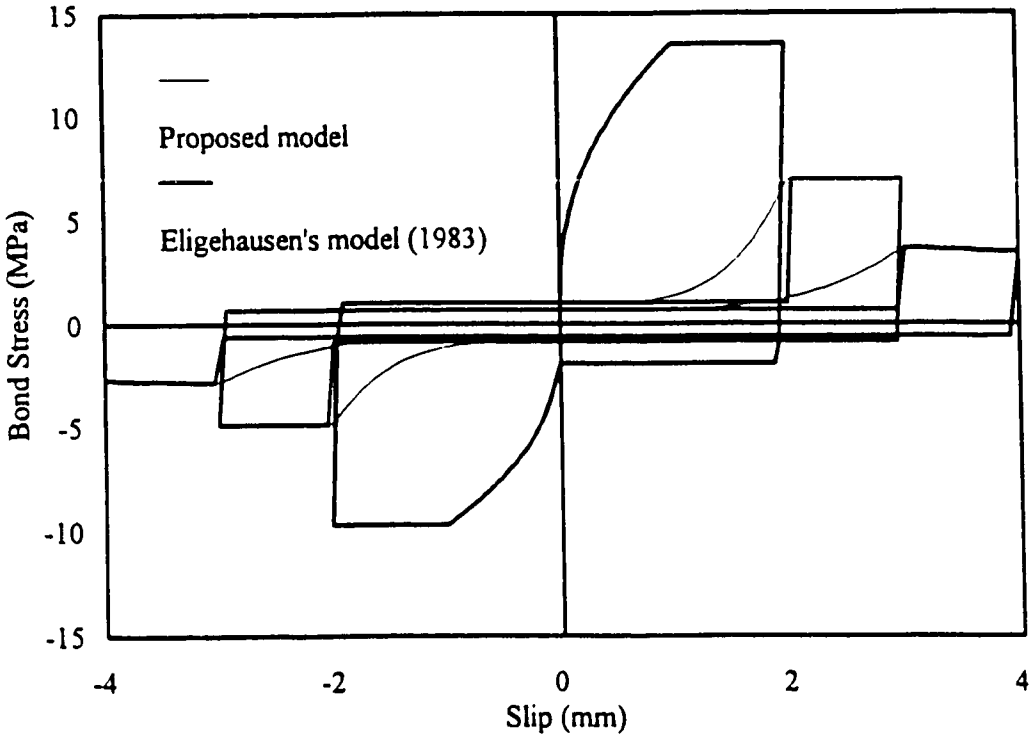

Figure 4.12 Comparison between the proposed bond slip model and Eligehausen's model

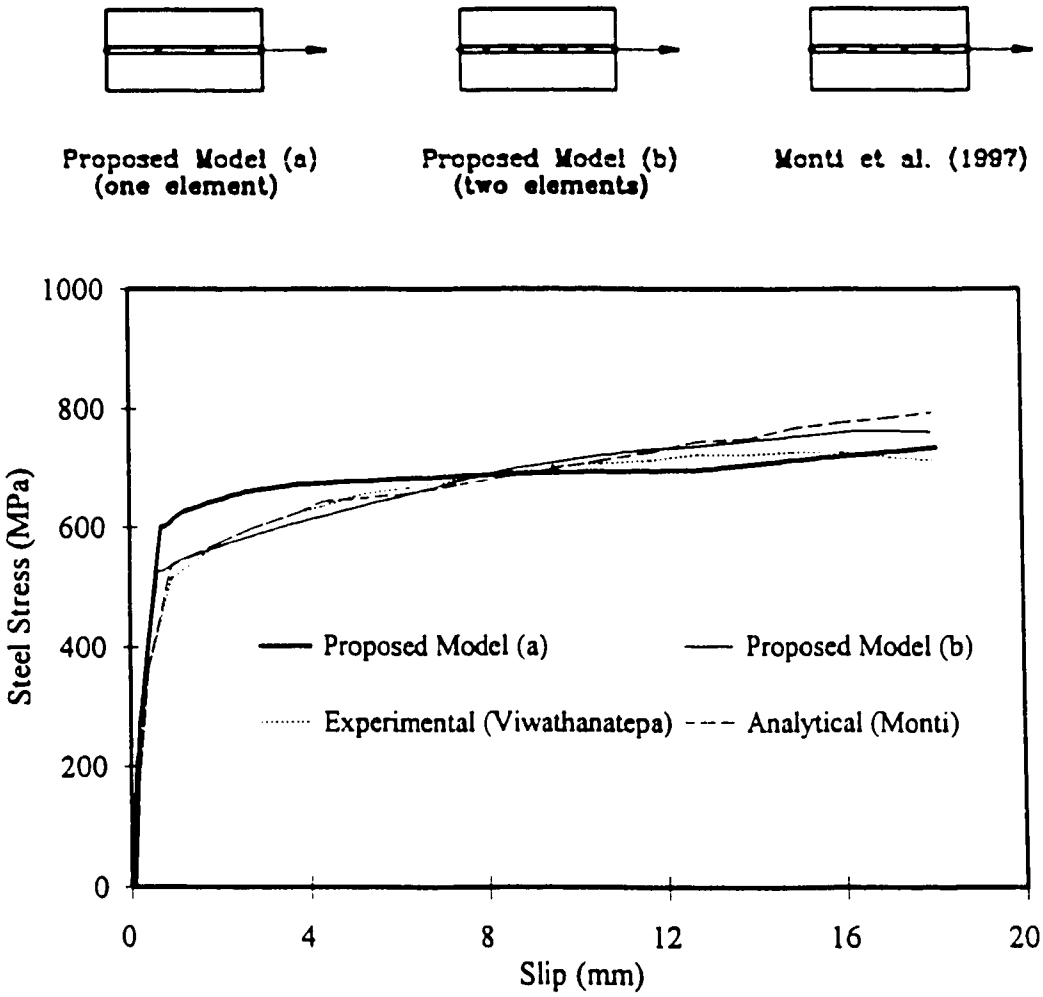

Figure 4.13 Monotonic pull out test for anchored reinforcing bar

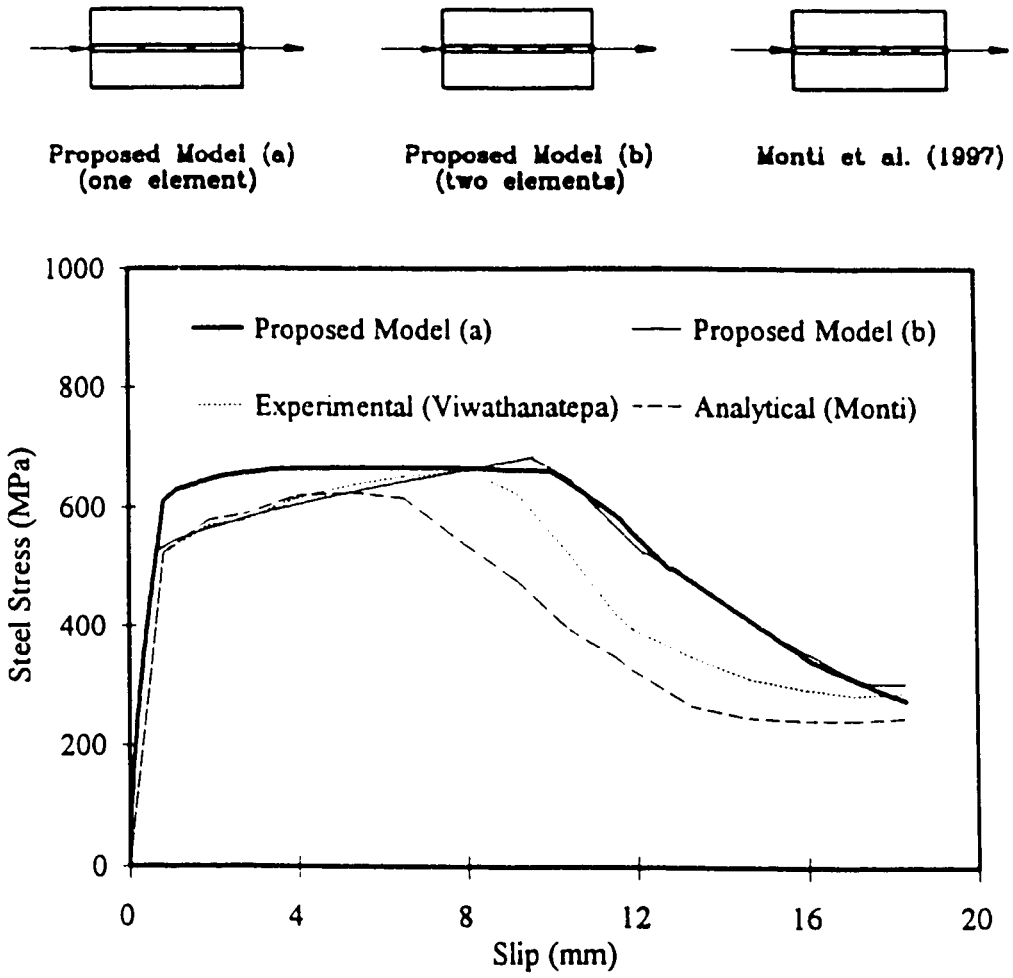

Figure 4.14 Monotonic push pull test for anchored reinforcing bar

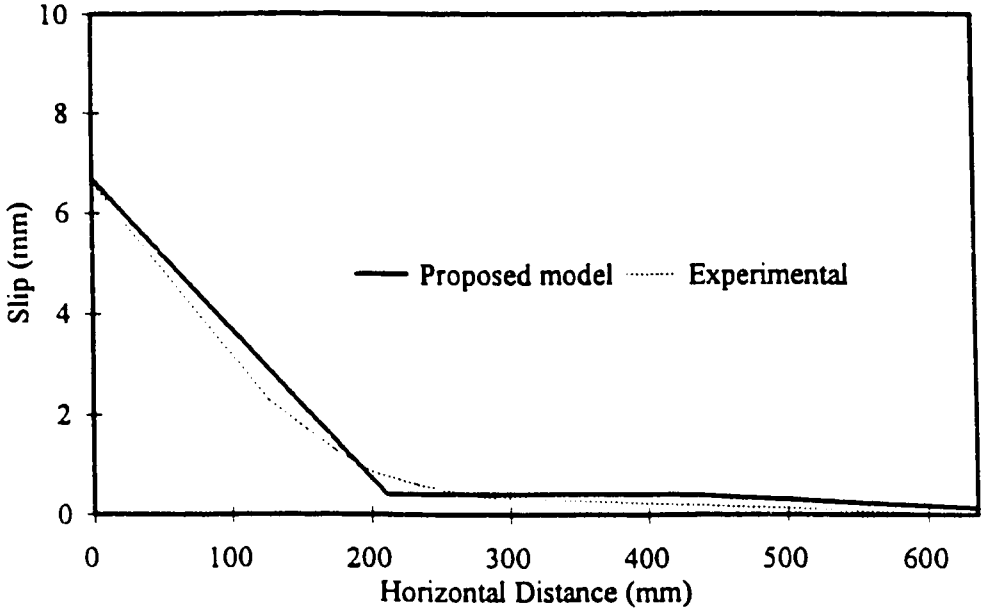

Figure 4.15 Slip distribution across anchored length for pull out test specimen

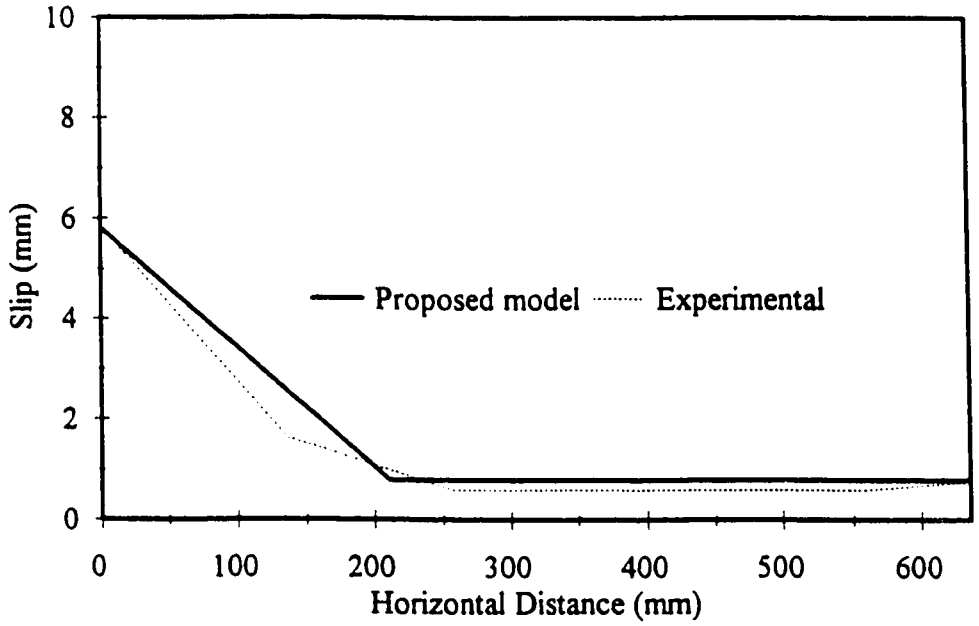

Figure 4.16 Slip distribution across anchored length for push pull test specimen

(a)

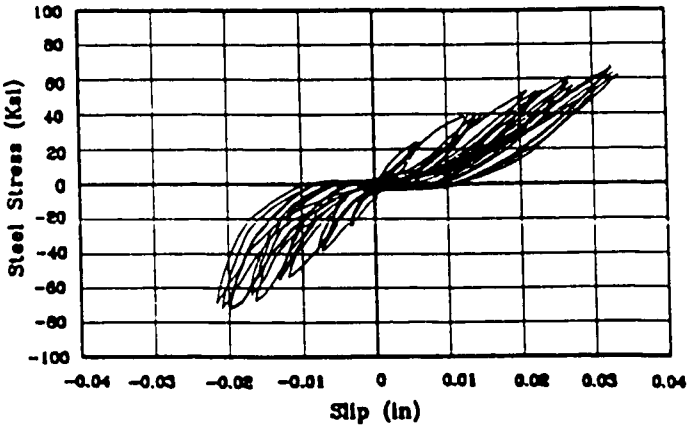

(b)

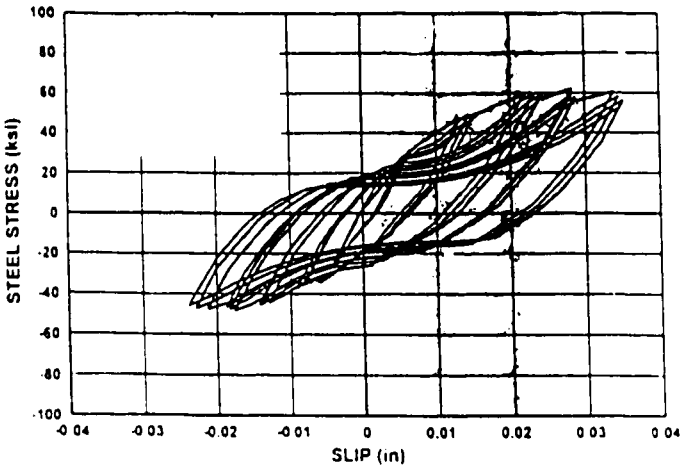

(c)

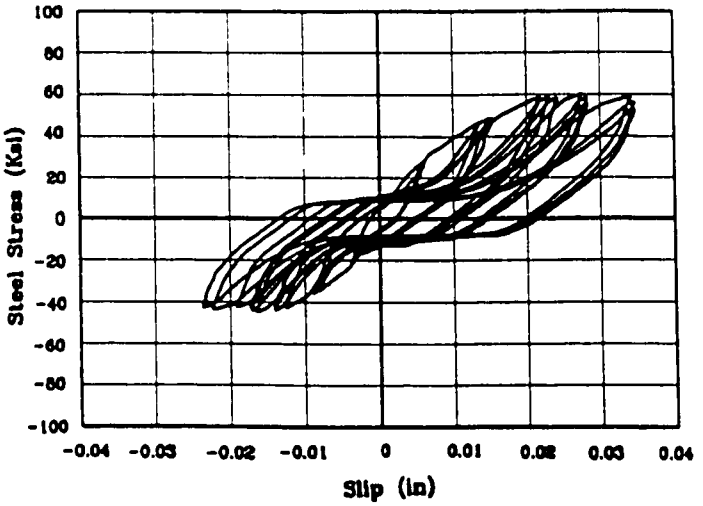

Figure 4.17 Stress slip response of anchored bar; load cycles before yielding of reinforcing steel; (a) Experimental (Viwathanatepa et al., 1979), (b) Analytical (Monti et al., 1997), (c) Analytical (Proposed model)

(a)

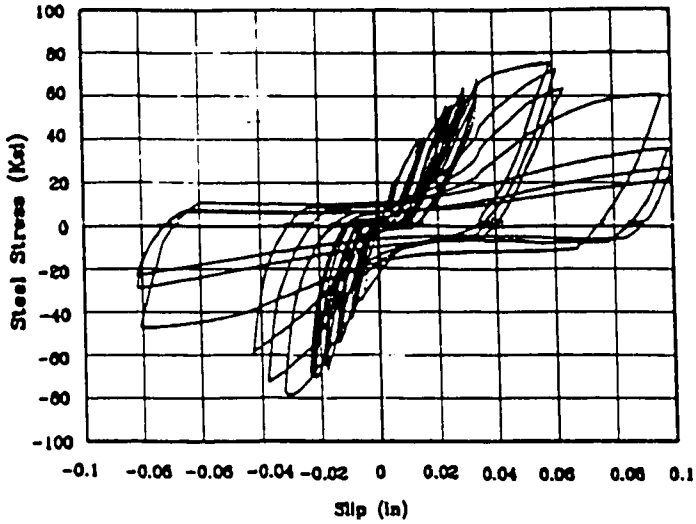

(b)

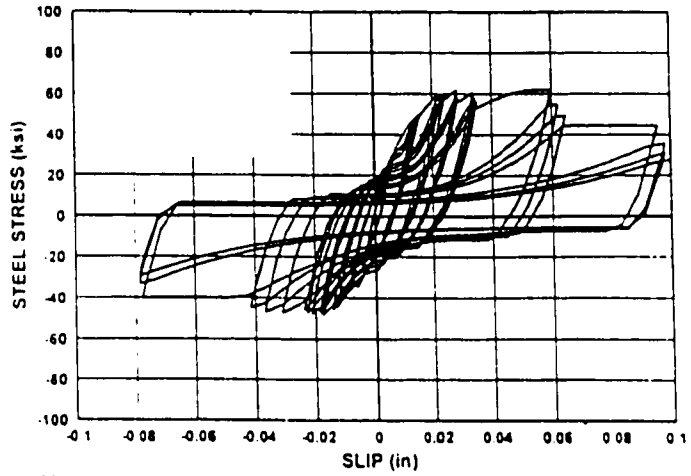

(c)

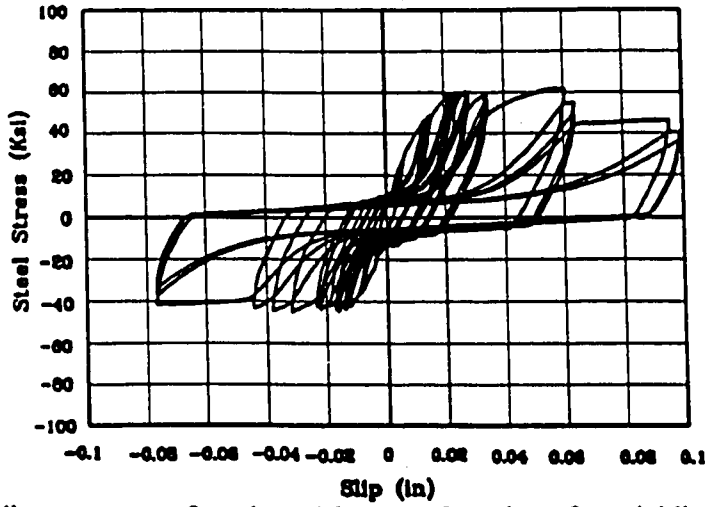

Figure 4.18 Stress slip response of anchored bar; load cycles after yielding of reinforcing steel; (a) Experimental (Viwathanatepa et al., 1979), (b) Analytical (Monti et al., 1997), (c) Analytical (Proposed model)

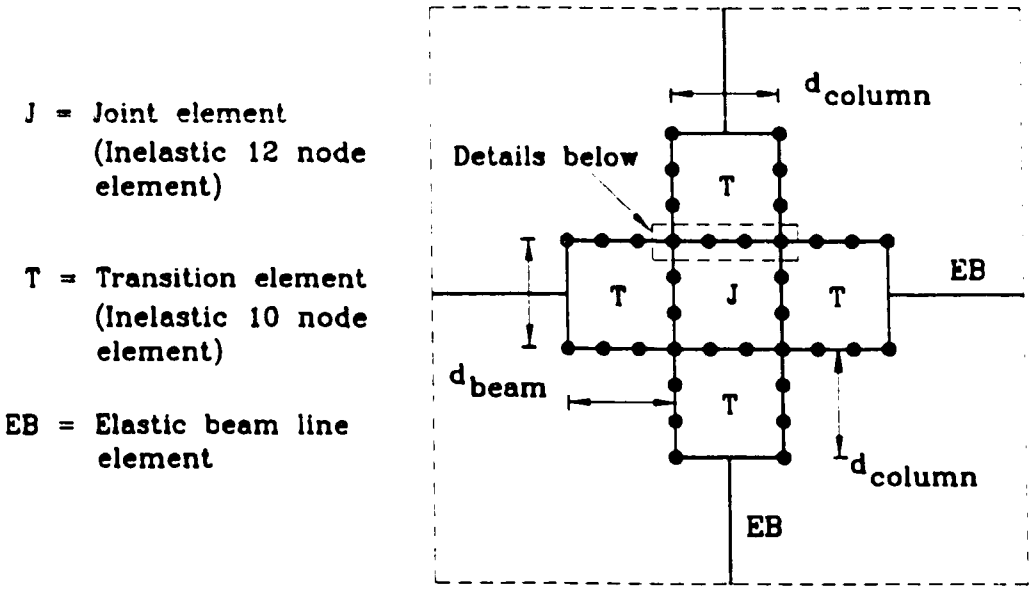

(a) Proposed element

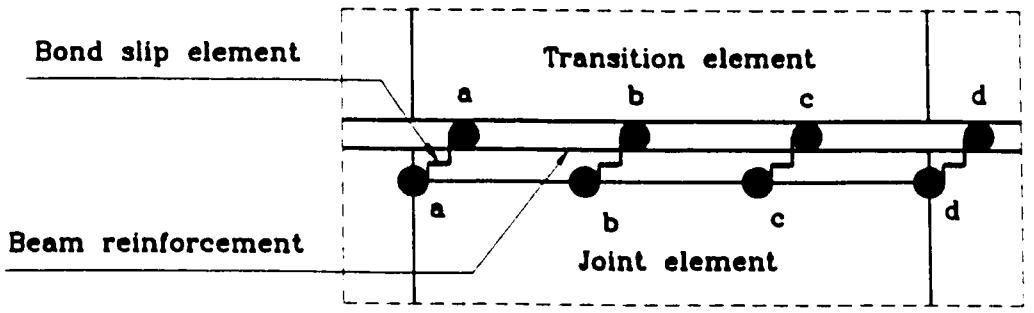

(b) Details of bond slip element

Figure 4.19 Proposed beam column connection element

CHAPTER 5

VERIFICATION OF THE BEAM COLUMN CONNECTION MODEL

5.1 GENERAL

The success of an analytical beam column connection model depends upon its ability to describe the experimental response of specimens experiencing different levels of shear and bond slip deformations under increasing monotonic and reversed cyclic loading. In this Chapter, comparisons are made between analytical predictions using the proposed model with available analytical and experimental data in the literature. Input data required for all specimens described in this Chapter is given in Appendix C.

5.2 TESTS UNDER INCREASING MONOTONIC LOADING

The first experimental verification used in this study is based on a specimen tested by Otani et al. (1985) referred to as C1. This specimen was used by Pantazopoulou and Bonacci (1994) to verify their analytical beam column connection model under increasing monotonic loading. This provides a good opportunity to compare the results of the proposed model with those of the aforementioned analytical model that is based on using refined finite element meshes. The specimen configuration and reinforcement details are given in Figure 5.1. The specimen has 12

10 bars and 6#10 for the top and bottom beam reinforcement respectively. Column reinforcement consists of 12 # 13 bars. Joint shear reinforcement consists of 3 sets of 2 # 2 bars which is equivalent to a reinforcement ratio of 0.27% in the joint panel. The finite element model of Pantazopoulou and Bonacci (1994) is given in Figure 5.2. Their model consists of 100 concrete elements in the joint panel, 240 concrete elements in each beam, and 120 concrete elements in each column. Truss and spring elements were used to model the steel reinforcement and the bond slip relationship. Although in laboratory conditions C1 was loaded by displacing the column ends relative to each other, in the current analysis and the analysis of Pantazopoulou and Bonacci, beam ends were displaced instead, to minimize P-Δ effects. Figure 5.3 compares the experimental results for the story shear story drift relationship with the analytical predictions of the current model and the model of Pantazopoulou and Bonacci. The Figure shows good correlation between the experimental and the analytical results. The proposed model is able to predict the story shear story drift relationship with the same accuracy of the other analytical model inspite of the major difference in the number of elements used. The variation in the results of the two analytical models is attributed to the differences in the kinematic and the material models used in each case. This example shows that choice of the high power element, as is done in the present work, can give good prediction of beam column connection response under increasing monotonic loading condition.

5.3 TESTS UNDER REVERSED CYCLIC LOADING

5.3.1 Specimens Tested by Kaku and Asakusa (1991)

This part of the verification of the proposed model deals with specimens tested by Kaku and Asakusa (1991) to evaluate the response of exterior beam column connections under reversed cyclic loading. Two identical specimens were used in this investigation. Dimensions and reinforcement details of both specimens are shown in Figure 5.4. The specimens have 4-D13 (4 # 4) beam bars for both top and bottom reinforcement. The column reinforcement consists of 12-D10 (12 # 3) bars. The joint shear reinforcement consists of 4 sets of 2 -ϕ 6 bars which is equivalent to a reinforcement ratio of 0.49% in the joint panel. The material properties and other details about the specimens are given in Table 5.1.

In the first specimen a constant axial load of 194 kN, which is about $f_c' A_g/8$, is initially applied to the column before the application of the cyclic load history. Reversed cyclic load is then applied at the beam tip. The loading history consists of one cycle with maximum displacement δ_y, and three cycles at each of the following peak displacements; $2\delta_y$, $3\delta_y$, $4\delta_y$, $6\delta_y$, and then one final cycle at $8\delta_y$. Figure 5.5 compares the experimental and the analytically predicted beam shear-story drift relationship for the connection. Good correlation between the analytical and the experimental results is noticed. The Figure shows that this connection exhibits a favorable ductile response throughout the loading history. The connection does not

show any drop in the connection strength and does not experience joint shear failure. However, the specimen shows some stiffness degradation and pinching as a result of the shear deformation. Figure 5.6 compares the experimental and the analytically predicted envelopes for the beam shear-story drift. The two curves are in good agreement. Figure 5.7 compares the experimental and the analytically predicted τ- γ (shear stress - shear strain) envelopes for the joint panel region. The Figure shows limited shear deformations where a maximum shear strain of about 0.01 is achieved. This shear strain is equivalent to 18% of the story drift which can be considered as a specimen in which the shear deformations are well controlled.

The second specimen has the same configuration and reinforcement details as the previous one. The only difference between these two specimens are the concrete strengths, which is higher for this specimen (see Table 5.1), and the loading histories. In this specimen no axial load is applied to the column. Only the cyclic loading is applied at the beam end. The loading history follows the same regime as described in the previous specimen. Figure 5.8 compares the experimental and the analytically predicted beam shear versus story drift relationship for the connection. There is also good correlation between the analytical and the experimental results for this specimen. Unlike the previous connection, this specimen shows considerable pinching and stiffness degradation as a result of the higher level of shear deformation experienced by the connection. Strength deterioration is also noticed in the last cycle. A deviation between the experimental and the analytical results is observed in the last cycle where

the experimental curve makes one more half cycle in the negative direction. This however is of little significance since failure has already been initiated and the strength has already dropped in the previous cycle. Figure 5.9 compares the experimental and the analytically predicted envelopes for the beam shear-story drift. The Figure shows the drop in the strength in the last cycle where joint shear failure has occurred.

Figure 5.10 compares the experimental and the analytically predicted τ- γ (shear stress - shear strain) envelopes for the joint panel region. Good correlation between the experimental and the analytical results can be noticed. The maximum shear strain value achieved is about 0.04 which is equivalent to 50% of the story drift. This indicates very high shear deformation in the joint panel especially when compared to the previous specimen.

This specimen experiences joint shear failure although it has also achieved yielding in the beam bars, because the initial joint shear strength is sufficient to transmit the forces for the beams to yield. However, this joint shear capacity rapidly deteriorates under the effect of cyclic loading and the failure is no longer of a ductile flexural type. This specimen illustrates the difference in the response of the connections that is achieved by the variation of only one parameter, namely the axial load. The proposed model is sufficiently sensitive to capture the change in the failure mode from beam yielding to joint shear failure.

5.3.2 Specimen Tested by Fujii and Morita (1991)

The fourth example deals with a specimen tested by Fujii and Morita (1991) for an exterior reinforced concrete beam column joint. The dimensions and reinforcement details of tested specimen are shown in Figure 5.11. The tested specimen has 8-D10 (8 # 3) beam bars for both top and bottom reinforcement. The column reinforcement consists of 12-D13 (12 # 4) bars, and the joint shear reinforcement consists of 3 sets of 2-ϕ 6 bars which is equivalent to a reinforcement ratio of 0.41 % in the joint panel. Material properties and other details about the specimens are given in Table 5.2.

A constant axial load of ($f_c' A_g$ / 15) is applied to the column and the loading is controlled by measured deflections at the beam tip. The load is reversed at the beam bar strains of $1x10^{-3}$, $2x10^{-3}$, $3x10^{-3}$, ..etc. until the commencement of the beam yielding. After beam yielding the amplitude of beam tip deflection is increased at constant increment.

Figure 5.12 compares the experimental and the analytically predicted story shear-story drift curves. Good correlation between the two curves is noticed. Both curves show significant pinching, stiffness degradation and strength deterioration as a result of the cyclic load application. Figure 5.13 compares experimental and the analytically predicted story shear-story drift envelopes. Both curves show a drop in the connection strength in the last cycle where joint shear failure has occurred. The

experimental and analytical shear stress - shear strain envelopes for the joint panel are compared in Figure 5.14. The Figure shows a maximum shear strain of about 0.035 which is also equivalent to 50% of the story drift. In this connection also the failure mode changes from flexural to shear as a result of the deterioration of the joint shear strength under the effect of reversed cyclic loading.

5.3.3 Specimens Tested by Viwathanatepa et al. (1979)

The experimental verifications used in this section are based on tests by Viwathanatepa et al. (1979) on half scale beam column subassemblies (Figure 5.15) specifically designed to study the behavior of interior joints under severe cyclic excitations. Specimens are proportioned and detailed so as to minimize diagonal shear cracking and preclude significant shear deformation in the joint panel region. During the loading history, all the inelastic actions are concentrated in the joint panel and in the beam inelastic regions while the columns remained essentially elastic. The tested specimens provide an excellent opportunity to examine the validity of the proposed model to represent bond slip deformations since all the deformations in the joint are mainly due to bond slip. For this reason these specimens were the subject of analysis by many researchers such as Filippou et al. (1983a, b), Filippou et al. (1986a, b), Mukaddam et al. (1986), and Russo at al. (1986).

Most researchers have limited their studies to the bottom or the top bar reinforcement The model by Filippou et al. (1983a, b) is the only model that studies

the complete problem of bond slip in a reinforced concrete joint. This involves solving the equations of bond slip for the top and bottom reinforcing bars and then combining their response by satisfying the equilibrium of forces and moments at the beam column interface. The boundary conditions in their model are the slip increments at opposite corners of the joint panel as shown in Figure 5.16.

In the proposed model, the column end is displaced first to the right and then to the left, as shown in Figure 5.17, so that the fixed end rotations at the left side of the joint follows the experimental values, thus simulating the experimental program. In this way only the fixed end rotations at the left side of the joint follow the experimental rotation history while the rotation at the right side will be calculated. This is similar to a displacement controlled test but in this case the rotations at one end is specified and the rotation at the other end is to be analytically predicted.

Two interior beam column subassemblies referred to as BC3 and BC4 are used in the current study. Both specimens have identical configuration and dimensions as shown in Figure 5.15. In both specimens the longitudinal reinforcement of the girders consists of 4 # 6 bars at the top and 3 # 5 bars at the bottom. Thus the area of the reinforcement at the bottom is about half that at the top. The two subassemblies are subjected to entirely different load histories: Specimen BC4 is subjected to a single large displacement reversal simulating the effect of a very severe pulse like seismic excitation. This kind of load history is basically used for testing the modeling of the monotonic part of loading. Specimen BC3 is subjected to a large number of

load reversals of gradually increasing magnitude. This kind of load history provides a good test on the modeling of the hysteretic part of loading.

The fixed end rotation at the beam column interface is computed based on the end slip of reinforcing bars which results due to bond deterioration within the joint only. The fixed end rotation is calculated, experimentally and analytically, using the following relation:

$$\Theta_{FE} = \frac{s^t - s^b}{d'} \tag{5.1}$$

where s is the relative slip between reinforcing bars and the surrounding concrete at the beam column interface. Superscripts t and b denote top and bottom reinforcing layers respectively, and d' is the distance between the top and bottom reinforcing bars.

Experimental and analytical results predicted by the proposed model and also by the model of Filippou at al. (1983a, b) are presented. The beam on the left of the column is referred to as "west beam" and the beam on the right of the column is referred to as "east beam". Relative slip values are defined as positive if reinforcing bars move in the positive X direction. This implies that bar pullout on the west beam side is associated with negative slip values, while positive slip values represent bar pull out on the east beam side.

Analytical and experimental results for specimen BC4 are presented in Figures 5.18-5.23. First the global behavior of the beam column joint is exhibited by means

of the moment fixed end rotation relationship at the two end sections of the joint in Figures 5.18 and 5.19. The Figures show good correlation between the analytical models and the experimental data. Figure 5.19 shows a discrepancy in the value of the fixed end rotation at which unloading starts in the positive direction at the east side of the joint. This is mainly due to the fact that fixed end rotations are given only at the east side of the joint while they are calculated at the west side as previously described. The analytical prediction for the rotation at this unloading point is about 13% less than the experimental value. It is interesting to know that the rigid beam column connection assumption implies that the angle of rotation is always equal to zero. The proposed model thus offers a significant improvement to that crude approximation. The analytical results of Filippou et al. (1983a,b) are closer to the experimental results than those of the proposed model. A possible explanation is that the model of Filippou et al. (1983a,b) depends on the prior knowledge of the slip increments at the joints' corners as shown in Figure 5.16.

Figures 5.20 to 5.23 compares the moment-slip relation at the four corners of the joint panel region. The predictions of the proposed model are in good agreement with the experimental data. The Figures show higher slip values for the bottom reinforcement. This is due to the fact that the area of bottom reinforcement is only about half that of the top reinforcement. This accelerates bond deterioration along the bottom bars embedded in the joint panel (Filippou et al. (1983a,b).

Experimental and analytical results for specimen BC3 are shown in Figures

5.24 and 25. These Figures compare the moment rotation at the beam column interface until the moment that, due to pull out of the bars in the bottom reinforcing layer, "joint anchorage" failure is initiated. Both models are able to predict the moment rotation relation within acceptable accuracy. However the model of Filippou et al (1983a, b) shows an early sudden loss of strength and failure of the specimen's load carrying capacity. Since the moment slip histories at the joint corners have not been recorded experimentally, comparisons are limited to the moment rotation diagrams.

5.4 CONCLUSIONS

This study shows that the proposed beam column connection model can be used successfully to predict the response of beam column joints under increasing monotonic and reversed cyclic loading. The verification examples used in this Chapter include specimens experiencing high shear deformations, a typical situation that LRC connections encounter during severe earthquakes. The success of the model in describing the behavior of these connections is demonstrated by the good correlation achieved with the experimental data. These data included the shear stress shear strain relationship for the joint panel and the load deflection relationship for the beam column connection.

The verification examples also include specimens with high bond slip deformations, another type of deformations that LRC connections experience under

earthquake loads. The success of the model in describing bond slip deformations is achieved by comparing the moment fixed end rotation and the moment end slip relationships with the experimental data.

Table 5.1 Properties of test specimens (Kaku and Asakusa, 1991)

	Specimen 1	Specimen 2
Beam Dimension (mm)	160 x 220	160 x 220
Beam Reinforcement (Top and Bottom Bars)	4 # 4 (F_y = 391 MPa)	4 # 4 (F_y = 391 MPa)
Column Dimension (mm)	220 x 220	220 x 220
Column Reinforcement	12 # 3 (F_y = 395 MPa)	12 # 3 (F_y = 395 MPa)
Joint Reinforcement	4 sets of 2-ϕ 6 ρ = 0.49 % (F_y = 281 MPa)	4 sets of 2-ϕ 6 ρ = 0.49 % (F_y = 281 MPa)
Concrete Strength (MPa)	32	40
Column Axial Load (kN)	194 ($f_c' A_g$ / 8)	0
δ_y (mm)	8.15	9.51

Table 5. 2 Properties of test specimen (Fujii and Morita, 1991)

Beam Dimension (mm)	160 x 250
Beam Reinforcement (Top and Bottom Bars)	8 # 3 (F_y = 417 MPa)
Column Dimension (mm)	220 x 220
Column Reinforcement	12 # 4 (F_y = 395 MPa)
Joint Reinforcement	3 sets of 2-ϕ 6 (ρ = 0.41 %) (F_y = 297 MPa)
Concrete Strength (MPa)	30
Column Axial Load (kN)	100 ($f_c' A_g$ / 15)

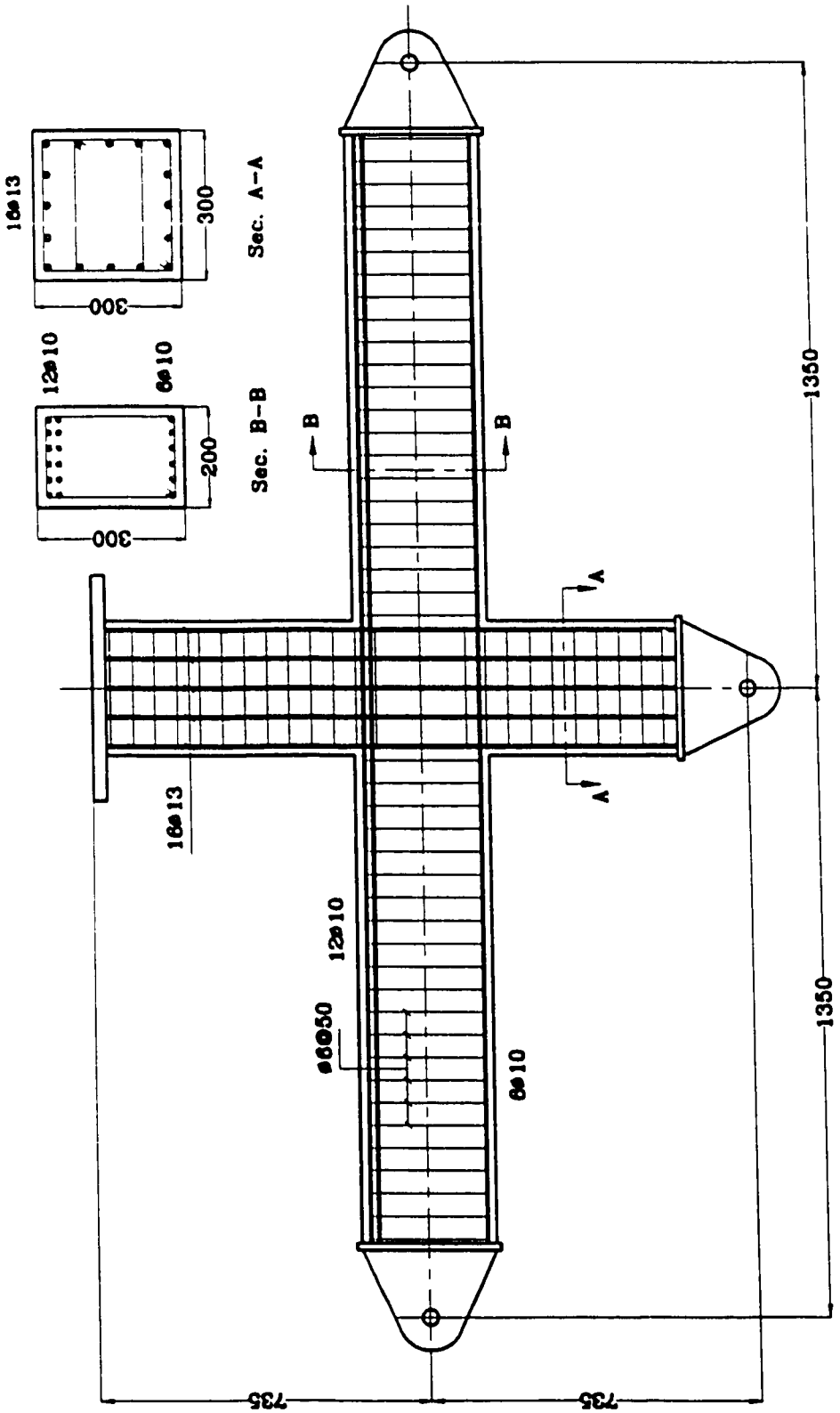

All dimensions are in mm

Figure 5.1 Dimensions and reinforcement details of specimen tested by Otani et al. (1985)

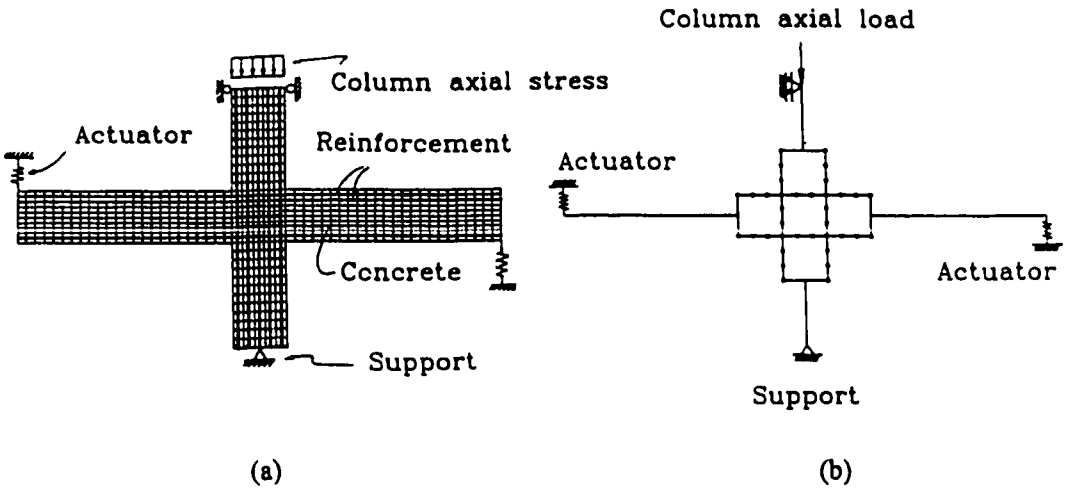

Figure 5.2 Finite element idealization for specimen C1; (a) Pantazopoulou and Bonacci's model, (b) proposed model

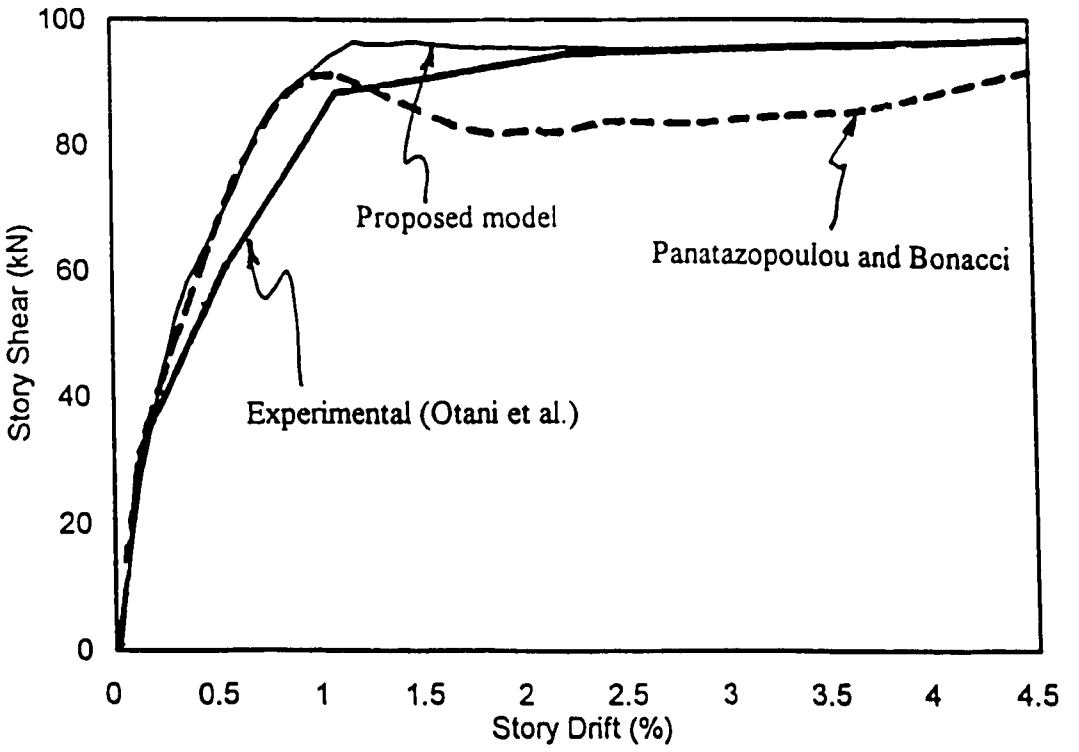

Figure 5.3 Story shear story drift relationships for specimen tested by Otani et al. (1985)

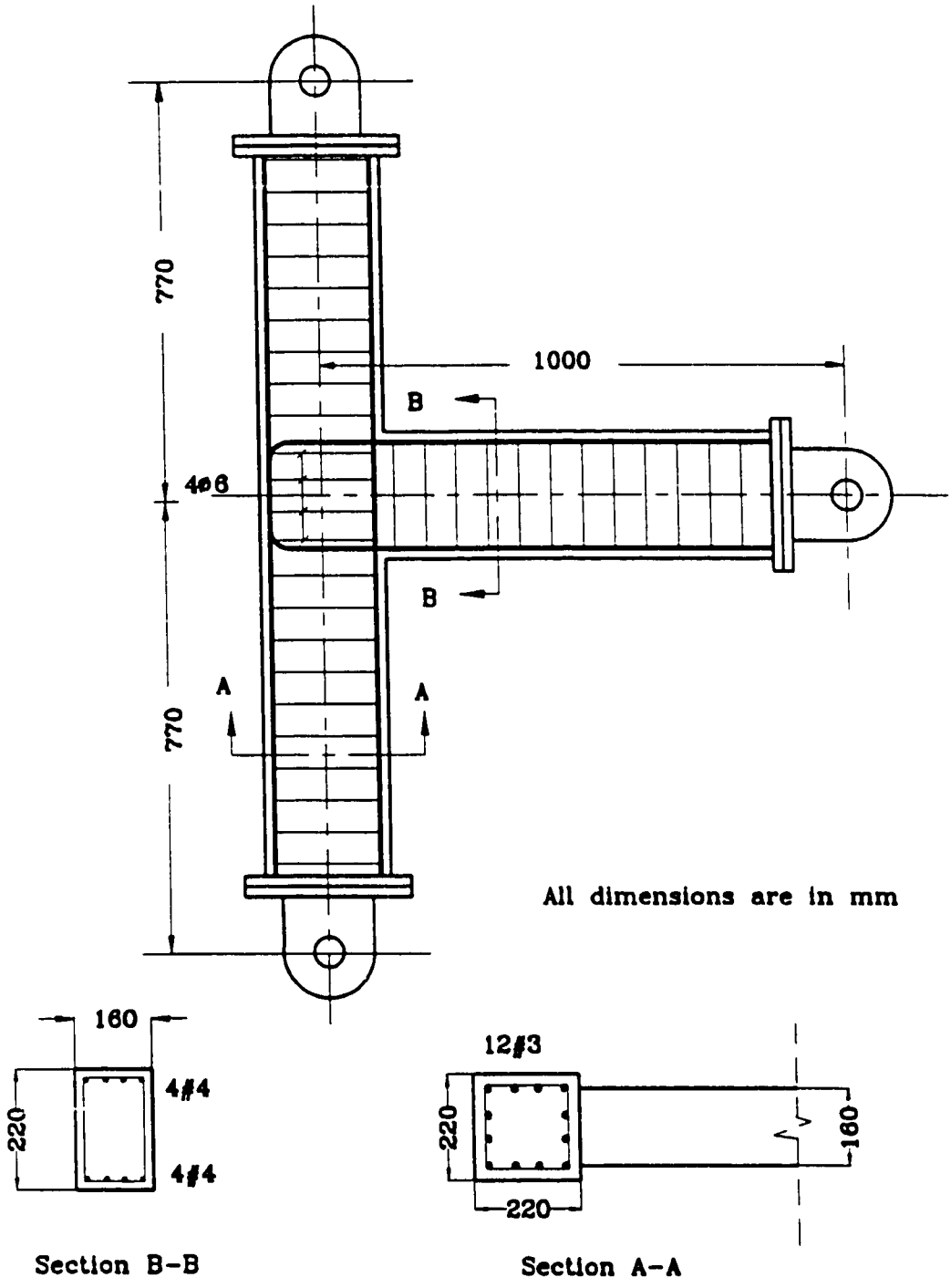

Figure 5.4 Dimensions and reinforcement details of specimen tested by Kaku and Asakusa (1991)

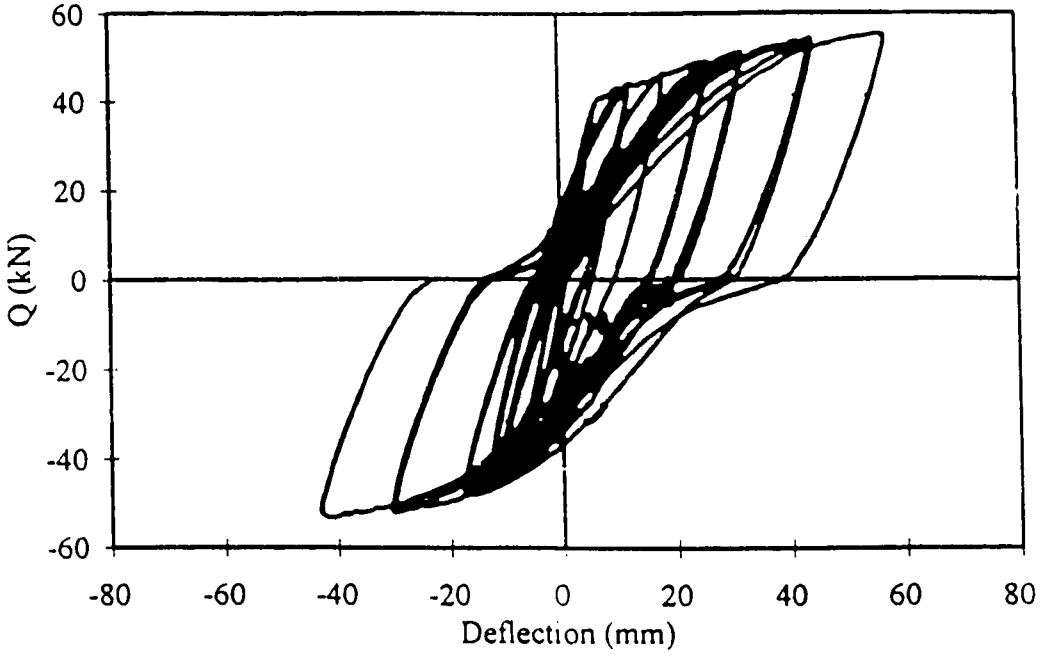

(a) Experimental

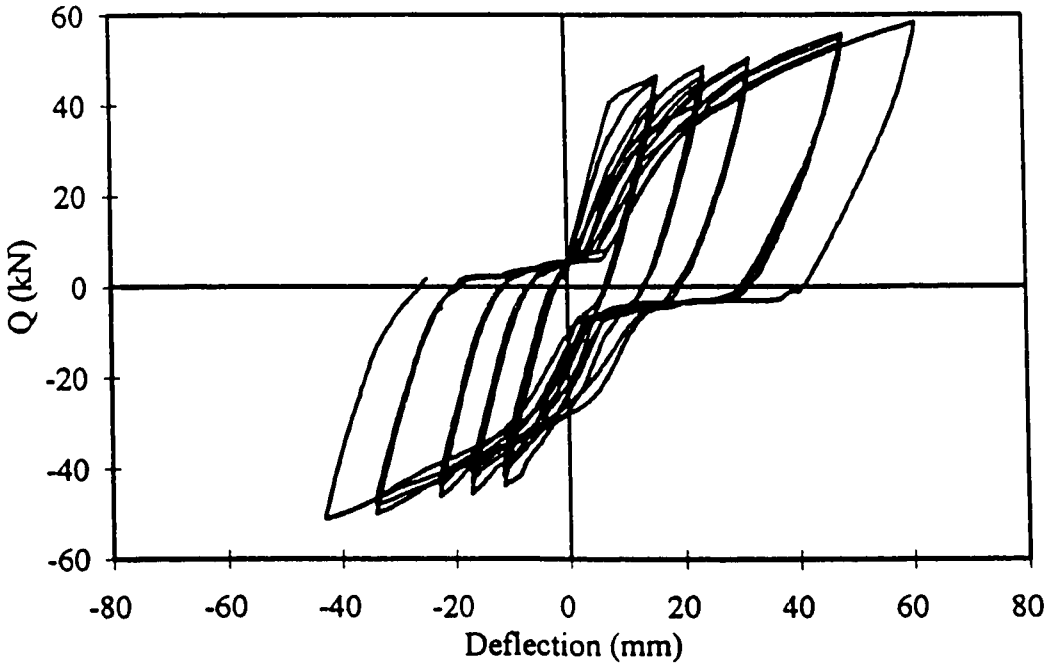

(b) Analytical

Figure 5.5 Beam shear force story drift relationships for specimen tested by Kaku and Asakusa (1991)

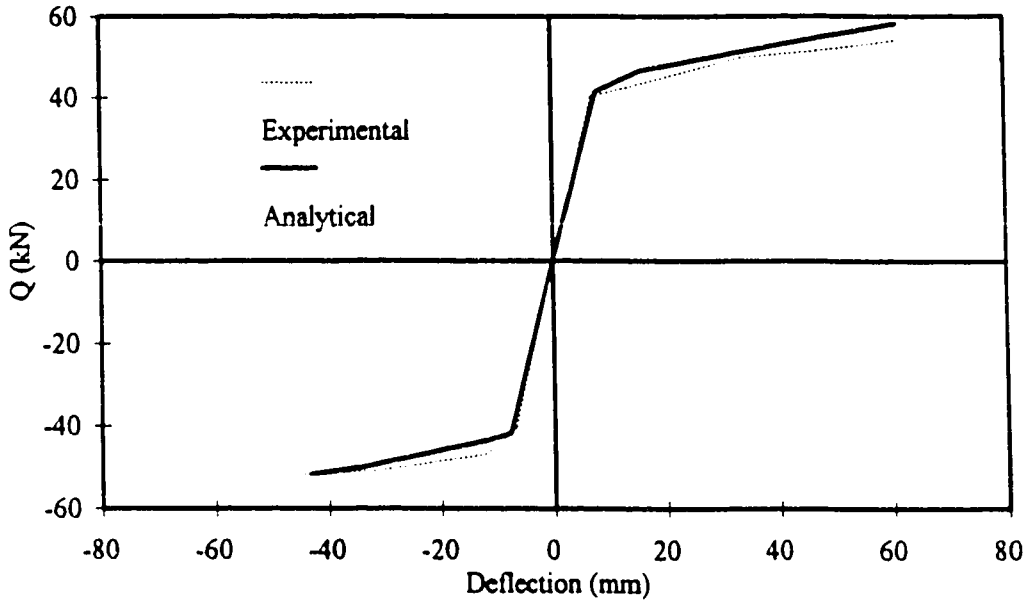

Figure 5.6 Envelopes of cyclic beam shear force story drift curves

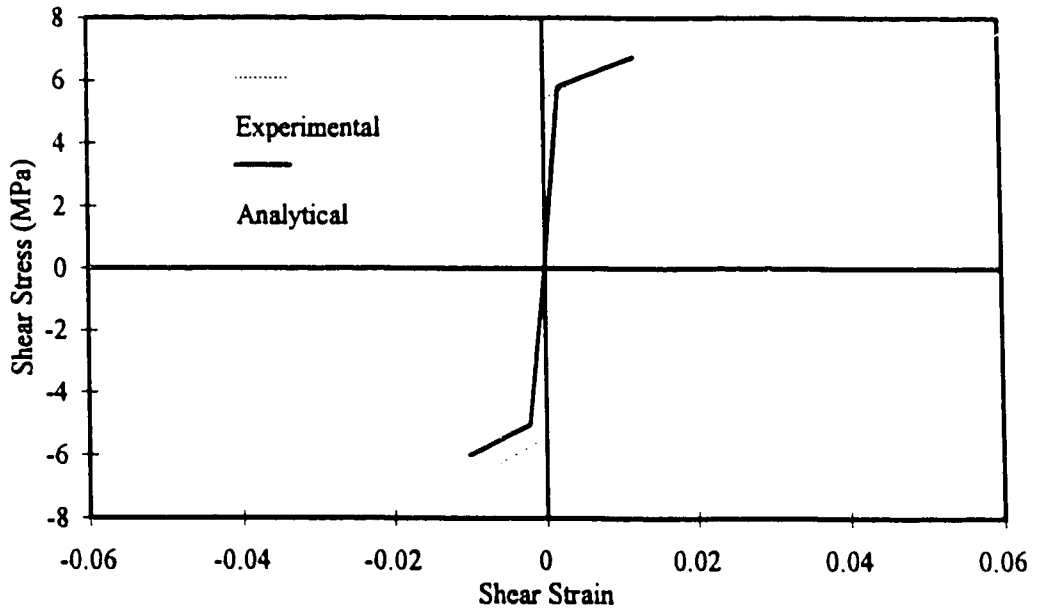

Figure 5.7 Envelopes of cyclic shear stress shear strain in the joint.

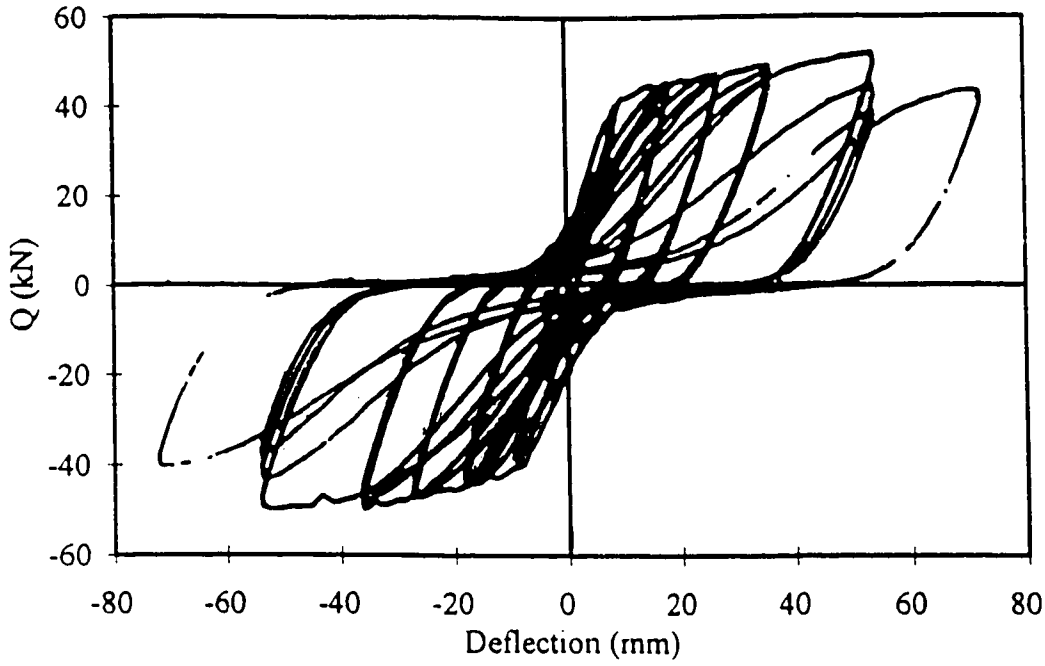

(a) Experimental

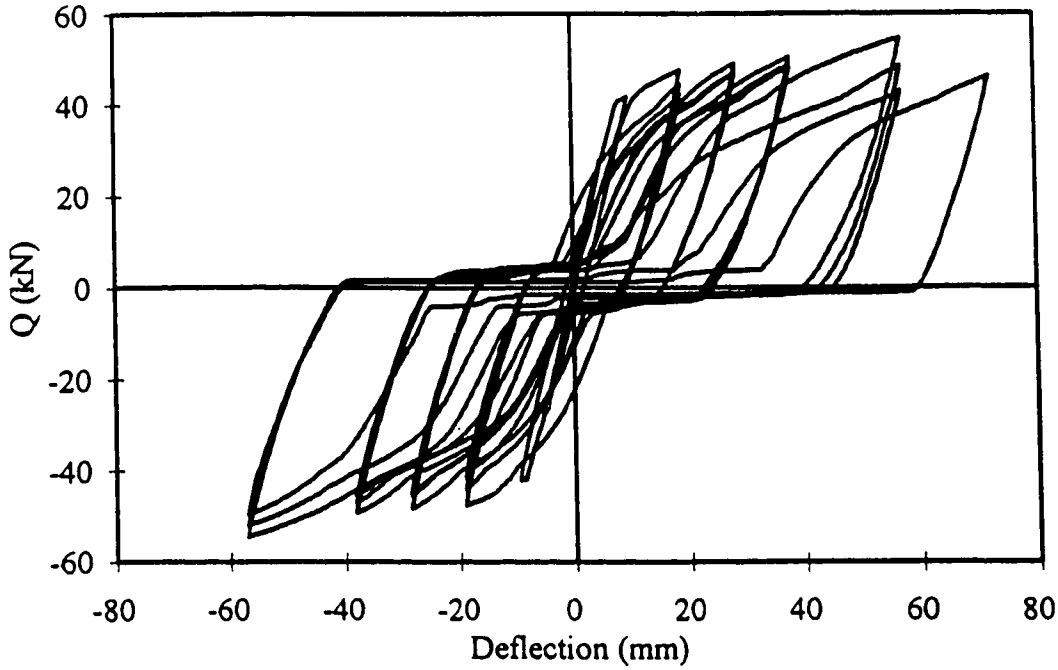

(b) Analytical

Figure 5.8 Beam shear force story drift relationships for specimen tested by Kaku and Asakusa (1991)

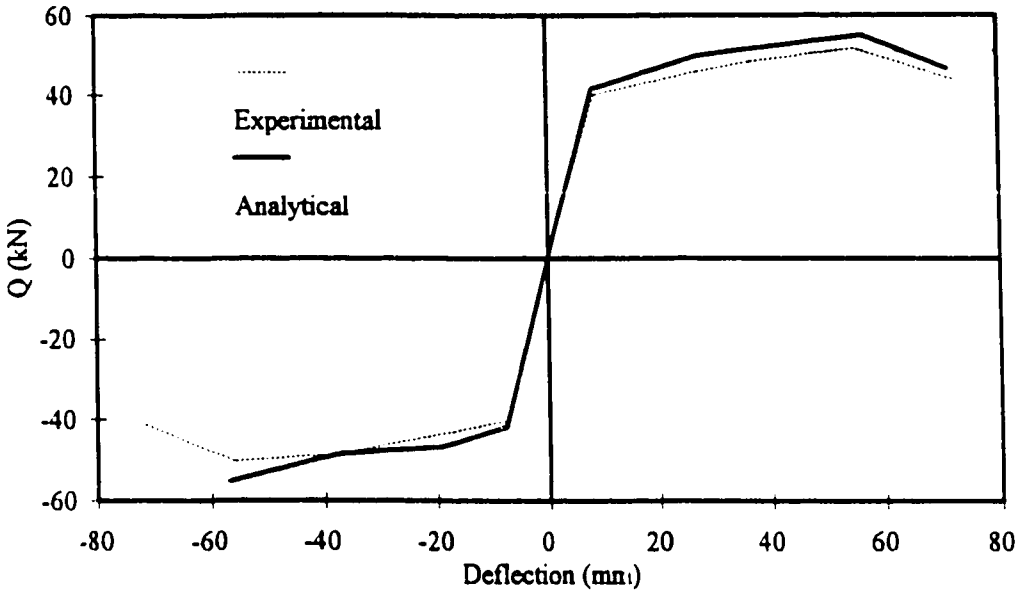

Figure 5.9 Envelopes of cyclic beam shear force story drift curves

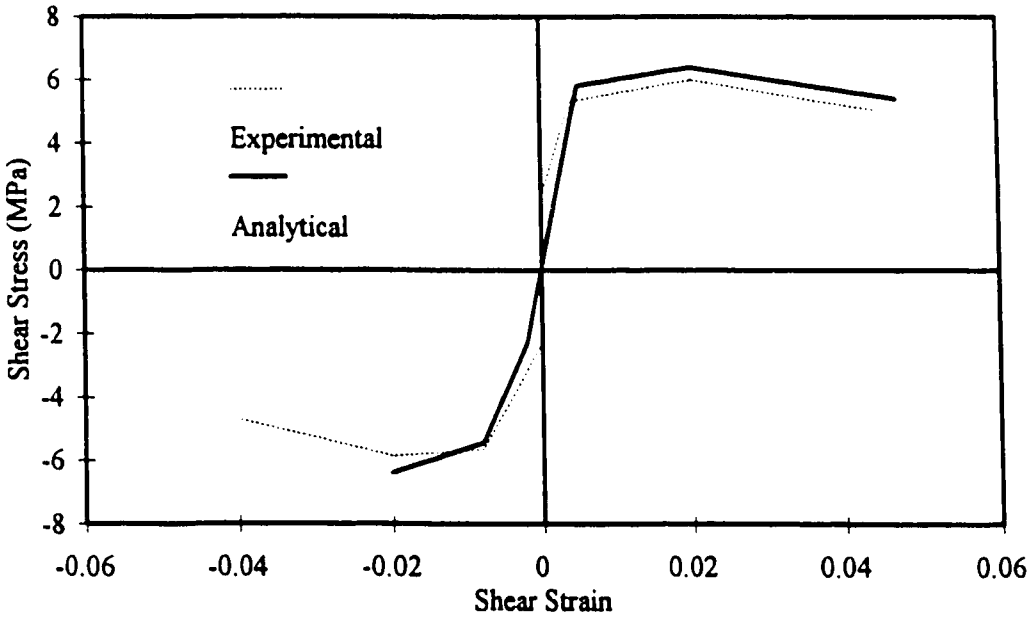

Figure 5.10 Envelopes of cyclic shear stress shear strain in the joint

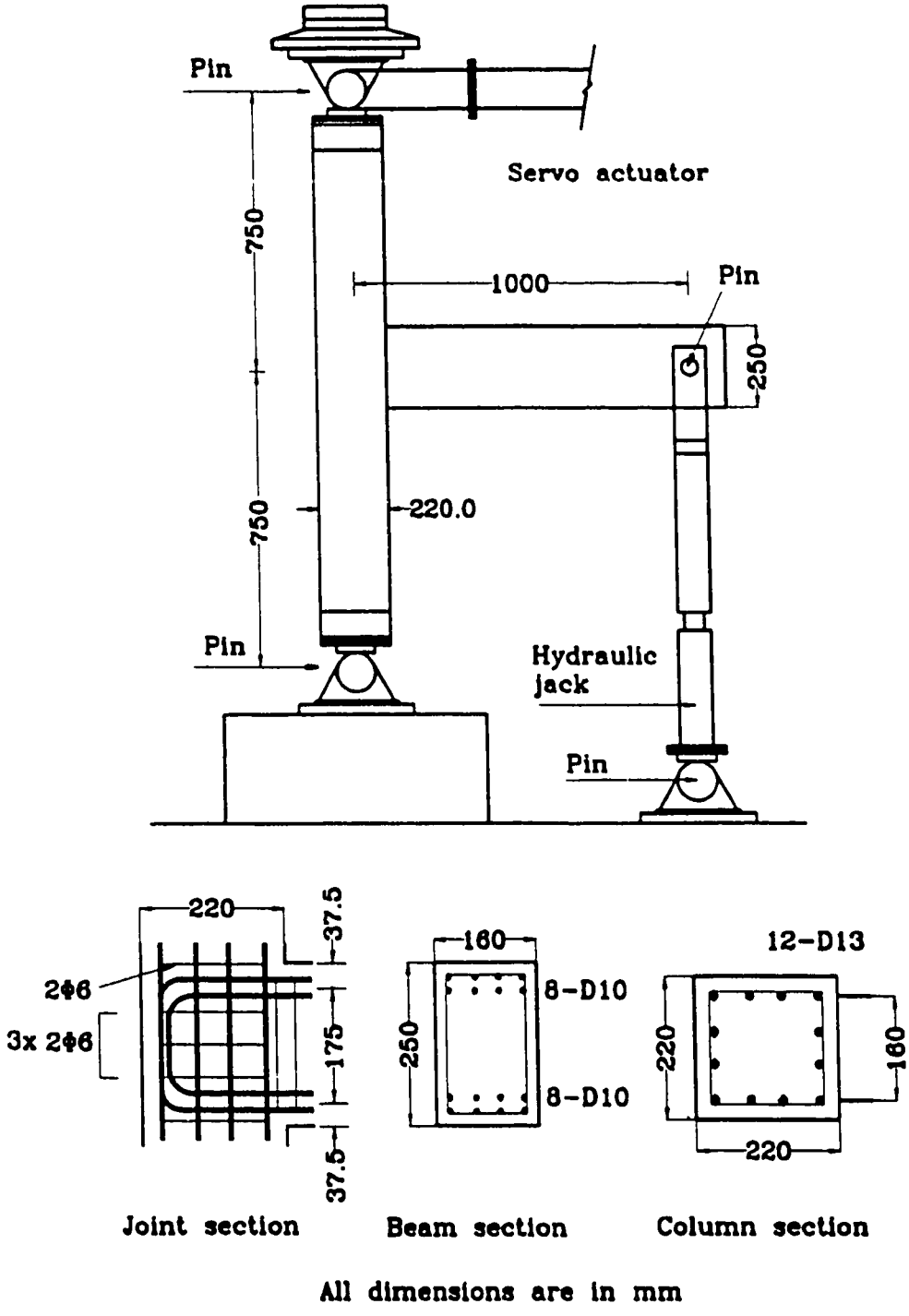

Figure 5.11 Dimensions and reinforcement details of specimen tested by Fujii and Morita (1991)

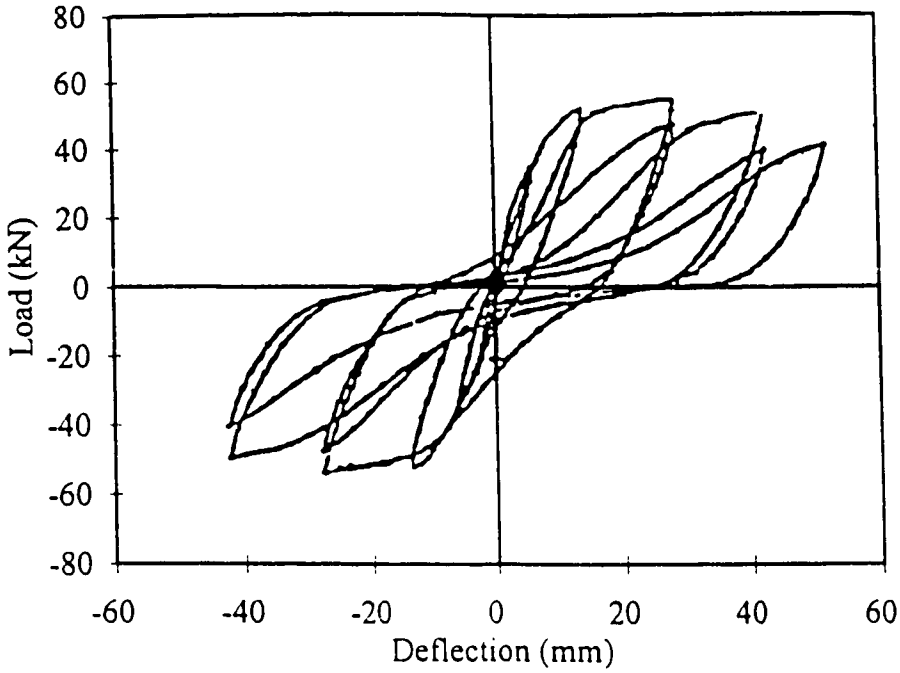

(a) Experimental

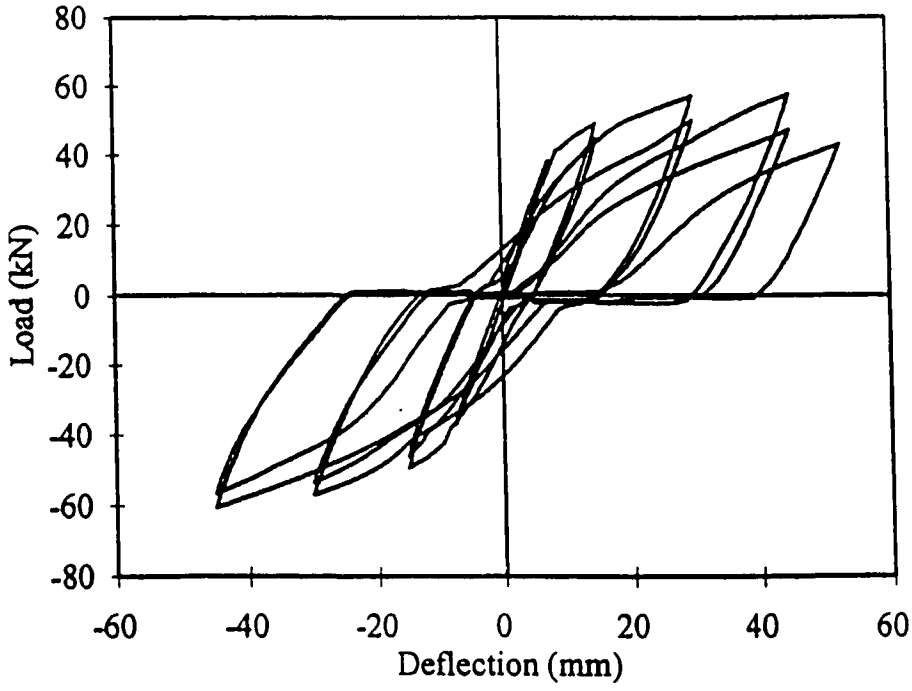

(b) Analytical

Figure 5.12 Beam shear force story drift relationships for specimen tested by Fujii and Morita (1991)

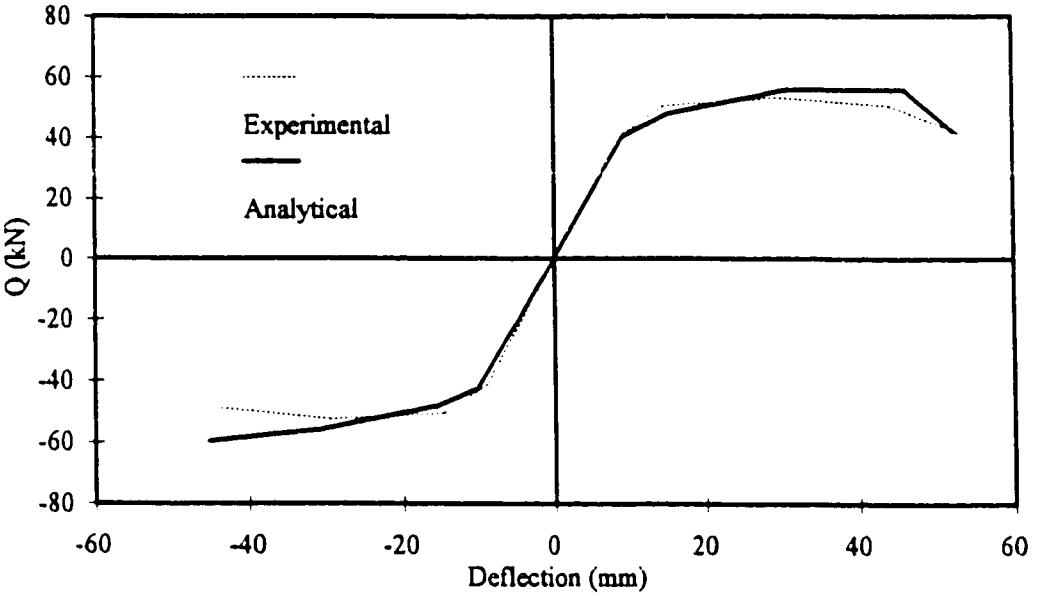

Figure 5.13 Envelopes of cyclic beam shear story drift curves

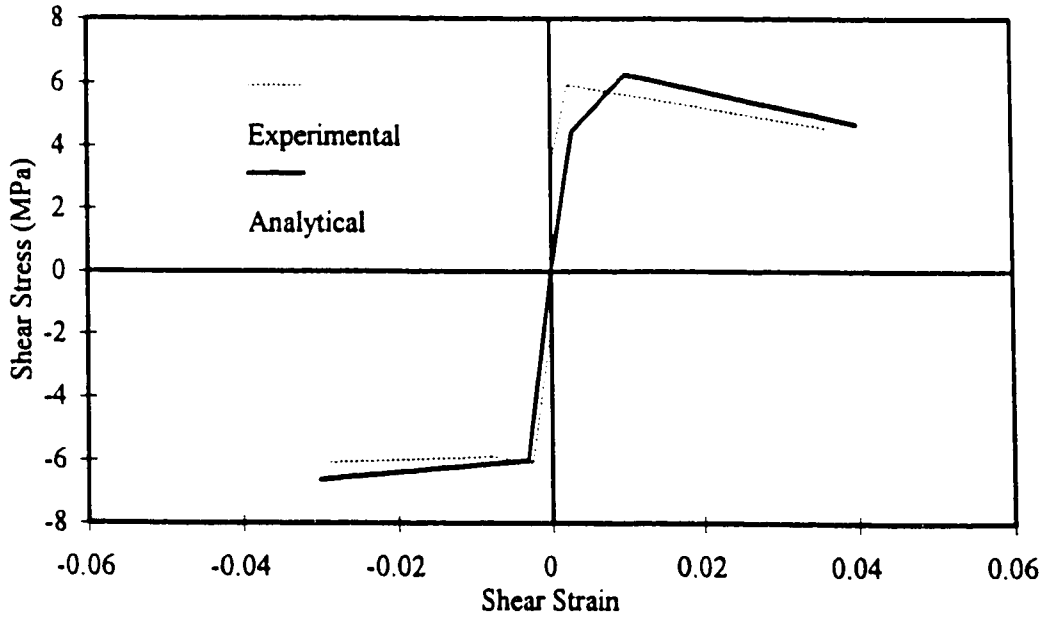

Figure 5.14 Envelopes of cyclic shear stress shear strain in the the joint

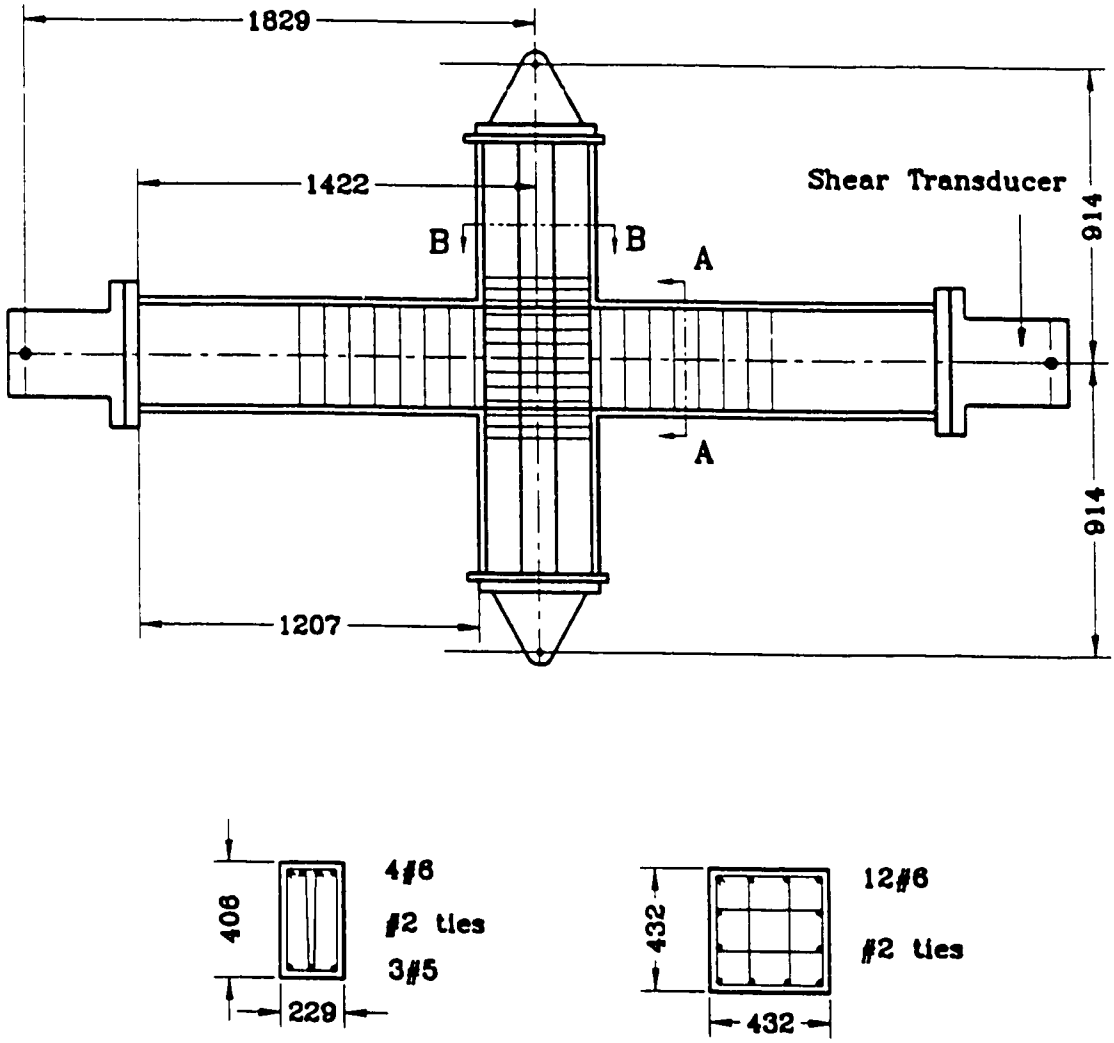

Figure 5.15 Dimensions and reinforcement details of specimens tested by Viwathanatepa et al. (1979)

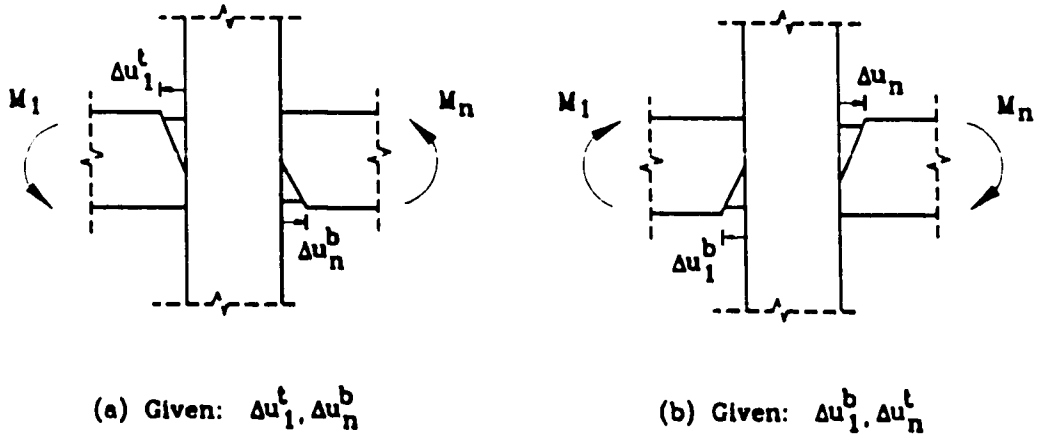

Figure 5.16 Load application to Filippou's model (Filippou et al., 1983a, b)

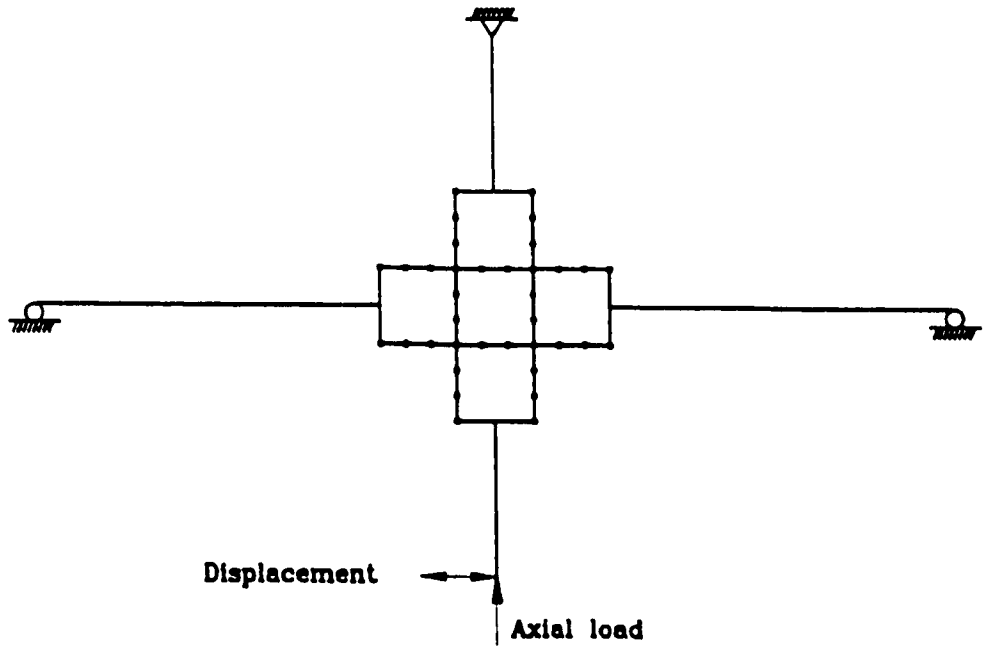

Figure 5.17 Load application to the proposed beam column connection model

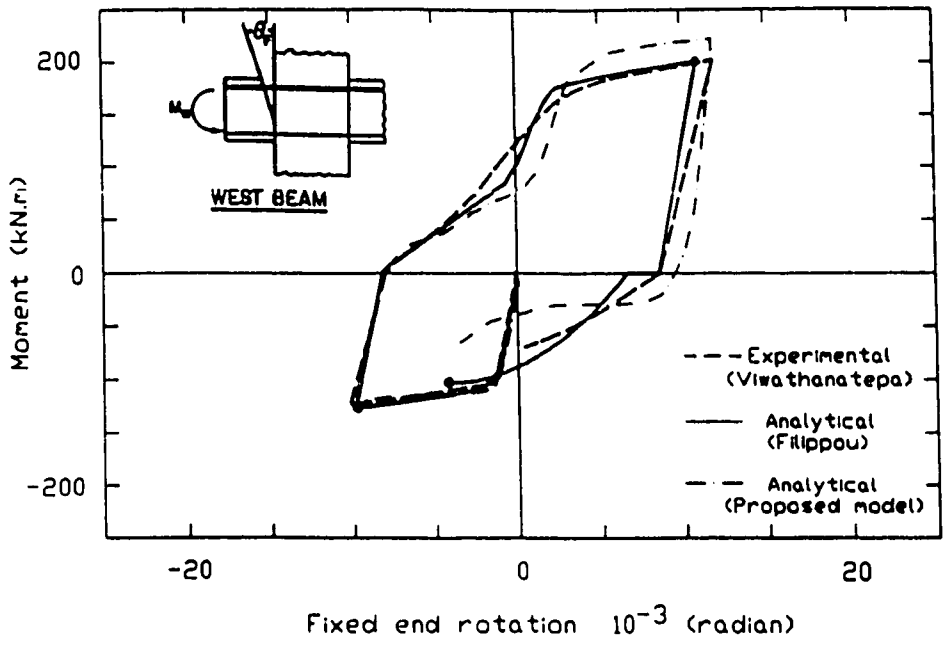

Figure 5.18 Moment rotation relationship for specimen BC4 (West beam)

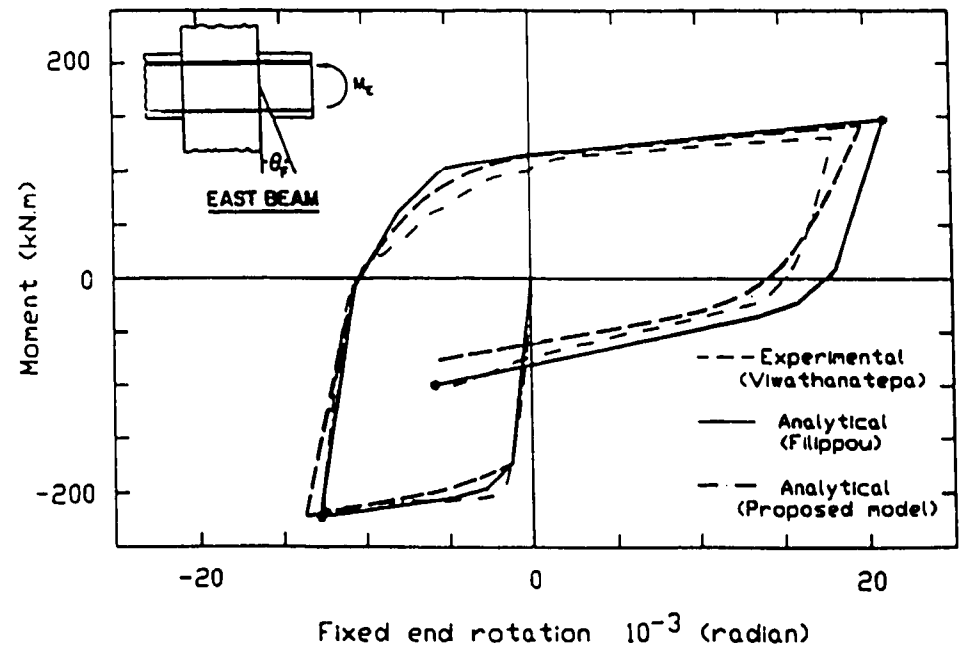

Figure 5.19 Moment rotation relationship for specimen BC4 (East beam)

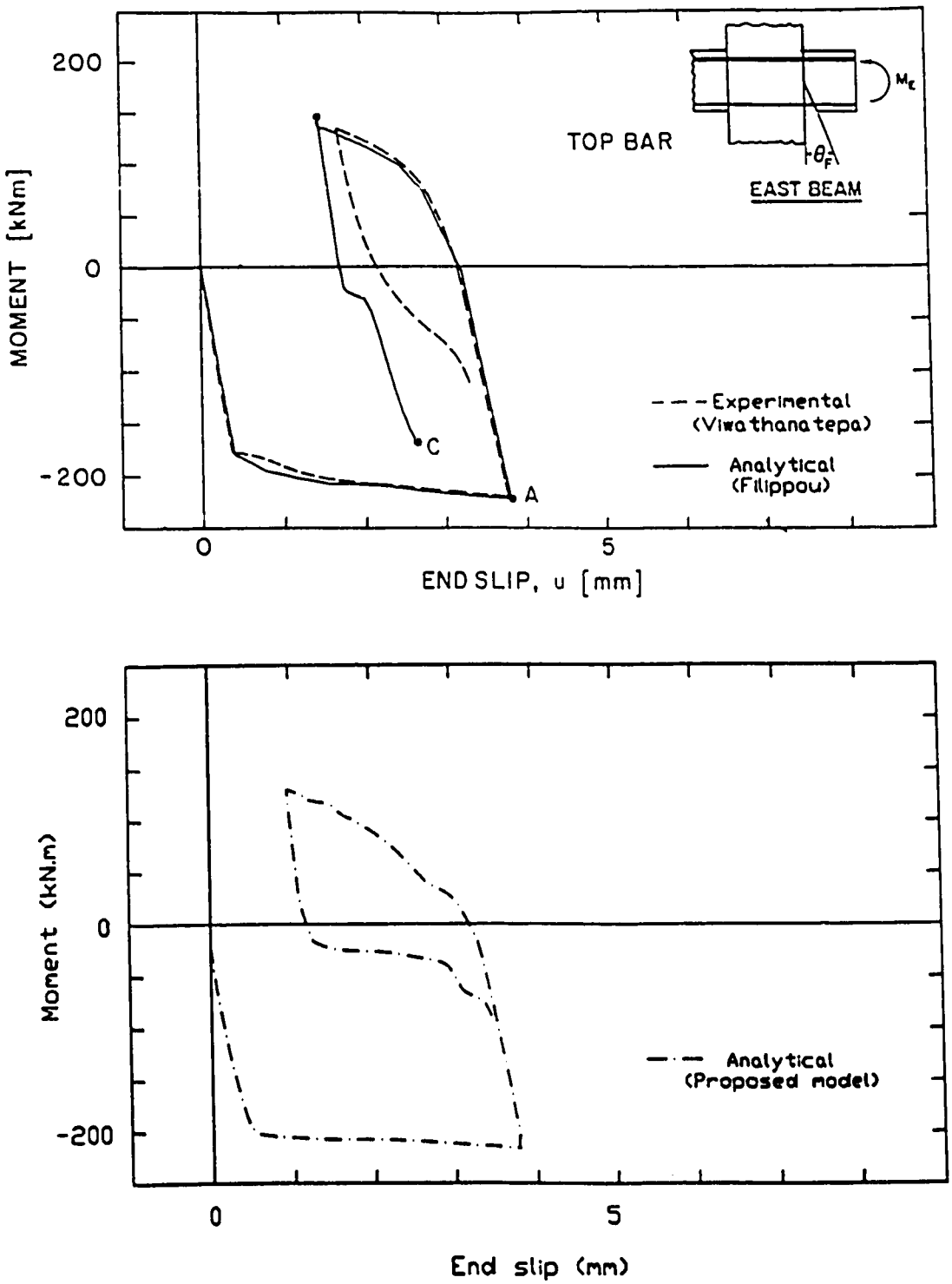

Figure 5.20 Moment slip relationship for specimen BC4

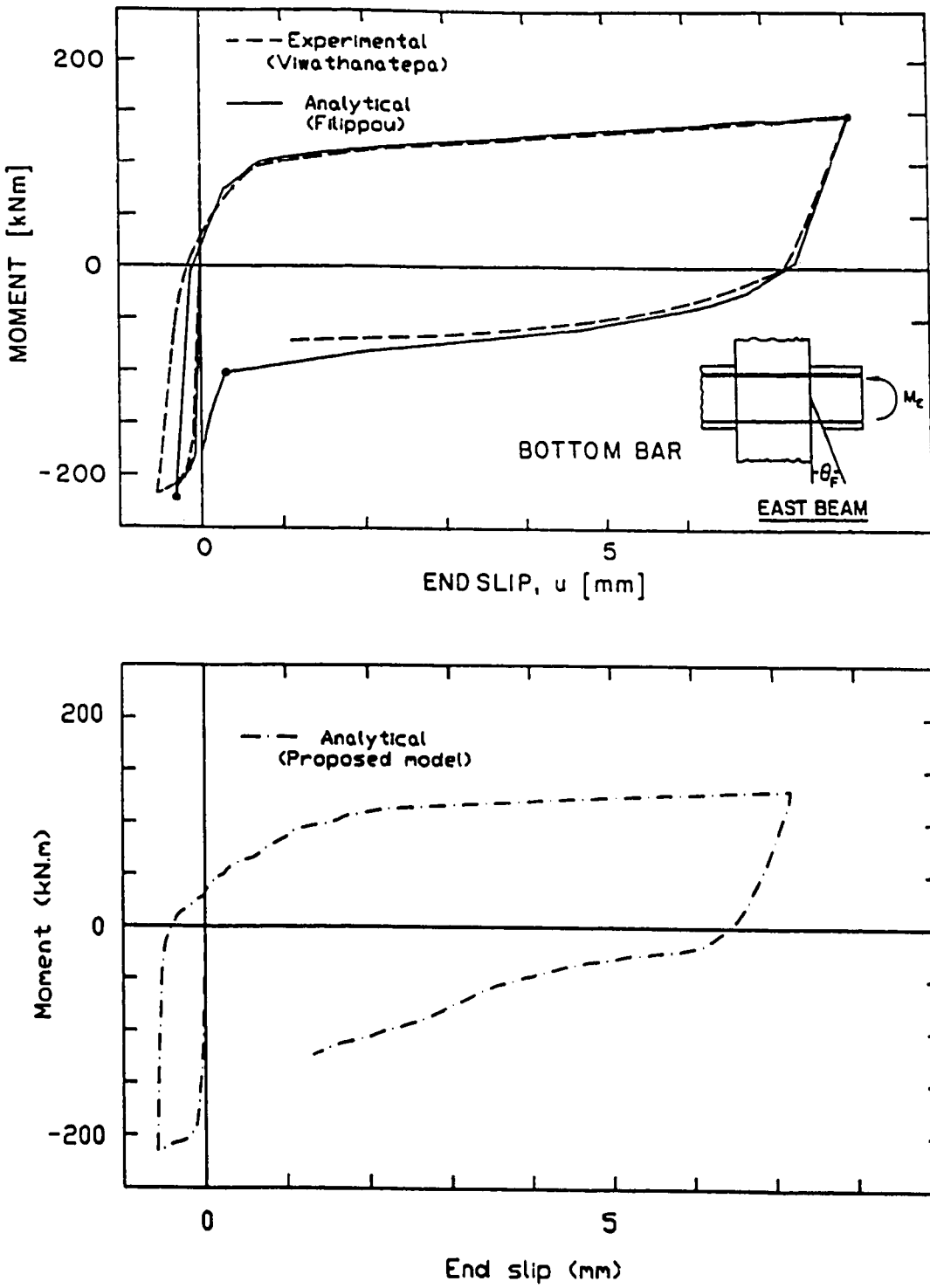

Figure 5.21 Moment slip relationship for specimen BC4

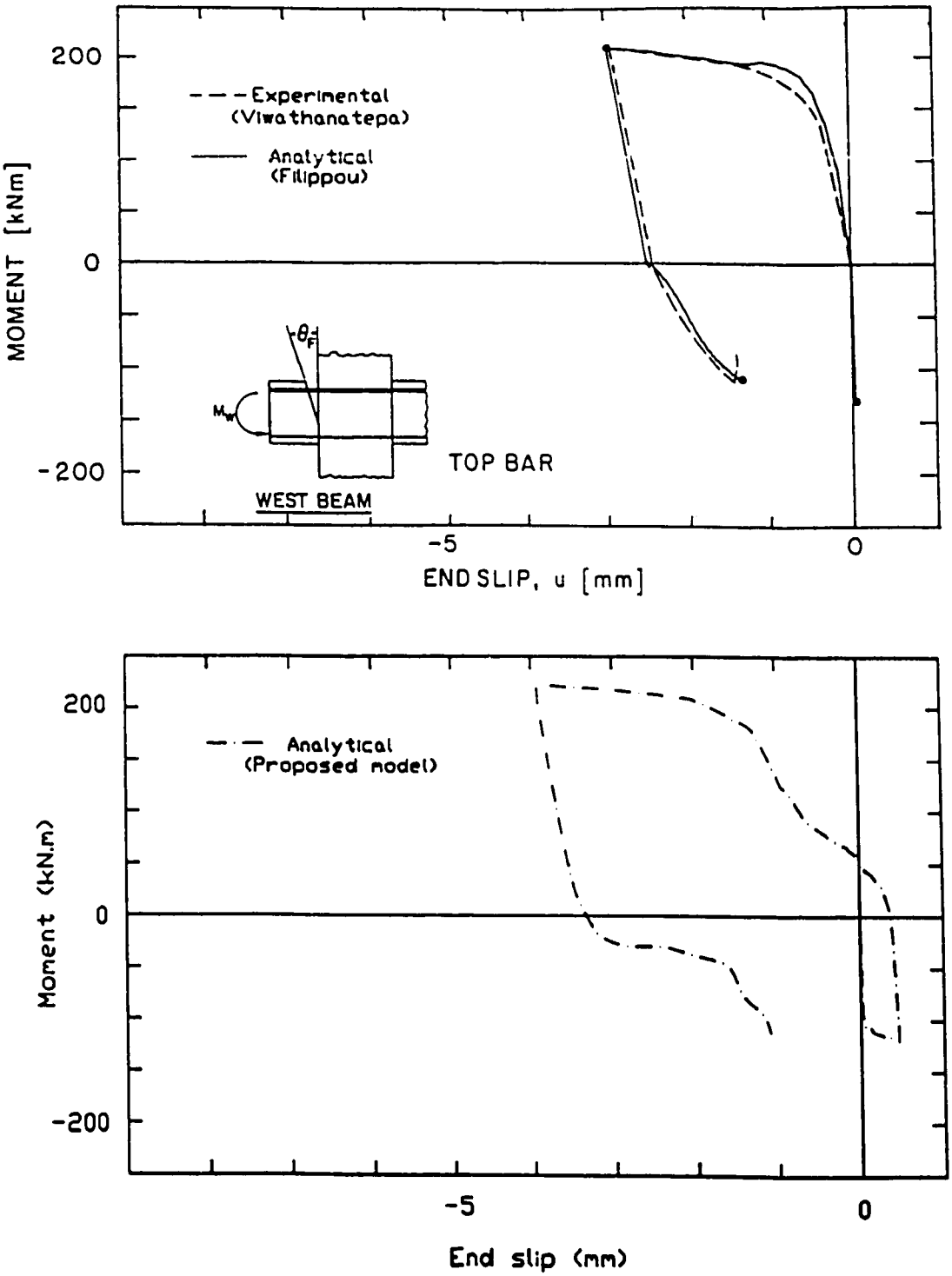

Figure 5.22 Moment slip relationship for specimen BC4

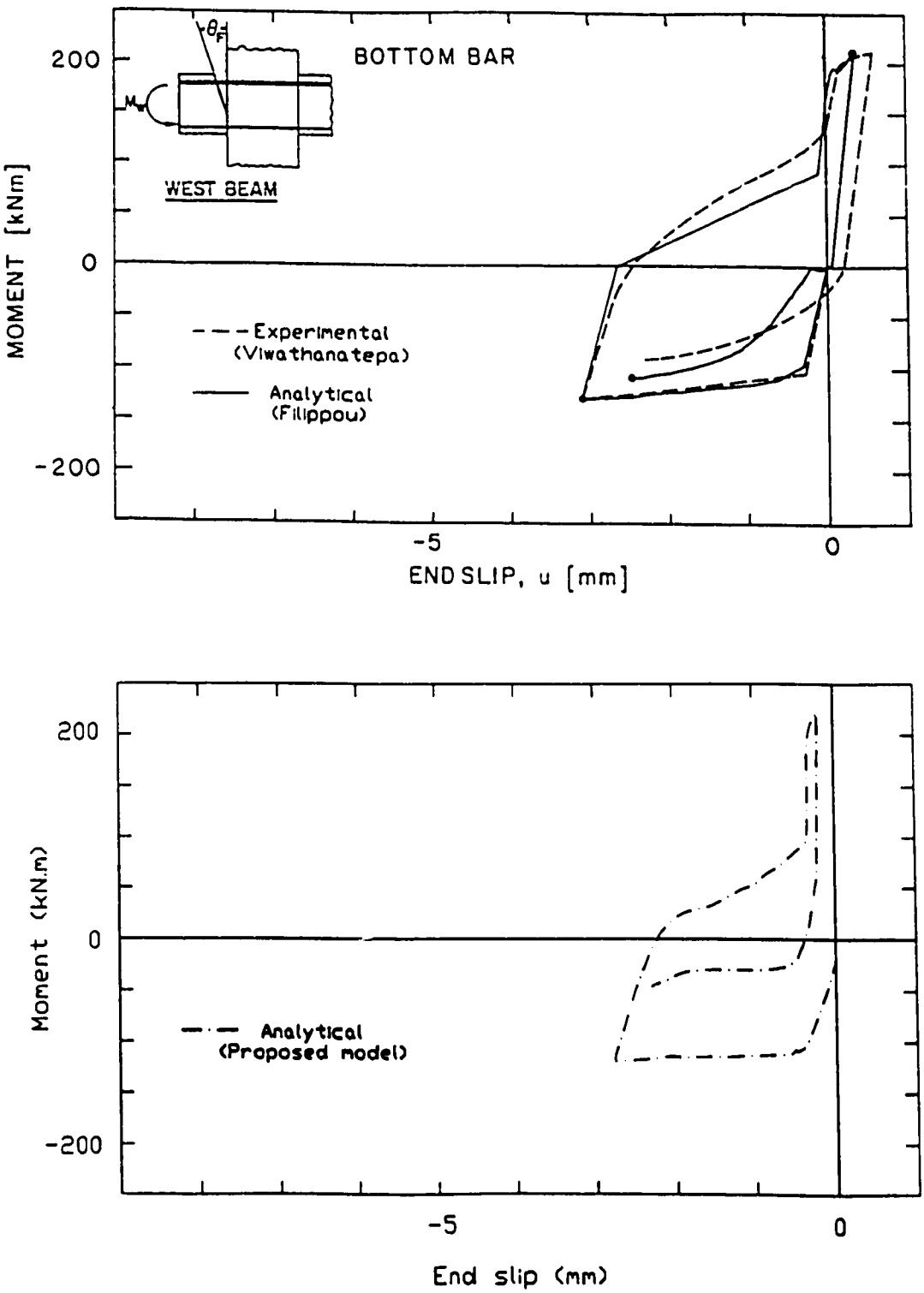

Figure 5.23 Moment slip relationship for specimen BC4

(a)

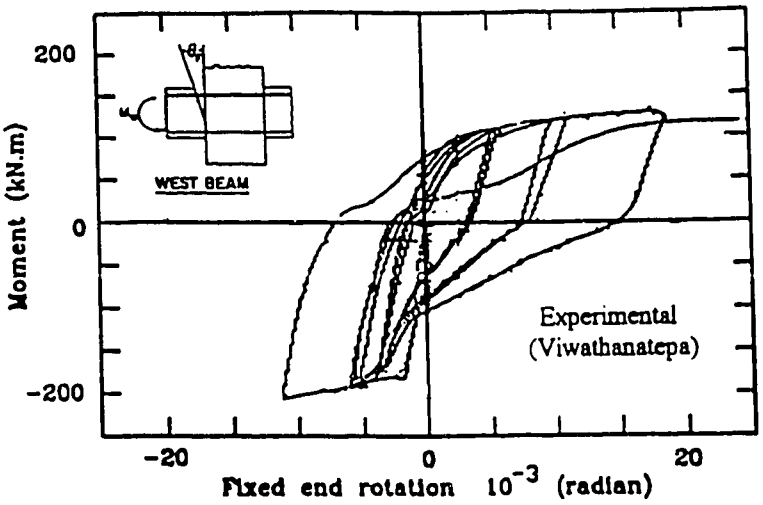

(b)

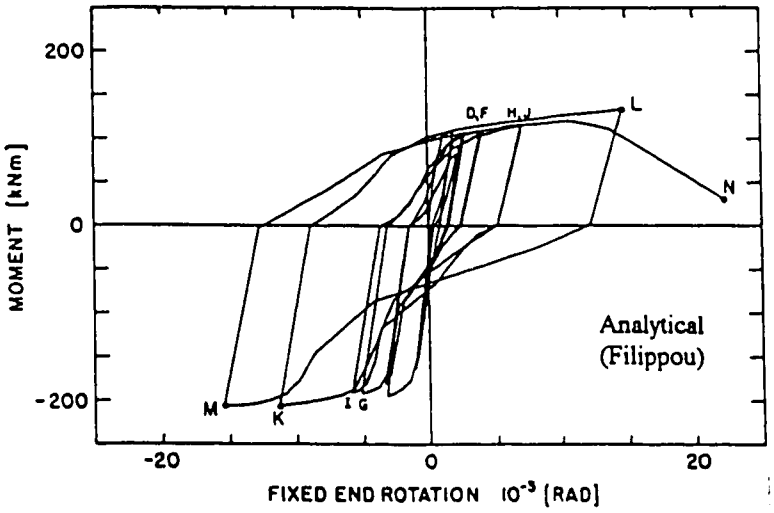

(c)

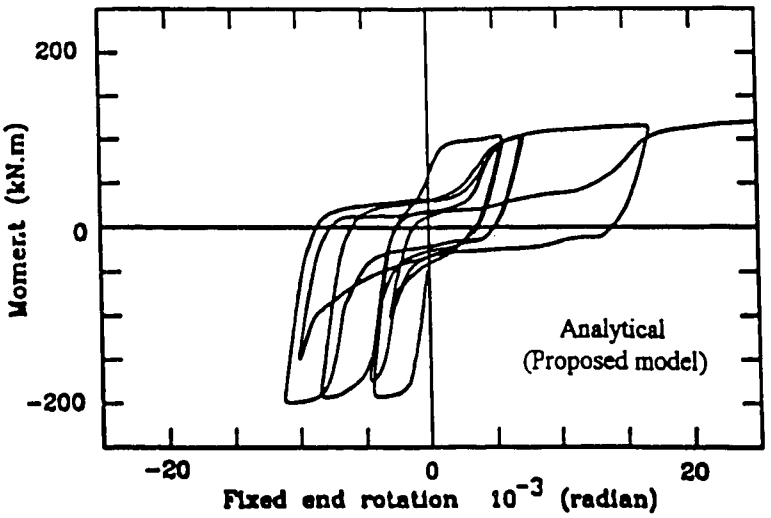

Figure 5.24 Moment rotation relationship for specimen BC3 (West beam)

(a)

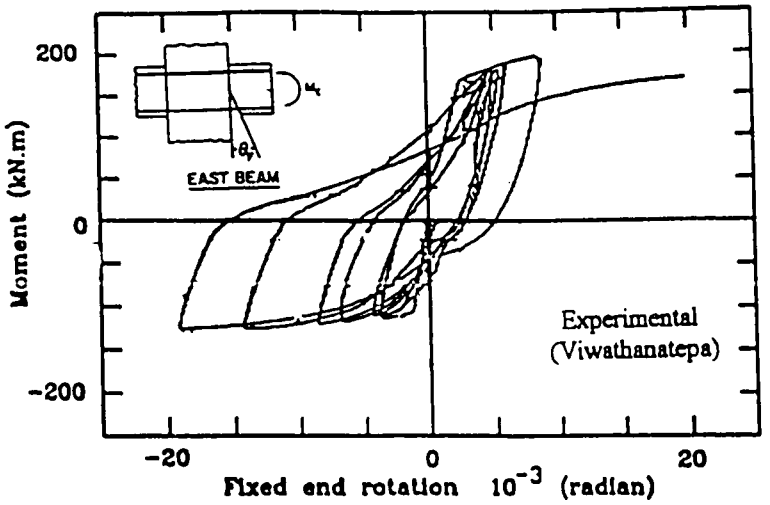

(b)

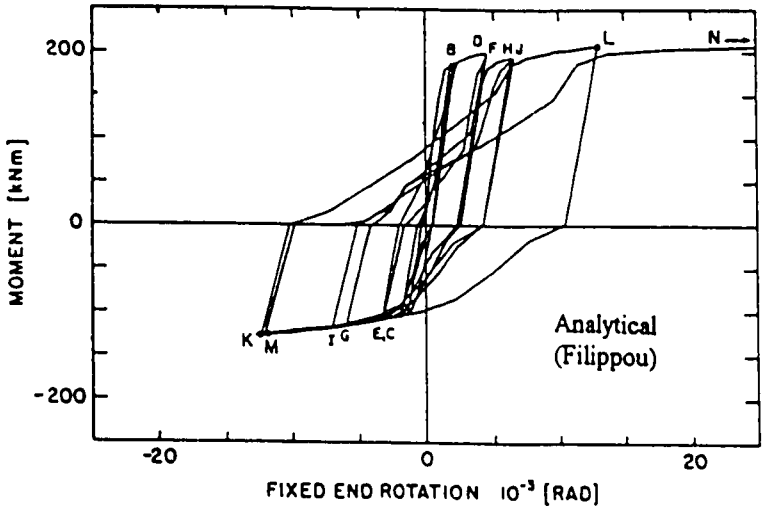

(c)

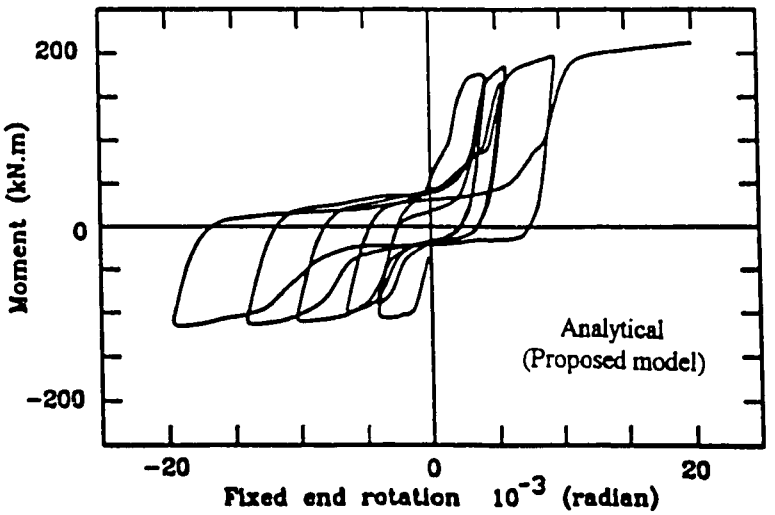

Figure 5.25 Moment rotation relationship for specimen BC3 (East beam)

CHAPTER 6

DYNAMIC ANALYSIS OF

A THREE STORY FRAME BUILDING

6.1 GENERAL

In this chapter, a three-story reinforced concrete frame structure with different joint detailing strategies is analyzed. This includes a rigid, a well detailed and a poorly detailed joint. Pushover analyses as well as time history analyses are conducted on the frame. The response of the structure using different joint details is compared to identify the effect of changing these details on the characteristic behavior of the frame. The purpose of using a rigid joint is to investigate the effects of ignoring the shear and the bond slip deformations in this critical region on the overall response of the structure.

6.2 DESCRIPTION OF THE STRUCTURE

The building configuration selected is a typical office building or a frame structure that can be found in many cities in North America. A symmetrical floor plan and floor levels of equal height are used to avoid any irregular behavior that may lead to complexities in interpreting the dynamic response. The building is designed at the

State University of New York at Buffalo (Hoffman et al, 1992) for gravity and wind loads; in accordance with code requirements prescribed in ACI 318-89. Seismic loads are not considered in the design of the building. Figure 6.1 shows the typical floor plan. The layout of the frame, the details of the beams and the columns, and the analytical model used are shown in Figure 6.2. The frame measures 16.5 x 16.5 m in plan, with a bay spacing of 5.5 m. Floor to floor height is taken to be 3.6 m. Since gravity load forces have governed over those from wind loads for beams, the reinforcing profiles and the beams cross sections are identical regardless of story level. The columns are designed to resist the worst combination of moment and axial load from wind and gravity loads. The column cross sections and reinforcement details are identical for all levels. Fair confinement is provided for the beams and the columns by using 1 # 3 bar (10 mm diameter) every 8" (200 mm).

Two detailing strategies are used for the joint panels as shown in Figure 6.3. In the first strategy, no stirrups are provided in the joint panels. The second detailing strategy involves using transverse steel for shear resistance. The stirrups are 6 # 4 bars (13 mm diameter) at 50 mm (2") spacing. The amount of stirrups used is based on providing sufficient shear resistance for the beam column joint so as to allow the framing beams and columns to reach their full flexural strength. The beam column joint shear strength provided by concrete is calculated using the equation developed by the ACI committee 352 (1976) described in Chapter 1.

The concrete unconfined compressive strength is assumed to be 27 MPa. The

steel reinforcement yield strength is assumed to be 270 MPa.

6.3 PUSHOVER ANALYSIS

The purpose of this study is to identify the lateral strength of the structure and its behavior under static loading conditions. The three story frame is subjected to an increasing monotonic lateral load simulating the seismic base shear. Three analyses are carried out on the structure using a poorly detailed joint having no shear reinforcement, a well detailed joint having adequate shear reinforcement, and a rigid joint model. The lateral load is distributed over height of the building, as shown in Figure 6.4, using the following formula (NBCC 1995);

$$F_x = \frac{V W_x h_x}{\sum_{i=1}^{N} W_i h_i} \tag{6.1}$$

where

W_i, W_x = Portion of weight assigned to levels of *i* or x respectively

h_i, h_x = Heights of level *i* or x above ground

N = Total number of stories in the building

F_x = Lateral load at level x

To evaluate the variation in the response of the structure achieved by using different joint detailing configurations certain aspects will be investigated. This includes studying the global response of the structure by comparing the base shear-

roof deflection relationships, the interstory drifts, the maximum story deflections, and the failure mechanisms. The local responses of the joints, the beams, and the columns are examined by studying their deformations under the applied lateral loads.

6.3.1 Overall Displacements and Drifts

Figure 6.5 shows the base shear roof displacement relationships for the three frames considered. The Figure shows that the three frames have equal lateral strength. The frame with poorly detailed joints experiences the highest roof displacements followed by the frame with well detailed joints until the yielding load is reached. On reaching the yield load, roof displacements are largely affected by the deformations of the columns, as will be discussed. This causes the effect of joint deformations on roof displacements to diminish. The fact that all the three frames reach almost the same base shear at yield indicates that the joint shear strengths for all the frames are sufficient for the framing members to reach their full yield capacity. The joint shear strength provided by the concrete contribution alone is sufficient to prevent a joint shear failure that would undermine the stability of the structure. This indicates an underestimation of the equation developed by the ACI committee 352 (1976) for calculating the joint shear strength provided by concrete. This observation is in agreement with the experimental findings of (Beres et al., 1992), as described in Chapter 1.

Figure 6.6 shows the distribution of story displacements along the height of

the structure at a lateral load of about 118.0 kN. The plots are shown at this load level to make an unbiased judgement by comparing the deflections at the same load level. The Figure indicates that the frame with poorly detailed joints incurred the highest story displacements. The frame with the rigid joints shows the least story deflections. The differences in the story deflections are more pronounced at the higher story levels.

Figure 6.6 also shows the distribution of the interstory drifts (ratio of maximum story drift to story height) over the height of the structure. All the frames show higher interstory drifts at the base which decrease gradually towards the top of the structure. The three frames show high level of interstory drifts which are in excess of 2% which is the maximum interstory drift allowed by NBCC 1995. The frame with poorly detailed joints shows the highest interstory drifts followed by that with the well detailed joints.

6.3.2 Failure Mechanisms

Figure 6.7 shows the plastic hinge distribution in the beams and the columns of the three frames. It is noticed that all of the plastic hinges have concentrated in the columns of the first two stories in all three frames considered. This is attributed to the fact that the flexural capacities of the beams are much higher than those of the columns. In the design of the frames, the effects of earthquake loads have been neglected which results in a strong beam-weak column frame configuration. Most of

the plastic hinges that have formed in the beams are mainly limited to those beams connected to the exterior columns. This is due to the lower demands on the interior beams, as opposed to the exterior. Finally, all the three frames have exhibited an undesirable strong beam weak column mechanism.

6.3.3 Joints Deformations

In this section, comparisons are made for the deformations of the joints along the heights of the structures. The joint deformations considered are the rotations resulting from shear and the fixed end rotations resulting from bond slip of beam bars in the joint panel region. The frame with rigid joints is excluded from the comparisons as there are no deformations in the joints. Figures 6.8 to 6.11 show the joint deformations along the columns C1, C2, C3, and C4 respectively. Figures 6.9 and 6.10 have two plots for the fixed end rotations to describe the rotations at the right and left side of each joint resulting from the right and left beams.

The Figures indicate that the shear deformations for the poorly detailed joints are always higher than those of the well detailed joints. On the other hand, poorly detailed joints have experienced less bond slip deformations. Usually, bond slip deformations are more pronounced in the interior joints as compared to the external ones. However, results of the studied frames reveal higher bond slip deformations for the exterior joints. This is due to the fact that beam reinforcement in the interior connections have not reached high strains to cause apparent fixed end rotations as is

the case for the exterior joints. The fact that most of the beam plastic hinges have occurred in the beams connected to the exterior columns supports this conclusion.

A more detailed study of the joint behavior can be done by comparing the base shear - joint deformations relationships for the poorly detailed and the well detailed joints. The joints selected are those in the first story since they experience the highest deformations as can be observed in Figures 6.8 to 6.11. Figure 6.12 shows the base shear - shear strain relationship for the joint J11. The Figure shows higher shear deformations for the poorly detailed joints. The difference in shear deformations between the poorly detailed and the well detailed joints gets higher as the base shear increases until a difference of about 100% in shear deformations is noticed at the base shear of 118 kN. Figure 6.12 also shows the base shear - fixed end rotation relationship for the same joint. It is noticed that at the base shear of about 40 kN the rate of increase in fixed end rotations for the well detailed joint starts to increase compared to the poorly detailed joint. It is interesting to know that at this same load level the cracking load is reached in the joint and the rate of increase in shear deformations in the poorly detailed joint starts to increase compared to the well detailed joint. The total joint rotation is the sum of the rotations due to shear and bond slip and it is clear that the total rotations of the poorly detailed joint are higher than those of the well detailed joint.

Figures 6.13 to 6.15 show the base shear-joint shear strain and base shear-fixed end rotations for the interior joints J12, J13, and the exterior joint J14. The

Figures show that the maximum shear deformations for the exterior joint J14 is the least as compared to the other joints. This is mainly due to the fact that this exterior joint has a higher axial compression load resulting from the lateral load application which causes higher compression loads on the east side of the frame. This compression load provides more confinement to the joint and thus lowers its shear deformations. The fixed end rotations for this joint, J14, are still higher than the internal joints due to higher strains in the beam bars as have previously been discussed.

6.3.4 Beams and Columns Deformations

The deformations in the beams and the columns are described by the maximum strains reached in their longitudinal reinforcement. A strain parameter, R, is used to indicate the level of local deformation in the beams and the columns. The strain ratios are defined as

$$R_b = \frac{maximum\ beam\ reinforcement\ strain}{yield\ strain} \tag{6.2}$$

$$R_c = \frac{maximum\ column\ reinforcement\ strain}{yield\ strain} \tag{6.3}$$

Figures 6.16 and 6.17 show the envelopes of the beam and column strain

ratios over the structures height. The figures show that the three frames experience similar levels of deformations. This is mainly due to the fact that the well detailed and the poorly detailed joints have maintained their integrity throughout the load history and have not caused significant changes in the force distribution in the frames. The Figures show that the beams experience high level of deformations only at the first story level while the columns deformations are still relatively high at the second story level. This is mainly due to the fact that the strength of the beams are higher than those of the columns.

6.4 DYNAMIC ANALYSIS

This section describes the response of the three story frame structures to earthquake excitations. The same frames in the previous section are used in this study. The frames are assumed to be fully fixed at their supports and all the supports are assumed to move in phase during earthquake motion. The masses of the tributary floor areas are assumed to be lumped at the beam column joints. The story masses are assumed to have both lateral and vertical inertia.

Damping is represented by a linear combination of the mass and initial stiffness. The damping coefficients are determined using the methodology of Clough and Penzin (1975) as follows;

$$\beta_m + \beta_o \omega_i^2 = 2 \omega_i \epsilon_i \qquad (6.4)$$

where

β_m, β_o = Mass and initial stiffness proportional damping factors respectively

ω_i = Frequency of i^{th} mode of vibration

ε_i = Damping ratio of the i^{th} mode of vibration

For this study, the first and second modes are used to determine the proportional factors β_m, β_o. The damping ratios of these two modes are assumed to be 5 percent of the critical. This value is considered to be appropriate for cracked reinforced concrete structures (Newmark and Hall, 1982).

The dynamic analysis of the frames subjected to earthquake excitations is carried out by solving the equation of motion using numerical step by step integration procedure. The integration time step used must not be too large to result in high unbalanced loads nor too small to be time consuming. For all the analyses that have been carried out herein, integration time step of 0.005 seconds is found to be appropriate. The computational time needed for 60 seconds of earthquake excitation for this structure using a Pentium personal computer of 75 MHZ is about eight hours.

The fundamental period of the frames is analytically predicted using a simple procedure. A unit load is applied at each story level and the deflections are recorded at these levels. These deflections are used to build the structures flexibility matrix and to calculate the structures vibrational characteristics. The fundamental period of the structure with deformable joints, well detailed and poorly detailed joints, is found to be 0.99 seconds while that for the one with rigid joints is 0.94 seconds. This means

that including the joints flexibility reduces the stiffness of the structures and leads to lengthening of the vibrational period of the structure by about 5.3%. The generally high fundamental periods of these GLD structures indicates high flexibility of these types of moment resisting frames.

6.4.1 Selection of Earthquake Records

For the dynamic analysis, two different acceleration records are considered as input ground motions; El Centro, California, 1940, S-E component and San Fernando, California, 1971, N-E. component. The properties of the two selected earthquakes are summarized in Table 6.1. These earthquake records are selected since their predominant periods of vibration are close to the fundamental periods of the structures studied. The response spectra for the considered earthquakes are shown in Figure 6.18. The fundamental periods of the frames are also plotted in the Figure to indicate the location of the structural period on the response spectra of the selected earthquakes. The earthquakes records are scaled to a peak ground acceleration of 0.3g to excite the structure well into the inelastic range of the response. Figure 6.19 shows the scaled ground motions that will be used in analysis.

6.4.2 Roof Displacement Time Histories

Figures 6.20 and 6.21 show the roof displacement time histories for the frames when subjected to El Centro and San Fernando earthquakes. The response of the

frames subjected to El Centro earthquake indicates that they have experienced inelastic deformations. A maximum roof displacement of approximately 156 mm is exhibited by the frame with poorly detailed joints after 5 seconds of the El Centro ground motion. This displacement is beyond the elastic limit as indicated by the pushover analysis on Figure 6.5. The frame with well detailed joints and the one with rigid joints have exhibited a maximum roof displacement of approximately 134 and 132 mm respectively. The poor detailing of the joints has thus resulted in an increase of about 16% in the frame roof displacements over the one with well detailed joints and about 18% over the one with rigid joints. All three frames however have incurred a residual displacement at the end of the record due to their inelastic response.

The response of the frames to San Fernando earthquake is less severe than that due to El Centro. The maximum roof displacement for the frame with poorly detailed joints is about 83 mm. The frames with well detailed joints and rigid joints show maximum roof displacements of about 77 and 74 mm respectively. These displacements are equivalent to an increase in roof displacement for the frame with poorly detailed joints by 8% and 12% over the displacements of the frames with well detailed joints and rigid joints respectively.

6.4.3 Envelopes of Story Shear and Failure Mechanisms

Figures 6.22 and 6.23 show the maximum predicted story shear for the frames as a percent of the weight of the structures due to both earthquakes. The Figures

show that the frame with rigid joints is able to attract the highest loads when subjected to both earthquakes as compared to the frames with well detailed joints and poorly detailed joints. The story shears for all the frames are higher at the base and decrease gradually towards the top indicating a predominant vibration in the first mode. The maximum base shear reached is about 8% of the building weight. The shear force demands on the beams and the columns are always less than the capacities of the members thus their failure mechanisms are governed by their flexural capacities.

Figures 6.24 and 6.25 show the plastic hinge distribution in the beams and the columns of the frames. Inspection of the frames reveals a widespread yielding in the columns due to their lower flexural capacities. The yielding of the beams are limited to those in the first two stories. The distribution of plastic hinges in all the three frames are very similar.

6.4.4 Envelopes of Lateral Displacements and Interstory Drifts

The envelopes of maximum displacements for the frames are shown in Figures 6.26 and 6.27. Two common observations are noticed from the two sets of graphs. The first observation is that the maximum lateral displacements for the frame with poorly detailed joints are always higher than the one with well detailed joints. The second observation is that the frames with deformable joints show less deflection at the lower stories of the structure as compared to the frame with rigid joints. Towards the top of the structure, the deflections of the frames with deformable joints gets

higher. The reason for such a distribution is attributed to the shear and bond slip deformations of the beam column joints which are more pronounced at the lower stories as will be discussed later.

Figures 6.28 and 6.29 show the envelopes of interstory drifts. The interstory drift distributions caused by both earthquakes appear to be different. The maximum interstory drifts for the frames with deformable joints are shifted from the base to the first story when subjected to EL Centro earthquake. This is due to the joints deformation. The interstory drift distribution do not follow the same trend in the San Fernando earthquake because the El Centro earthquake has generally caused more deformations in the structure than the San Fernando earthquake. Thus the effect of the joints deformations is less influential on the interstory distribution. The frame with poorly detailed joints has exhibited higher interstory drifts than the one with well detailed joints for the two earthquakes.

The frame with rigid joints exhibits the maximum interstory drifts at the base of the structure for the two earthquakes as can be expected. This level of interstory drift is the highest as compared to the two other frames. This is due to the fact that the frame with rigid joints is subjected to higher base shear forces as have been explained in the previous section. Moreover the shift of the maximum interstory drifts to higher stories in the frames with well detailed and poorly detailed joints have served in reducing the maximum interstory drifts.

6.4.5 Envelopes of Joint Deformations

Figures 6.30 and 6.31 show the envelopes of joint shear deformations for the structures studied. The Figures show that providing adequate shear reinforcement in the joints have significantly reduced their shear deformations. An increase in joint shear deformations of about 100% and 110% is noticed for the San Fernando and El Centro earthquakes for the frames with poorly detailed joints as compared to the well detailed joints. The maximum shear deformations decrease gradually towards the top of the structure.

It is noticed that shear deformations predicted under earthquake loads are much higher than those resulting from the pushover analysis. This is due to the fact that the shear rigidities of the joints have significantly deteriorated due to the cyclic load applications.

Figures 6.32 and 6.33 show the envelopes of fixed end rotations resulting form bond slip in the joint panels for the structures studied. The figures show that the bond slip deformations are more pronounced for the frames with well detailed joints. The joints with higher bond slip deformations have exhibited lower shear deformations. This is in agreement with the results of the pushover analysis.

6.4.6 Envelopes of Beam and Column Deformations

Figures 6.34 and 6.35 show the envelopes of maximum deformations in beams of the frames studied. The deformations are expressed in terms of maximum strains

reached in the beam bars as have been explained previously. The Figures show that the frame with rigid joints exhibits the highest beams deformations and the frame with poorly detailed joints experience the lowest beam deformations. The joints deformations, which allow for the rotations between the beams, have alleviated the demands on the beams. Moreover, inclusion of the beam column joints as another source of energy dissipation have helped reduce the demands on the other members of the structure. The higher strains in the beams reinforcement of the frame with well detailed joints explains the reason for the higher bond slip deformations that have been experienced by these frames.

Figures 6.36 and 6.37 show the envelopes of maximum deformations in the columns of the frames studied. The Figures show that the columns deformations for the frame with well detailed joints are higher at the first story and are lower at the upper stories as compared to the other frames. The frame with poorly detailed joints shows higher deformations at the top and lower at the bottom as compared to the other frames. The columns deformations for the frame with rigid joints are slightly higher than the other two frames under the effect of El Centro earthquake. The difference is more pronounced in the San Fernando earthquake. The reason for that can be attributed to the higher base shear experienced by the frame with rigid joints as have been previously explained.

6.5 CONCLUSIONS

This Chapter includes the analysis of three gravity load designed reinforced concrete frames; one with poorly detailed joints having no joint shear reinforcement, one with well detailed joints having adequate joint shear reinforcement and one with rigid joints. Pushover analyses and time history analyses are conducted on these frames. Results of the pushover analyses shows that the three frames have equal lateral strength since the joint capacities are sufficient to transmit the shear forces without failure. This result is in agreement with available experimental data. The frame with poorly detailed joints shows higher shear deformations and lower bond slip deformations as compared to the frame with well detailed joints. The results of the pushover analyses also show higher deflections and interstory drifts for the frames with deformable joints as compared to the frame with rigid joints.

Dynamic analyses show a slight increase in the periods of vibration for the frames with deformable joints as compared to that with rigid joints. The time history analyses show more pronounced joint shear deformations, as compared to the pushover analyses, due to the degradation of the joint shear rigidities under reversed cyclic load applications. The joint deformations in the frames with deformable joints increase their lateral deflections as compared to the frame with rigid joints. The frame with poorly detailed joints shows the highest deflections. The joint deformations shift the interstory drifts to their maximum values from the base to the first story. The high

joint shear deformations in the frame with poorly detailed joints result in lower demands on the beams and thus lower bond slip deformations in the joint region. The frame with rigid joints is able to attract more loads due to their higher stiffness as compared to the other frames.

Finally, it must be noticed that the results presented in this Chapter are drawn from the limited analyses on a specific frame with specific earthquakes. A more comprehensive study is needed to establish general conclusions on the characteristic behavior of gravity load designed structures.

Table 6.1 Properties of selected earthquakes

Earthquake	Site	Magnitude	Comp.	PGA A(g)	PGV V(m/s)	A/V
Imperial Valley, California	El Centro	6.6	S00E	0.348	0.334	1.04
San Fernando, California	L.A.	6.4	N37E	0.199	0.167	1.19

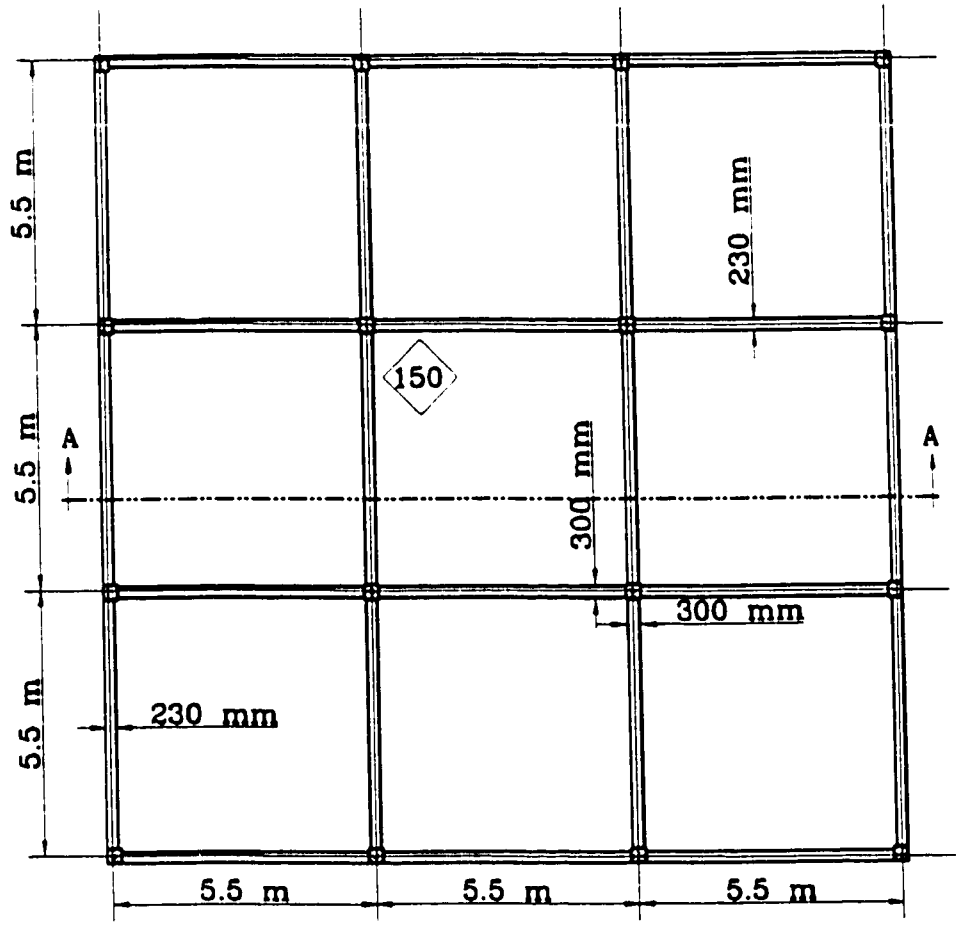

All columns are 300x300 mm.
All beams are 230x450 mm.
Slab thickness is 150 mm.

Figure 6.1 Typical floor plan

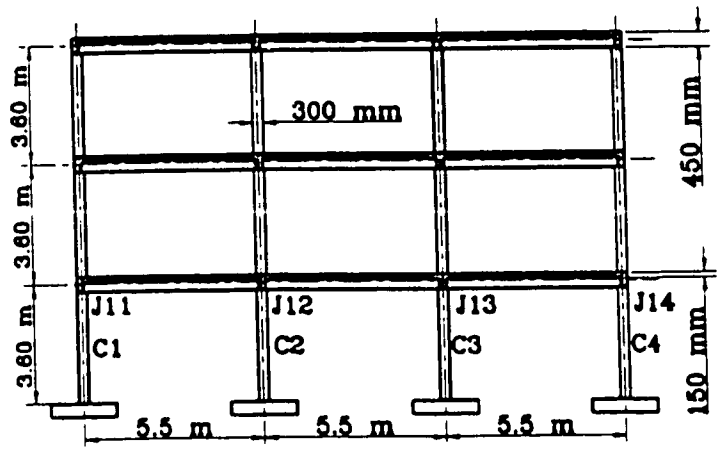

(a) Sectional elevation A–A

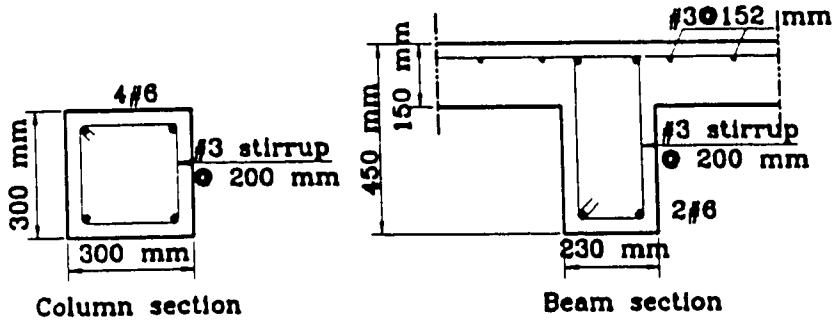

(b) Cross section details

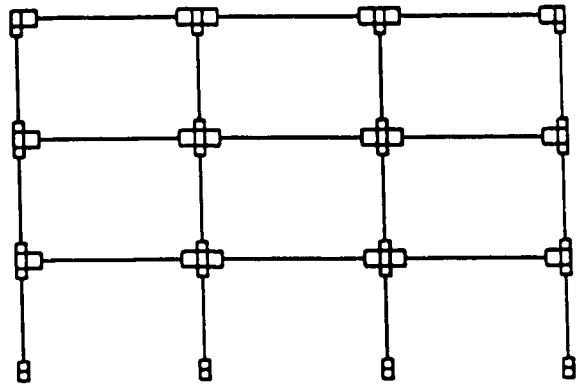

(c) Analytical model

Figure 6.2 Details of analyzed frame

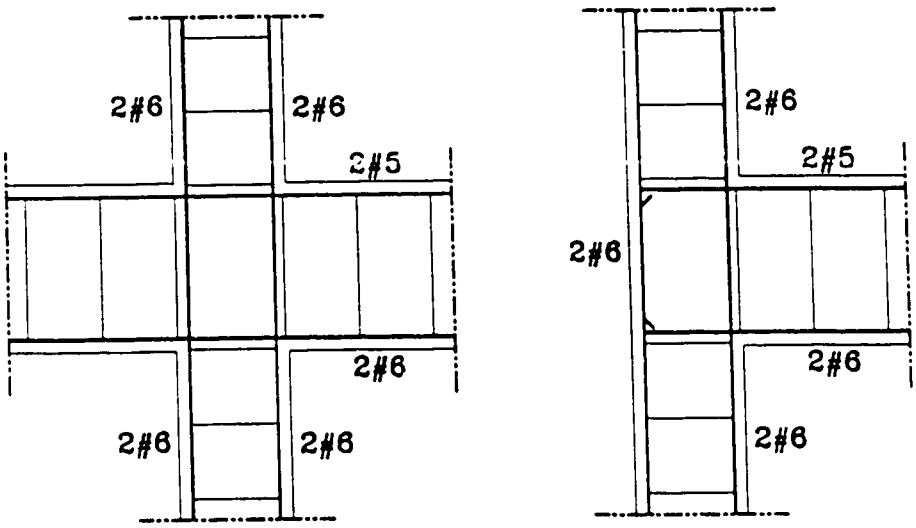

(a) Typical interior and exterior joints with no joint shear reinforcement

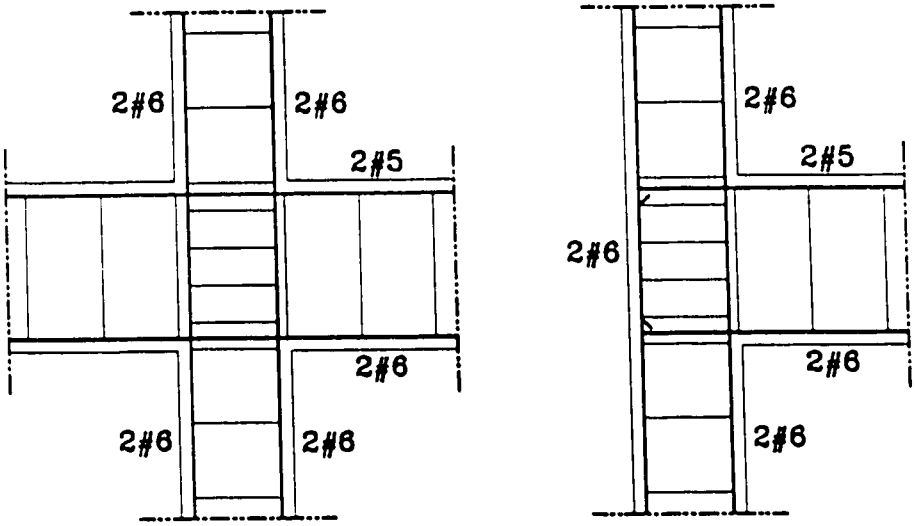

(b) Typical interior and exterior joints with joint shear reinforcement

Figure 6.3 Analyzed beam-column joints configurations

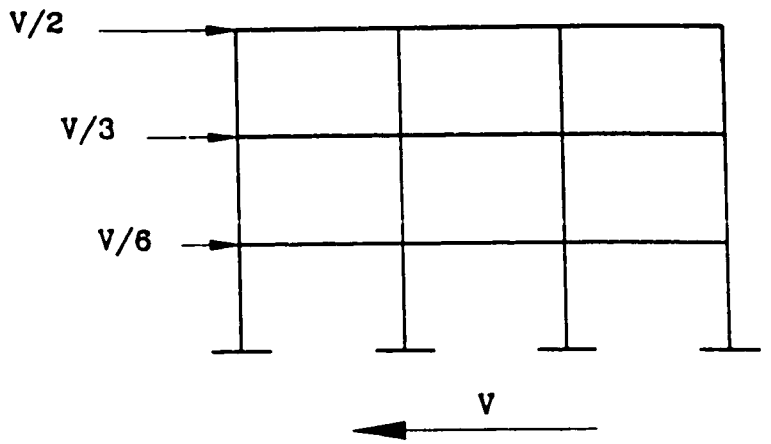

Figure 6.4 Lateral load distribution for pushover analysis

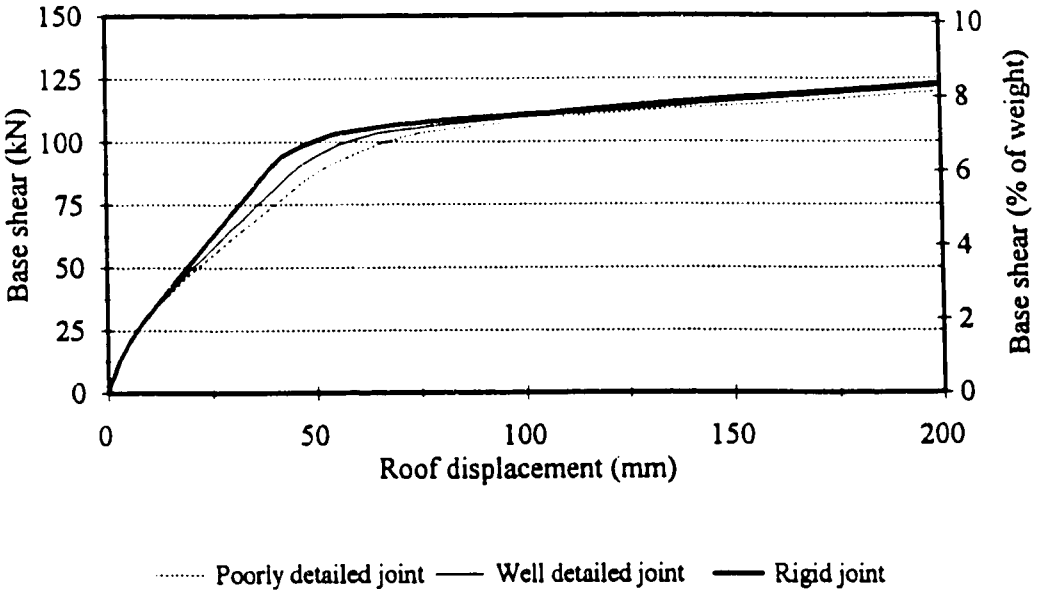

Figure 6.5 Base shear roof displacement relationship due to pushover loading

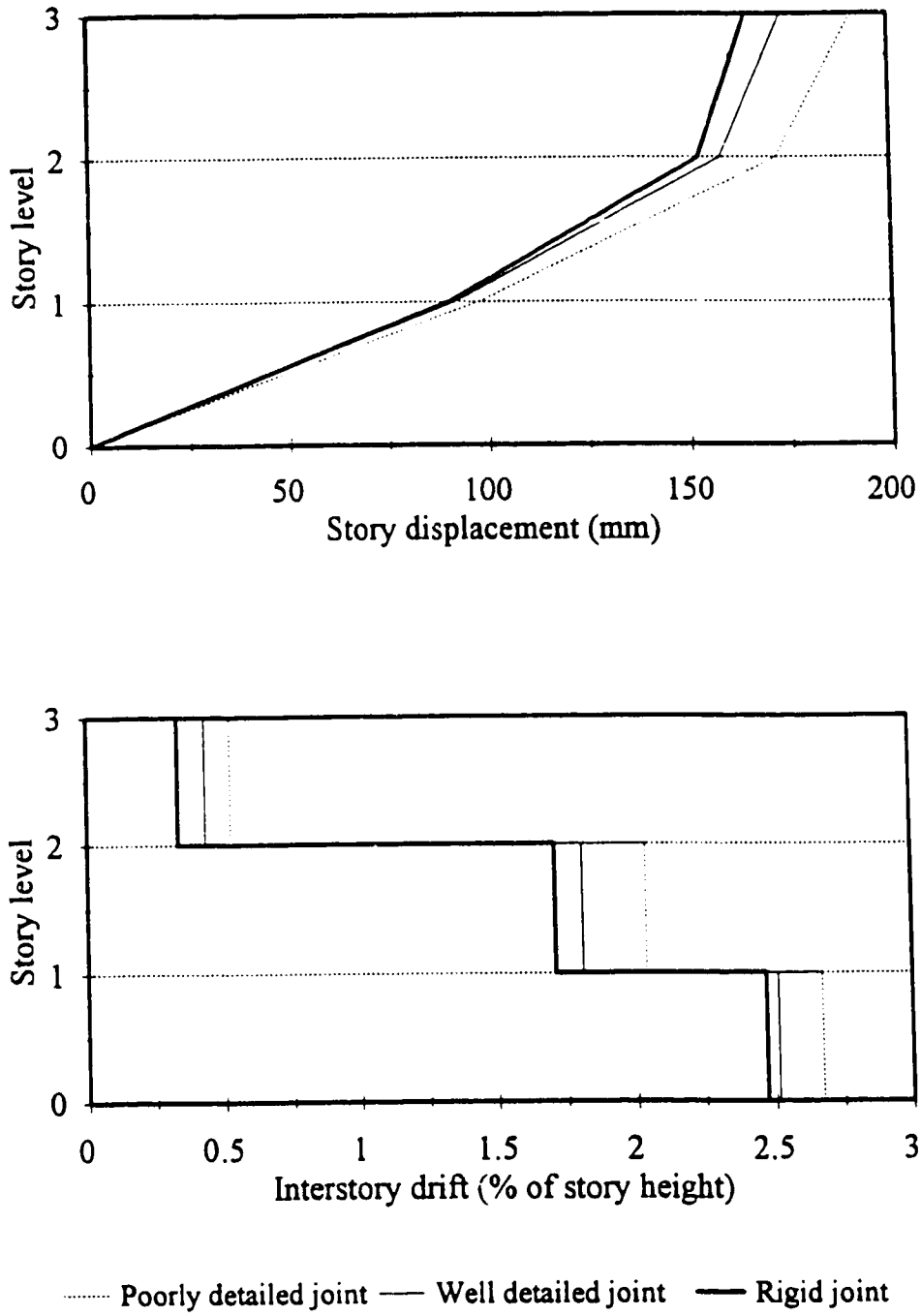

Figure 6.6 Maximum story displacements and interstory drifts due to pushover loading

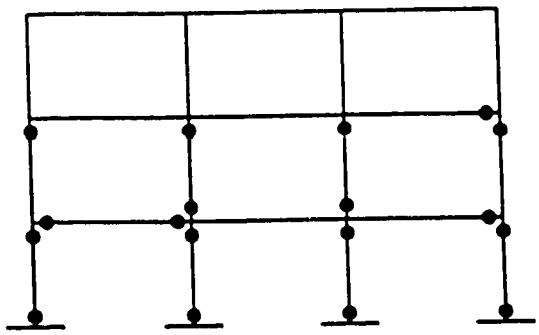

Frame with poorly detailed joints

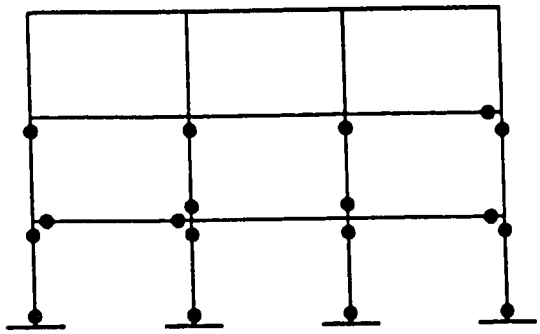

Frame with well detailed joints

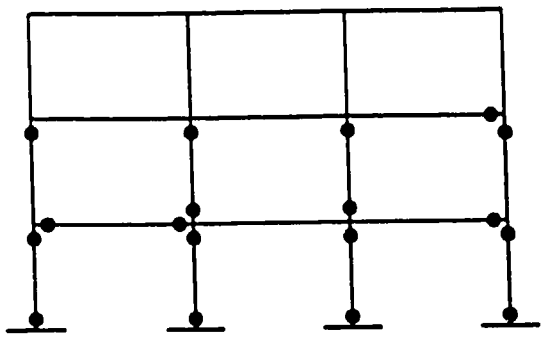

Frame with rigid joints

Figure 6.7 Plastic hinges formation due to push over loading

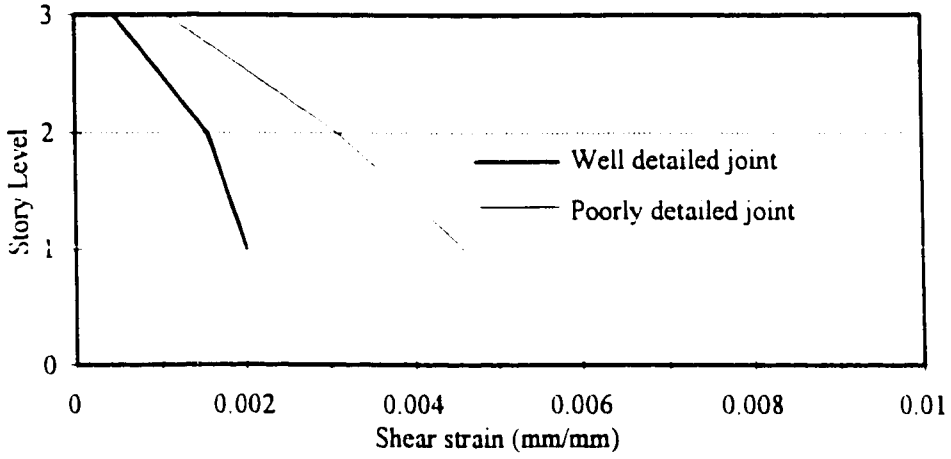

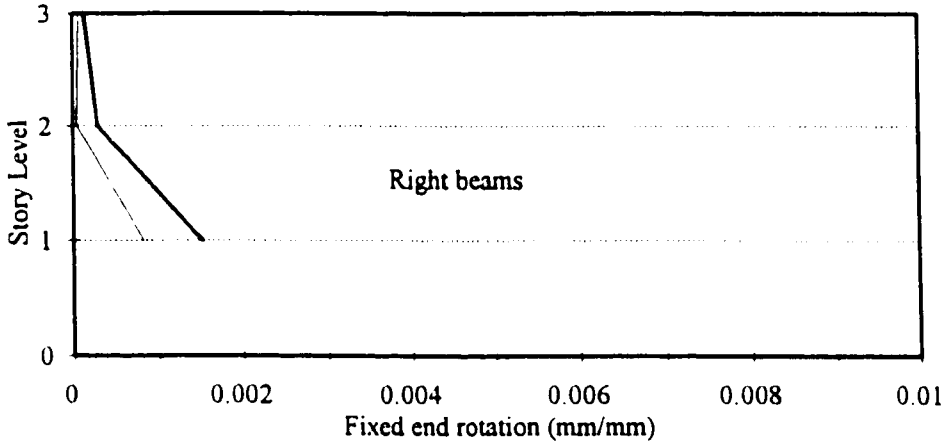

Figure 6.8 Envelopes of joint deformations for connections on column C1 due to pushover loading

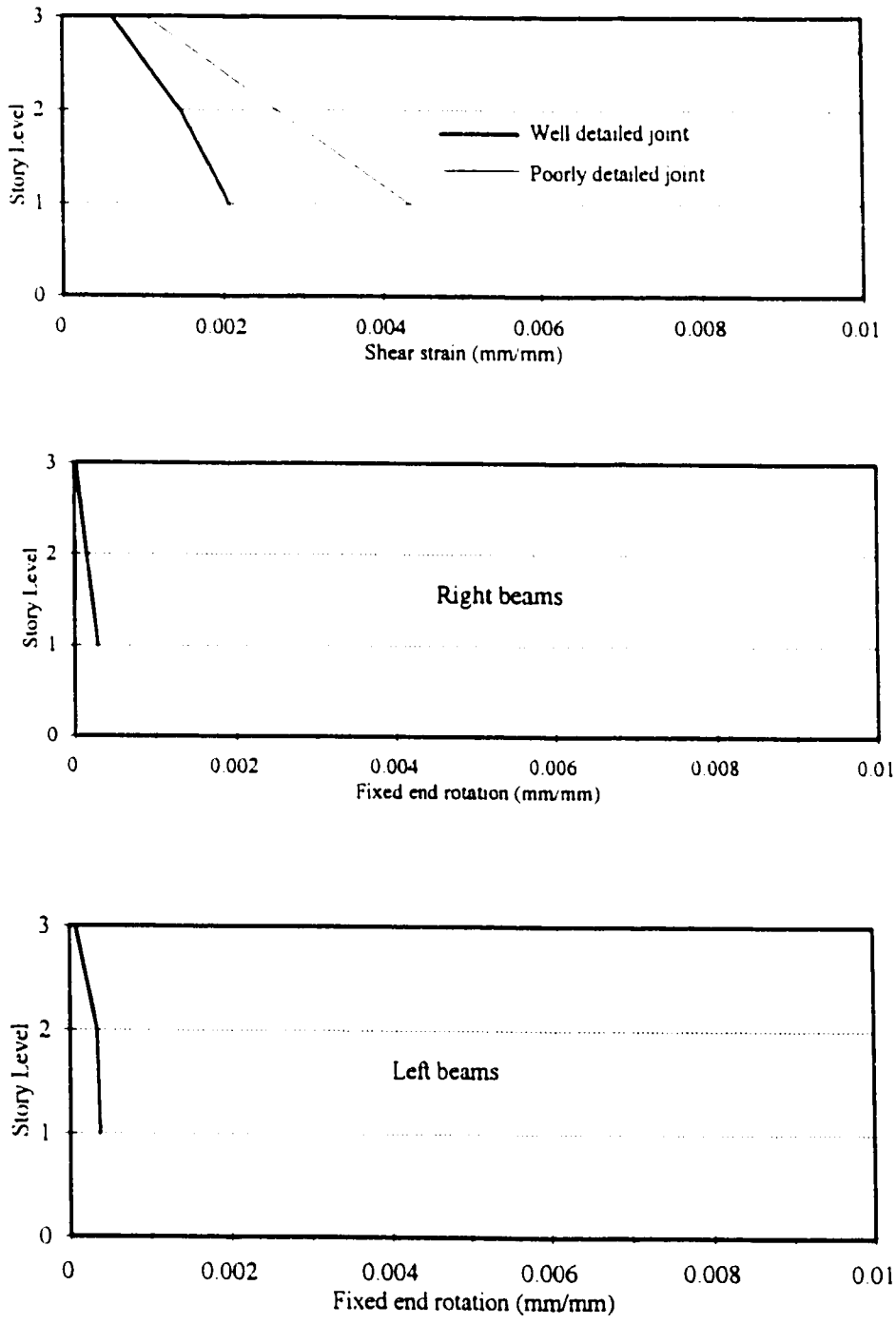

Figure 6.9 Envelopes of joint deformations for connections on column C2 due to pushover loading

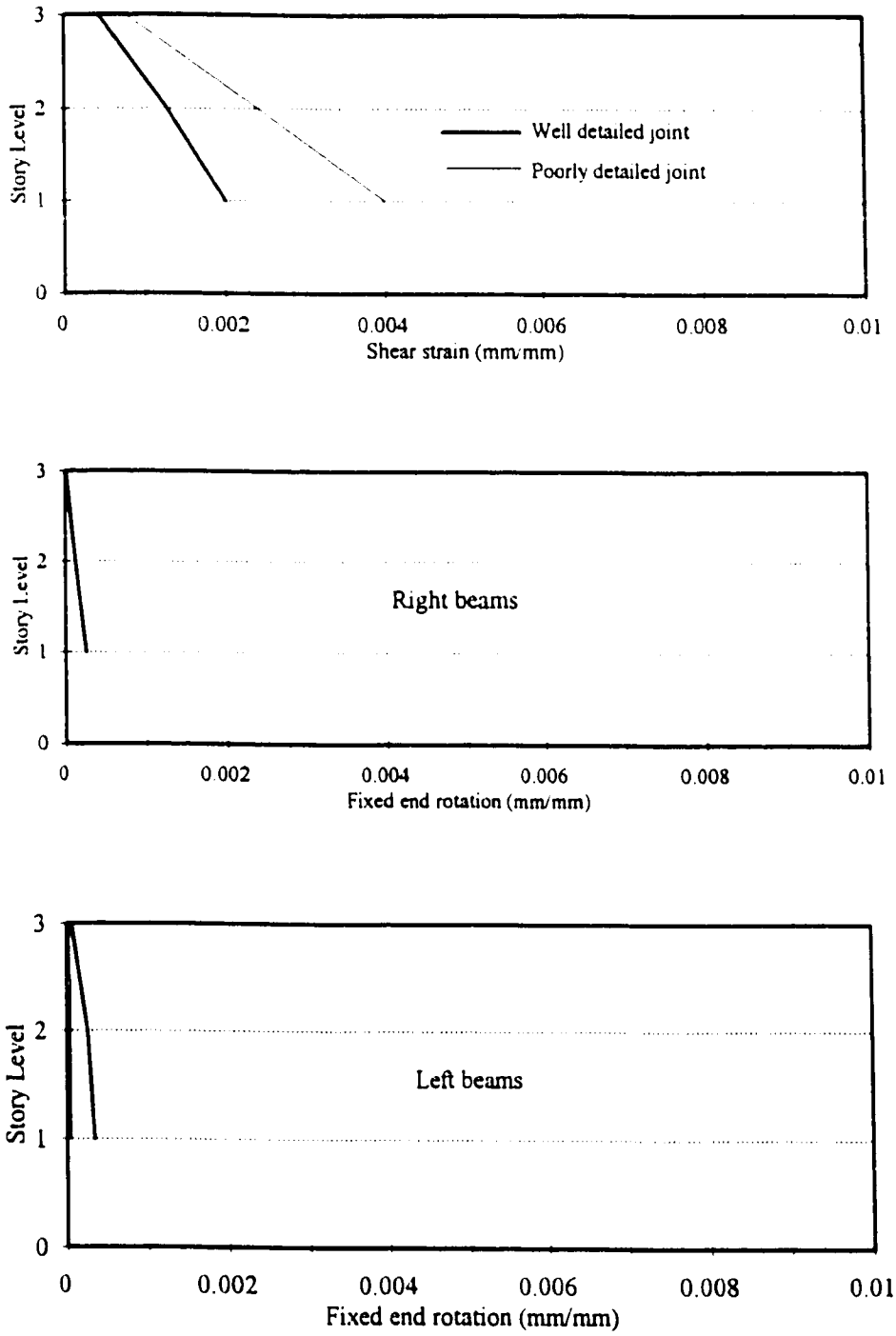

Figure 6.10 Envelopes of joint deformations for connections on column C3 due to pushover loading

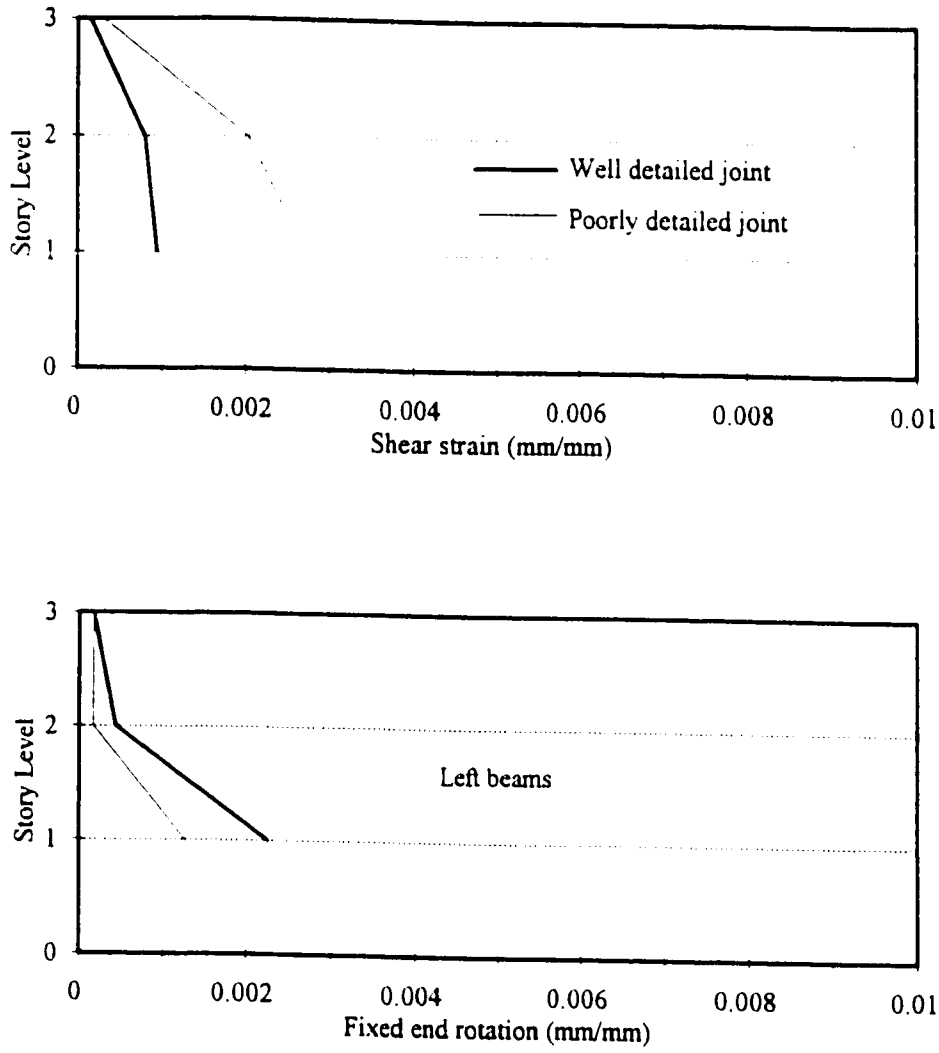

Figure 6.11 Envelopes of joint deformations for connections on column C4 due to pushover loading

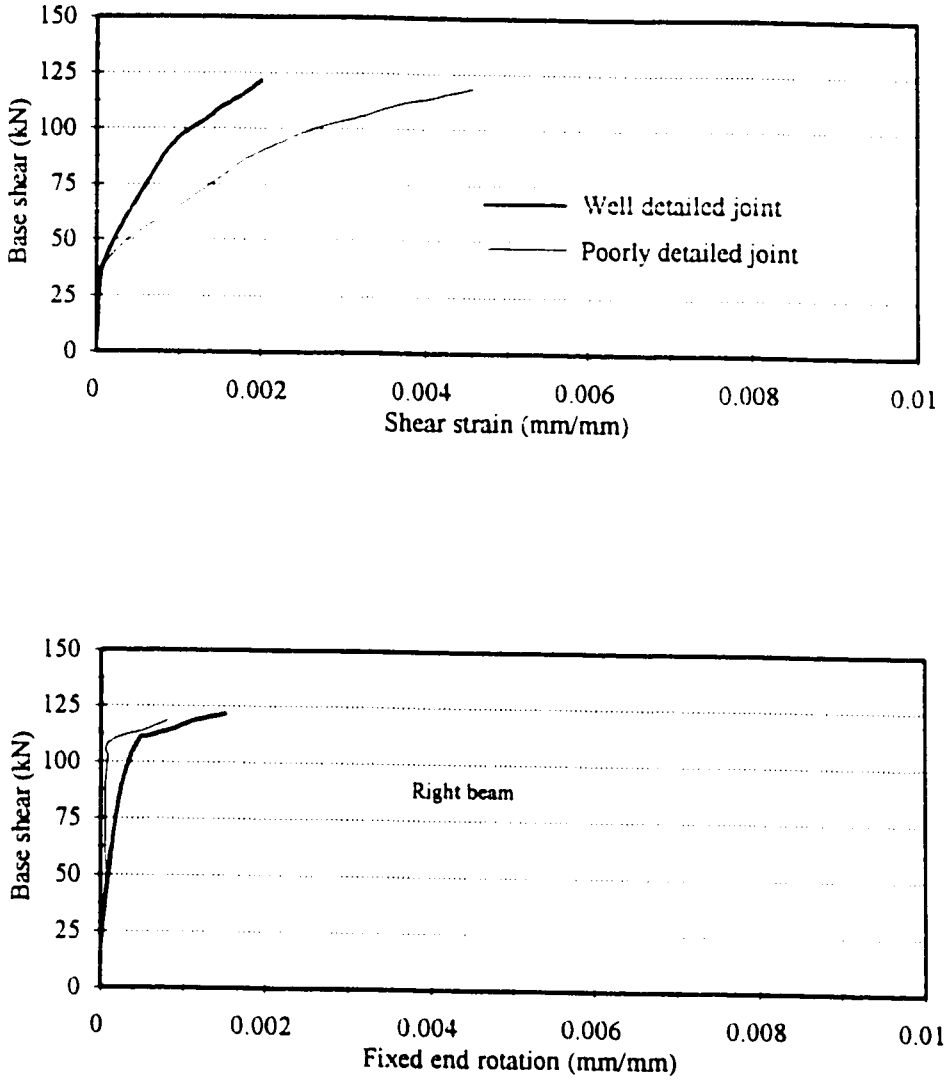

Figure 6.12 Base shear joint deformation relationships for joint J11 due to pushover loading

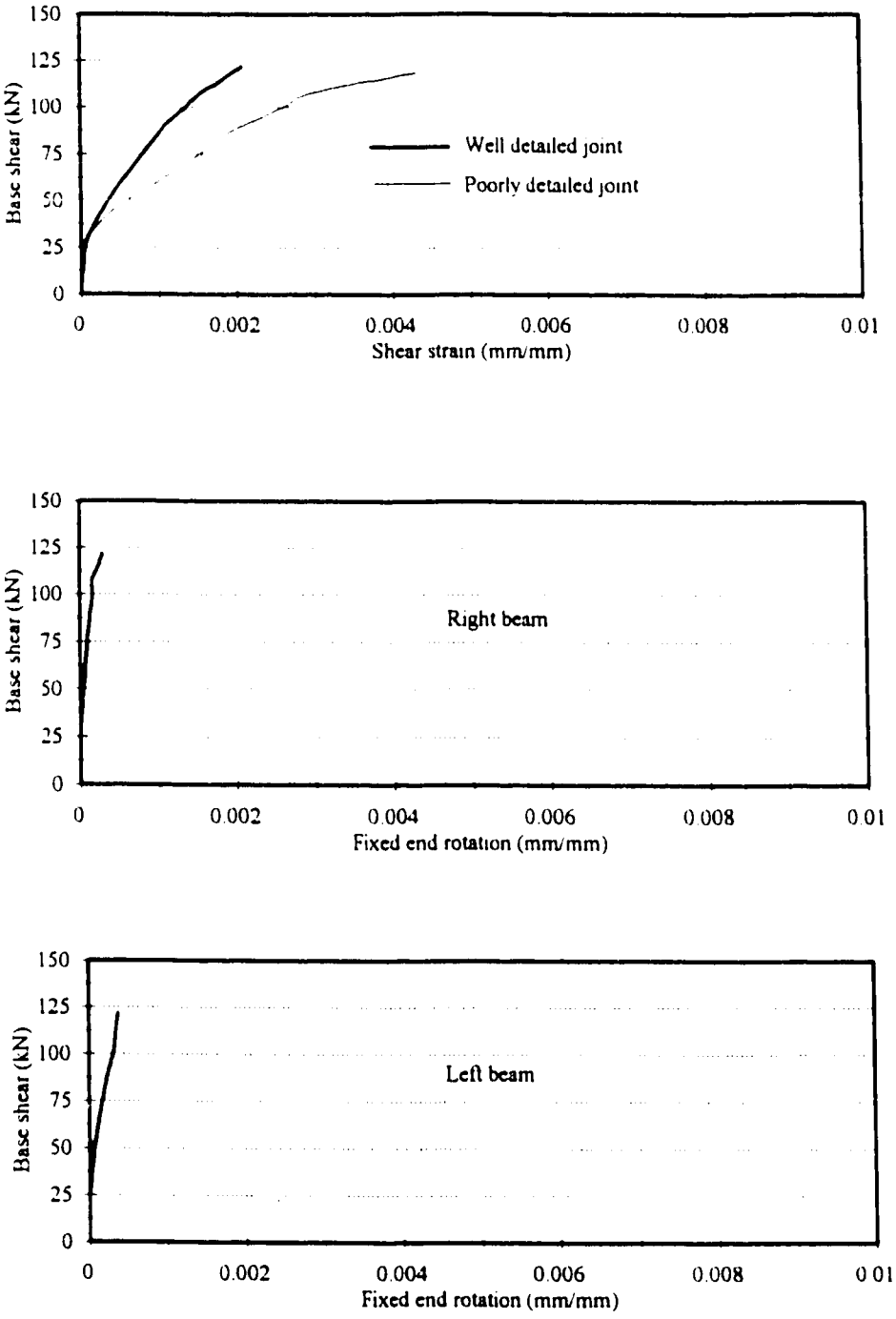

Figure 6.13 Base shear joint deformation relationships for joint J12 due to pushover loading

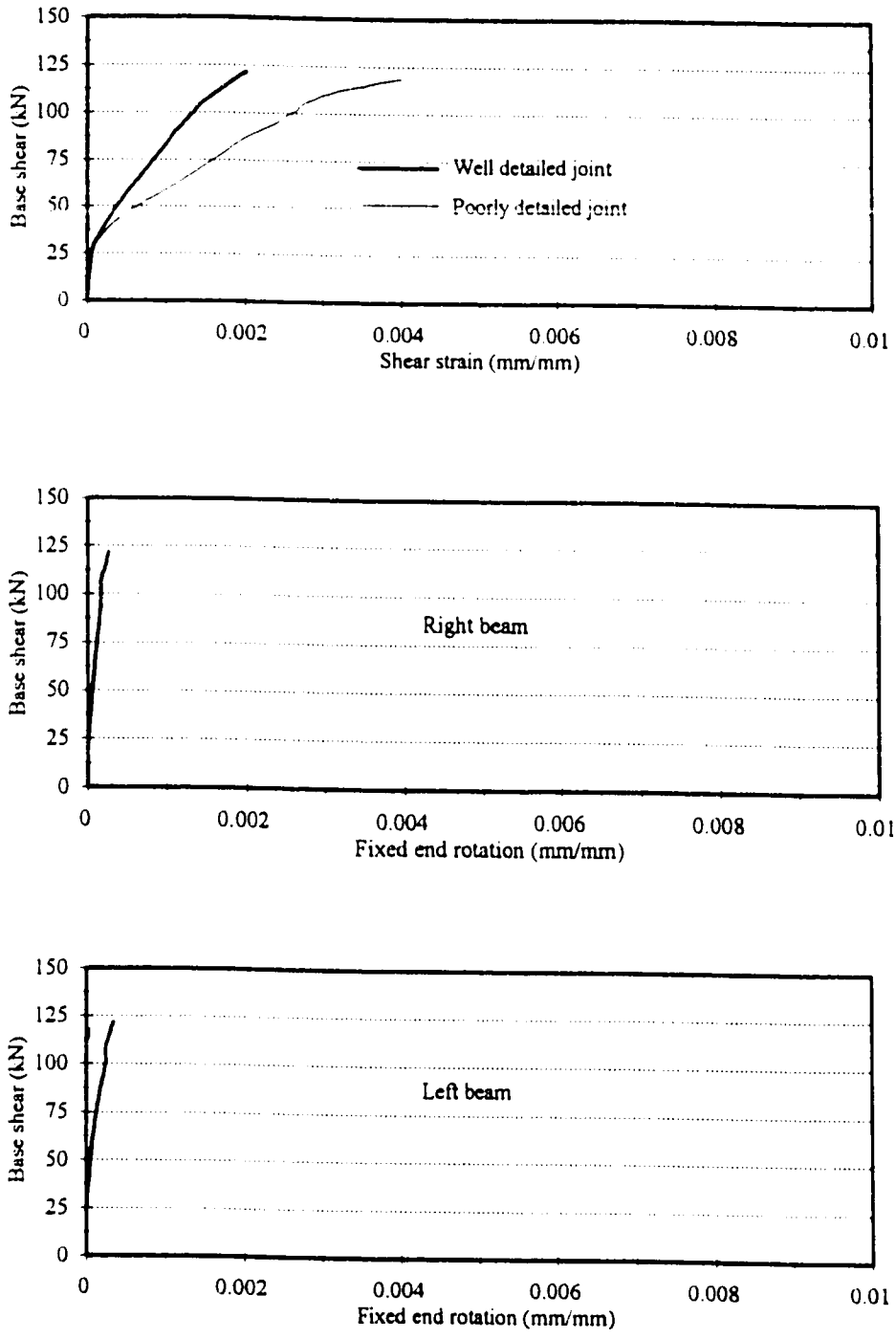

Figure 6.14 Base shear joint deformation relationships for joint J13 due to pushover loading

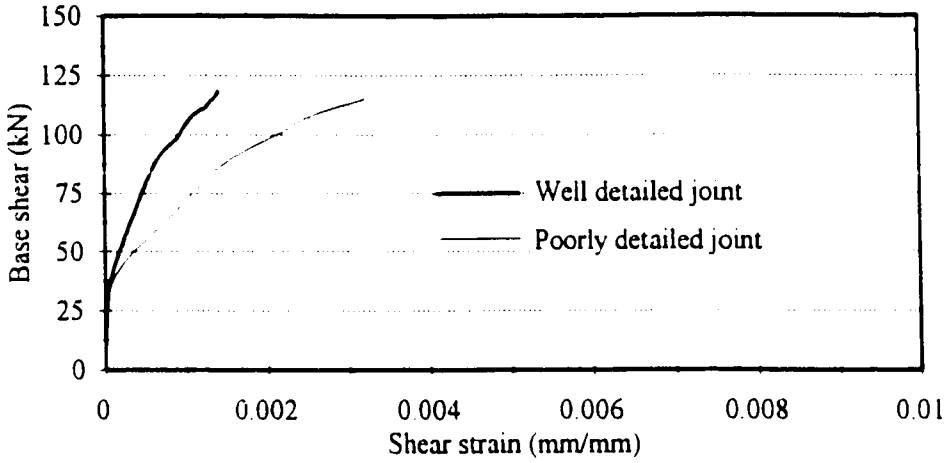

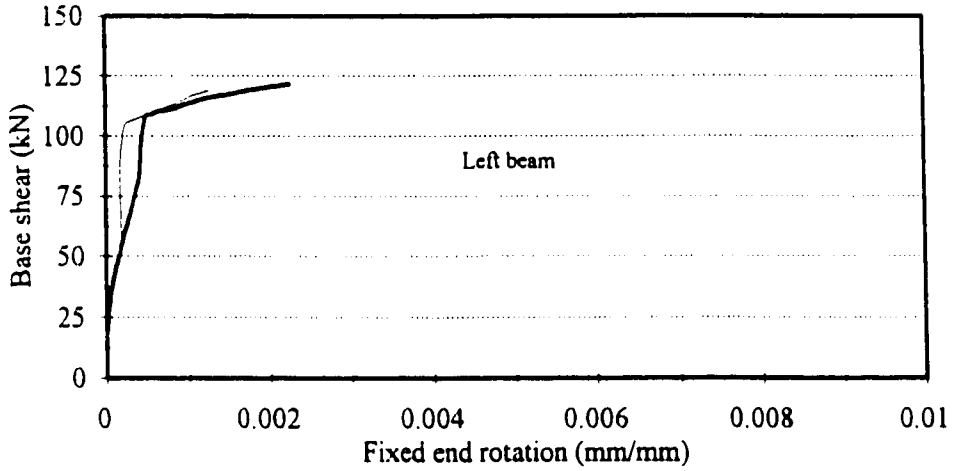

Figure 6.15 Base shear joint deformation relationships for joint J14 due to pushover loading

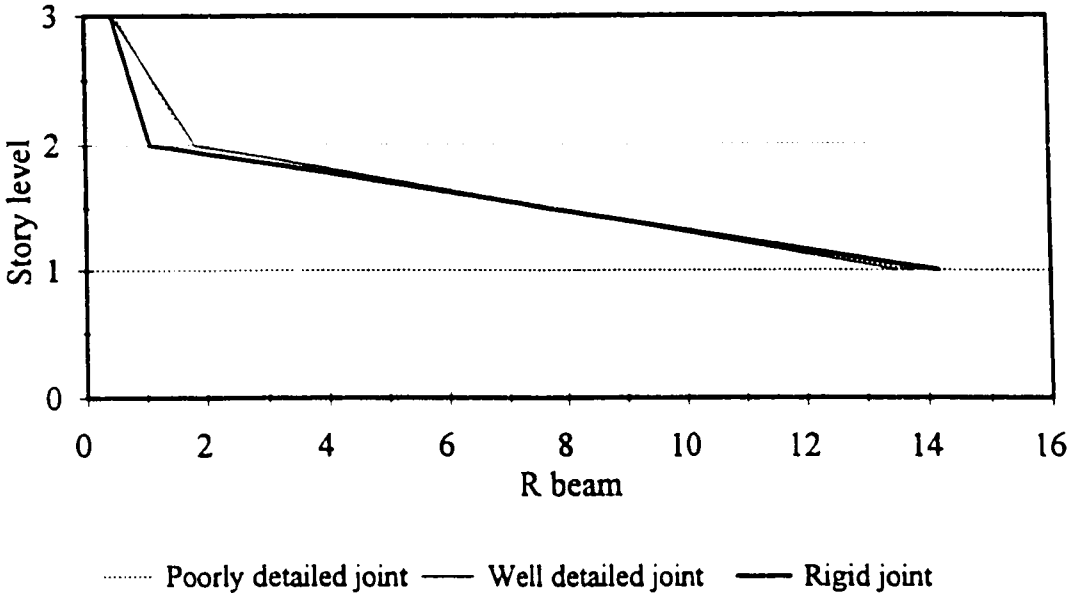

Figure 6.16 Envelopes of beam strain ratio due to pushover loading

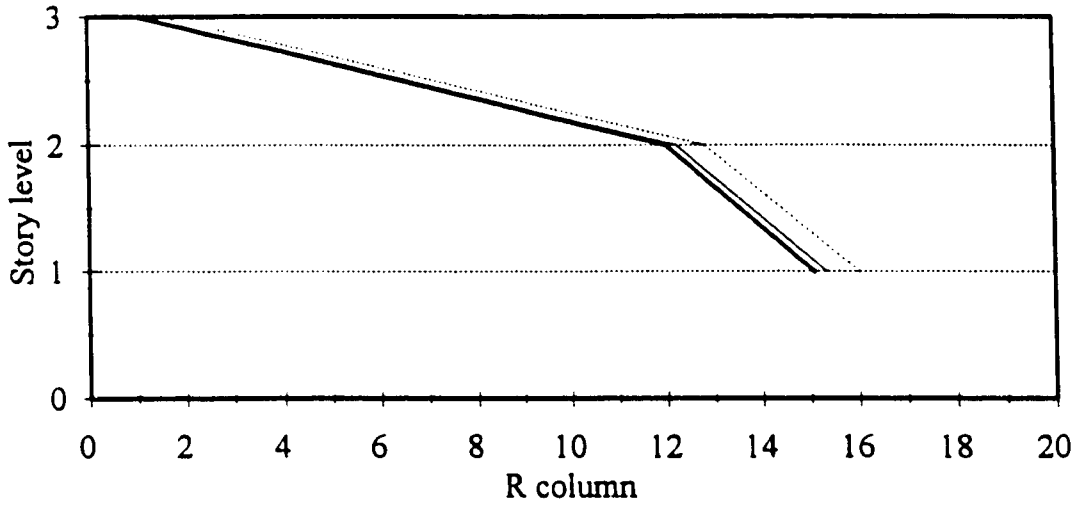

Figure 6.17 Envelopes of column bar strain ratio due to pushover loading

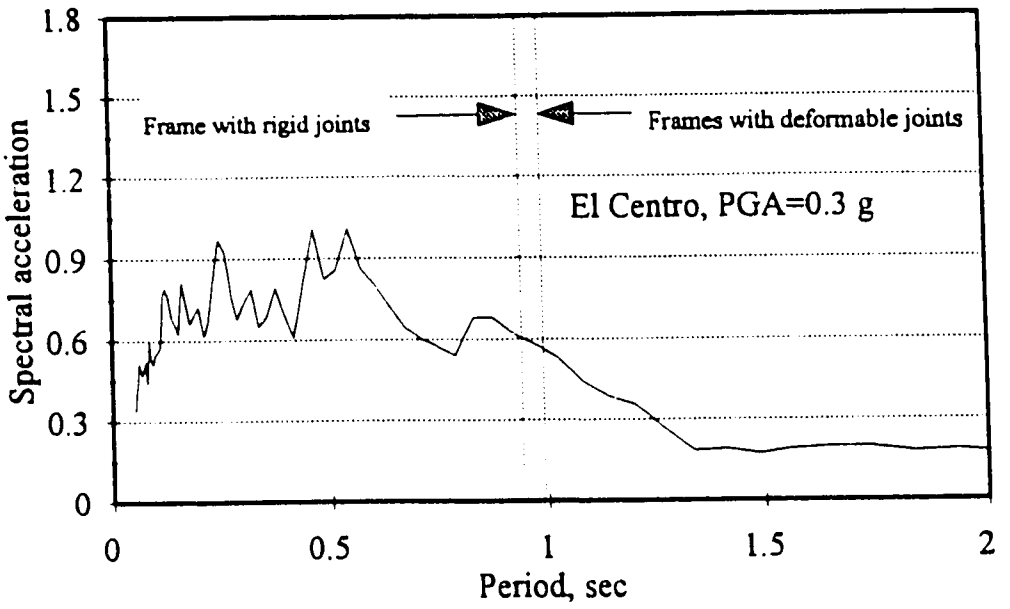

(a) El Centro Earthquake

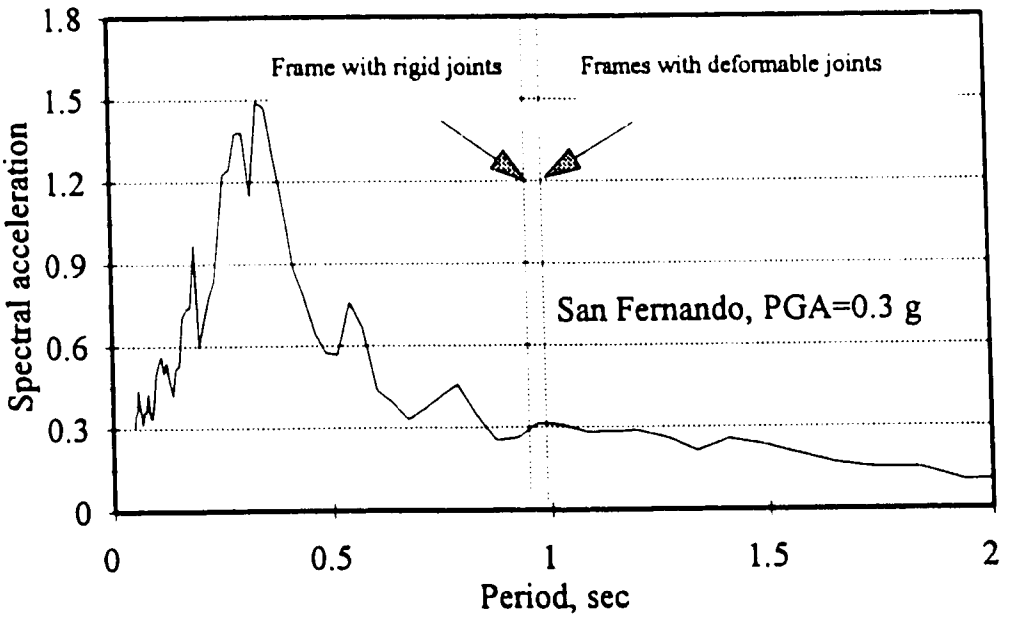

(b) San Fernando Earthquake

Figure 6.18 Response spectra for selected earthquakes

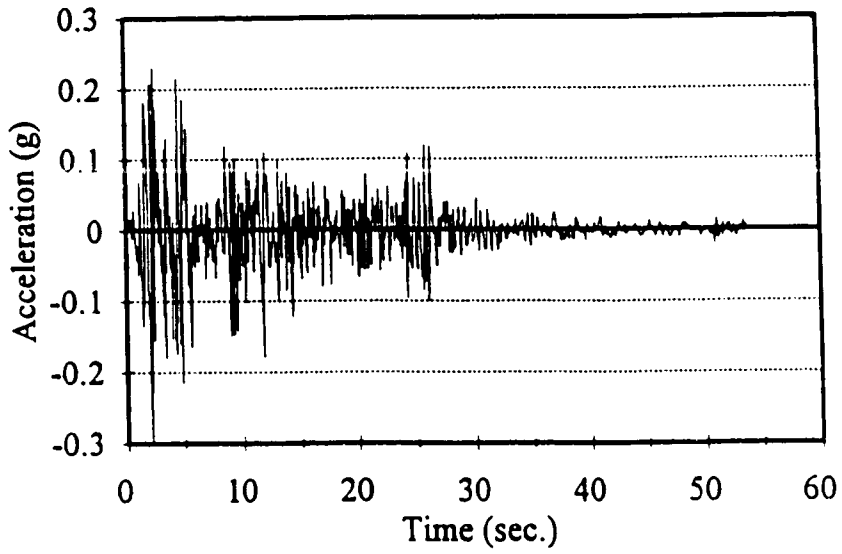

(a) El Centro Earthquake

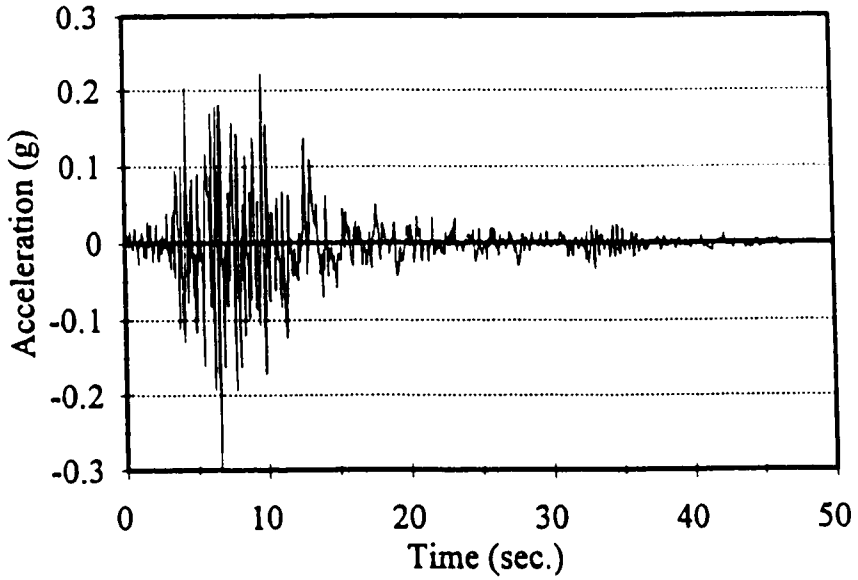

(b) San Fernando Earthquake

Figure 6.19 Scaled acceleration time histories for selected earthquakes

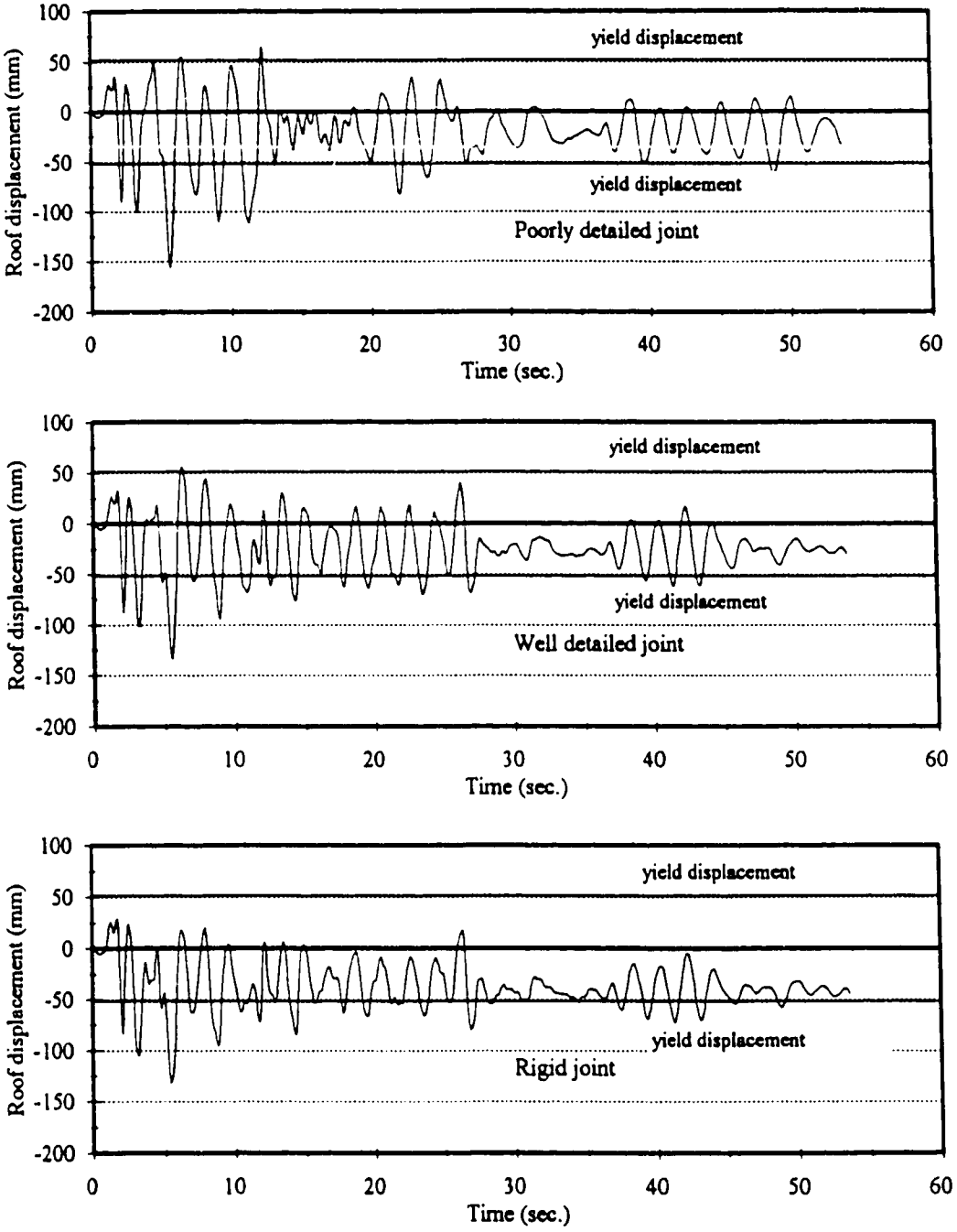

Figure 6.20 Roof displacement time histories due to the El Centro earthquake

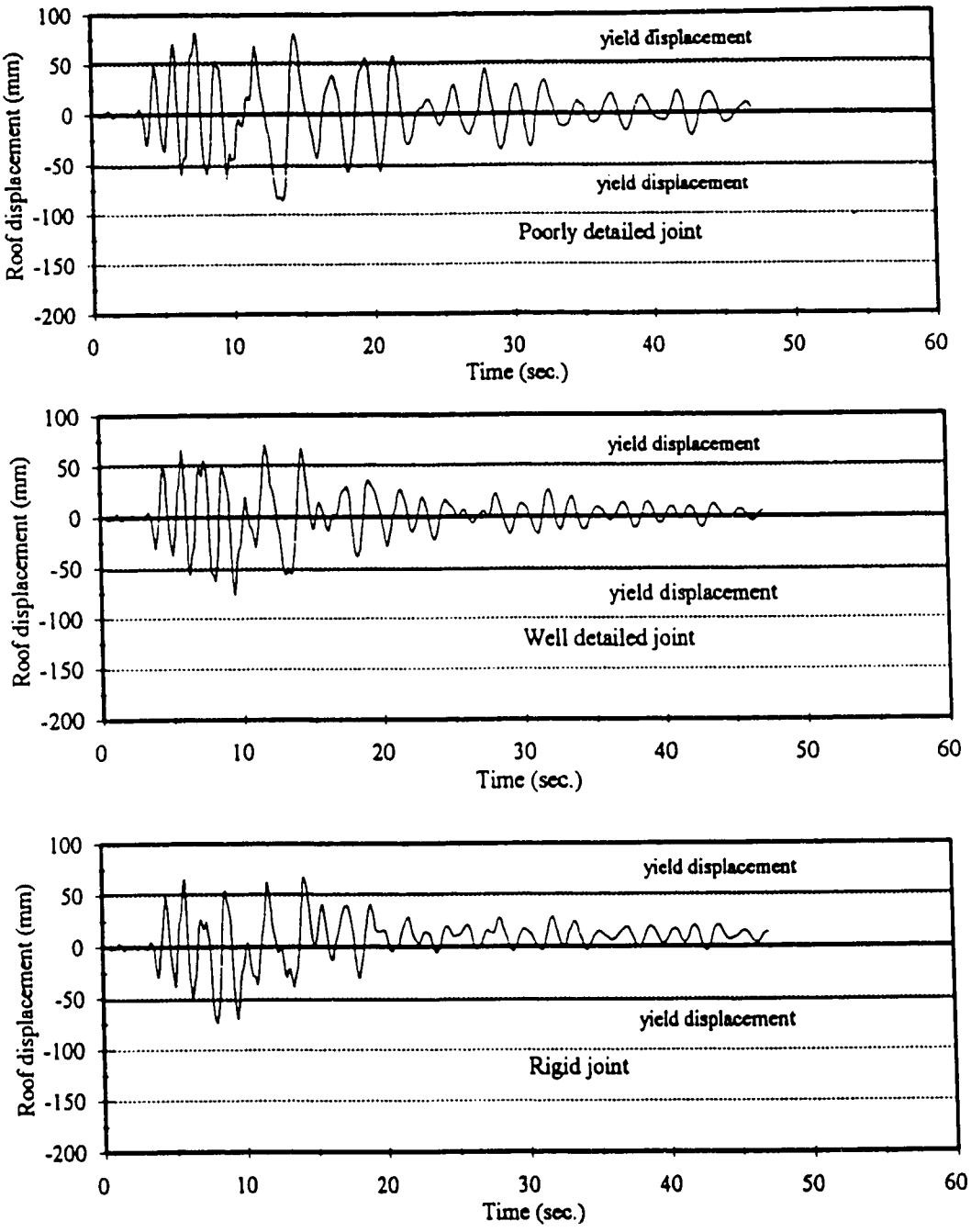

Figure 6.21 Roof displacement time histories due to the San Fernando earthquake

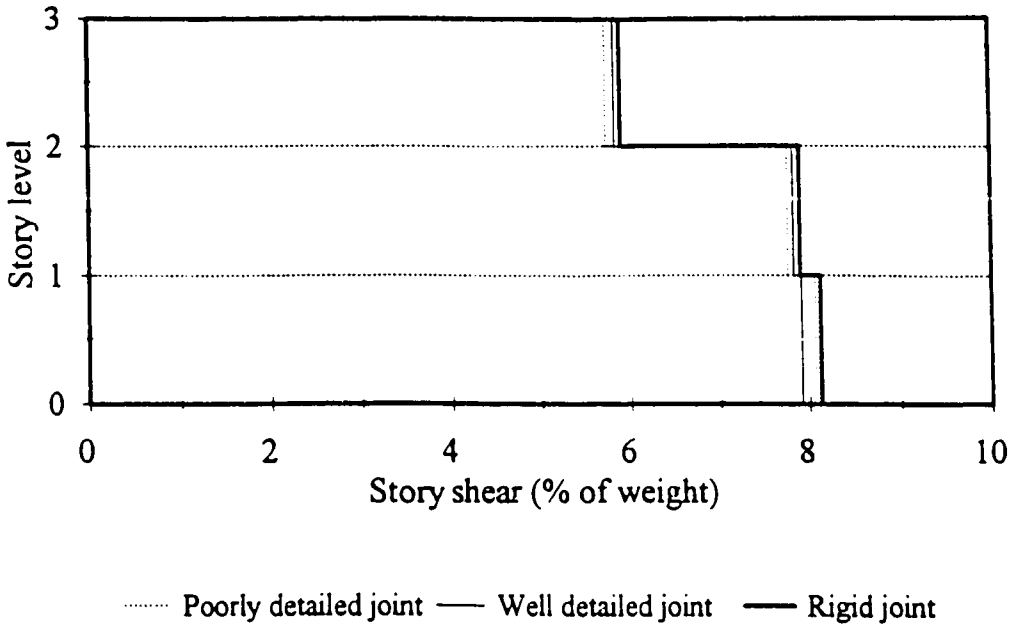

Figure 6.22 Maximum story shear force due to El Centro earthquake

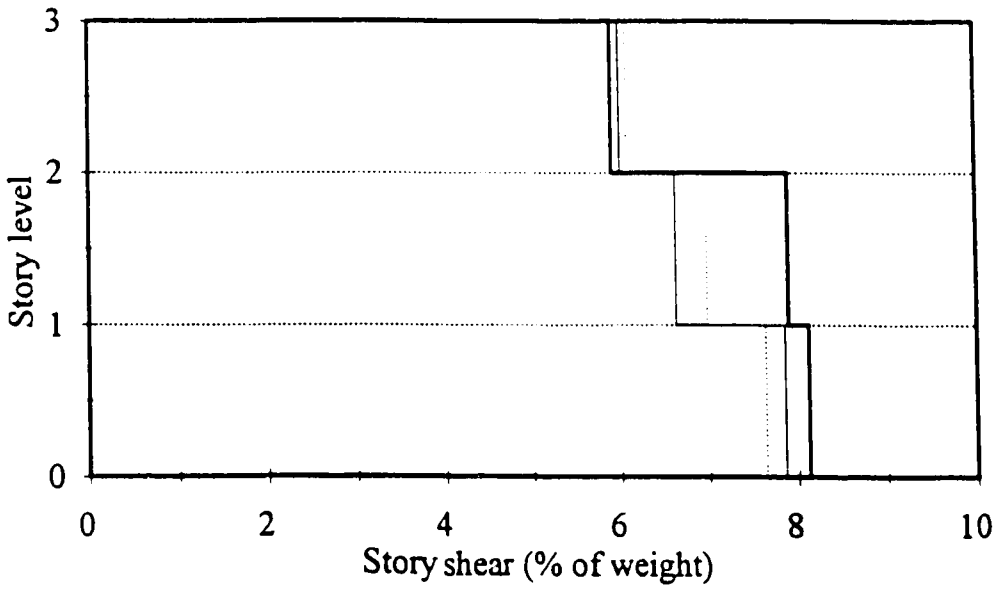

Figure 6.23 Maximum story shear force due to San Fernando earthquake

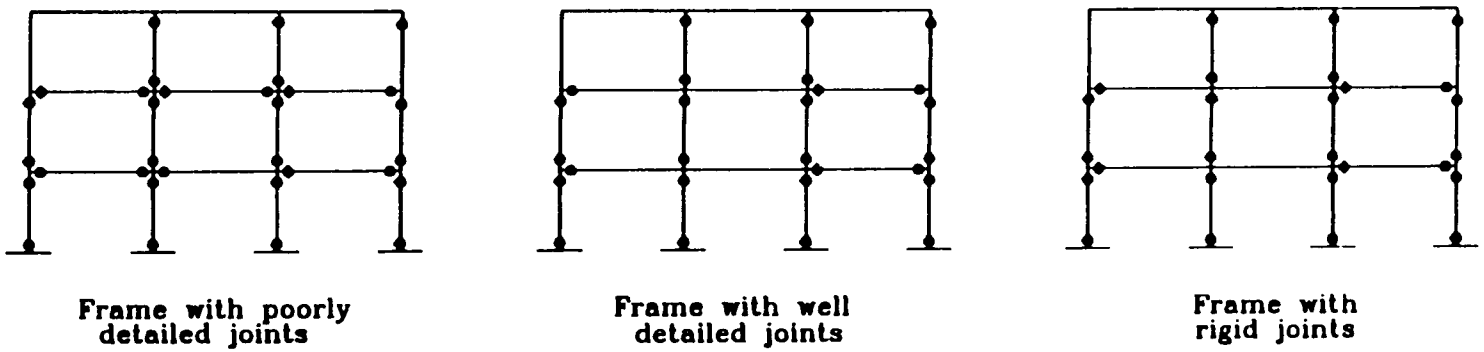

Figure 6.24 Plastic hinges formation due El Centro earthquake

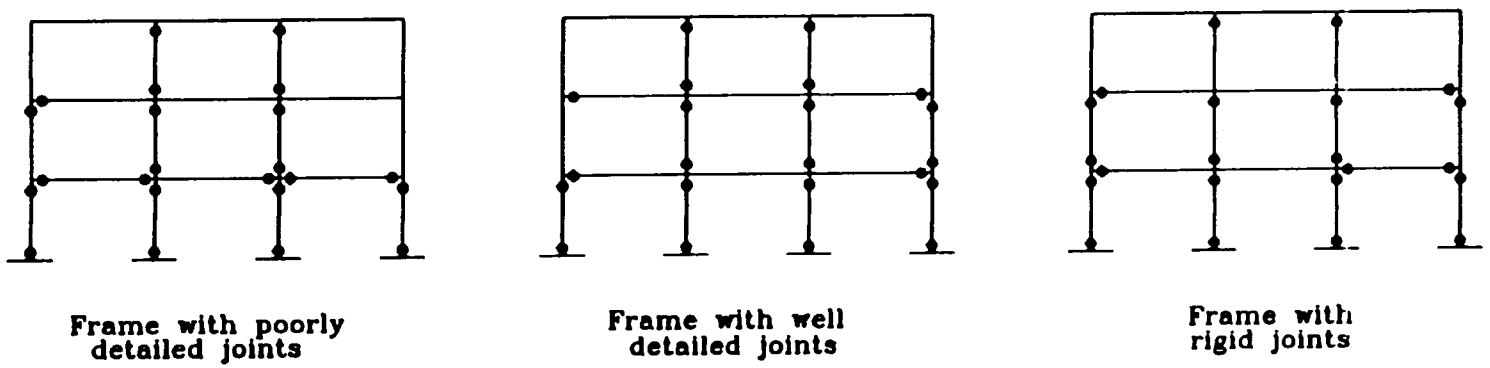

Figure 6.25 Plastic hinges formation due San Fernando earthquake

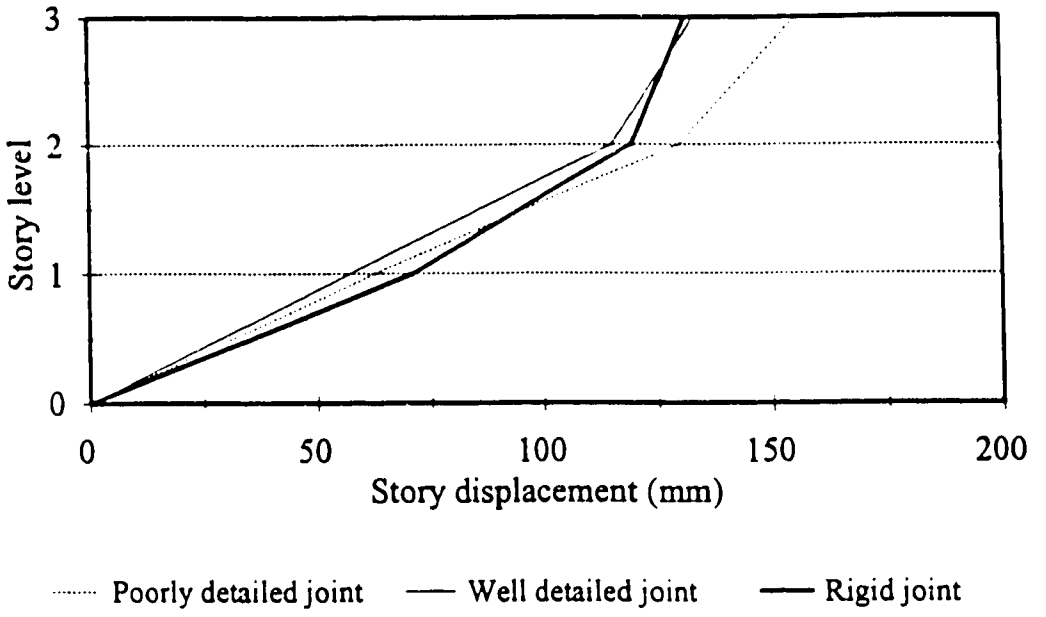

Figure 6.26 Maximum story displacements due to El Centro earthquake

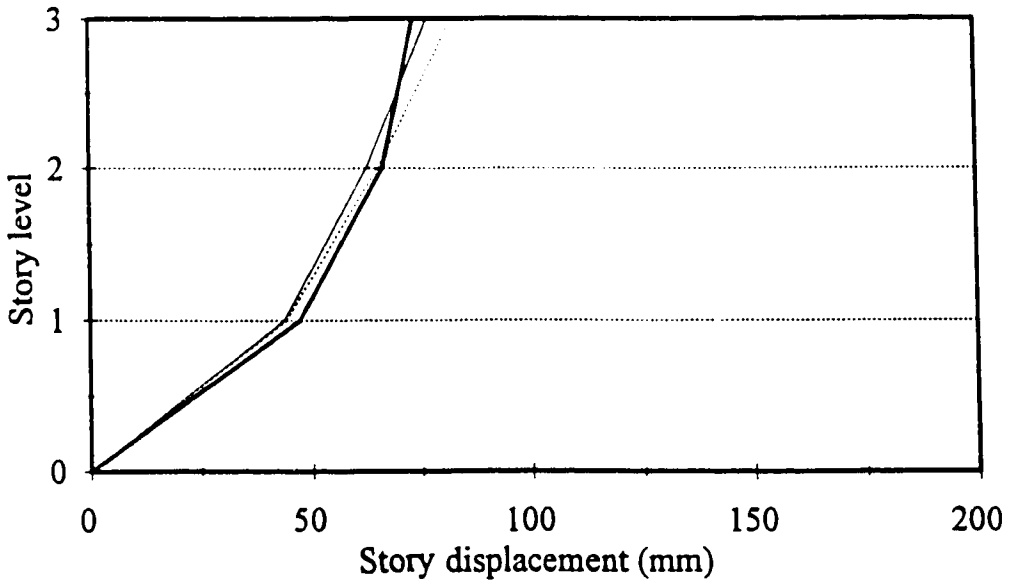

Figure 6.27 Maximum story displacements due to San Fernando earthquake

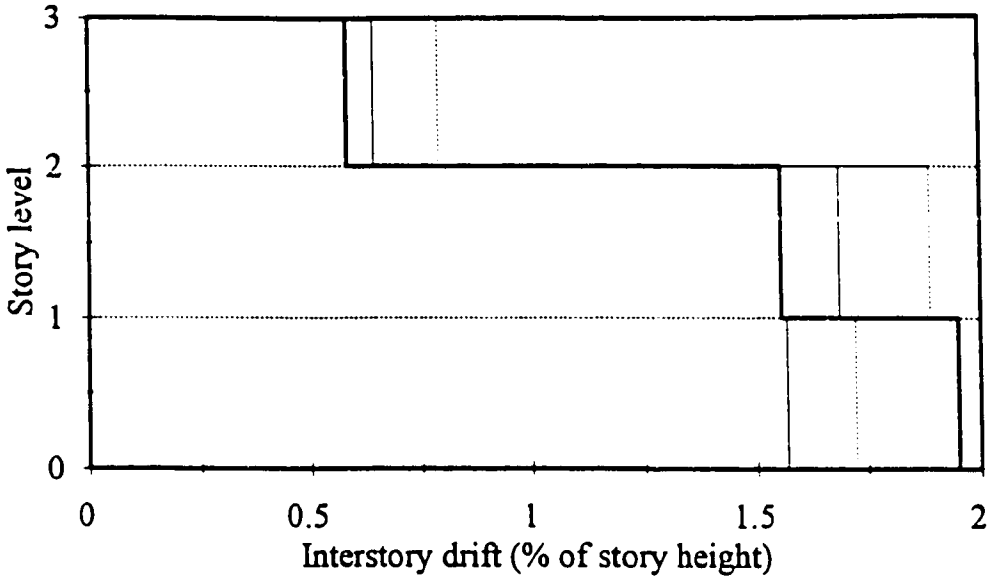

Figure 6.28 Maximum interstroy drifts due to El Centro earthquake

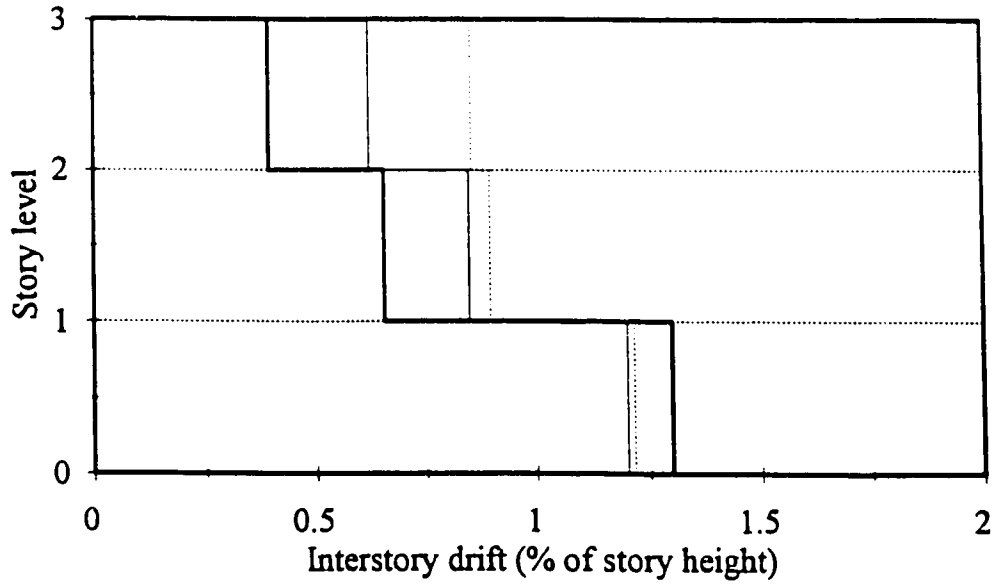

Figure 6.29 Maximum interstory drifts due to San Fernando earthquake

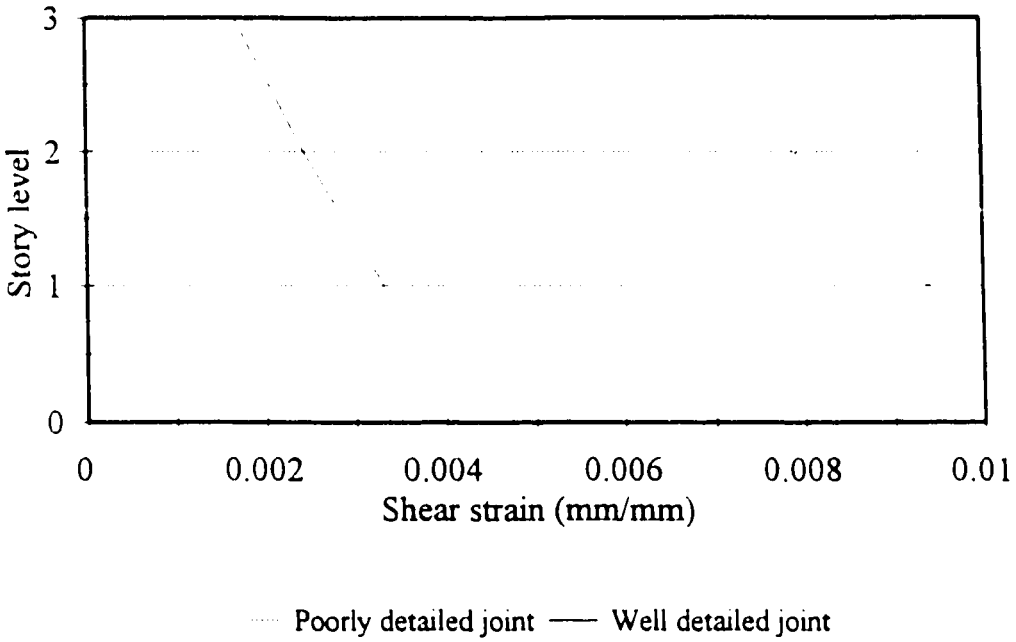

Figure 6.30 Maximum joints shear deformations due to El Centro earthquake

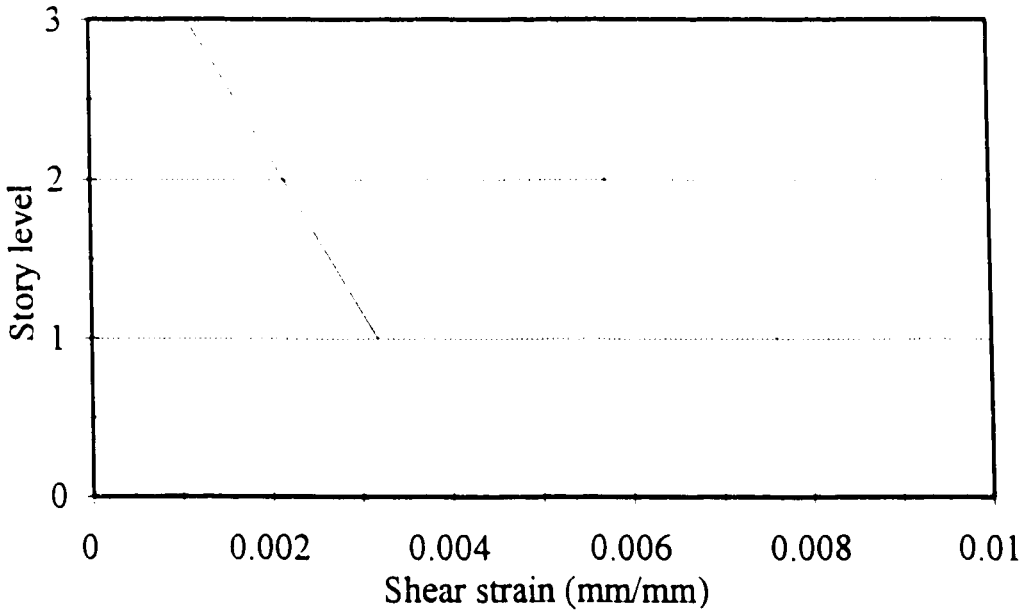

Figure 6.31 Maximum joints shear deformations due to San Fernando earthquake

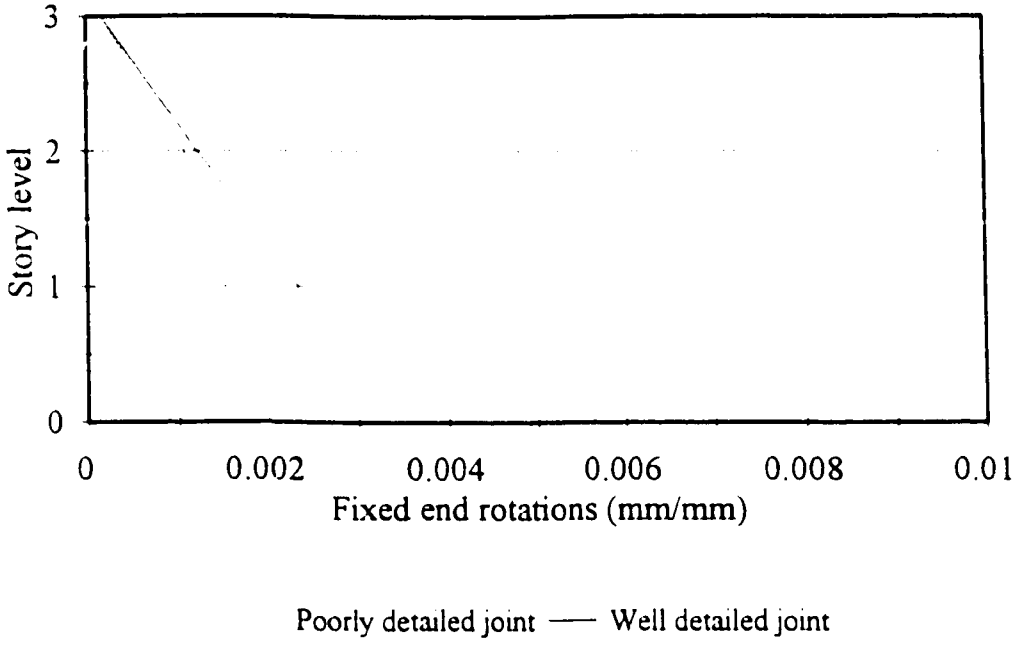

Figure 6.32 Maximum joints bond slip deformations due to El Centro earthquake

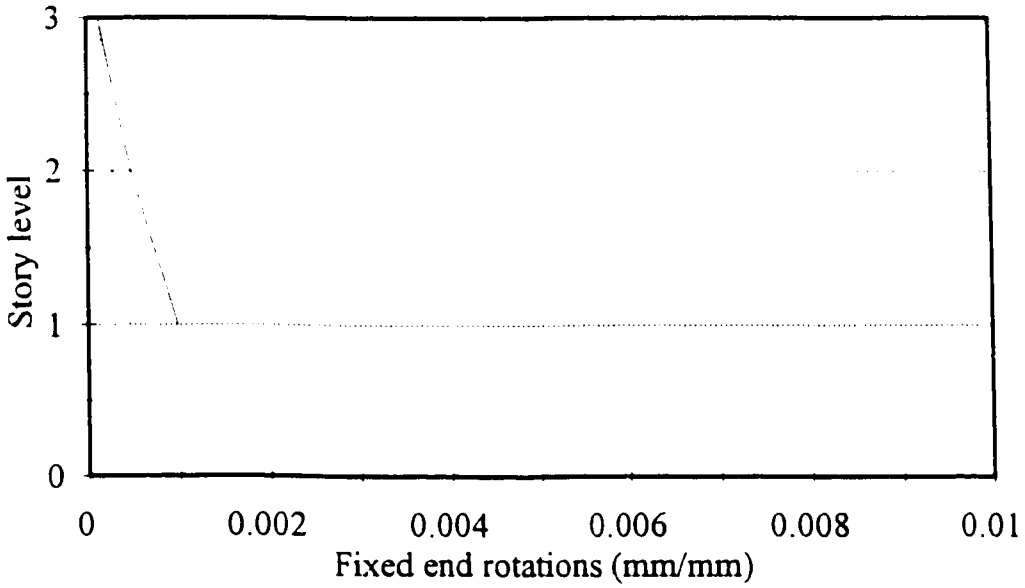

Figure 6.33 Maximum joints bond slip deformations due to San Fernando earthquake

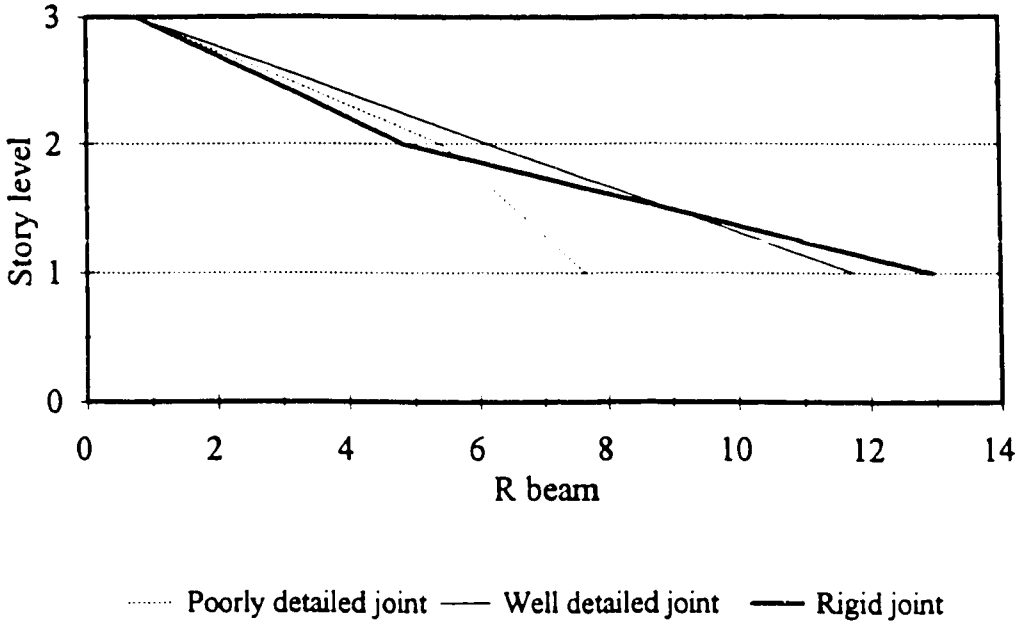

Figure 6.34 Maximum beam bar strain ratios due to El Centro earthquake

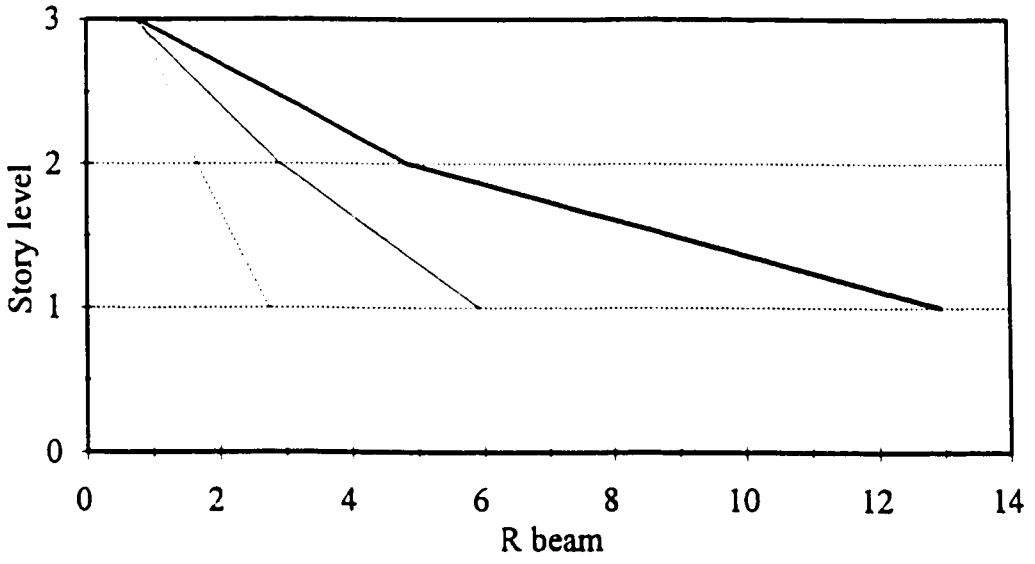

Figure 6.35 Maximum beam bar strain ratios due to San Fernando earthquake

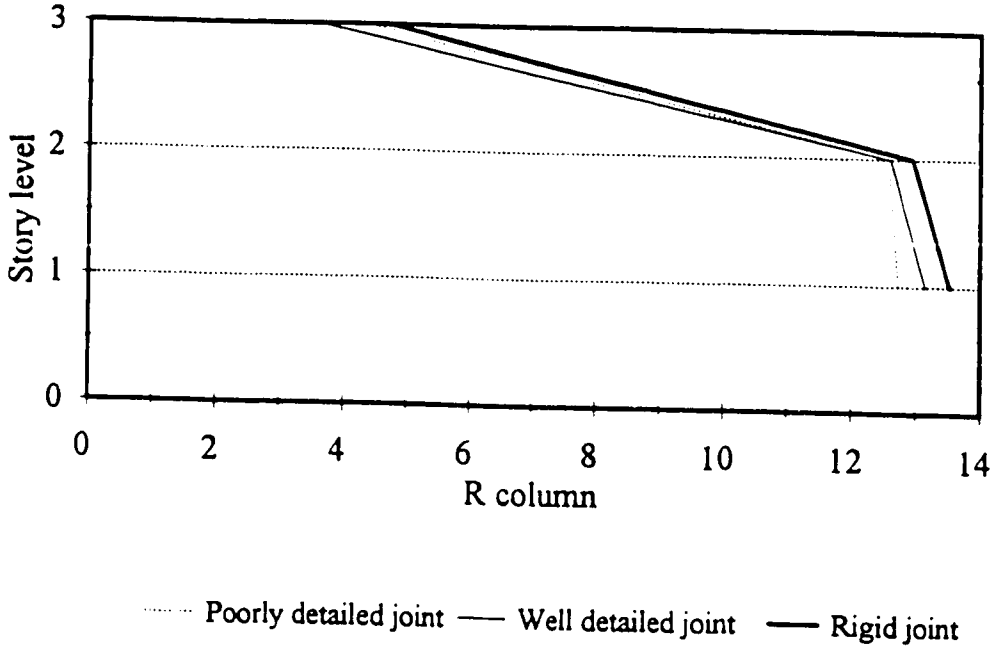

Figure 6.36 Maximum column bar strain ratios due to El Centro earthquake

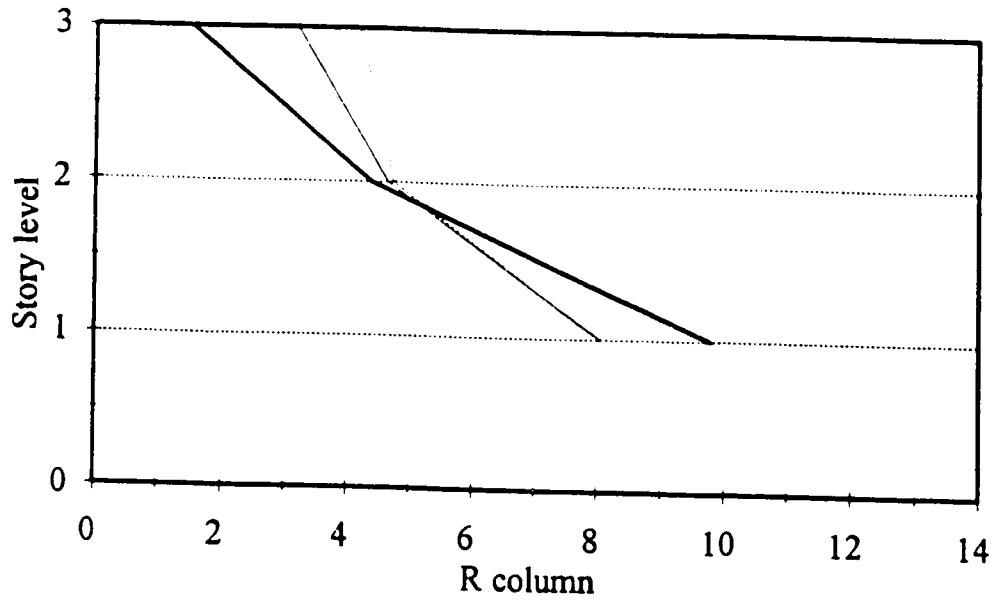

Figure 6.37 Maximum column bar strain ratios due to San Fernando earthquake

CHAPTER 7

CONCLUSIONS AND RECOMMENDATIONS

7.1 SUMMARY AND CONCLUSIONS

The major objective of this study was to develop an analytical model for reinforced concrete beam column connections for use in frame analysis. To achieve this objective a kinematic model and material models were developed as follows;

[1] The kinematic model was used to describe the shear and the bond slip deformations in the joint panel as well as flexural and shear deformations in the plastic hinge zones in the beams and the columns. The model avoided the problem of using refined meshes of simple elements by using a high power element in the critical regions of the joint panel and the plastic hinge zones in the beams and the columns. This was achieved by taking advantage of the smeared nature of the constitutive reinforced concrete model. In the model, a joint, a transition and a line element were used. Compatibility of transition and line element were considered by replacing the rotational degrees of freedom of the line elements by translation degrees of freedom.

[2] The material models developed in this study included a nonlinear finite element model for reinforced concrete. The model adopted the concept of smeared crack approach with orthogonal cracks and assumes plane stress condition. It

comprised two independent functions; the normal stress function and the shear stress function. The normal stress function defined the stress strain behavior of concrete under cyclic tension and compression. The important aspects of concrete behavior included in the normal stress function are tension stiffening, crack opening and closing, compression hardening and softening, degradation of concrete strength and stiffness in the direction parallel to the crack, and compression unloading and reloading. The shear stress function defined the cyclic relationship between the shear stress and the shear strain of concrete. A smeared reinforcing steel model was included to describe the cyclic stress strain behavior of the steel reinforcement. The aspects included in the steel model are yielding, strain hardening, Bauschinger effect as well as the cyclic unloading and reloading rules. The validation of the proposed reinforced concrete model was verified by comparing its results with the experimental data for reinforced concrete walls experiencing high shear deformations under reversed cyclic load applications. The success of the proposed model was illustrated by the good correlation achieved between its predictions and the experimental data.

[3] The bond slip model was another material model developed in this study. The proposed bond slip element used displacement interpolation functions for representing bond slip relationship along the anchored length of reinforcing bars. The model considered the gradual damage of bond and the resulting loss of strength and stiffness of anchored bar under reversed cyclic loading. The proposed bond slip model was examined at the element level by comparing its predictions with other analytical

and experimental data. This included validation examples for anchored reinforcing bars subjected to push and push-pull loading conditions under increasing monotonic and reversed cyclic loading. The verification examples showed the ability of the model to simulate the bond deterioration and eventual pull out of anchored reinforcing bars under severe cyclic excitation. The proposed bond slip model was then incorporated into the global beam column joint connection. The bond slip contact element connected and transmitted forces between beam reinforcing steel and concrete in the joint panel and allowed continuous interaction between them.

[4] After the success of the kinematic and the material models were illustrated separately the ability of the proposed beam column connection model to describe the behavior of entire beam column subassemblies was investigated. This was achieved by comparing its predictions with experimental data for connections tested under increasing monotonic and reversed cyclic loading. The verification examples used included specimens experiencing high shear and bond slip deformations, a typical situation that lightly reinforced concrete (LRC) connections would encounter during severe earthquakes. This study showed that the proposed beam column connection model can be used successfully to predict the response of beam column joints under increasing monotonic and reversed cyclic loading.

[5] The beam column joint model was used in the analysis of a gravity load designed reinforced concrete frame having three different joint detailing configurations. The first one without joint shear reinforcement, the second one with

adequate shear reinforcement and the third one with rigid connections. Pushover and time history analyses were conducted on the three story structures. Results of the pushover analysis showed that the three frames had equal lateral strength. The frames without joint shear reinforcement showed higher shear deformations and lower bond slip deformations as compared to the frame with joint shear reinforcement. The pushover analysis also showed higher deflections and interstory drifts for the frames with flexible joints as compared to the frame with rigid connections. Dynamic analysis showed higher periods of vibration for the frames with flexible joints as compared to the frame with rigid connections. Time history analysis showed more pronounced joint shear deformations, as compared to the pushover analysis, due to the degradation of the joint shear rigidities under cyclic load applications. The joint deformations in the frame with flexible joints resulted in higher lateral deflections, with the frame with unreinforced joints showing the highest deflections. The joint deformations shifted the interstory drifts to their maximum values from the base to the first story. The high joint shear deformations in the frame with unreinforced joints resulted in lower demands on the beams and thus lower bond slip deformations in the joint region. The frame with rigid connections were able to attract more loads due to their higher stiffness as compared to the other frames.

7.2 RECOMMENDATIONS FOR FUTURE RESEARCH

The following recommendations may be considered in future research

involving modeling and analysis of LRC connections:

[1] The rotating and the multidirectional crack model can be added to the concrete model. This will allow the concrete model to simulate the response of structural elements where crack rotation and formulation of multi cracks play an important role in their response.

[2] The bond slip element can be extended to allow for the representation of discontinuous beam bars in the joint panel in which case the bar pull out will govern the response of the connections.

[3] A comprehensive study on LRC buildings of different heights and subjected to a wide range of different earthquakes can be carried out to identify their general characteristic behavior and their response under seismic loading.

[4] Based on the results of the comprehensive study, as mentioned in the previous point, different retrofitting schemes can be proposed and their effect on improving the structural behavior of the LRC buildings can be assessed.

REFERENCES

ACI Committee 318, Building Code requirements and Commentary for Reinforced Concrete, American Concrete Institute, Detroit, MI.

ACI-ASCE Committee 352, 1976. " Recommendations for Design of Beam Column Joints in Monolithic Reinforced concrete Structures", (ACI-352R), American Concrete Institute, Detroit, MI.

Aktan, A.E., Karlson, B.I., and Sozen, M.A., 1973 "Stress Strain Relationships of Reinforced Bars Subjected to Large Strain Reversals." Civil Engineering Studies, Structural Research Series No. 397, University of Illinois at Urbana-Champaign, Urbana, Illinois.

Al-Mahaidi, R.S., 1978. "Nonlinear Finite Element Analysis of Reinforced Concrete Deep Members." Ph.D. Thesis, Department of Structural Engineering, Cornell University, Ithaca, New York.

Aycardi, L.E., Mander, J.B., and Reinhorn, A.M., 1992. "Seismic Resistance of Reinforced Concrete Frame Structures Designed only for Gravity Loads in Low seismicity Zones: Part II -Experimental Performance of Subassemblages." Technical Report NCEER-92-0028, National Centre for Earthquake Engineering Research, SUNY/Buffalo.

Balakrishan, S., and Murray, D.W., 1988. "Concrete Constitutive Model for NLFE Analysis of Structures," Journal of Structural Engineering, ASCE, Vol.114, No.7, pp.1449-1466.

Barzegar, F., 1989. "Analysis of RC Membrane Elements with Anisotropic Reinforcement," Journal of Structural Engineering, ASCE, Vol.115, No.3, pp.647-665.

Belarbi, A., and Hsu, T.T., 1991. "Constitutive Laws of Reinforced Concrete in Biaxial Tension Compression." Research Report UHCEE 91-2, Univ. of Houston, Houston, Texas.

Belarbi, A., and Hsu, T.T., 1995. "Constitutive Laws of Reinforced Concrete in Biaxial Tension Compression," Journal of the American Concrete Institute, Vol.92, pp.562- 573.

Beres, A. B., White, R. N., and Gergely, P. 1992, "Detailed Experimental Results of Interior and Exterior Beam Column Joint Tests Related to Lightly Reinforced Concrete Frame Buildings, Technical Report, 92-7, Cornell University, Ithaca, NY.

Berra, M., Castellani, A., Ciccotelli, S., and Coronelli, S., 1994. "Bond Slip Effects on Reinforced Concrete Elements Under Earthquake Loading," Journal of the European Association For Earthquake Engineering, Vol. 3, pp. 3-10.

Bertero, V.V., and Popov, E.P., 1977. "Seismic Behavior of Ductile Moment Resisting Reinforced Concrete Frames." Reinforced Concrete Structures in Seismic Zones, ACI Spec. Publ. SP-53, Detroit

Bicanic, N., and Mang, H., 1990. "Computer Aided Analysis and Design of Concrete Structures." Proceedings of SCI - C 1990, Second International Conference held in Zell am See, Pineridge Press, Austria.

Bolander, J.E., and Wight, J.K., 1991. "Finite Element Modeling of Shear-Wall-Dominant Buildings," Journal of Structural Engineering, ASCE, Vol.117, No.6, pp.1719-1739.

Bracci, J. M., Reinhorn, A. M., and Mander, J. B., 1992. "Seismic Resistance of R/C Frame Structures Designed only for Gravity Loads, Part III: Experimental Performance and Analytical Study of Structural Model." Technical Report NCEER-92-0029, National Centre for Earthquake Engineering Research, SUNY/Buffalo.

Cervenka, V., 1985. "Constitutive Model for Cracked Reinforced Concrete," Journal of the American Concrete Institute, Vol.82, No.6, pp.877-882.

Chang, G.A., and Mander, J.B., 1994. "Seismic Energy Based Fatigue Damage Analysis of Bridge Columns: Part I- Evaluation of Seismic Capacity." Technical Report NCEER-94-0006, National Center for Earthquake Engineering Research, State University of New York at Buffalo.

Cheung, P. C., Paualay, T., and Park, R., 1993. "Behavior of Beam Column joints in Seismically Loaded Reinforced Concrete Frames." The structural Engineer Journal, 71 (8), pp. 129-138

Chung, W., and Ahmad, S.H., 1995. "Analytical Model for Shear Critical Reinforced Concrete Members," ACI Structural Journal, Vol.121, No.6, pp.1023-1029.

Clough, R. W., and Penzin, J., 1975. Dynamics of Structures. McGraw-Hill, New York, N. Y. company

Collins, M.P., and Mitchell, D., 1991. Prestressed Concrete Structures, Prentice-Hall, New Jersey.

Cowell, A.D., Bertero, V.V., and Popov, E.P., 1982. An Investigation of Local Bond Slip Under Variation Of Specimen Parameters." EERC Report 82-23, Earthquake Engineering Research Centre, University of California, Berkeley.

Crisfield, M.A., and Wills, J., 1989. "Analysis of R/C Panels Using Different Concrete Models," Journal of Engineering Mechanics, ASCE, Vol.115, No.3, pp.578-597.

Darwin, D., and Pecknold, D.A., 1974. "Inelastic Model for Cyclic Biaxial Loading of Reinforced Concrete." Civil Engineering Studies, Structural Research Series No.409, University of Illinois at Urbana-Champaign, Urbana, Illinois.

Darwin, D., and Pecknold, D.A., 1976. "Analysis of RC Shear Panels under Cyclic Loading," Journal of the structural Division, ASCE, Vol.107, No.ST2, pp.355-369.

Eligehausen, R., Popov, E., and Bertero, V.V., 1983. "Local Bond Stress Slip Relationship of Deformed Bars Under Generalized Excitations." EERC Report 83-23, Earthquake Engineering Research Centre, University of California, Berkeley

Fardis, M.N, and Buyukozturk, O., 1980. "Shear Stiffness of Concrete by Finite Elements," Journal of the Structural Division, ASCE, Vol. 106, No. ST6, pp. 1311-1327.

Filippou, F.C., 1986a. "A Simple Model for Reinforcing Bar Anchorages Under Cyclic Excitations." EERC Report 85-05, Earthquake Engineering Research Centre, University of California, Berkeley.

Filippou, F.C., 1986b. "A Simple Model for Reinforcing Bar Anchorages Under Cyclic Excitations," Journal of Structural Engineering, ASCE, 112 (7), pp. 1639-1659.

Filippou, F.C., Popov, E.P., and Bertero, V.V., 1983a. "Effects of Bond Deterioration on Hysteretic Behaviour of Reinforced concrete Joints." EERC Report

83-19, Earthquake Engineering Research Centre, University of California, Berkeley.

Filippou, F.C., Popov, E.P., and Bertero, V.V., 1983b. "Modeling of Reinforced Concrete Joints Under Cyclic Excitations," Journal of Structural Engineering, ASCE, 109 (11), pp. 2666-2684.

Fujii, S., and Morita, S., 1991. "Comparison Between Interior and Exterior RC Beam Column Joint Behaviour. Design of Beam Column Joints for Seismic Resistance." ACI SP-123, American Concrete Institute, Detroit, Michigan.

Ghobarah, A., Aziz, T., and Biddah, A., 1996. "Seismic Rehabilitation of Reinforced Concrete Beam Column Connections." Earthquake Spectra Journal, Volume 12, No.4, pp. 761-780.

Hoffmann, G.W., Kunnath, S.K., Reinhorn, A.M., and Mander, J.B., 1992. "Gravity-Load-Designed Reinforced Concrete Buildings: Seismic Evaluation of Existing Construction and Detailing Strategies for Improved Seismic Resistance." Technical Report NCEER-92-0016. National Centre for Earthquake Engineering Research, SUNY/Buffalo.

Hu, H., and Schnobrich, W.C., 1988. "Nonlinear Analysis of Plane Stress State Reinforced Concrete under Short Term Monotonic Loading." Civil Engineering Studies, Structural Research Series No.539, University of Illinois at Urbana-Champaign, Urbana, Illinois.

Hu, H., and Schnobrich, W.C., 1990. "Nonlinear Analysis of Cracked Reinforced Concrete," ACI Structural Journal, Vol.87, No.2, pp.199-207.

Jimenez, R., Perdikaris, P., Gergely, P., and White, R., 1976. "Interface Shear Transfer and Dowel Action in Cracked Reinforced Concrete Subject to Cyclic Shear," Proceedings of the Speciality Conference of Structural Analysis, ASCE, pp. 457-475.

Jimenez, R., Gergely, P., and White, R.N., 1978. "Shear Transfer across Cracks in Reinforced Concrete." Report No. 78-4, Department of Structural Engineering, Cornell University.

Gupta, A.J., and Akbar, H., 1984. "Cracking in Reinforced Concrete Analysis," Journal of Structural Engineering, ASCE, Vol.110, No. 8, pp.1735-1746.

Kaku, T., and Asakusa, H. 1991. "Ductility Estimation of Exterior Beam Column Subassemblages in RC Frames." Design of Beam Column Joints for Seismic

Resistance. ACI SP-123, American Concrete Institute, Detroit, Michigan.

Kardestuncer, H. 1987, Finite Element Handbook, McGraw-Hill, New York, N. Y.

Karsan, I.D., and Jirsa, J.O., 1969. "Behavior of Concrete Under Compressive Loading," Journal of the Structural Division, ASCE, Vol.95, No.ST12, pp.2543-2563.

Kent, D.C, and Park, R., 1971. "Flexural Members with Confined Concrete," Journal of the Structural Division, ASCE, Vol. 97, No. 97, No. ST7, pp. 1969-1990.

Keuser , M., and Mehlhorn, G. 1987. "Finite Element Models for Bond Problems," Journal of Structural Engineering, ASCE, 113 (10), 2160-2173.

Laible, J.P., White, R.N., and Gergely, P., 1977. "Experimental Investigation of Seismic Shear Transfer Across Cracks in Concrete Nuclear Containment Vessels." Reinforced Concrete Structures in Seismic Zone, Special Publication SP53-9, American Concrete Institute, pp. 203-226.

Maison, B.F. 1992. "PC ANSR: A Computer Program for Nonlinear Structural Analysis." University of California, Berkeley.

Massicotte, B., and MacGregor, J.G., 1990. "Tension Stiffening Model of Planar Reinforced Concrete Members," Journal of Structural Engineering, Vol. 116, No. 11, pp.3039-3058.

Mattock, A.H., 1981. "Cyclic Shear Transfer and Type of Interface," Journal of the Structural Division, ASCE, Vol. 107, No. ST10, pp. 1945-1964.

Menegotto, M., and Pinto, P.E., 1973. "Method of Analysis for Cyclically Loaded Reinforced Concrete Plane Frames Including Changes in Geometry and Non-elastic Behaviour of Elements Under Combined Normal Force and Bending." IABSE Symposium on the Resistance and Ultimate Deformability of Structures Acted on by Well-Defined Repeated Loads, Lisbon.

Mikame, A., Uchida, K., and Noguchi, H., 1991. "A Study of Compressive Deterioration of Cracked Concrete." Proc. Int. Workshop on Finite Element Analysis of Reinforced Concrete, Columbia Univ., N.Y.

Miyahara, T., Kawakami, T., and Maekawa, K., 1988. "Non Linear Behavior of Cracked Reinforced Concrete Plate Element Under Uniaxial Compression." Concrete

Library International, Japan Society of Civ. Engrs., JSCE, Vol. 11, pp. 306-319.

Monti, G., Filippou, F.C., and Spacone, E., 1997. "Finite Element for Anchored Bars Under Cyclic Load Reversals," Journal of Structural Engineering, ASCE, 123 (5), pp. 614-623.

Mukaddam, M., and Kasti, M.B., 1986. "Reinforced Concrete Joints Under Cyclic Excitations," Journal of Structural Engineering, ASCE, 112 (4), pp. 937-954.

Nilson, A. H., 1971. "Internal Measurement of Bond Slip," ACI Journal, 69(7), pp. 439-441.

Ngo, D., and Scordelis, A.C., 1967. "Finite Element Analysis of Reinforced Cocnerete Beams," ACI Journal, 64(3), pp.152-163.

Noguchi, H., 1985. "Analytical Models for Cyclic Loading in RC Members." Finite Element Analysis of Reinforced Concrete, State of the Art Report, ASCE, New York, pp. 486-506.

Oesterle, R.G., Fiorato, A.E., Johal, J.E., Carpenter, H.G., Russel, H.G., and Corley, W.G., 1978. "Earthquake Resistance Structural Walls - Tests of Isolated Walls - Phase II." PCA Construction Technology Laboratory / National Science Foundation, Washington, D.C.

Okamoto, S., Shiomi, S., and Yamabe, K., 1976. "Earthquake Resistance of Prestressed Concrete Structures." Proceeding, Annual Convention, AIJ, pp.1251-1252.

Okamura, H., Maekawa, K., and Izumo, J., 1987. "Reinforced Concrete Plate Element Subjected to Cyclic Loading." Report of IABSE Colloquium, Delft, Vol. 54, pp. 575-590.

Otani, S., Kitayama, K., and Aoyama, H., 1985. "Beam Bar Bond Stress and Behaviour of Reinforced Concrete Interior Beam Column Connections." Proceedings, 2nd U.S.- N.Z.-Japan Seminar on Design of reinforced concrete beam column Joints, Department of Architecture, University of Tokyo, Tokyo, Japan, pp. 1-40.

Pantazopoulou, S.J., and Bonacci, J.F., 1994. "On Earthquake-Resistant Reinforced Concrete Frame Connections," Canadian Journal for Civil Engineering, Vol. 21, pp. 307-328.

Paulay, T., 1989. "Equilibrium Criteria for Reinforced Concrete Beam Column Joints". ACI structural Journal, 86 (6), pp. 635-643.

Paulay, T., Park, R., and Phillips, MH, 1974. "Horizontal Construction Joints in Cast in Place Reinforced Concrete." Shear in Reinforced Concrete, Special Publication SP42-27, American Concrete Institute, pp. 599-616.

Pessiki, S.P., Conley, C.H., Gergely, P., and White, R.N., 1990. "Seismic Behavior of Lightly-Reinforced-Concrete Column and Beam-column Joint Details." Technical Report NCEER-90-0014. National Centre for Earthquake Engineering Research, SUNY/Buffalo.

Russo, G., Zingone, G., Romano, F. 1990. "Analytical Solution for Bond Slip of Reinforcing Bars in Reinforced Concrete Joints," Journal of Structural Engineering, ASCE, 116 (2), pp. 336-355.

Saenz, L.P., 1964. "Equation for the Stress-Strain Curve of Concrete (Discussion)," Journal of the American Concrete Institute, Vol.61, No.9, pp.1229-1235.

Scott, B.S., Park, R., and Priestley, M.J.N., 1982. "Stress Strain Behavior of Concrete Confined by Overlapping Hoops at Low and High Strain Rates," ACI Structural Journal, Vol. 79, No. 1, pp. 13-27.

Seckin, M., 1981. "Hysteretic Behavior of Cast-in-Place Exterior Beam Column Sub-Assemblies." Ph.D. Thesis, University of Toronto, 266 p.

Sittipunt, C., and Wood, S.L., 1993. "Finite Element Analysis of Reinforced Concrete Shear Walls." Civil Engineering Studies, Structural Research Series No.584, University of Illinois, Urbana, 384 p.

Soroushian, P., Obasaki, K., and Marikunte, S., 1991. "Analytical Modeling of Bonded Bars Under Cyclic Loads." Journal of Structural Engineering, ASCE, 117 (1), pp. 48-60.

Stevens, N.J., Uzumeri, S.M., and Collins, M.P., 1987. "Analytical Modeling of Reinforced Concrete Subjected to Monotonic and Reversed Loadings." Publication No.87-1, Department of Civil Engineering, University of Toronto, Toronto, Canada.

Sulayfani, A., and Lamirault, J., 1987. "Contribution a lanalyse Experimentale du Comportement Mecanique Cyclique du Beton," (in French), Materials and Structures / Materaux et Constructions, Vol. 20, No. 118, pp. 283-292

Surana, K.S. 1983. FINESSE (Finite Element System for Non Linear Analysis), Theoretical Manual, McDonnel Douglas Automation Company, St. Louis.

Tsai, W.T., 1988. "Uniaxial Compression Stress Strain Curve for Concrete," Journal of Structural Engineering, Vol. 114, No. 9, pp. 2133-2136.

Vecchio, F.J., and Collins, M.P., 1986. "The Modified Compression Field Theory for Reinforced Concrete Elements Subjected to Shear," ACI Structural Journal, Vol.83, pp.219-231.

Viwathanatepa, S., Popov, E.P., and Bertero, V.V., 1979. "Effects of Generalized Loadings on Bond of Reinforcing Bars Embedded in Confined Concrete Blocks." EERC Report 79-22, Earthquake Engineering Research Centre, University of California, Berkeley.

Xu, C., 1991. "Analytical Model for Reinforced Concrete under Cyclic Loading." Ph.D. Dissertation, Department of Civil Engineering, University of Illinois at Urbana-Champaign, Urbana, Illinois.

Yankelevsky, O.Z., and Reinhardt, H.W., 1989. "Uniaxial Behavior of Concrete in Cyclic Tension," Journal of Structural Engineering, ASCE, Vol.115, No. 1, pp.166-182.

APPENDIX A

MANUAL FOR NEW ELEMENTS IN PC-ANSR

****

ELEMENT (2) INELASTIC TRUSS ELEMENT (REINFORCING BAR ELEMENT)

****

CONTROL INFORMATION

COLUMNS 01-05: Element type. TYPE 2
06-10: Number of elements in this group
11-15: Element number of first element in this group.
16-20: Number of material types.
21-50: Blank
51-55: Initial Stiffness damping factor
56-60: Current Stiffness damping factor

MATERIAL PROPERTY INFORMATION

COLUMNS 01-05: Material number, in sequence starting with 1.
06-15: Young's modulus of elasticity, E.
16-25: Strain hardening modulus as proportion of young's modulus (Eh/E)
26-35: Yield stress in tension and in compression.
36-45: Cross sectional area

ELEMENT GENERATION COMMANDS

COLUMNS 01-05: Element number, or number of first element in a sequentially numbered series of elements to be generated by this line.
06-10: Node number at element end I,
11-15: Node number at element end j,
16-20: Material number, if blank or zero, assumed to be equal to1
21-25: Node number increment for element generation. If blank or zero, assumed to be equal to 1
26-30: Time history output code as follows
(a) Type 0 for no time history output
(b) Type 1 for output of time history response

(c) Type -1 for output and saving of time history response

****

ELEMENT (3) ELASTIC HORIZONTAL BEAM ELEMENT CONNECTED TO A TRANSITION ELEMENT FROM BOTH SIDES

****

CONTROL INFORMATION

COLUMNS 01-05: Element type. TYPE 3
06-10: Number of elements in this group
11-15: Element number of first element in this group.
16-20: Number of element stiffness types (max 15).
21-25: Type 0
26-50: Blank
51-55: Initial Stiffness damping factor
56-60: Current Stiffness damping factor

MATERIAL PROPERTY INFORMATION

COLUMNS 01-05: Material number, in sequence starting with 1.
06-15: Young's modulus of elasticity, E.
16-25: Cross sectional area.
26-35: Reference Moment of inertia

ELEMENT GENERATION COMMANDS

COLUMNS 01-05: Element number, or number of first element in a sequentially numbered series of elements to be generated by this line.
06-10: Node number at element end I, NODI (Bottom left corner)
11-15: Node number at element end j, NODJ (Top left corner)
16-20: Node number at element end K, NODK (Top right corner)
21-25: Node number at element end L, NODL (Bottom right corner)

ELEMENT :	J	K
	I	L

26-30: Node number increment for element generation. If blank or zero, assumed to be equal to 1
31-35: Material number, if blank or zero, assumed to be equal to 1

36-40: Blank
41-45: Time history output code as follows
(a) Type 0 for no time history output
(b) Type 1 for output of time history response
(c) Type -1 for output and saving of time history response

****

ELEMENT (4) ELASTIC BEAM OR COLUMN ELEMENT CONNECTED TO A TRANSITION ELEMENT FROM ONE END AND A SINGLE NODE FROM THE OTHER END

****

CONTROL INFORMATION

COLUMNS 01-05: Element type. TYPE 4
06-10: Number of elements in this group
11-15: Element number of first element in this group.
16-20: Number of element stiffness types (max 15).
21-25: Type 0
26-50: Blank
51-55: Initial Stiffness damping factor
56-60: Current Stiffness damping factor

MATERIAL PROPERTY INFORMATION

COLUMNS 01-05: Material number, in sequence starting with 1.
06-15: Young's modulus of elasticity, E.
16-25: Cross sectional area.
26-35: Reference Moment of inertia

ELEMENT GENERATION COMMANDS

COLUMNS 01-05: Element number, or number of first element in a sequentially numbered series of elements to be generated by this line.

06-10: Node number at element end I, NODI
11-15: Node number at element end j, NODJ
16-20: Node number at element end K, NODK (The single node)

BEAMS

	K		J	I
COLUMNS		or		
	J	I		K

21-25: Node number increment for element generation. If blank or zero, assumed to be equal to 1
26-30: Material number, if blank or zero, assumed to be equal to 1
31-35: Blank
36-40: Time history output code as follows
(a) Type 0 for no time history output
(b) Type 1 for output of time history response
(c) Type -1 for output and saving of time history response

****

ELEMENT (5) INELASTIC 10 NODE ISOPARAMETRIC PLANE STRESS ELEMENT IN THE X-Y PLANE

****

CONTROL INFORMATION

COLUMNS 01-05: Element type. TYPE 5
06-10: Number of elements in this group
11-15: Element number of first element in this group.
16-20: Number of material types.
21-50: Blank
51-55: Initial Stiffness damping factor
56-60: Current Stiffness damping factor

MATERIAL PROPERTY INFORMATION
(FREE FORMAT)

N	Material number, in sequence starting with 1.
T	Thickness of element
fc'	(Compressive strength)
f t	(Tensile strength)
ϵc'	(Strain at peak compressive stress)
v	(Poisson's Ratio)

Alpha (Tension Stiffening Parameter)
Esteel (Youngs Modulus For Steel)
Hard (Strain Hardening Eh/Esteel)
(Fy)x (Yield stress in X-direction)
(Fy)y (Yield stress in Y-direction)
(Ro)x (Reinforcement ratio in X-direction)
(Ro)y (Reinforcement ratio in Y-direction)

ELEMENT GENERATION COMMANDS
(FREE FORMAT)

. Element number, or number of first element in a sequentially numbered series of elements to be generated by this line.
: Node number at element end I,(Bottom left corner)
. Node number at element end j,
: Node number at element end k,
: Node number at element end l, (Bottom right corner)
: Node number at element end m, (Top right corner)
: Node number at element end n,
: Node number at element end o,
: Node number at element end p, (Top left corner)
. Node number at element end q,
: Node number at element end r,

	P	O	N	M
ELEMENT:	Q			
	R			
	I	J	K	L

: Node number increment for element generation.
: Material number
: Time history output code as follows
(a) Type 0 for no time history output
(b) Type 1 for output of time history response
(c)Type -1 for output and saving of time history response

****

ELEMENT (6) INELASTIC 12 NODE ISOPARAMETRIC PLANE STRESS ELEMENT IN THE X-Y PLANE

****

CONTROL INFORMATION

COLUMNS 01-05: Element type. TYPE 6
06-10: Number of elements in this group
11-15: Element number of first element in this group.
16-20: Number of material types.
21-50: Blank
51-55: Initial Stiffness damping factor
56-60: Current Stiffness damping factor

MATERIAL PROPERTY INFORMATION
(FREE FORMAT)

N	Material number, in sequence starting with 1.
T	Thickness of element
Fc'	(Compressive strength)
Ft	(Tensile strength)
Ec'	(Strain at peak compressive stress)
v	(Poisson's Ratio)
Alpha	(Tension Stiffening Parameter)
Esteel	(Youngs Modulus For Steel)
Hard	(Strain Hardening Eh/Esteel)
(Fy)x	(Yield stress in X-direction)
(Fy)y	(Yield stress in Y-direction)
(Ro)x	(Reinforcement ratio in X-direction)
(Ro)y	(Reinforcement ratio in Y-direction)

ELEMENT GENERATION COMMANDS
(FREE FORMAT)

:	Element number, or number of first element in a sequentially numbered series of elements to be generated by this line.
:	Node number at element end I,(Bottom left corner)
:	Node number at element end j,
:	Node number at element end k,
:	Node number at element end l, (Bottom right corner)
:	Node number at element end m,
:	Node number at element end n,
:	Node number at element end o, (Top right corner)
:	Node number at element end p, (Top left corner)
:	Node number at element end q,
:	Node number at element end r,
:	Node number at element end S,

: Node number at element end T,

ELEMENT	R S T I	Q	P	O N M L
		J	K	

: Node number increment for element generation.
: Material number
: Time history output code as follows
(a) Type 0 for no time history output
(b) Type 1 for output of time history response
(c)Type -1 for output and saving of time history response

****

ELEMENT (9) Inelastic SPRING ELEMENT IN X DIRECTION

****

CONTROL INFORMATION

COLUMNS 01-05: Element type. TYPE 9
06-10: Number of elements in this group
11-15: Element number of first element in this group.
16-20: Number of material types.
21-50: Blank
51-55: Initial Stiffness damping factor
56-60: Current Stiffness damping factor

MATERIAL PROPERTY INFORMATION
(FREE FORMAT)

: Material number, in sequence starting with 1.
: S_1 (in mm)
: S_2 (in mm)
: S_3 (in mm)
: τ_1 (in N/mm2) (MPa)
: τ_3 (in N/mm2) (MPa)
: Alpha
: E-unl (in N/mm3)
: fc' (in N/mm2) (MPa)
: Area (in m2) (2πR L)

ELEMENT GENERATION COMMANDS

COLUMNS

	Element number, or number of first element in a sequentially numbered series of elements to be generated by this line.
	Node number at element end I
	Node number at element end j,
	Node number at element end k,
	Node number at element end l,
	Node number at element end m,
	Node number at element end n,
	Node number at element end o,
	Node number at element end p,
	Node number increment for element generation.
	Material number
	Time history output code as follows (a) Type 0 for no time history output (b) Type 1 for output of time history response (c)Type -1 for output and saving of time history response

****

APPENDIX C

INPUT DATA FOR TESTED SPECIMENS

1. SPECIMEN OF OTANI ET AL. (1985)

d_{beam} = 260 mm, Beam width = 200 mm
d_{column} = 280 mm, Column width = 300 mm

CONCRETE PROPERTIES:

f_c' = 25 Mpa ε_c' = 0.002 Mpa f_t = 1 Mpa α = 0.15

BOND SLIP PROPERTIES:

TOP REINFORCEMENT:

Confined Region: S1 = 1.0 mm, S2 = 3.0 mm, S3 = 10.5 mm, $\tau 1$ = 17.00 MPa, $\tau 3$ = 5.0 Mpa, α = 0.40

Unconfined Region: S1 = 1.0 mm, S2 = 3.0 mm, S3 = 10.5 mm, $\tau 1$ = 17.00 MPa, $\tau 3$ = 5.0 Mpa, α = 0.40 (Bar is pushed)

Unconfined Region: S1 = 0.3 mm, S2 = 0.3 mm, S3 = 1.0 mm, $\tau 1$ = 7.0 MPa, $\tau 3$ = 0 Mpa, α = 0.40 (Bar is pulled)

BOTTOM REINFORCEMENT:

Confined Region: S1 = 1.0 mm, S2 = 3.0 mm, S3 = 10.5 mm, $\tau 1$ = 17.0 MPa, $\tau 3$ = 5.0 Mpa, α = 0.40

Unconfined Region: S1 = 1.0 mm, S2 = 3.0 mm, S3 = 10.5 mm, $\tau 1$ = 17.0 MPa, $\tau 3$ = 5.0 Mpa, α = 0.40 (Bar is pushed)

Unconfined Region: S1 = 0.3 mm, S2 = 0.3 mm, S3 = 1.0 mm, $\tau 1$ = 7 0 MPa, $\tau 3$ = 0 Mpa, α = 0.40 (Bar is pulled)

BEAM REINFORCEMENT:

Top Reinforcement: Area = 856 mm^2, Yield stress = 326 Mpa, Strain Hardening = 2 %

Bottom Reinforcement: Area = 428 mm^2, Yield stress = 326 Mpa, Strain Hardening = 2 %

Distributed Reinforcement: ρ_X = 0.0
ρ_Y = 0.64%, Yielding stress = 330 MPa, Strain Hardening = 2 %

COLUMN REINFORCEMENT:

Right Reinforcement: Area = 508 mm^2, Yield stress = 430 MPa, Strain Hardening = 2 %

Left Reinforcement: Area = 508 mm^2, Yield stress = 430 MPa, Strain Hardening = 2 %

Distributed Reinforcement: ρ_x = 0.85%, Yield stress = 330 MPa, Strain Hardening = 2%
ρ_y = 1.13 %, Yield stress = 430 MPa, Strain Hardening = 2%

JOINT REINFORCEMENT:

Distributed Reinforcement: ρ_x = 0.27%, Yield stress = 330 MPa, Strain Hardening = 2%
ρ_y = 1.13 %, Yield stress = 430 MPa, Strain Hardening = 2%

ELASTIC BEAM:

Young's Modulus = 25000 MPa, Moment of inertia= $450x10^6$ mm^4, Area = $60x10^3$ mm^2

ELASTIC COLUMN:

Young's Modulus = 25000 MPa, Moment of inertia= $675x10^6$ mm^4, Area = $90x10^3$ mm^2

2. SPECIMENS OF KAKU AND ASAKUSA (1991)

d_{beam} = 200 mm, Beam width = 160 mm
d_{column} = 200 mm, Column width = 220 mm

CONCRETE PROPERTIES:

f_c' = 30 Mpa ε_c' = 0.002 Mpa f_t = 1 Mpa α = 0.15

BOND SLIP PROPERTIES:

TOP REINFORCEMENT:

Hooked Region: S1 = 1.0 mm, S2 = 3.0 mm, S3 = 100 mm, $\tau 1$ = 25.00 MPa, $\tau 3$ = 5.0 Mpa, α = 0.20

Confined Region: S1 = 1.0 mm, S2 = 3.0 mm, S3 = 10.5 mm, $\tau 1$ = 17.00 MPa, $\tau 3$ = 5.0 Mpa, α = 0.40

Unconfined Region: S1 = 1.0 mm, S2 = 3.0 mm, S3 = 10.5 mm, $\tau 1$ = 17.00 MPa, $\tau 3$ = 5.0 Mpa, α = 0.40 (Bar is pushed)

Unconfined Region: S1 = 0.3 mm, S2 = 0.3 mm, S3 = 1.0 mm, $\tau 1$ = 6.0 MPa, $\tau 3$ = 0 Mpa, α = 0.40 (Bar is pulled)

BOTTOM REINFORCEMENT:

Hooked Region: S1 = 1.0 mm, S2 = 3.0 mm, S3 = 100 mm, $\tau 1$ = 25.00 MPa, $\tau 3$ = 5.0 Mpa, α = 0.20

Confined Region: S1 = 1.0 mm, S2 = 3.0 mm, S3 = 10.5 mm, $\tau 1$ = 17.0 MPa, $\tau 3$ = 5.0 Mpa, α = 0.40

Unconfined Region: S1 = 1.0 mm, S2 = 3.0 mm, S3 = 10.5 mm, $\tau 1$ = 17.0 MPa, $\tau 3$ = 5.0 Mpa, α = 0.40 (Bar is pushed)

Unconfined Region: S1 = 0.3 mm, S2 = 0.3 mm, S3 = 1.0 mm, $\tau 1$ = 7.0MPa, $\tau 3$ = 0 Mpa, α = 0.40 (Bar is pulled)

BEAM REINFORCEMENT:

Top Reinforcement: Area = 508 mm^2, Yield stress = 390 Mpa, Strain Hardening = 2 %

Bottom Reinforcement: Area = 508 mm^2, Yield stress = 390 Mpa, Strain Hardening = 2 %

Distributed Reinforcement: ρ_X = 0.0
ρ_Y = 0.8%, Yielding stress = 280 MPa, Strain Hardening = 2 %

COLUMN REINFORCEMENT:

Right Reinforcement: Area = 398 mm^2, Yield stress = 360 MPa, Strain Hardening = 2 %

Left Reinforcement: Area = 398 mm^2, Yield stress = 360 MPa, Strain Hardening = 2 %

Distributed Reinforcement: ρ_X = 0.8%, Yield stress = 280 MPa, Strain Hardening = 2%
ρ_y = 0

JOINT REINFORCEMENT:

Distributed Reinforcement: ρ_X = 0.49%, Yield stress = 280 MPa, Strain Hardening = 2%
ρ_y = 0.0

ELASTIC BEAM:

Young's Modulus = 30000 MPa, Moment of inertia= 142×10^6 mm^4, Area = 35×10^3 mm^2

ELASTIC COLUMN:

Young's Modulus = 30000 MPa, Moment of inertia= 195×10^6 mm^4 ,
Area = 48×10^3 mm^2

3. SPECIMEN OF FUJII AND MORITA (1991)

d_{beam} = 200 mm, Beam width = 160 mm
d_{column} = 200 mm, Column width = 220 mm

CONCRETE PROPERTIES:

f_c' = 30 Mpa ε_c' = 0.002 Mpa f_t = 1 Mpa α = 0.15

BOND SLIP PROPERTIES:

TOP REINFORCEMENT:

Hooked Region:	S1 = 1.0 mm, S2 = 3.0 mm, S3 = 100 mm, $\tau 1$ = 25.0 MPa, $\tau 3$ = 5.0 Mpa, α = 0.20
Confined Region:	S1 = 1.0 mm, S2 = 3.0 mm, S3 = 10.5 mm, $\tau 1$ = 17.0 MPa, $\tau 3$ = 5.0 Mpa, α = 0.40
Unconfined Region:	S1 = 1.0 mm, S2 = 3.0 mm, S3 = 10.5 mm, $\tau 1$ = 17.0 MPa, $\tau 3$ = 5.0 Mpa, α = 0.40 (Bar is pushed)
Unconfined Region:	S1 = 0.3 mm, S2 = 0.3 mm, S3 = 1.0 mm, $\tau 1$ = 7.0 MPa, $\tau 3$ = 0 Mpa, α = 0.40 (Bar is pulled)

BOTTOM REINFORCEMENT:

Hooked Region:	S1 = 1.0 mm, S2 = 3.0 mm, S3 = 100 mm, $\tau 1$ = 25.0 MPa, $\tau 3$ = 5.0 Mpa, α = 0.20
Confined Region:	S1 = 1.0 mm, S2 = 3.0 mm, S3 = 10.5 mm, $\tau 1$ = 17.0 MPa, $\tau 3$ = 5.0 Mpa, α = 0.40
Unconfined Region:	S1 = 1.0 mm, S2 = 3.0 mm, S3 = 10.5 mm, $\tau 1$ = 17.0 MPa, $\tau 3$ = 5.0 Mpa, α = 0.40 (Bar is pushed)
Unconfined Region:	S1 = 0.3 mm, S2 = 0.3 mm, S3 = 1.0 mm, $\tau 1$ = 7.0 MPa, $\tau 3$ = 0 Mpa, α = 0.40 (Bar is pulled)

BEAM REINFORCEMENT:

Top Reinforcement:	Area = 570 mm^2, Yield stress = 417 Mpa, Strain Hardening = 2 %
Bottom Reinforcement:	Area = 570 mm^2, Yield stress = 417 Mpa, Strain Hardening = 2 %
Distributed Reinforcement:	ρ_X = 0.0
	ρ_Y = 0.8%, Yielding stress = 280 MPa,

Strain Hardening = 2 %

COLUMN REINFORCEMENT:

Right Reinforcement: Area = 380 mm^2, Yield stress = 395 MPa, Strain Hardening = 2 %

Left Reinforcement: Area = 380 mm^2, Yield stress = 395 MPa, Strain Hardening = 2 %

Distributed Reinforcement: ρ_X = 0.8%, Yield stress = 297 MPa, Strain Hardening = 2%
ρ_Y = 1.57%, Yield stress = 395 MPa, Strain Hardening = 2%

JOINT REINFORCEMENT:

Distributed Reinforcement: ρ_X = 0.49%, Yield stress = 297 MPa, Strain Hardening = 2%
ρ_Y = 1.57%, Yield stress = 395 MPa, Strain Hardening = 2%

ELASTIC BEAM:

Young's Modulus = 30000 MPa, Moment of inertia= $208x10^6$ mm^4, Area = $40x10^3$ mm^2

ELASTIC COLUMN:

Young's Modulus = 30000 MPa, Moment of inertia= $195x10^6$ mm^4, Area = $48x10^3$ mm^2

4. SPECIMENS OF VIWATHANATEPA ET AL. (1979)

d_{beam} = 386 mm, Beam width = 229 mm
d_{column} = 412 mm, Column width = 432 mm

CONCRETE PROPERTIES:

f_c' = 30 Mpa ε_c' = 0.002 Mpa f_t = 1 Mpa α = 0.15

BOND SLIP PROPERTIES:

TOP REINFORCEMENT:

Confined Region: S1 = 1.0 mm, S2 = 3.0 mm, S3 = 10.5 mm, $\tau 1$ = 15.00 MPa, $\tau 3$ = 5.0 Mpa, α = 0.40

Unconfined Region: S1 = 1.0 mm, S2 = 3.0 mm, S3 = 10.5 mm, $\tau 1$ =

15.00 MPa, $\tau 3$ = 5.0 Mpa, α = 0.40 (Bar is pushed)

Unconfined Region: S1 = 0.3 mm, S2 = 0.3 mm, S3 = 1.0 mm, $\tau 1$ = 6.0 MPa, $\tau 3$ = 0 Mpa, α = 0.40 (Bar is pulled)

BOTTOM REINFORCEMENT:

Confined Region: S1 = 1.0 mm, S2 = 3.0 mm, S3 = 10.5 mm, $\tau 1$ = 15.0 MPa, $\tau 3$ = 5.0 Mpa, α = 0.40

Unconfined Region: S1 = 1.0 mm, S2 = 3.0 mm, S3 = 10.5 mm, $\tau 1$ = 15.0 MPa, $\tau 3$ = 5.0 Mpa, α = 0.40 (Bar is pushed)

Unconfined Region: S1 = 0.3 mm, S2 = 0.3 mm, S3 = 1.0 mm, $\tau 1$ = 6.0 MPa, $\tau 3$ = 0 Mpa, α = 0.40 (Bar is pulled)

BEAM REINFORCEMENT:

Top Reinforcement: Area = 1140 mm^2, Yield stress = 450 Mpa, Strain Hardening = 2 %

Bottom Reinforcement: Area = 593 mm^2, Yield stress = 450 Mpa, Strain Hardening = 2 %

Distributed Reinforcement: ρ_X = 0.0
ρ_Y = 0.6%, Yielding stress = 450 MPa, Strain Hardening = 2 %

COLUMN REINFORCEMENT:

Right Reinforcement: Area = 855 mm^2, Yield stress = 450 MPa, Strain Hardening = 2 %

Left Reinforcement: Area = 855 mm^2, Yield stress = 450 MPa, Strain Hardening = 2 %

Distributed Reinforcement: ρ_X = 0.5%, Yield stress = 450 MPa, Strain Hardening = 2%
ρ_Y = 0.9%, Yield stress = 450 MPa, Strain Hardening = 2%

JOINT REINFORCEMENT:

Distributed Reinforcement: ρ_X = 0.50%, Yield stress = 450 MPa, Strain Hardening = 2%
ρ_Y = 0.9%, Yield stress = 450 MPa, Strain Hardening = 2%

ELASTIC BEAM:

Young's Modulus = 30000 MPa, Moment of inertia=1277x10^6 mm^4, Area = 93x10^3 mm^2

ELASTIC COLUMN:

Young's Modulus = 30000 MPa, Moment of inertia=2902×10^6 mm^4, Area =186×10^3 mm^2